Spectroscopic Analysis of Electronic Energy Transfer in Molecular Cassettes Formed Around Boron Dipyrromethene Dyes

Effat Bahaidarah

A PhD Thesis submitted to:

Newcastle University-School of Chemistry

April 2014

Abstract

Photosynthesis, in its many diverse forms, has provided inspiration for countless researchers over several centuries and continues to spring surprises and new concepts. At the simplest level, photosynthesis can be considered to store sunlight in the form of chemical (or electrochemical) potential. As such, it is often proposed as a model for artificial systems aimed at the conversion and storage of solar energy. One of many key components of photosynthesis concerns the collection of sunlight by various pigments and the transfer of the resultant exciton to a reaction centre, where fuel formation can take place. In this thesis, we examine chemical systems that facilitate electronic energy transfer (EET) between chromophores arranged in rather simple molecular architectures built around boron dipyrromethene (Bodipy) dyes. These latter compounds are taken from an ever-expanding family of robust, highly fluorescent synthetic reagents developed originally as laser dyes and bio-labels.

Chapter 1 gives a brief introduction to the general field of EET and covers a few basic concepts special to the photosynthetic apparatus. This is followed by a brief consideration of Förster theory, which is the staple mechanism underpinning much of the work covered in later chapters, and mention of the alternative Dexter theory for EET. By way of acknowledging that we are not the only researchers to explore this type of work, we provide a few key examples of molecular systems designed to probe various aspects of intramolecular EET. These examples cover Bodipy-based arrays and certain bio-inspired molecular systems.

In Chapter 2, we describe the behaviour of certain sterically unhindered Bodipy dyes as fluorescent probes for rheology changes, most notably variations in viscosity under ambient conditions. This situation depends on changing the degree of (micro) friction between an appended *meso*-aryl ring and the surrounding medium. In order to vary in a systematic manner the resistance to gyration of the aryl ring, the photophysical properties of the dye have been recorded in different media and as functions of temperature and pressure. Local viscosity is also affected by the presence of an inert polymer. Extending the system to include an unusual bichromophore where the linkage is through boron-oxygen bonds switches off the sensory action due to light-induced electron transfer.

Chapter 3 includes a critical comparison of EET within two disparate molecular types; namely, covalently-linked and non-covalently-linked molecular dyads bearing

identical subunits drawn from the Bodipy family. Here, the intention is to explore how the binding motif affects the likelihood of intramolecular EET between the subunits. Both systems, which consist of a yellow Bodipy dye as a donor and a blue Bodipy dye as the complementary acceptor, show highly efficient EET. Again, the probability of EET has been probed as a function of applied pressure and temperature to better expose the mechanism. The non-covalently-linked system, which makes use of electrostatic binding between charged species, forms a liquid crystalline state upon heating and it is notable that efficacious EET occurs within this phase.

Chapter 4 looks at the nano-mechanical properties of molecular-scale bridges in linear donor-spacer-acceptor compounds by monitoring the probability of intramolecular EET as a function of bridge length. The bridge (or spacer) consists of 1 to 5 ethynylene-carborane units that allow the centre-to-centre distance between the donor and acceptor to be varied systematically from 38 to 115 Å. Interestingly, the probability of EET is higher than the predicted value for all systems except the shortest bridge. On cooling to 77K, the agreement between theory and experiment agrees much better but depends on applied pressure in fluid solution at room temperature. We rationalise these various results in terms of structural distortion of the longer bridges, thereby allowing determination of the strain energy and Young's modulus for the spacer unit.

In Chapter 5, we report on a study of intramolecular EET in a molecular triad where the highest-energy donor is situated in the centre and there are two disparate Bodipy at the terminals. Overall, the probability of EET exceeds 95% and the individual EET steps can be resolved; the rate of EET follows the order of spectral overlap integrals. By selective protonation of one of the Bodipy-based terminals, it is possible to change the relative ordering of the spectral overlap integrals and thereby switch the direction of EET. This chapter also includes an investigation of the general photophysical behaviour of the symmetric triads, where the same Bodipy dye is present at each terminal, in addition to the spectroscopic properties of the isolated chromophores. Experimental variations include changes in solvent polarity, effect of lowing the temperature, moving from fluid to solid phases and applying high pressure to the fluid medium are discussed in this chapter.

Finally, Chapter 6 provides a brief summary of the experimental approaches used throughout the work, including instrumentation and chemicals. In addition, the many mathematical equations and computer programs employed are mentioned here.

List of abbreviations

λ_{abs}	Absorption maximum in nm
λ_{flu}	Fluorescence maximum in nm
λ_{ex}	Excitation wavelength in nm
Φ_{flu}	Fluorescence quantum yield
τ_s	Lifetime of singlet-excited state
SS	Stokes' shift in cm^{-1}
ε_{max}	Molar absorption coefficient in $M^{-1}cm^{-1}$
ν	Wave number in cm^{-1}
EET	Electronic energy transfer
k_{EET}	Electronic energy transfer rate constant
k_{rad}	Radiative rate constant
k_{nrd}	Non-radiative rate constant
k_{act}	Activated rate constant
k_{et}	Electron transfer rate constant
P_{EET}	Probability of electronic energy transfer
THF	Tetrahydrofuran
MTHF	2-methyltetrahydrofuran
BuCN	Butyronitrile
AcCN	Acetonitrile
PC	Propylene carbonate
DCM	Dichloromethane
$CHCl_3$	Chloroform
EtOAc	Ethyl acetate
Et_2O	Diethyl ether
Bu_2O	Dibutyl ether
ε_s	Solvent dielectric constant
PMMA	Poly(methyl methacrylate)

Acknowledgements

I would like to express my deep appreciation and gratitude to my supervisor Professor Anthony Harriman, for his guidance with a lot of patience from the first day in my PhD until the last letter in this thesis and after. Many thanks also to Professor Andrew Benniston for his assistance and to all past and current members of the molecular photonics laboratory. Special thanks are due to Dr. Mohammed Alamiry for his assistance with the pressure experiments.

I would also like to thank Dr. Raymond Zeissel and his group (Université Louis Pasteur, Strasbourg, France) for synthesis of the compounds studied here, without which this work would not have been possible.

Special thanks are directed to King AbdulAziz University as represented through the Saudi Embassy for providing scholarship funds and the financial support. Thanks are also due to Newcastle University for providing access to necessary facilities.

Finally, I would like to thank all of my big family and the little one, my husband and my sweet son, for their support and prayers. It is very much appreciated.

List of publications

1. Olivier, J.-H.; Barberá, J.; Bahaidarah, E.; Harriman, A.; Ziessel, R. *J. Am. Chem. Soc.* **2012**, *134*, 6100.

2. Alamiry, M. A. H.; Bahaidarah, E.; Harriman, A.; Bura, T.; Ziessel, R. *RSC Adv.* **2012**, *2*, 9851.

3. Alamiry, M. A. H.; Bahaidarah, E.; Harriman, A.; Olivier, J. H.; Ziessel, R. *Pure Appl. Chem.* **2013**, *85*, 1349.

4. Hablot, D.; Ziessel, R.; Alamiry, M. A. H.; Bahaidarah, E.; Harriman, A. *Chem. Sci.* **2013**, *4*, 444.

Contents

Chapter 1. Introduction

1.1 Background

The demand for renewable and sustainable energy sources has grown rapidly during the past century and is now receiving more attention across the globe. This critical need for new supplies of energy has been stimulated by a massive growth in world population, by a change in manufacturing protocols that has enforced major industrialisation across the third-world, and by an escalation in energy consumption. The situation is acerbated by the realisation that some 80% of our current energy consumption is supplied by fossil fuels, such as oil, coal and natural gas, that themselves give rise to important pollutants during combustion. We have the added incentive that our convenient supplies of fossil fuels are depleting rapidly and new stocks are only being identified in inaccessible places. The net result is global insecurity, political unrest, the build-up of greenhouse gases, onset of climate change, appearance of acidified oceans and proliferation of oil spills. So, one of the major challenges for contemporary science is to identify and develop renewable sources of energy that are abundant, environmentally clean, inexpensive and readily available across the planet. Sunlight remains the most attractive solution to this global problem, but no doubt augmented by other sources such as tidal energy, wind turbines and geothermal stocks. It has been quoted that we need to collect only about 0.02% of the total sunlight that reaches the surface of the earth to cover our projected energy demand. However, sunlight is intermittent, of variable intensity and difficult to store in the form of chemical potential.

The use of sunlight as a form of heating is very well known and, of course, solar energy is utilised extensively to generate biomass. More recently, there has been a large-scale expansion of using semiconductor-based devices to convert sunlight to electricity that can be fed directly into the national grid. This is a very important approach towards moving forward to embrace renewable energy supplies but it is expensive and regional. With suitable adaptation, the photo-electrochemical approach can be used to produce hydrogen gas and thereby head towards a storable product. Other fuels are possible, most notably the reduction of carbon dioxide to carbon monoxide or formic acid, while the photochemical oxidation of water to molecular oxygen allows the full dissociation of water to be realised. Molecular catalysts are needed for such reactions and, although progress continues to be made in this area, a

great amount of fundamental research is needed before effective water-splitting processes become available. This generic field of research is often termed "artificial photosynthesis" and sets out to mimic many of the key features of natural photosynthesis. In some cases, the reagents used are inspired by Nature but more often unnatural analogues are used. At present, only the natural photosynthetic apparatus is able to operate on a large scale under ambient conditions.[1-5]

In natural photosynthesis, solar energy is captured and stored by way of the multi-electron reduction of carbon dioxide to produce carbohydrates and (in green plants) by the four-electron oxidation of water to molecular oxygen. As it appears in Figure 1, this combined process takes place in two main steps: namely, a light-dependent stage and a corresponding light-independent (or dark) reaction. In the primary step, light-harvesting complexes absorb sunlight and funnel the excitation energy to the photosynthetic reaction centre complex where electron transfer is initiated. The dark steps employ mild catalysis to produce the required sugars.[1,6-8] The overall process requires three main components: namely, a set of light-harvesting antennae, a carefully designed reaction centre complex, and a series of highly specific catalysts. The light-harvesting antenna consists of one or more chromophores (pigments) that are bound to specific proteins so as to form organized groups. This unit has three main functions related to: (i) light absorption, (ii) effective transport of the exciton around the array until trapped by the reaction centre complex, and (iii) protection of the system from damage by excess excitation energy or active oxygen.[9]

Figure 2 shows the light-harvesting array present in cyanobacteria as an example of the chromophoric arrangement used to focus excitonic energy in terms of frequency distribution and spatial location.[3] Chlorophylls are the most abundant natural photosynthetic pigment group, supported by phycobilins and carotenoids, and serve the purpose as primary light absorbers.[10,11] Carotenes are responsible for the photo-protective mechanism by quenching triplet chlorophyll (or more precisely chlorophyll-sensitized singlet oxygen formation) and, in addition, collecting light at wavelengths where chlorophyll absorbs only weakly. They may be responsible also for photosynthetic regulation.[12-15] The goal of the reaction centre complex is to produce stable charge separation and thereby convert the excitation energy to chemical potential. In principle, the reaction centre can absorb sunlight without the need for the ancillary light-harvesting setup but there are many advantages to be gained by having the latter in place.[3] In general, the light harvesting efficiency exceeds 90% and the energy-transfer probability is at least 95%.[1,16] As a result, most of the photons incident on the light-

harvesting array under low intensity excitation can be used for fuel production. At high photon flux, exciton-exciton annihilation takes place and a certain fraction of the absorbed photons is lost by way of heat generation.

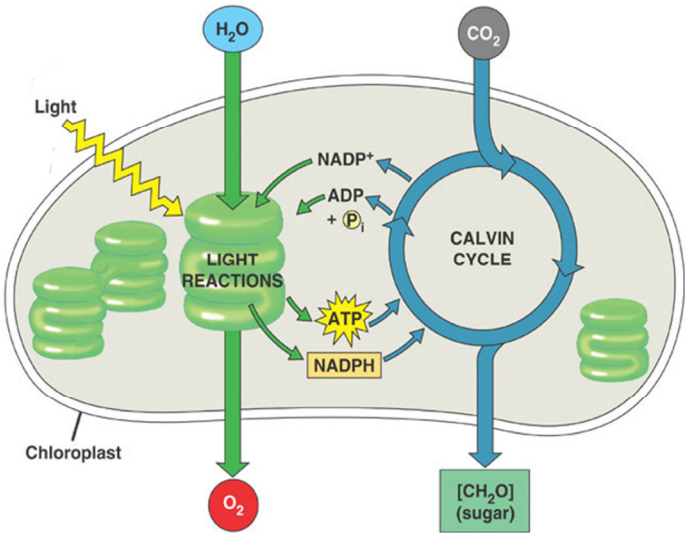

Figure 1. General overview of natural photosynthesis.[7]

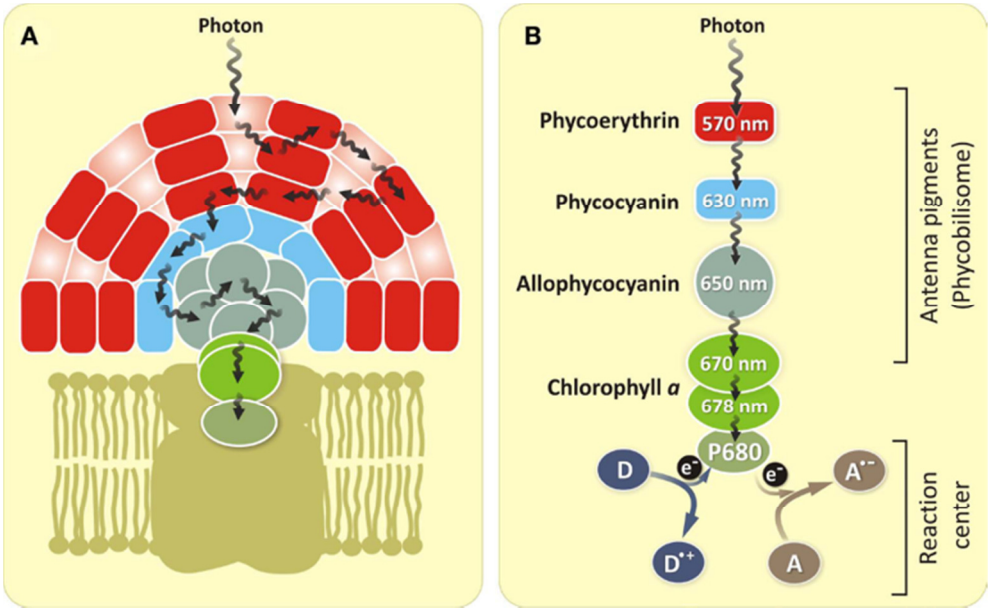

Figure 2. A crude overview of the cyanobacteria photosynthetic system.[3]

Natural photosynthesis has inspired an enormous number of researchers to seek ways to identify new molecular systems able to convert solar energy to chemical potential. In the main, such artificial photosynthetic systems try to make use of a small number of components arranged in a logical manner and each designed for a set purpose. The essential components include a sensitiser able to absorb visible light and

generate a redox-active excited state, a complementary redox partner that can enter into an electron-transfer reaction with the excited state of the sensitiser (but not the ground state), and a catalyst of some type able to store the redox equivalent for a short time. Ideally, two different catalysts would be appended to the same sensitiser such that water splitting could be effected but this situation has not been achieved with a molecular system.[1,17,18] Figure 3 presents the generic features of an artificial photosynthetic system.

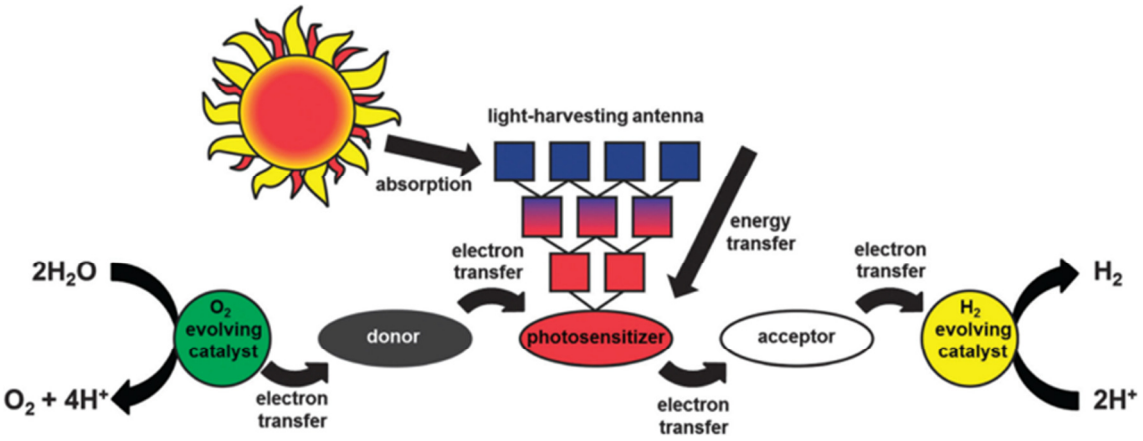

Figure 3. Illustration of a prototypic set up for artificial photosynthesis.[1]

In our work, we have been concerned primarily with the light-harvesting machinery. It is notable that natural photosynthesis utilises highly elaborate architectures as photon collectors. Here, absorbed photons are transferred between adjacent pigment molecules by the general process of electronic energy transfer (EET). Individual EET steps can be extremely fast but incoherent as illustrated by way of Figure 4. Two complementary events can be recognised: Thus, there is a cascade effect whereby EET occurs between different chromophores selected to collect photons over wide frequency range. In addition, there is a large-scale energy migration process that shuttles photons between identical pigments until trapped at the reaction centre.[19] In artificial photosynthesis, the reaction centre might be a solar cell.

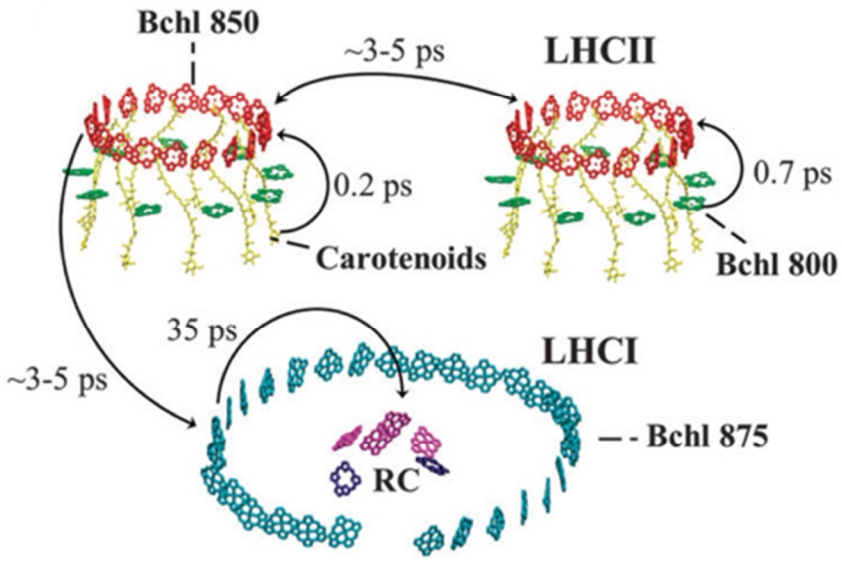

Figure 4. Summary of energy-transfer dynamics in non-sulphur, purple bacteria.[1]

A wealth of structural information now exists regarding the natural light-harvesting complexes and also about the dynamics of EET within such organisms. In part, this information stems from the availability of excellent X-ray structural determinations that have identified the composition and arrangement of the molecular architectures.[20,21] Such work has been supported by numerous biochemical and spectroscopic studies that have aided our detailed understanding of the EET mechanisms.[22] Artificial analogues have followed and have been used to direct photons to chemical or electrochemical devices. Related materials have been used in quite disparate applications, such as multiplexed fluorescent labels for biotechnology, organic light-emitting diodes, photochromic devices, and sensitized solar cells.[23-26] Many of these artificial antennae are constructed from porphyrin-based modules, as mimics of the natural process, and some also include carotenes. Recently, however, there has been a move away from purely bio-inspired models in an effort to introduce increased levels of photochemical stability and versatility.[1,12,19,27-31] Selected examples of artificial light harvesting arrays are presented later in this chapter. Our own work has made heavy usage of boron dipyrromethene (Bodipy) dyes as the basic chromophoric unit but we wish to stress that such reagents are far from the only choice. Other research groups, in what has become a very active field, have opted for different building blocks and it is not yet clear if there are any major advantages associated with any particular class of dye.

The remainder of this chapter sets out to introduce key features associated with electronic energy transfer and with the spectroscopic properties of Bodipy dyes. It is not

intended as an exhaustive review of these fields but is meant to introduce sufficient background information to enable presentation of specialised research in subsequent chapters.

1.2 Electronic energy transfer

Electronic energy transfer (EET) is ubiquitous in Nature, especially in photosynthesis and DNA repair enzymes, and is employed as a tool by which to direct absorbed energy to a site where some type of multi-electron catalysis can take place. This physical process does not involve the breaking or making of chemical bonds and can occur without nuclear motion. The light-harvesting arrays developed by natural organisms maintain a steady photon flux and achieve a remarkable degree of focussing in as much as photons absorbed over a wide area are directed down to a single molecule. By keeping a steady flow of photons arriving at the catalytic site, Nature tries to avoid the migration or short-circuiting of highly-reactive free-radical species. A similar strategy might be envisioned for purely artificial devices such as OLEDs and organic solar cells. One remarkable feature of EET is that it is possible to transfer excitation energy over substantial distances, well above the sum of the radii of the reactants, without appreciable orbital overlap. A second, and indeed related, aspect is that the EET event can be highly directional and sensitive to the distance between the reactants. Apart from leading to an exquisite level of selectivity and specificity, this realisation has many important opportunities in structural chemistry. For example, EET has been used extensively as a spectroscopic ruler in molecular topology and as a convenient tool for studying protein-protein interactions. Further applications range from lasers, to light-emitting diodes and to conjugated polymers.[32-34]

In general, the EET process can be expressed by the following generic expression:

$$D^* + A \rightarrow D + A^*$$

Here D and A, respectively, refer to the energy donor and acceptor while the "*" denotes an excited state. According to the type of connection between the donor and the acceptor, energy transfer can be classified as being intramolecular or intermolecular. In the former case, energy transfer takes place between two components of a single molecule so that diffusion might be unimportant, the reactants are necessarily close together and the nature of the connection can be critical in controlling the EET dynamics. This connection might be flexible, allowing the reactants to diffuse into

orbital contact within the lifetime of the excited donor, or sufficiently rigid to impose structural integrity throughout the EET event. In the latter case, EET has to compete with inherent decay of the short-lived excited state and the rate will invariably depend on the actual separation distance. In either case, orientation effects are hard to control. Further classification can be made in terms of the spins of the reactants and/or products. When the reactants are well separated, EET is likely to occur via the through-space mechanism but close proximity favours the electron-exchange mechanism. Intermediate separation distances are interesting because both mechanisms might be in operation.[13]

The main energy-transfer mechanisms were explained independently by Förster and Dexter more than 60 years ago.[35,36] Both theories require appropriate spectral overlap between the donor emission and acceptor absorption. Nevertheless, there are many differences between the two basic theoretical models that can be exploited to glean mechanistic insight into the EET event. For example, Förster theory depends on coulombic interactions while the Dexter mechanism is based on electron exchange. These features lead to markedly different distance-dependent rates of EET; generally, Dexter-type EET requires close approach of the reactants but Förster theory can operate over distances as large as 150 Å. More precisely, the distance dependence can be summarised as being exponential for Dexter-type EET but with the rate decreasing according to R^{-6} for the corresponding Förster mechanism, where R is the distance between the centres of the donor and acceptor. Other differences between these mechanisms relate to temperature dependence, radiative probabilities and orientation effects as will be outlined later. Energy transfer occurs on timescales ranging from femtoseconds to microseconds for singlet-singlet transfer and up to seconds for triplet energy transfer.[8,37] In natural photosynthesis, the main EET events appear to occur via the Förster mechanism since the reactants are rarely in orbital contact and are often separated by 10 Å or more.[13]

1.2.1 The Förster mechanism

Förster resonance energy transfer (FRET) is the process whereby the excitation energy localised momentarily on the donor migrates to the complementary acceptor, which might reside well outside orbital contact.[38,39] In this process, the rate of excitation energy transfer is controlled by a variety of factors, including the radiative rate of the isolated donor. For this reason, the process is sometimes referred to as radiative energy transfer.[40] At the heart of the Förster mechanism is the understanding that the actual EET step depends on the strength of coulombic interactions between the reactants in the

medium of interest. It is usually sufficient, except at short separations, to consider only dipole-dipole interactions and the associated solvent screening but multipole-multipole interactions become increasingly more important as the reactants approach each other. The basic process can be bimolecular or intramolecular, according to the molecular structure, and the rate of EET is only weakly dependent on temperature. Figure 5 gives a highly simplified depiction of Förster-type EET from a donor to an acceptor.

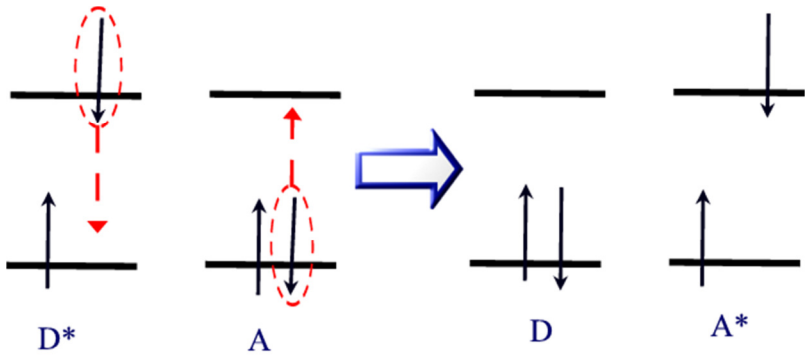

Figure 5. Basic illustration of the Förster mechanism for EET.

The rate constant (k_{EET}) for EET under these conditions depends on the donor radiative rate constant ($k_{rad}=\Phi_{flu}/\tau_s$), the mutual orientation of the reactants (K), the refractive index of the surrounding medium (n), the centre-to-centre separation distance between the chromophores (R_{DA}), and the spectral overlap integral between donor and acceptor (J_{DA}) as is indicated through Equation (1).[7,41] This equation will be discussed in detail in Chapter (6).

$$k_{EET} = \frac{8.8\times10^{-25}K^2\Phi_{flu}}{n^4\tau_s R_{DA}^6}J_{DA} \qquad \text{Equation (1)}$$

Several different methods are available that facilitate quantification of the EET probability under particular conditions. For bimolecular EET, it is important to specify the concentration and mobility of the acceptor but this is rarely so for intramolecular EET.[42] In the most popular method, the quantum yield for donor emission is measured in the absence and presence of the acceptor; the same approach can be taken for the excited-state lifetime of the donor. The transfer efficiency, or the probability of electronic energy transfer (P_{EET}), can now be established from these two measurements provided the acceptor quenches donor fluorescence exclusively by way of EET. Proof for the onset of EET can be obtained by monitoring the appearance of acceptor fluorescence following exclusive excitation into the donor. The EET probability is conveniently expressed by way of the following equations:

$$P_{EET} = 1 - \left(\frac{\tau_{DA}}{\tau_D}\right) \quad \text{Equation (2)}$$

$$P_{EET} = k_{EET}/(\tau_D^{-1} + k_{EET}) \quad \text{Equation (3)}$$

$$P_{EET} = R_0^6/(R_0^6 + R_{DA}^6) \quad \text{Equation (4)}$$

Here, the symbols DA and D refer, respectively, to systems having both donor and acceptor present or to the donor in the absence of acceptor. The term R_0 refers to the Förster critical distance, which is the separation distance when the energy-transfer probability is exactly 50%. This is an important parameter when using the EET process as a simple means for obtaining structural information.

Figure 6 shows how the energy transfer probability depends on the centre-to-centre distance between the donor and acceptor species while Figure 7 gives similar consideration to the effect of the excited-state lifetime of the donor. Related curves could be generated for other parameters such as the overlap integral or the orientation factor. A further point for concern relates to the screening factor, which in the original theory is taken as the square of the solvent refractive index. This cannot be correct for intramolecular EET between reactants in reasonably close proximity and there is a need to think about the size and shape of the solvent cavity. This is not a major correction, however, but is important when trying to accurately compare the theory with experiment or, as mentioned above, when trying to establish dimensions for the reactant pair.

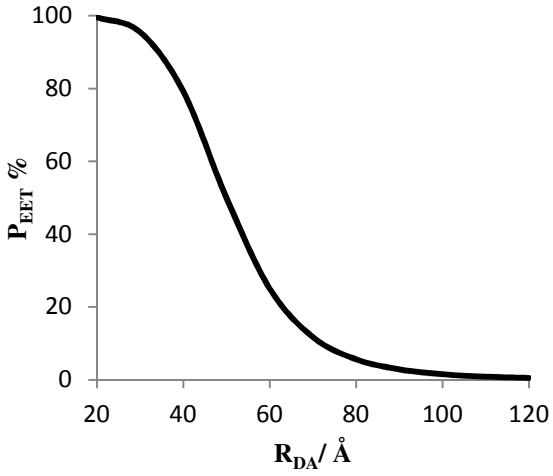

Figure 6. The relationship between the donor-acceptor distance and the energy-transfer probability.

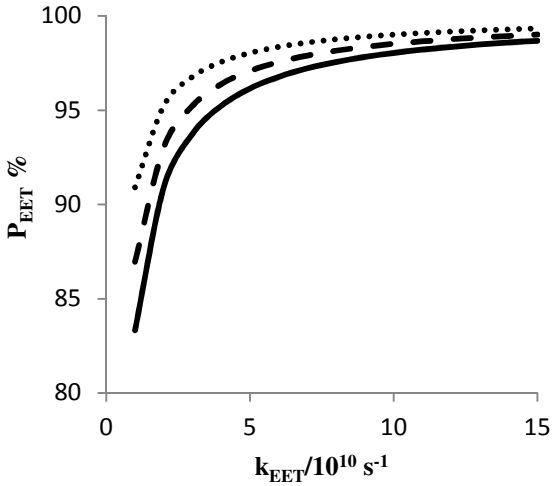

Figure 7. The relationship between the energy transfer rate constant and the EET probability at different lifetimes; 10 ns (points), 15 ns (dashes) and 20 ns (solid line).

It should be mentioned that the Förster expression is believed to give a good representation of the experimental rate of EET at large separation distances but the agreement might not be so good at close proximity. Unfortunately, most experimental studies are conducted within this "grey" area because of the need to ensure that the rate of EET competes satisfactorily with the inherent decay processes open to the donor. Other interesting features relate to the spectral overlap integral, recognising that EET might involve upper-lying excited states or states of a different spin multiplicity. This situation is especially relevant for exciton-exciton annihilation processes. The orientation factor requires special consideration since it relates to the mutual positioning of transition dipole moment vectors rather than the actual molecules. These vectors can be difficult to define, especially at short separations, and it is clear that the ideal dipole approximation is inoperable in many cases. Recent work with biological complexes has shown the involvement of quantum coherence effects[43] and there are important difficulties for application of the theory to conjugated polymers.[44] These factors help to maintain strong interest in the field and lead to a vibrancy and alertness.[45,46]

In addition to direct effects on the Förster EET rate, it is possible to manipulate the conditions so as to modulate the efficiency. For example, solvent polarity can affect the overlap integral or solvent cavity size. Pressure and/or temperature can be used to alter molecular conformation. Aggregation, self-association, hydrogen bonding and related non-covalent interactions can cause interesting side-effects. Changes in pH or complexation of species from solution can offer alternative routes for switching the direction or efficacy of the EET process while photobleaching can be utilised in a constructive manner. Such secondary effects have been exploited for numerous applications and it is important to stress that the field is extremely dynamic at the present time.[47-53]

1.2.2 The Dexter mechanism

The Dexter mechanism of electronic energy transfer is often considered to be a simultaneous dual exchange of electrons between excited-state donor and ground-state acceptor. There are close analogies with the Marcus theory of electron transfer and Dexter-type EET is frequently referred to as "electron exchange".[35,54] It operates over quite short distances, for bimolecular EET this means orbital contact between the reactants, but super-exchange interactions with bridging orbitals can extend the distance for intramolecular EET. The rate constant for Dexter-type EET depends on the spectral overlap integral and on an electronic coupling matrix element, V_{DA}, that describes

electronic mixing between wave functions localised on donor and acceptor. This term decreases in magnitude according to an exponential distance dependence, similar to that found for electron-transfer reactions ($V_{DA} \propto \exp\left(\frac{-\beta}{2} R_{DA}\right)$, where β is an attenuation factor that depends on the energy gap (ΔE) between the donor orbital and the corresponding bridge orbital and on the product of the atomic orbital coefficients(γ) for the connection between donor and bridge; $\beta = \frac{2}{R_0} ln \left|\frac{\Delta E}{\gamma}\right|$).[55] The basic features of this mechanism are illustrated by way of Figure 8. Although there are many examples of through-bond (i.e., electron exchange) EET for singlet-excited states, the mechanism is more widely applied to triplet-triplet energy transfer. It is also important for EET in conjugated polymers and in molecular systems where the reactants are interconnected through a conjugated bridge that facilitates super-exchange interactions.[56] The rate constant is generally formulated as in Equation (5) and carries with it an activation-energy due to the mismatch between driving force and re-organisation energy.[57] Thus, unlike through-space EET, the rate of through-bond EET is more often than not dependent on temperature.[35,58]

$$k_{EET} = \frac{2\pi}{\hbar} J_{DA} V_{DA} \exp\left(\frac{-2R_{DA}}{L}\right) \qquad \text{Equation (5)}$$

Here, R_0 is the effective distance while R_{DA} is the donor-acceptor centre-to-centre distance and L refers to sum of the van der Waals radii. Often, the expression is written in a slightly simplified way that makes use of the edge-to-edge separation distance but this parameter can be difficult to identify with conjugated bridges since it is not always obvious to recognise where one reagent ends and the next one begins. This is certainly a major problem for EET occurring in conjugated polymers. The activation energy, which is poorly defined for electron exchange unlike the case for electron transfer, can be measured experimentally and compared with that expected on the basis of the Marcus expression.[59]

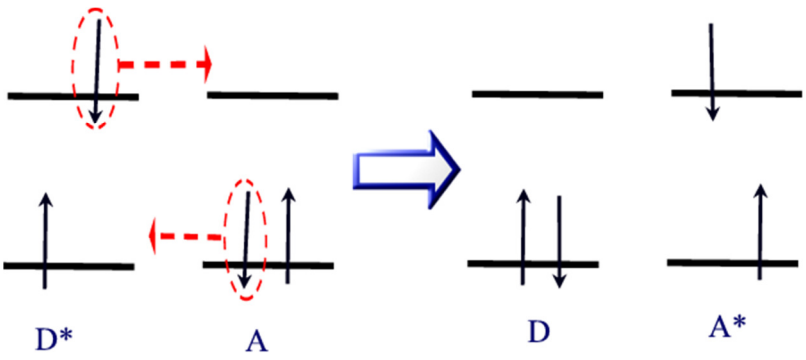

Figure 8. Illustration of the Dexter mechanism for EET between excited-singlet states.

1.2.3 Examples of artificial molecular systems involving EET

There have been numerous model systems designed and studied as a means by which to better understand and challenge the main EET theories. Many of these systems have addressed the issue of how the rate of EET evolves with increasing separation distance or with varying spectral overlap integral. It is not easy to construct appropriate molecular structures where only a single variable can be altered systematically. Likewise, there are problems to maintain a fixed geometry during the EET event, taking into account that even a small change in separation distance and/or orientation factor might cause a large change in rate. Additional difficulties relate to designing experiments that unambiguously separate EET from other quenching events, such as light-induced electron transfer or isomerisation. As the separation decreases it becomes more difficult to accurately define the molecular dimensions, especially the centre-to-centre or edge-to-edge distances. Similar problems exist for defining the orientation factor. Dexter-type electron exchange has the added factor of knowing how the bridge interacts with the donor. These challenges lead to a dynamic and diverse field while it has to be recognised that synthetic chemistry has played a major role in bringing about new and exciting model systems.

Our first example is shown in Figure 9 and refers to a quinone-substituted, phenyl-linked porphyrin trimer (compound 1). This rather elaborate bio-inspired molecule represents a simple example of a crude light-harvesting antenna that serves to collect incident photons and subsequently direct the excitation energy to the terminal quinone. In this case, EET between porphyrin units could occur by both Förster and Dexter mechanisms, and it has to be stressed that there is no rational way in which to control which porphyrin absorbs the photon. In the Förster mechanism, the centre-to-centre separation distances are 12.8 and 25.5 Å whereas the corresponding edge-to-edge distances are 5.9 and 19.9 Å respectively for the adjacent and distal porphyrins. It might also be noted that EET between the non-quinone terminal porphyrin and its neighbour might be reversible, although the two chromophores are not identical. Figure 9 illustrates the differences in the energy transfer rates anticipated for direct excitation into the non-quinone terminal porphyrin. The presence of the terminal quinone switches on electron transfer from the excited-singlet state of the adjacent porphyrin, which is believed to occur on a time-scale of <350 fs for the adjacent unit but up to 16 ns for the distal one.[60]

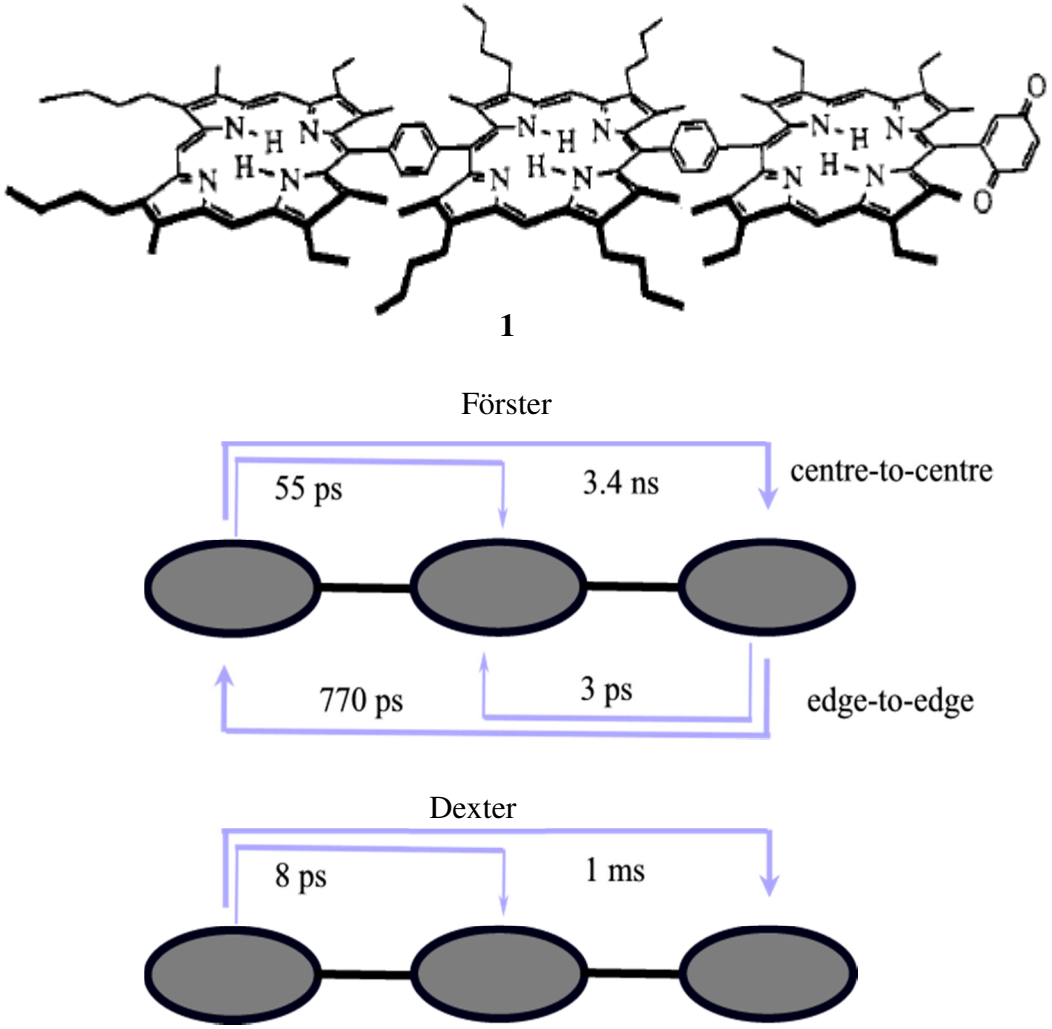

Figure 9. The molecular structure of the trimer (1) and an illustration of the average time taken for an absorbed photon to migrate between porphyrins according to Förster (top) and Dexter (bottom) mechanisms.

An equally interesting system is shown in Figure 10, where carotene derivatives are attached to a silicon phthalocyanine residue through the silicon atom (compounds 2 and 3). In compound 2, the carotene possesses a total of nine double bonds while in compound 3 there is an extra double bond in the carotene backbone. This has the effect of increasing the effective conjugation length and perturbing the spectral overlap integral. The net result is that the probability of EET from carotene to phthalocyanine drops from 92% for triad 2 to only 30% for triad 3.[61] A similar result has been observed for other carotenoid systems where changing the conjugation length has a marked effect on the EET probability.[62] It is worth noting that in a similar dyad where the carotene is attached covalently to the tetrapyrrolic pigment and shows high EET probability, Dexter electron exchange from triplet tetrapyrrole to carotene has to be taken into consideration.[63]

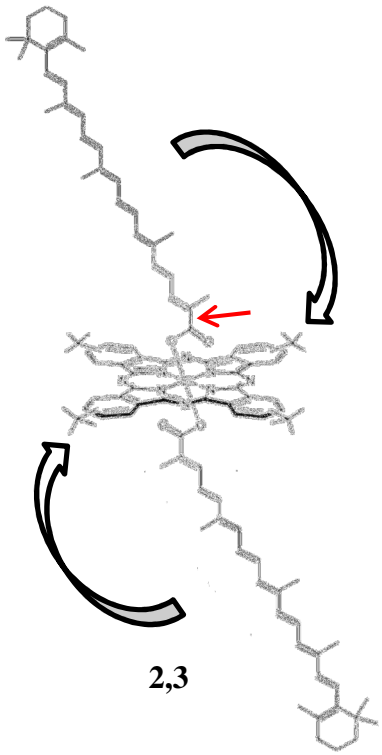

Figure 10. Example of EET in artificial system assembled via coordinative bonding. The red arrow shows the position of the extra double bond.

Figure 11 shows an example of a molecular hexad, compound 4, which consists of four coumarin dyes held in close proximity to two zinc(II) porphyrin units by way of a hexa-phenylbenzene scaffold. This makes for a compact unit bearing two disparate types of chromophore. In addition, the porphyrins are positioned close to a fullerene unit that can operate as a redox-active reagent and also as an acceptor for triplet-energy transfer from the porphyrin. Illumination into the coumarin dye with near-UV light induces a very fast EET event in which excitation energy is transferred to one of the porphyrins. The estimated distance between coumarin and porphyrin is 8-14 Å for the proximal coumarin and 14-21 Å for the corresponding distal coumarin derivative. The EET rate constants have been measured for both types of donor and found to be extremely fast but slower for the distal donor. It is possible, but not too likely, that EET occurs from distal to proximal coumarin before being transferred to the porphyrin. It is worth mentioning that light-induced electron transfer occurs from porphyrin to the fullerene to generate a relatively long-lived, charge separated state.[64]

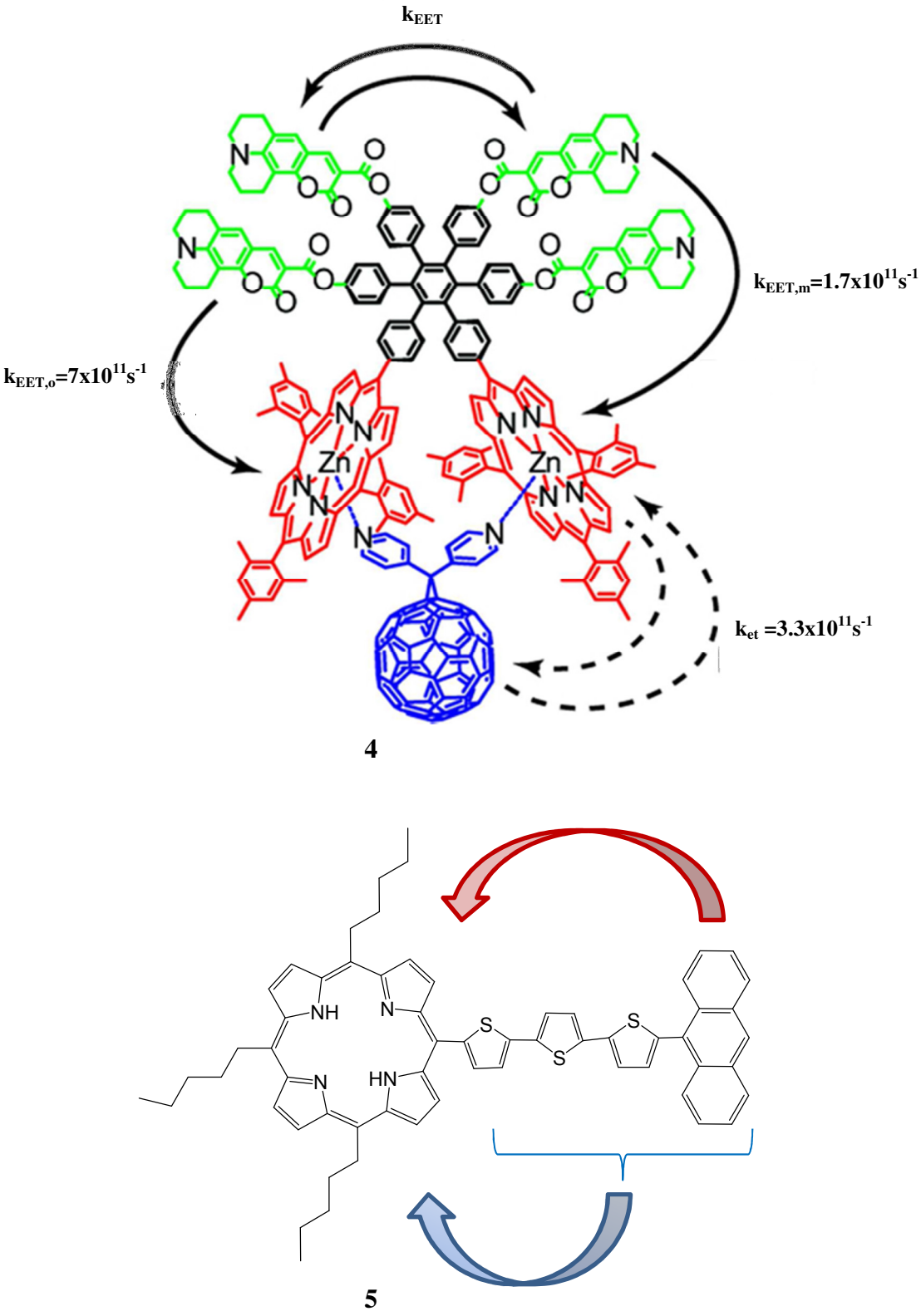

Figure 11. A few selected examples of molecular systems displaying intramolecular EET.

Compound 5 in Figure 11 provides an example of EET in a rigid molecular entity comprising units known for their participation in OLEDs and organic solar cells. Here, the terminal acceptor is the free-base porphyrin which emits fluorescence at around 650 nm. The porphyrin absorbs weakly across the visible region but displays an extremely intense (Soret band) absorption transition at around 420 nm. Anthracene absorbs in the UV region where the porphyrin is essentially transparent but the oligo-thiophene, an important ingredient in most organic solar cells, absorbs to the red of the anthracene unit. Thus, compound 5 is really a molecular triad with each unit held in close proximity to the next component. Excitation into the anthracene unit leads to highly efficient EET that results in fluorescence from the terminal porphyrin. Because of the close proximity of the reactants, it is difficult to be precise about the actual EET mechanism. Certainly, EET occurs to populate the S_2 state on the porphyrin and this is followed by fast internal conversion to produce the corresponding S_1 state. The primary donor is the S_1 state localised on anthracene but the role of the oligo-thiophene bridge is not at all clear. It could be a short-lived intermediate in a two-step through-space or electron-exchange process since EET from the S_1 state of the oligo-thiophene to the S_2 state on the porphyrin is likely to be very fast. It might also operate as a vehicle for promoting super-exchange interactions between the terminals, which are separated by 10-15 Å.[65] We use this system to indicate how difficult it can be to define the EET mechanism, even in a relatively simple molecular architecture.

Another example of a covalently-linked artificial system is shown in Figure 12 and refers to a pair of molecular dyads where a carotenoid chromophore has been attached to either a porphyrin (dyad 6) or a fullerene derivative (dyad 7). This example shows the competition between EET and light-induced electron transfer and serves to illustrate how small changes in the structure can modulate the reaction mechanism. In dyad 6, the carotene is slightly (i.e., one double bond) longer than that in dyad 7 and there are further

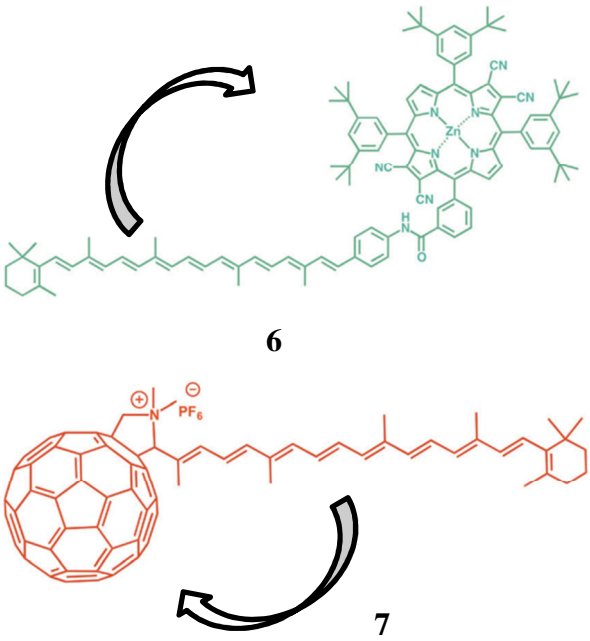

Figure 12. Examples of carotene-based artificial system.

differences relating to the connection point through which the carotene links to the other terminal. Dyad 7 shows both electron and energy transfer from the S_1state of carotene to the appended fullerene. However, in the case of dyad 6 only light-induced electron transfer occurs when illumination is made into either S_1 or S_2 states localised on the carotene.[66]

Nature seems not be dependent on covalent chemistry. Instead, subtle changes in colour and reactivity are arranged by small variations in protein binding and/or conformation. This simple, but elegant, strategy allows the same chromophores to be used in slightly different environments so as to build up the EET cascade effect. This realisation has stimulated the appearance of artificial analogues wherein non-covalent interactions have been utilised to assemble multi-chromophoric light-harvesting systems in both two- and three- dimensional architectures.[67-69] Figure 13 presents an example of a self-assembled multi-porphyrin array (compound 8) consisting of four *meso*-pyridine-appended zinc(II) porphyrins built into a square arrangement in suitable non-coordinating solvents. The resulting tetrameric array exhibits efficient EET that is well described by the Förster mechanism. A key feature of this system relates to the well-defind molecular architecture that positions the transition dipole moment vectors in a prependicular manner. It is notable that the dimensions of the array can be varied by changing the length of the pyridyl arms (n) and this has an effect on both the association constants and the EET dynamics.[67]

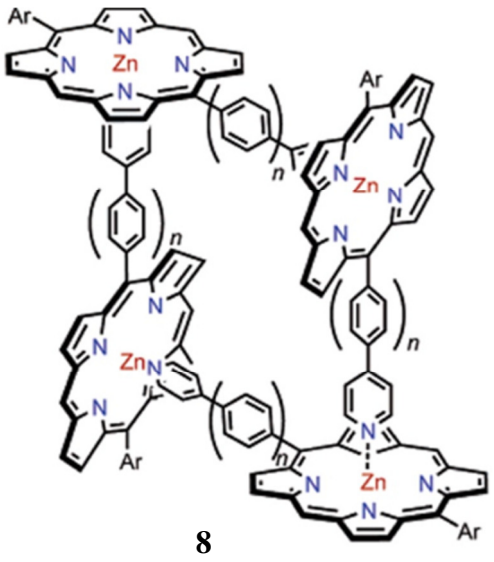

8

Figure 13. Example of a porphyrin self-assembled light-harvesting system, where n is 0, 1 or 2.

1.3 Bodipy

Boron dipyrromethene (Bodipy) dyes, more correctly referred as 4,4-difluoro-4-bora-3a,4a-diaza-s-indacene, were first reported in 1968 by Treibs and Kreuzer[70,71] and have become one of the most popular reagents in biochemistry. Their initial use was as laser dyes but they have found important applications in bio-labelling, mapping and imaging, as information reporters, rheology probes, sensitisers and pigments. Specific dyes have

been developed for use as bio-molecular labels,[72-74] chemical sensors,[75-77] fluorescent switches,[78,79] laser dyes,[80] light harvesters,[2,24] solar concentrators,[81] drug delivery groups and anti-bacterial agents.[82,83] All these applications, and many more, are growing because of the excellent features of Bodipy dyes; high molar absorption coefficients and fluorescence quantum yields with narrow peaks, high stability towards heat and light, resistance to corrosive chemicals, negligible triplet state formation, good optical properties that can be modified by simple synthetic chemistry and excellent compatibility with other reagents. Mostly, the dyes are insensitive towards aggregation in solution and readily dissolved in organic media. Strategies are available for the production of water-soluble derivatives and analogues that can be incorporated into organo-gels, polymers, liquid crystals, etc.[2,71,72,84,85] However, the rather small Stokes' shift can be a problem in certain biological applications because of self-absorption.[86]

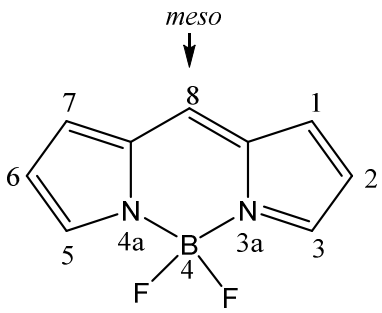

Figure 14. Labelling scheme for the basic Bodipy scaffold.

Figure 14 presents the IUPAC numbering scheme used for the Bodipy scaffold without substituents but that has not yet been synthesized. Figure 15 shows a simple example of strategies that can be employed to extend the degree of π-electron conjugation running along the molecular backbone. This type of approach is useful for shifting the absorption and emission spectral maxima towards lower energy and it should be noted that there is immense interest in generating stable Bodipy-based dyes that absorb and emit in the near-IR region for bio-sensors and medical applications. This comes about because the so-called biological window (between 650 and 900 nm) minimizes light scattering, adventitious absorption by tissue and cellular media, and auto-fluorescence.[85,86]

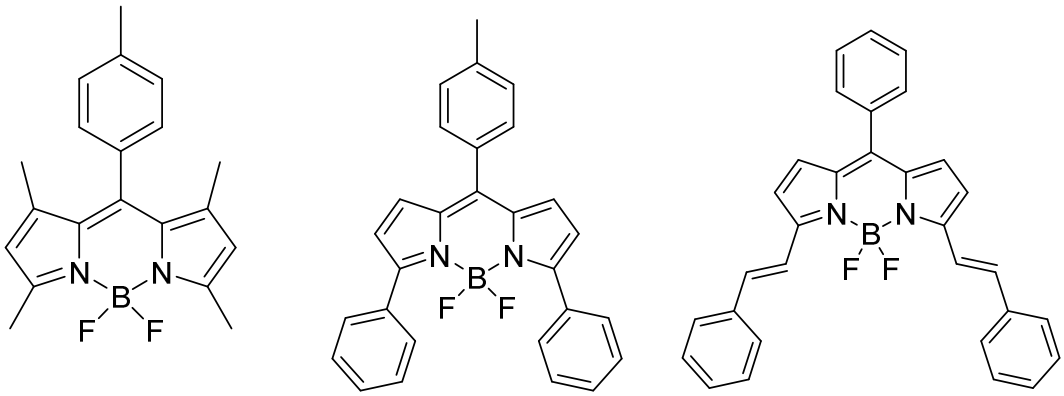

Figure 15. Examples of some Bodipy dyes possessing extended conjugation length.[85]

A comprehensive range of Bodipy dyes exists for use as fluorescent sensors in analytical chemistry with specific targets being various medical, biological and environmental applications. Depending on the target analyte, different functional groups are added to the Bodipy dye so as to trap the target and thereby induce notable alterations in the fluorescence behaviour of the sensor. Figure 16 shows some typical examples of pH sensors that can be used at selected acidity ranges. In compound 4, for example, the amino group quenches inherent fluorescence from the Bodipy dye as a result of intramolecular charge transfer. Protonation of the amino group in acidic solution curtails light-induced charge transfer and leads to recovery of the Bodipy fluorescence. On the contrary, deprotonation of the phenol group present in compound 5 at high pH serves to switch on photo-induced intramolecular electron transfer (PET) and this quenches Bodipy fluorescence. In general, both examples depend on the fluorescence "on/off" switching mechanism.[87] Likewise, Bodipy can be used for detection of cations in solution by building the N atom into a crown-ether able to sequester the cation from solution. Appropriate examples are compounds 6 and 7 as shown in Figure 16.[75,78]

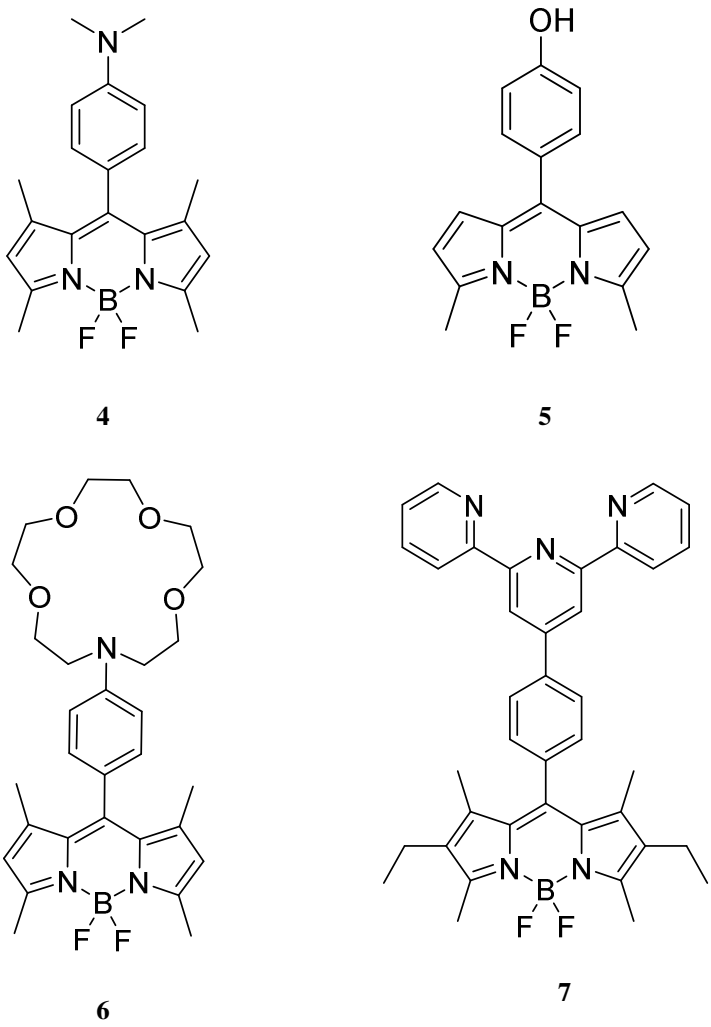

Figure 16. Examples of Bodipy-based fluorescent sensors.[72]

Although Bodipy-based dyes absorb strongly in the UV-Vis region, they cover only a relatively narrow region when compared with the solar spectrum because they have sharp absorption bands as shown in Figure 17. Such properties are good for chemical sensors and optical probes but not so useful when it comes to assembling artificial light-harvesting arrays. To overcome this particular problem it has been necessary to develop systems containing multiple chromophores that each absorb over a pre-determined spectral range. Such panchromatic molecules require extensive synthesis and careful purification but have many important applications. Several examples of such cassette systems constructed from various Bodipy dyes now exist and are known to display intramolecular EET as a means by which to redistribute absorbed photonic energy. The Bodipy dye can function as either donor or acceptor according to the nature of the attached substituents. In addition to expanding the absorption spectral region, these arrays offer a simple route by which to enlarge the Stokes' shift.

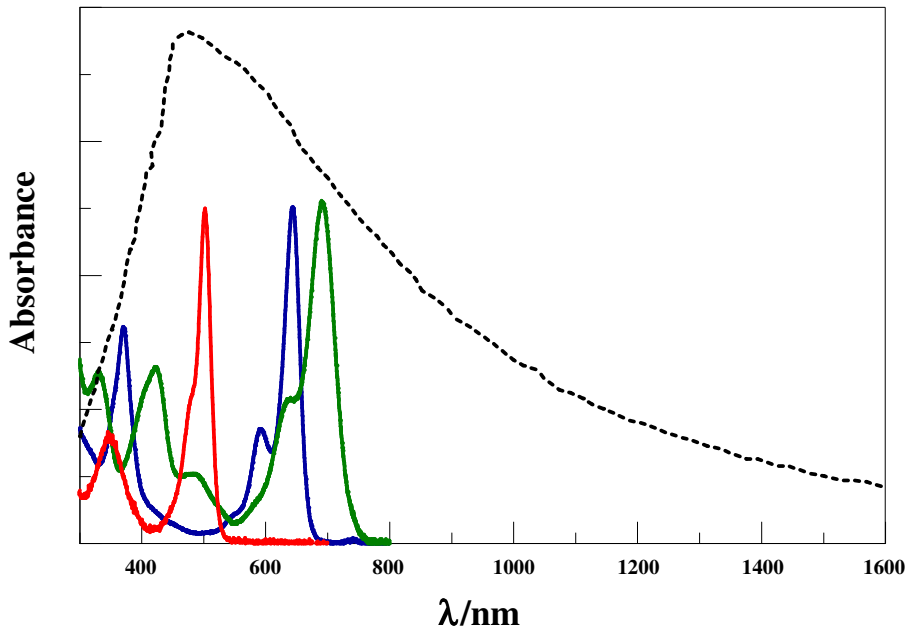

Figure 17. The average absorption spectral output of sunlight at the earth surface (black dotted curve), overlaid with absorption profiles recorded for the conventional Bodipy dye (red curve) and two styryl-expanded Bodipy dyes (blue and green curves).

In Figure 18 we see two simple Bodipy derivatives (compounds 8 and 9) where the absorption spectral features of the Bodipy dye have been supplemented by absorption transitions associated with ethynyl-anthracene. These latter bands appear in the near-UV region, so they don't make a valuable addition in terms of a solar concentrator, but they serve to illustrate the basic principle of a cassette dye. Photons absorbed by the anthracene unit are transferred quantitatively to the Bodipy-based terminal, which retains the same photophysical properties as seen for the isolated dye. The rates of EET depend on the substitution pattern and there is a marked variation in the orientation factor for the two compounds.[88] Compound 10 is a landmark addition to the field in as much as the appendages are connected via the boron atom, a strategy that opens up the field and permits the design of innumerable derivatives. This particular example has two disparate aryl hydrocarbons attached to the Bodipy nucleus. These absorb over different spectral ranges and each transfers excitation energy to the Bodipy-based dye with >99% efficiency. There is also the possibility for sideways EET whereby photons collected by pyrene are directed towards perylene before being transferred to the Bodipy dye.[89,90]

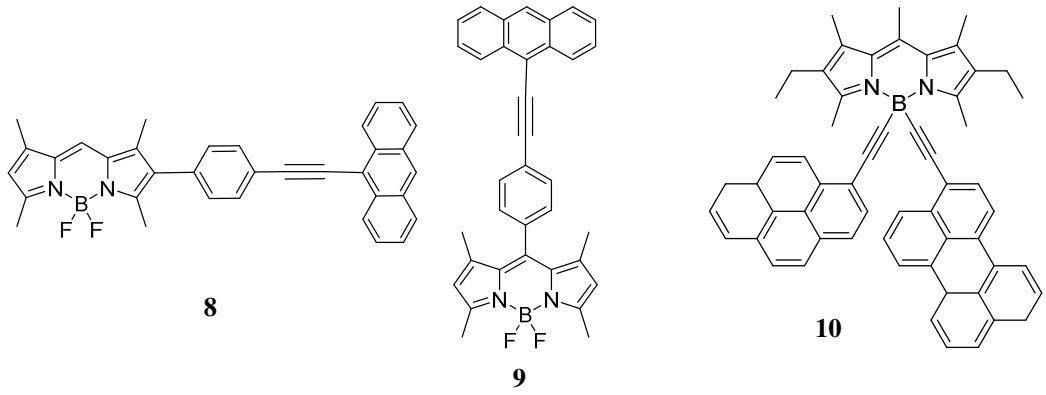

Figure 18. Selected examples of donor-acceptor systems designed to study intramolecular EET.[88]

A more sophisticated example is presented in Figure 19. Thus, compound 11 comprises four Bodipy units attached to a central perylene diimide (PDI) unit. The latter group fulfils the role of energy acceptor and various spectroscopic studies indicate that the overall probability of EET in this system exceeds 99%.[71,91] The large organic moiety is soluble in common organic solvents and free from problems associated with aggregation. A notable weakness of this system, however, stems from the use of highly flexible arms to interlink the components since this favours attainment of multiple conformations. An even more elaborate light-harvesting architecture is presented in Figure 20 and shows many EET steps, according to which chromophore absorbs the incident photon. There are a total of 21 chromophoric units accreted into a single unit, including three disparate Bodipy-based dyes. At low

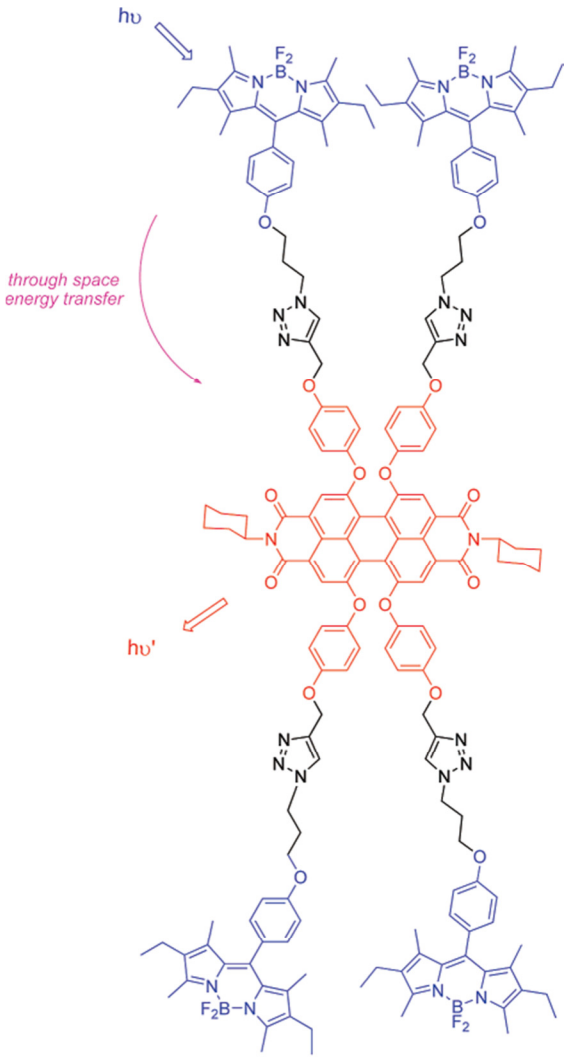

Figure 19. Example of a panchromatic artificial antenna.

light intensities, the overall probability of absorbed photons reaching the terminal Bodipy dye is greater than 75% and a wide spectral range is harvested by the array. At high photon densities, excitons are shuttled across the array via through-space interactions.[2] This latter event has the effect of delaying arrival of an absorbed photon at the terminal acceptor. Somewhat unusually, this array has been demonstrated to be highly effective at the sensitisation of a solar cell.

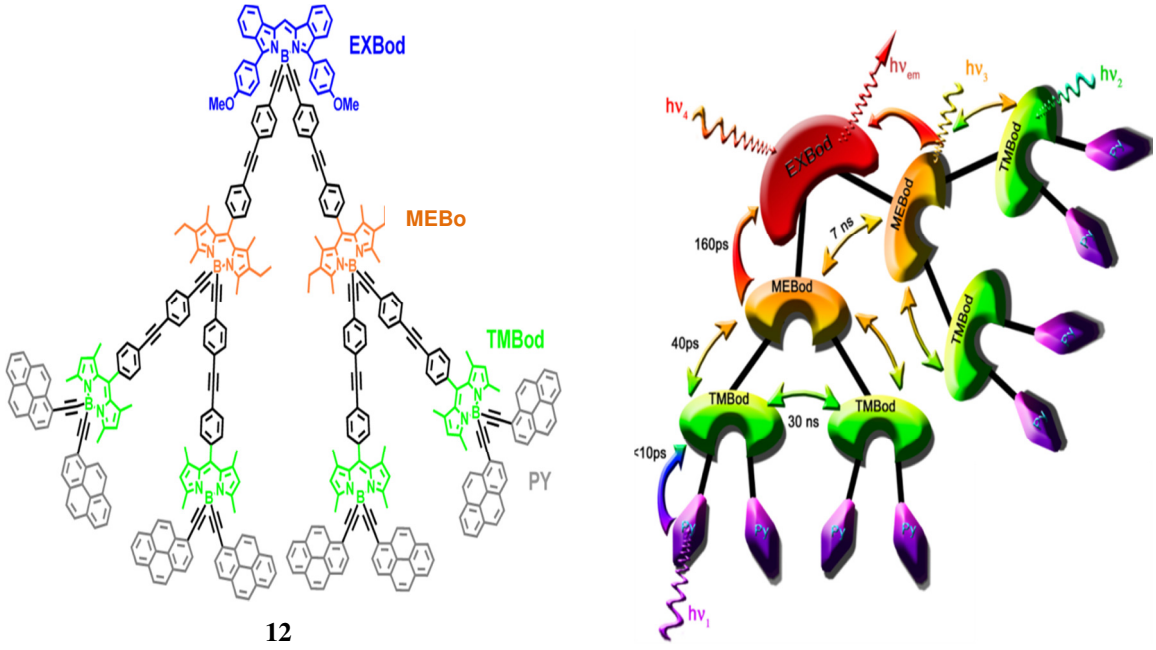

Figure 20. Illustration of the multi energy-transfer steps occurring in an artificial light-harvesting array.

Many of the latest artificial light-harvesting arrays to be built around Bodipy-based dyes make use of the "synthesis-at-boron" protocol and this strategy lends itself naturally to the construction of "V-shaped" structures. These architectures are ideal for directing photons along the molecular axis towards a terminal acceptor that can be positioned adjacent to a solar cell. They are less suited for arrangements where the photon needs to be sent to a separate "V-shaped" molecule. The same kind of problem is solved in natural photosynthesis by assembling the chromophores into large rings[21,92] where the exciton can be directed incoherently around the ring before being off-loaded to an adjacent ring. Consequently, there is a ready means by which to allow the photon to sample an unusually large area and, as mentioned above, vary the arrival time at the final acceptor (i.e., the reaction centre complex). In trying to mimic this pattern, recent work has introduced an artificial light-harvesting antenna with a 3-D arrangement of the

chromophores that also facilitates EET between isolated units. The panchromatic material is shown as compound 13 in Figure 21 and consists of ten yellow Bodipy dyes and two blue Bodipy dyes attached to an inert fullerene support. Illumination into one of the yellow dyes leads to EET to a blue Bodipy dye but also to energy migration among the yellow dyes. At high concentration in a polymer film, EET can occur between dyes attached to different fullerene supports and dispersed in three different directions.[93] Currently, this array is considered to be the "state-of-the-art" prototype but requires intensive synthesis. It might be mentioned in passing that little attention has been given to the photochemical stability of these intricate molecular systems but it is clear that the high stability shown by the simpler Bodipy dyes does not necessarily pass over to the π-extended derivatives. There are no artificial analogues of the natural repair mechanisms.

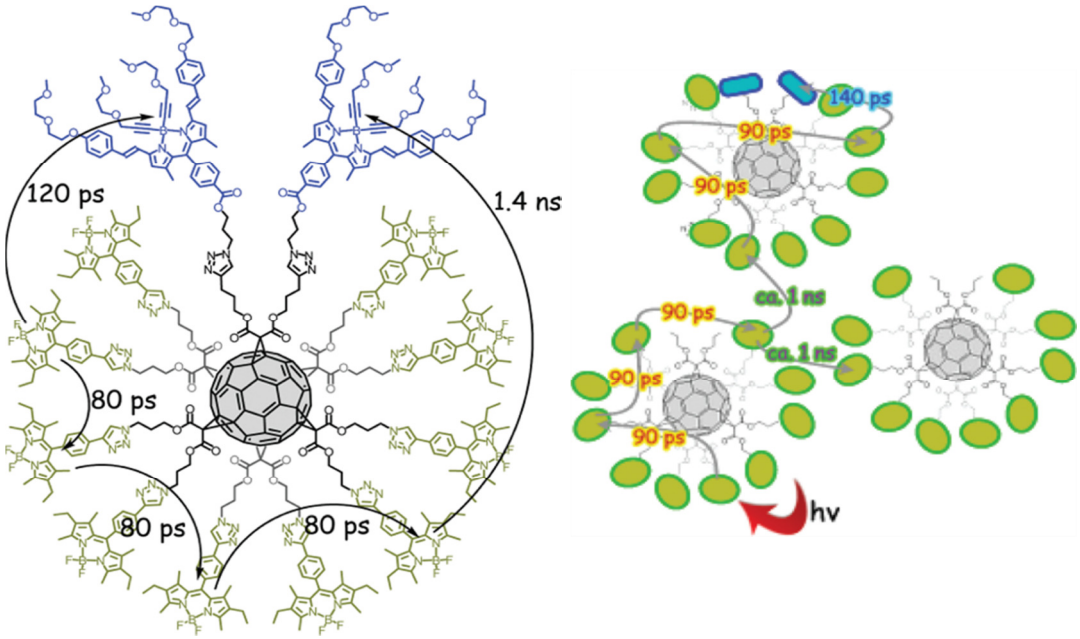

13

Figure 21. Example of a 3-D cluster comprising two types of Bodipy chromophore attached to a fullerene support**.**

1.4 Concluding remarks

The generic field of molecular photophysics continues to attract interesting and highly versatile research initiatives and there is no indication that the subject is in decline. New instrumentation and protocols for data analysis appear at regular intervals and there is ever-growing collaboration with synthetic chemists able to design and isolate intriguing molecular architectures. The ready availability of lasers, LEDs and related light sources

make it easier to interrogate complex samples while advances in molecular modelling allow meaningful derivation of structures in the absence of crystallographic information. In hand with fundamental research, there has been an upsurge in the number and scope of applications for luminescent molecules, not least in the areas of anti-forgery, chemical sensing, bio-labelling, tracing of pollutants, powering of remote installations, advanced microscopy and sophisticated signalling. Furthermore, molecular photophysics is set to play a key role in certain aspects related to the development of renewable energy supplies. The subject benefits enormously from interactions between biology, chemistry and physics and we continue to marvel at the discoveries made with respect to natural photosynthesis. This is surely the most beautiful of all molecular machines but its wonderful complexity is outside the possible reconstruction in the laboratory. Instead, we can only dream about putting into practice some crude models of the real system.

In the upcoming chapters we present a summary of research carried out in the Molecular Photonics Laboratory at Newcastle University. We have used a range of boron dipyrromethene (Bodipy) dyes as our staple building blocks and a large part of this thesis is devoted to understanding the photophysics of these molecules. We have attempted to learn how Bodipy responds to changes in the local environment, using fluorescence as the monitoring tool. Initial work focuses on the isolated molecule and its interaction with the surroundings as a function of temperature and pressure. Minor modification of the Bodipy structure switches on intramolecular charge transfer and this process is extremely efficient, at least in the molecules under consideration. Next we move towards studying intramolecular electronic energy transfer (EET) in model systems. This section concentrates on exploring how the rate of EET depends on the separation distance for molecular dyads where EET most likely occurs via the coulombic mechanism. We use the experimental results to suggest minor deformations of the molecular bridges that bring the terminals into close proximity. Using pressure and temperature effects we are able to gain new insight into the torsional mobility of these bridges as they are subjected to stress.

One of the more important applications for EET in artificial systems is to sensitize solar cells but there are substantial practical problems to overcome before we reach that stage. One, of several, such problems relates to how best to construct conjugates capable of efficacious collection of sunlight and the subsequent channeling of the harvested excitons to the solar cell. To do this effectively, we probably have to move away from covalently-linked systems and design new ways to bring about active

molecular-scale light-harvesting arrays. To this end, we have studied EET in self-assembled complexes and in the ensuing liquid crystals that emerge upon annealing. We have looked at other ways to attach the dyes to a solid surface, including spin coating of thin films and the development of a highly novel viscous Bodipy dye. The latter can be painted onto surfaces in a form that retains some fluorescence, despite the unusually high local concentration.

Our work, whether applied or fundamental, demands the ready availability of dyes that absorb and emit at different frequencies. One convenient way to expand the range of available dyes involves systematic modulation of their π-electron conjugation lengths. This represents a return to covalent chemistry but we have been able to examine a small range of yellow, blue and green dyes in this way. By linking together several dyes in a logical manner, it becomes possible to study intramolecular EET and this is the main focus of our work. Using steady state and time-resolved fluorescence spectroscopy, aided by variable temperature and pressure studies, we have explored the probabilities and directions of EET in several new molecular entities. Certain Bodipy dyes respond to applied pressure by undergoing structural deformation and this provides access to novel pressure-sensitive materials. Other compounds are highly solvato-chromic such that the spectral overlap integral for EET is easily tuned. Most of the work employs Bodipy dyes, synthesized by our collaborators in Strasbourg, but a few related materials have been used to expand the scope of the EET processes.

1.5 Refrences

1. Frischmann, P. D.; Mahata, K.; Wurthner, F. *Chem. Soc. Rev.* **2013**, *42*, 1847.
2. Ziessel, R.; Ulrich, G.; Haefele, A.; Harriman, A. *J. Am. Chem. Soc.* **2013**, *135*, 11330.
3. McConnell, I.; Li, G.; Brudvig, G. W. *Chem. Biol.* **2010**, *17*, 434.
4. Hammarström, L.; Hammes-Schiffer, S. *Acc. Chem. Res.* **2009**, *42*, 1859.
5. Gust, D.; Moore, T. A.; Moore, A. L. *Acc. Chem. Res.* **2009**, *42*, 1890.
6. Niedzwiedzki, D. M.; Blankenship, R. E. *Photosynth. Res.* **2010**, *106*, 227.
7. Scholes, G. D. *Annu. Rev. Phys. Chem.* **2003**, *54*, 57.
8. Laquai, F.; Park, Y. S.; Kim, J. J.; Basche, T. *Macromol. Rapid Commun.* **2009**, *30*, 1203.
9. Green, B. R.; Parson, W. W. *Light-Harvesting Antennas in Photosynthesis*; Kluwar Academic Publishers: The Netherlands, 2003.
10. Scholes, G. D.; Fleming, G. R.; Olaya-Castro, A.; van Grondelle, R. *Nat. Chem.* **2011**, *3*, 763.
11. Niedzwiedzki, D.; Blankenship, R. *Photosynth. Res.* **2010**, *106*, 227.
12. Gust, D.; Moore, T. A.; Moore, A. L. *Acc. Chem. Res.* **2000**, *34*, 40.
13. Lin, S. H.; Xiao, W. Z.; Dietz, W. *Phys. Rev. E* **1993**, *47*, 3698.
14. Frank, H. A.; Cogdell, R. J. *Photochem. Photobiol.* **1996**, *63*, 257.
15. Polli, D.; Cerullo, G.; Lanzani, G.; De Silvestri, S.; Hashimoto, H.; Cogdell, R. J. *Biophys. J.*, *90*, 2486.
16. Pullerits, T.; Sundström, V. *Acc. Chem. Res.* **1996**, *29*, 381.
17. Brotosudarmo, T. H. P.; Prihastyanti, M. N. U.; Gardiner, A. T.; Carey, A.-M.; Cogdell, R. J. *Energy Procedia* **2014**, *47*, 283.
18. Cogdell, R. J.; Brotosudarmo, T. H. P.; Gardiner, A. T.; Sanchez, P. M.; Cronin, L. *Biofuels* **2010**, *1*, 861.
19. Ziessel, R.; Harriman, A. *Chem. Commun.* **2011**, *47*, 611.
20. McDermott, G.; Prince, S. M.; Freer, A. A.; Hawthornthwaite-Lawless, A. M.; Papiz, M. Z.; Cogdell, R. J.; Isaacs, N. W. *Nature* **1995**, *374*, 517.
21. Cogdell, R. J.; Isaacs, N. W.; Freer, A. A.; Howard, T. D.; Gardiner, A. T.; Prince, S. M.; Papiz, M. Z. *FEBS Lett.* **2003**, *555*, 35.
22. Niedzwiedzki, D. M.; Bina, D.; Picken, N.; Honkanen, S.; Blankenship, R. E.; Holten, D.; Cogdell, R. J. *Biochim. Biophys. Acta* **2012**, *1817*, 1576.
23. Ueno, Y.; Jose, J.; Loudet, A.; Pérez-Bolívar, C.; Anzenbacher, P.; Burgess, K. *J. Am. Chem. Soc.* **2011**, *133*, 51.

24. Bonaccorsi, P.; Aversa, M. C.; Barattucci, A.; Papalia, T.; Puntoriero, F.; Campagna, S. *Chem. Commun.* **2012**, *48*, 10550.
25. Zhao, Y.; Zhang, Y.; Lv, X.; Liu, Y.; Chen, M.; Wang, P.; Liu, J.; Guo, W. *J. Mater. Chem.* **2011**, *21*, 13168.
26. Li, L. L.; Diau, E. W. *Chem. Soc. Rev.* **2013**, *42*, 291.
27. Burrell, A. K.; Officer, D. L.; Plieger, P. G.; Reid, D. C. W. *Chem. Rev.* **2001**, *101*, 2751.
28. Wojaczyński, J.; Latos-Grażyński, L. *Coord. Chem. Rev.* **2000**, *204*, 113.
29. Imamura, T.; Fukushima, K. *Coord. Chem. Rev.* **2000**, *198*, 133.
30. El-Khouly, M. E.; Fukuzumi, S.; D'Souza, F. *ChemPhysChem* **2014**, *15*, 30.
31. Bozic-Weber, B.; Constable, E. C.; Housecroft, C. E. *Coord. Chem. Rev.* **2013**, *257*, 3089.
32. Stryer, L. *Annu. Rev. Biochem* **1978**, *47*, 819.
33. Kawatsu, T.; Matsuda, K.; Hasegawa, J. Y. *J. Phys. Chem. A* **2011**, *115*, 10814.
34. Hillisch, A.; Lorenz, M.; Diekmann, S. *Curr. Opin. Struct. Biol.* **2001**, *11*, 201.
35. Dexter, D. L. *J. Chem. Phys.* **1953**, *21*, 836.
36. Forster, T. *Naturwissenschaften* **1946**, *33*, 166.
37. Andrews, D. L.; Demidov, A. A. *Resonance Energy Transfer*; Wiley: Chichester 1999.
38. Forster, T. *Disc. Faraday Soc.* **1959**, *27*, 7.
39. Beljonne, D.; Curutchet, C.; Scholes, G. D.; Silbey, R. J. *J. Phys. Chem. B* **2009**, *113*, 6583.
40. Claudio, G. C.; Bittner, E. R. *J. Phys. Chem. A* **2003**, *107*, 7092.
41. Knox, R. S.; van Amerongen, H. *J. Phys. Chem. B* **2002**, *106*, 5289.
42. Berney, C.; Danuser, G. *Biophys. J.* **2003**, *84*, 3992.
43. Engel, G. S.; Calhoun, T. R.; Read, E. L.; Ahn, T.-K.; Mancal, T.; Cheng, Y.-C.; Blankenship, R. E.; Fleming, G. R. *Nature* **2007**, *446*, 782.
44. Dolghih, E.; Ortiz, W.; Kim, S.; Krueger, B. P.; Krause, J. L.; Roitberg, A. E. *J. Phys. Chem. A* **2009**, *113*, 4639.
45. Curutchet, C.; Mennucci, B.; Scholes, G. D.; Beljonne, D. *J. Phys. Chem. B* **2008**, *112*, 3759.
46. Mårtensson, J. *Chem. Phys. Lett.* **1994**, *229*, 449.
47. Benniston, A. C.; Harriman, A.; Li, P.; Sams, C. A. *J. Am. Chem. Soc.* **2005**, *127*, 2553.

48. Jockusch, S.; Timpe, H. J.; Schnabel, W.; Turro, N. J. *J. Phys. Chem. A* **1997**, *101*, 440.

49. Robinson, G. W. *J. Mol. Spectrosc.* **1961**, *6*, 58.

50. Grusenmeyer, T. A.; Chen, J.; Jin, Y.; Nguyen, J.; Rack, J. J.; Schmehl, R. H. *J. Am. Chem. Soc.* **2012**, *134*, 7497.

51. Andreasson, J.; Kyrychenko, A.; Martensson, J.; Albinsson, B. *Photochem. Photobiol. Sci.* **2002**, *1*, 111.

52. Yu, J.; Hu, D.; Barbara, P. F. *Science* **2000**, *289*, 1327.

53. Chatterjee, S.; Nandi, S.; Bhattacharya, S. C. *J. Photochem. Photobiol., A* **2005**, *173*, 221.

54. Kohler, A.; Bassler, H. *J. Mater. Chem.* **2011**, *21*, 4003.

55. Eng, M. P.; Ljungdahl, T.; Mårtensson, J.; Albinsson, B. *J. Phys. Chem. B* **2006**, *110*, 6483.

56. Albinsson, B.; Martensson, J. *Phys. Chem. Chem. Phys.* **2010**, *12*, 7338.

57. Eng, M. P.; Albinsson, B. *Chem. Phys.* **2009**, *357*, 132.

58. Gust, D.; Moore, T. A.; Moore, A. L.; Devadoss, C.; Liddell, P. A.; Hermant, R.; Nieman, R. A.; Demanche, L. J.; DeGraziano, J. M.; Gouni, I. *J. Am. Chem. Soc.* **1992**, *114*, 3590.

59. Devi, L. S.; Al-Suti, M. K.; Dosche, C.; Khan, M. S.; Friend, R. H.; Kohler, A. *Phys. Rev. B* **2008**, *78*.

60. Sessler, J. L.; Capuano, V. L.; Harriman, A. *J. Am. Chem. Soc.* **1993**, *115*, 4618.

61. Kodis, G.; Herrero, C.; Palacios, R.; Mariño-Ochoa, E.; Gould, S.; de la Garza, L.; van Grondelle, R.; Gust, D.; Moore, T. A.; Moore, A. L.; Kennis, J. T. M. *J. Phys. Chem. B* **2004**, *108*, 414.

62. Maruta, S.; Kosumi, D.; Horibe, T.; Fujii, R.; Sugisaki, M.; Cogdell, R. J.; Hashimoto, H. *Phys. Status Solidi B* **2011**, *248*, 403.

63. Macpherson, A. N.; Liddell, P. A.; Kuciauskas, D.; Tatman, D.; Gillbro, T.; Gust, D.; Moore, T. A.; Moore, A. L. *J. Phys. Chem. B* **2002**, *106*, 9424.

64. Garg, V.; Kodis, G.; Liddell, P. A.; Terazono, Y.; Moore, T. A.; Moore, A. L.; Gust, D. *J. Phys. Chem. B* **2013**, *117*, 11299.

65. Wiirthner, F.; Vollmer, M. S.; Effenberger, F.; Emele, P.; Meyer, D. U.; Port, H.; Wolf, H. C. *J. Am. Chem. Soc.* **1995**, *117*, 8090.

66. Pillai, S.; Ravensbergen, J.; Antoniuk-Pablant, A.; Sherman, B. D.; van Grondelle, R.; Frese, R. N.; Moore, T. A.; Gust, D.; Moore, A. L.; Kennis, J. T. M. *Phys. Chem. Chem. Phys.* **2013**, *15*, 4775.

67. Hwang, I.-W.; Kamada, T.; Ahn, T. K.; Ko, D. M.; Nakamura, T.; Tsuda, A.; Osuka, A.; Kim, D. *J. Am. Chem. Soc.* **2004**, *126*, 16187.
68. Kelley, R. F.; Lee, S. J.; Wilson, T. M.; Nakamura, Y.; Tiede, D. M.; Osuka, A.; Hupp, J. T.; Wasielewski, M. R. *J. Am. Chem. Soc.* **2008**, *130*, 4277.
69. Bahng, H. W.; Kim, P.; Sung, Y. M.; Maeda, C.; Osuka, A.; Kim, D. *Chem. Commun.* **2012**, *48*, 4181.
70. Treibs, A.; Kreuzer, F.-H. *Justus Liebigs Ann. Chem.* **1968**, *718*, 208.
71. Loudet, A.; Burgess, K. *Chem. Rev.* **2007**, *107*, 4891.
72. Boens, N.; Leen, V.; Dehaen, W. *Chem. Soc. Rev.* **2012**, *41*, 1130.
73. Bai, J.; Pagano, R. E. *Biochem.* **1997**, *36*, 8840.
74. Niu, S. L.; Massif, C.; Ulrich, G.; Ziessel, R.; Renard, P.-Y.; Romieu, A. *Org. Biomol. Chem.* **2011**, *9*, 66.
75. Rurack, K.; Kollmannsberger, M.; Resch-Genger, U.; Daub, J. *J. Am. Chem. Soc.* **2000**, *122*, 968.
76. Baki, C. N.; Akkaya, E. U. *J. Org. Chem.* **2001**, *66*, 1512.
77. Beer, G.; Rurack, K.; Daub, J. *Chem. Commun.* **2001**, 1138.
78. Turfan, B.; Akkaya, E. U. *Org. Lett.* **2002**, *4*, 2857.
79. Liao, Y.; Genot, V.; Meallet-Renault, R.; Vu, T. T.; Audibert, J. F.; Lemaistre, J. P.; Clavier, G.; Retailleau, P.; Pansu, R. B. *Phys. Chem. Chem. Phys.* **2013**, *15*, 3186.
80. Chen, T.; Boyer, J. H.; Trudell, M. L. *Heteroat. Chem* **1997**, *8*, 51.
81. Geng, H.; Hill, C. M.; Zhu, S.; Liu, H.; Huang, L.; Pan, S. *RSC Adv.* **2013**, *3*, 2306.
82. McCusker, C.; Carroll, J. B.; Rotello, V. M. *Chem. Commun.* **2005**, 996.
83. Caruso, E.; Banfi, S.; Barbieri, P.; Leva, B.; Orlandi, V. T. *J. Photochem. Photobiol., B* **2012**, *114*, 44.
84. Lakshmi, V.; Ravikanth, M. *Dyes Pigm.* **2013**, *96*, 665.
85. Descalzo, A. B.; Xu, H. J.; Shen, Z.; Rurack, K. *Ann. N.Y. Acad. Sci.* **2008**, *1130*, 164.
86. Martin, A.; Long, C.; Forster, R. J.; Keyes, T. E. *Chem. Commun.* **2012**, *48*, 5617.
87. Gareis, T.; Huber, C.; S. Wolfbeis, O.; Daub, J. *Chem. Commun.* **1997**, 1717.
88. Wan, C.-W.; Burghart, A.; Chen, J.; Bergström, F.; Johansson, L. B. Å.; Wolford, M. F.; Kim, T. G.; Topp, M. R.; Hochstrasser, R. M.; Burgess, K. *Chem. - Eur. J.* **2003**, *9*, 4430.
89. Harriman, A.; Izzet, G.; Ziessel, R. *J. Am. Chem. Soc.* **2006**, *128*, 10868.

90. Goze, C.; Ulrich, G.; Mallon, L. J.; Allen, B. D.; Harriman, A.; Ziessel, R. *J. Am. Chem. Soc.* **2006**, *128*, 10231.

91. Kolb, H. C.; Finn, M. G.; Sharpless, K. B. *Angew. Chem. Int. Ed.* **2001**, *40*, 2004.

92. Prince, S. M.; Papiz, M. Z.; Freer, A. A.; McDermott, G.; Hawthornthwaite-Lawless, A. M.; Cogdell, R. J.; Isaacs, N. W. *J. Mol. Biol.* **1997**, *268*, 412.

93. Iehl, J.; Nierengarten, J. F.; Harriman, A.; Bura, T.; Ziessel, R. *J. Am. Chem. Soc.* **2012**, *134*, 988.

Chapter 2. The effect of solvent viscosity on the photophysical properties of a prototypic fluorescent rotor and its complementary bichromophoric analogue

2.1 Executive summary

Sterically unhindered boron dipyrromethene (Bodipy) dyes bearing aryl hydrocarbons at the *meso*-position can function as fluorescent probes for monitoring changes in the rheology of the surrounding environment. The key aspect of such behaviour relates to the ease of rotation of the aryl ring, which is set in part by frictional forces with nearby solvent molecules. For the target dye under consideration here, gyration of the *meso*-phenylene ring shows significant temperature dependence but only a modest sensitivity towards applied pressure. Changing the specific viscosity of the solvent by adding a linear polymer has but a small effect on the fluorescence yield of the dye under ambient conditions and thereby indicates that there is little contact between dye and polymer. Under pressure in the presence of polymer, the fluorescence yield increases dramatically and allows design of an effective fluorescence-based pressure sensor. The simplest explanation of this phenomenon has the polymer wrapping around the dye under applied pressure and curtailing the rotary action. In addition, it has to be considered that the inert polymer renders the chloroform solvent more susceptible to a pressure induced increase in density by minimising electrostatic repulsion between chlorine lone pairs. In this respect, the polymer acts as a lubricant for compression of chloroform under pressure. The corresponding bichromophoric compound, which also possesses an unrestricted *meso*-phenylene ring, does not operate as an effective rheology probe due to internal quenching effects caused by the bridge.

2.2 Structure

Figure 1 presents energy-minimised structures of the four target compounds under study in this chapter; where **ROBOD** is the sterically unhindered (i.e., rotor) Bodipy dye, **BODIPY** is the control (i.e., sterically constrained) compound, **di-ROBOD** and **di-BODIPY** are the corresponding bichromophoric dyes bridged with 1,2,4,5-tetrahydroxybenzene. These geometries were computed at the semi-empirical AM1 level using SPARTAN. The compounds were provided by members of Dr Raymond Ziessel's group in Strasbourg and were purified extensively before being dispatched. They were used as supplied. The halogen atoms attached to the periphery are intended as anchors by which to append secondary functions and do not perturb the photophysical properties in any observable way.

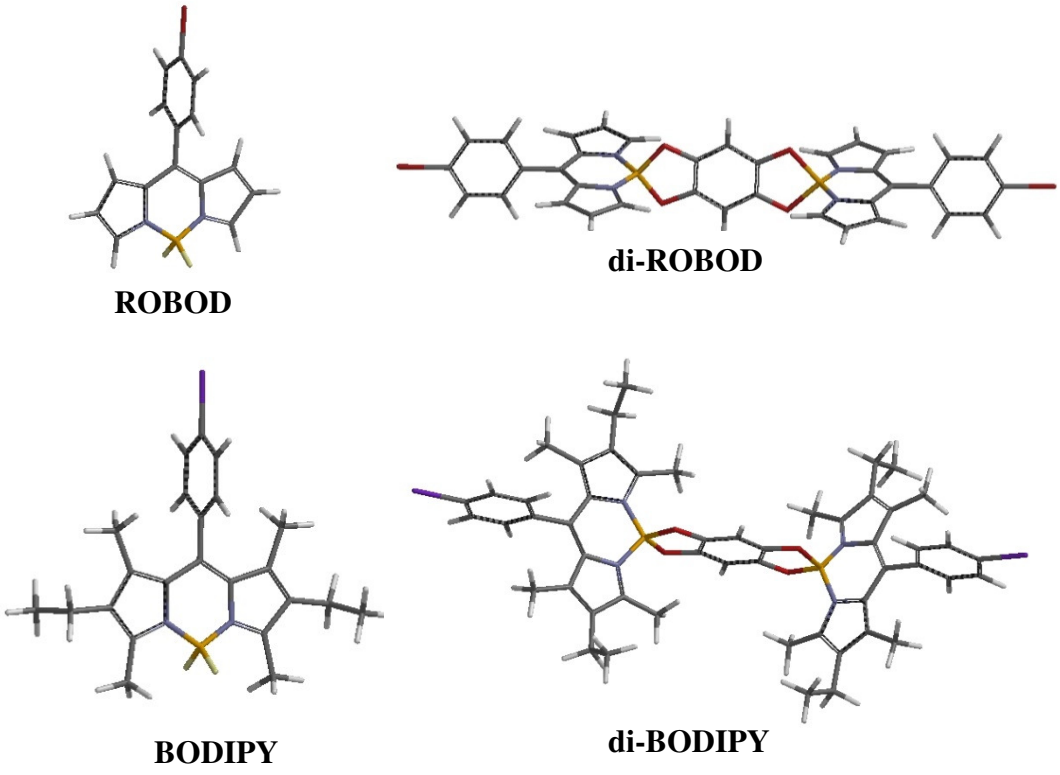

Figure 1. Molecular structures of the target compounds as computed at the AM1 level: carbon (grey), hydrogen (white), boron (dark yellow), fluorine (light yellow), nitrogen (light purple), oxygen (red), iodine (dark red) and bromine (purple).

2.3 Introduction

Considerable theoretical[1-3] and experimental[4-6] attention has been directed towards understanding the role of the solvent in controlling the dynamics of barrier crossing[7] in simple molecular systems. The most widely studied processes involve light-induced conformational exchange in fluid solution at ambient pressure. Indeed, such studies

have identified[8,9] a range of fluorescent rotors that can be applied for the *in situ* determination of local viscosity changes. Although much progress has been made in this field since the seminal contributions by Kramer in 1940,[10] our comprehension of such reactions remains rather incomplete. This is due, at least in part, to the interplay between several overlapping effects that are not easily resolved by experiment. For example, it becomes difficult to isolate polarity effects from corresponding changes in viscosity[11-13] and in extracting barrier heights from activation energies associated with solvent properties.[14] Even in n-alkane solvents, the isomerisation rate constant rarely exhibits the anticipated correlation with inverse viscosity.[15] This has precipitated the introduction of various models to correct for the inadequacy of bulk viscosity to depict frictional forces between solute and solvent.[16] These modifications and adaptations, while being suitable for the development of fluorescent rheology probes, fall well short of providing improved theoretical understanding. This situation also holds for the correlation of rotational diffusion times with solvent properties.

Within the generic area of rheology probes,[17,18] unhindered boron dipyrromethene (Bodipy) dyes have found prominent use in both biological[9,19,20] and artificial environments.[21-24] The key premise here is that a *meso*-phenylene ring is subjected to mild stereochemical blocking by hydrogen atoms on the dipyrrin backbone. This H,H clash hinders full rotation of the phenylene ring but does not stop the process. As a result, the fluorescence quantum yield and excited-state lifetime increase steadily with increasing viscosity of the surrounding medium, although the correlation is rarely linear.[25-27] It is normal practice to vary viscosity by changing the composition of the solvent or by ramping the temperature. Both effects introduce complications for data analysis. Clearly, there are benefits for covering the entire friction regime of interest using a single solvent under isothermal conditions and this can be achieved by subjecting the system to applied pressure.[25-27] Pressure compresses[28] the solvent, raising the density and thereby affecting the viscosity. Of course, there are ancillary effects on both refractive index[29] and dielectric constant[30] that have to be taken into account.

An alternative way to change solvent viscosity in a controlled way is to add an inert polymer.[31] The conformation of a dissolved polymer is a complex function of the properties of both solute and solvent and can be further modified by applying pressure to the system. Here, while seeking to examine how well Kramer's model[10] works with a Bodipy-based fluorescent rotor in solvent-polymer mixtures, we have encountered an unusual synergy. In particular, it is shown that adding polymer to a solution of the dye under ambient conditions has less effect on the fluorescence yield than predicted from

the global change in viscosity. When subjected to applied pressure, however, the presence of the polymer causes restoration of fluorescence from the dye by switching off the rotary action. The net result is a much-improved fluorescent sensor by which to monitor pressure changes at fixed temperature. In seeking to extend the work, we have examined the complementary bichromophoric compounds[32,33] (Figure 1) where two Bodipy units are interlinked through the boron atoms. The actual linkage is a 1,2,4,5-tetrahydroxybenzene unit that allows the *meso*-phenylene ring to remain unconstrained. Throughout the study, comparison is made between unrestricted and restricted dyes.

2.4 Comparison of the simple rotor and its sterically constrained analogue

2.4.1 Photophysical properties

The absorption and fluorescence spectra of **BODIPY** and **ROBOD** were recorded in 2-methyltetrahydrofuran (MTHF) at room temperature. As can be seen from inspection of Figure 2, **ROBOD,** which is a member of a well-known class of viscosity probes,[25] displays a strong absorption transition with a clear maximum at 502 nm and reasonable mirror symmetry fluorescence centred at 530 nm. The Stokes' shift of 1,050 cm^{-1} is modest and attests to minor structural distortion accompanying population of the first-excited singlet state.[34]

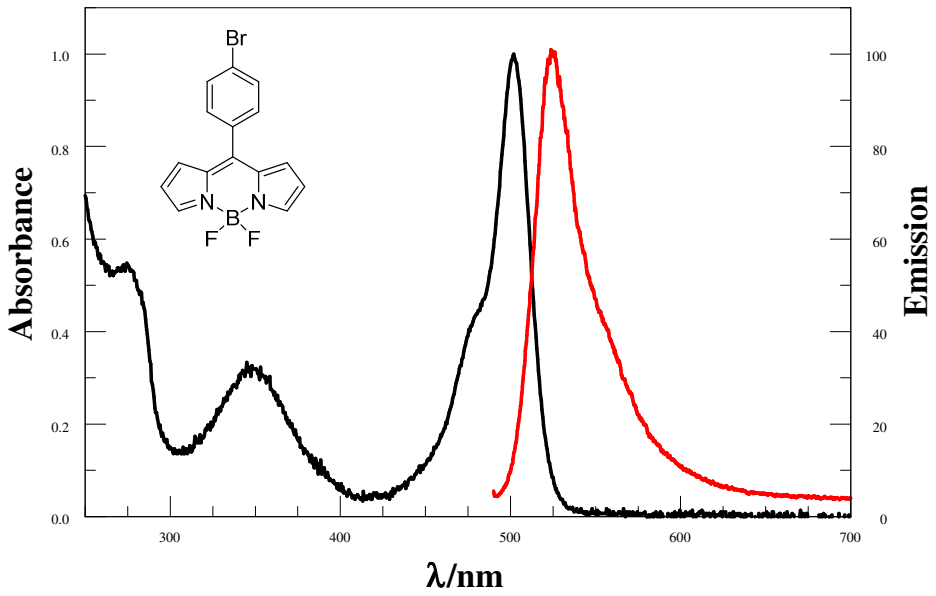

Figure 2. Normalised absorption (black) and fluorescence (red) spectra recorded for **ROBOD** in MTHF at room temperature.

The *meso*-phenylene ring gyrates around the connecting single bond,[21] causing slight buckling of the dipyrrin backbone, in fluid solution at ambient temperature. In turn, this rotary effect enhances nonradiative decay of the first-excited-singlet state and causes a pronounced loss of fluorescence (>95%). The significance of this rotary action can be gauged by comparing the photophysical properties of **ROBOD** with those of the sterically blocked analogue, **BODIPY**, where the only important structural change relates to the presence of methyl groups at the 1,7-positions. It might be argued that these methyl groups are not sufficiently bulky to prevent rotation of the phenylene ring. Certainly, the ring will gyrate about a mean position and molecular dynamics simulations made *in vacuo* can be used to suggest that infrequent full rotation takes place. Related dyes studied by Lindsey and coworkers[21] having blocking methyl groups at the 2,6-positions of the phenylene ring but no dipyrrin substituents do behave as molecular rotors, albeit ineffective ones. Also, Kuimova et al.[9] have reported a clear dependence of the fluorescence quantum yield on the availability of methyl groups at the *meso*-phenylene and/or dipyrrin unit. Furthermore, we show below that the nonradiative rate constant determined for **BODIPY** contains an activated component that could reflect minor rotation of the *meso*-phenylene ring.

To ensure that **BODIPY** fulfills its primary role as a control compound, we have recorded the pressure-induced absorption and fluorescence spectral changes for perylene,[30] where internal rotation cannot take place. Such critical comparison indicates that **BODIPY** is, at best, a very poor molecular rotor under our conditions. Table 1 lists the maximum absorption (λ_{abs}) and emission (λ_{flu}) peaks recorded for the two dyes in MTHF at room temperature. The slight shifts are due to the inductive effect of the alkyl substituents. Also shown are fluorescence quantum yields (Φ_{flu}), singlet-excited state lifetimes (τ_s), radiative (k_{rad}) and nonradiative (k_{nrd}) rate constants and Stokes' shifts (SS) for the two compounds recorded under identical conditions. It can be seen that whereas nonradiative decay is relatively unimportant for **BODIPY**, it is the dominant deactivation route for **ROBOD**. The quenching rate constant, which is attributed to the rotation of the *meso*-phenylene ring as described above, can be calculated from the total constant rate ($k = \frac{1}{\tau_s}$) to give a value 6 x 10^9 s^{-1}.

Table 1. Photophysical properties recorded for the two target dyes in MTHF at room temperature. [(a)]The standard uncertainty is ± 5%. [(b)]The standard uncertainty is ±10%. [(c)] Obtained from $\tau_s=\Phi_{flu}/k_{rad}$.

Dye	λ_{abs}/nm	λ_{flu}/nm	Φ_{flu}[(a)]	τ_s/ns[(b)(c)]	k_{rad}/ $10^8 s^{-1}$ [(b)]	k_{nrd}/ $10^7 s^{-1}$ [(b)]	SS/cm^{-1}
ROBOD	502	530	0.023	0.15	1.5	630	1050
BODIPY	525	547	0.72	4.8	1.5	6	765

Closely comparable results were found in a small range of other solvents (Table 2) and there are no obvious effects of solvent polarity on the photophysical properties of these compounds.[35]

Table 2. Recorded photophysical properties in different solvents at room temperature. [(a)]The standard uncertainty is ± 5%. [(b)]The standard uncertainty is ±10%.[(c)] Obtained from $\tau_s=\Phi_{flu}/k_{rad}$. DCM is dichloromethane, MTHF is 2-methyltetrahydrofuran, EtOAc is ethyl acetate and $CHCl_3$ is chloroform.

Dye	Solvent	λ_{abs}/nm	λ_{flu} /nm	SS /cm^{-1}	Φ_{flu}[(a)]	τ_s /ns[(b)(c)]	k_{nrd}/ 10^7 s^{-1}[(b)]
ROBOD	DCM	504	523	720	0.03	0.19	500
	MTHF	502	530	1050	0.023	0.15	630
	EtOAc	502	521	725	0.02	0.14	670
	$CHCl_3$	506	524	680	0.037	0.24	400
BODIPY	DCM	528	544	555	0.77	5.13	4.5
	MTHF	525	547	765	0.72	4.8	6
	EtOAc	520	541	745	0.99	6.6	0.2
	$CHCl_3$	530	546	550	0.67	4.47	7.4

To confirm that the enhanced nonradiative decay of **ROBOD** is due to the rotor effect, the emission properties of both compounds were recorded in MTHF as a function of temperature. In accordance with the Englman–Jortner energy-gap law,[36] fluorescence from **BODIPY** is quite insensitive to changes in temperature over the range from 77 to 300K.[21] However, Φ_{flu} recorded for **ROBOD** increases markedly as the temperature decreases and becomes comparable to that of **BODIPY** below the freezing point of the solvent (Figure 3). As the temperature falls, the emission profile narrows slightly but does not undergo a significant spectral shift until the solvent freezes at ca. 150K. On forming a glassy matrix at ca. 100K, the fluorescence profile sharpens further and

undergoes a small blue shift. Comparable spectral changes are found for **BODIPY** but here Φ_{flu} increases only slightly (i.e., <10%) as the temperature decreases (Figure 4).

$$k_{nrd} = k^{\circ}_{nrd} + k_{act}e^{-\frac{E_A}{RT}} \qquad \text{Equation (1)}$$

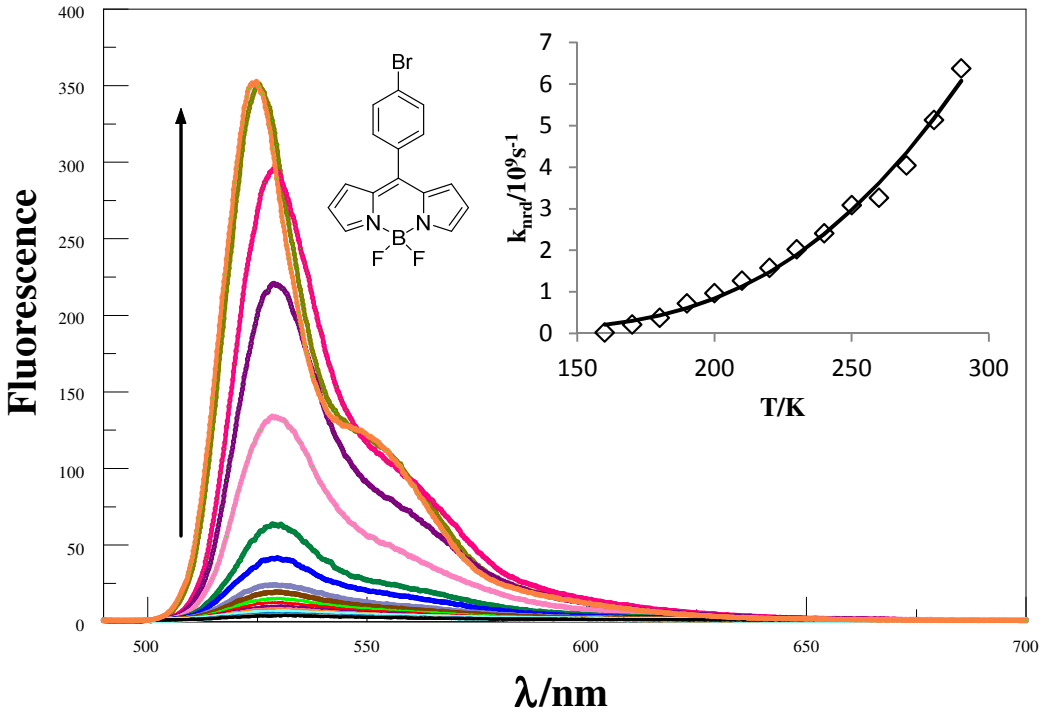

Figure 3. Effect of temperature on the fluorescence spectrum of **ROBOD** in MTHF. The emission increases as the temperature falls in the direction of the arrow. The insert shows the effect of temperature on the nonradiative rate constant. The solid line is the fit according to Eqn.1.

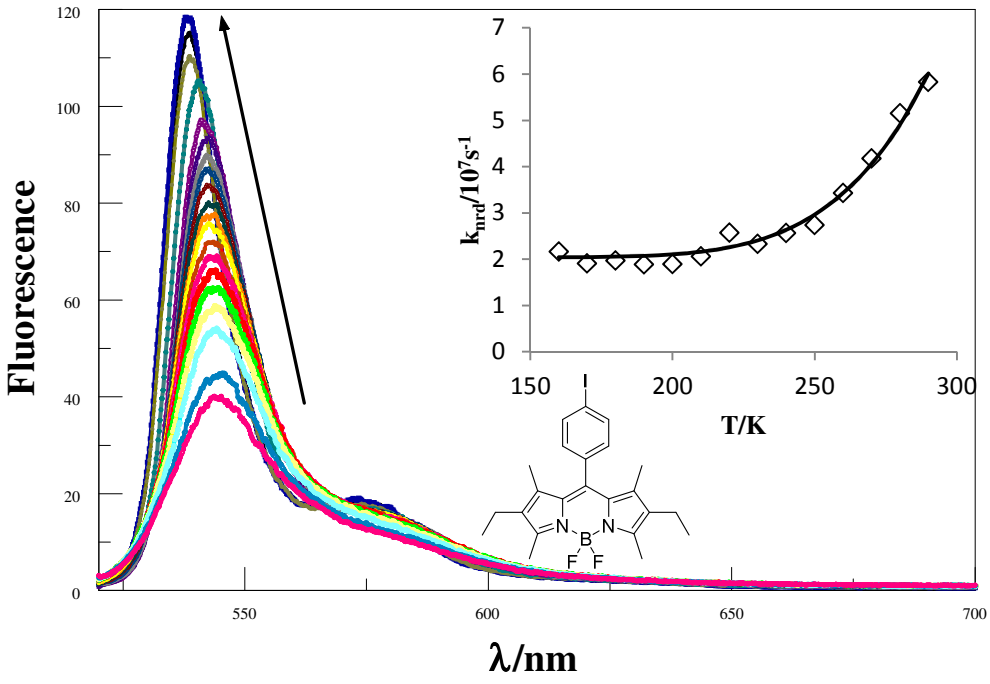

Figure 4. Effect of temperature on the fluorescence spectrum of **BODIPY** in MTHF. The emission increases as the temperature falls in the direction of the arrow. The insert shows the effect of temperature on the nonradiative rate constant. The solid line is the fit according to Eqn.1.

For both dyes, the nonradiative rate constant falls smoothly as the temperature drops and can be explained quantitatively in terms of Equation (1), where k_{nrd}° is a temperature independent rate constant that tends to dominate in the glassy region, k_{act} is an activated rate constant for nonradiative decay in the liquid phase, and E_A is the activation energy for the latter process (Figures 3 and 4). The derived parameters for the two dyes are collected in Table 3. It might be considered that the activationless rate constant included in Equation (1) is redundant, especially in the liquid phase, although it must improve the overall quality of the fit. When extending the fit to include the frozen and glassy states (MTHF freezes at about 140K but does not form an optical glass until around 110K) the fit demands inclusion of k_{nrd}°. This latter term includes intersystem crossing to the triplet manifold and vibrational relaxation to the ground state. Both of these processes should be activationless.[36] It is not possible to simply ascribe the activated step to rotation of the phenylene ring (i.e., the rotary action that underpins the ability of **ROBOD** to monitor local viscosity) because the exact nature[21] of the excited-singlet state potential energy curve is not known. It is likely that, in these unconstrained Bodipy derivatives, more than one structural motion is linked to nonradiative decay. Even for **BODIPY**, the fit to the experimental data collected over the full temperature range requires both k_{act} and k_{nrd}°.

It can be seen that whereas k_{nrd}° is similar for the two compounds, there are significant differences in the activated terms. Thus, the temperature-dependence studies indicate that **ROBOD** is characterised by a relatively small activation barrier of ca. 11 kJ.mol^{-1}. This barrier is believed to correspond to gyration of the phenylene ring around the dipyrrin backbone and is unavailable for the sterically locked dye; as such, E_A includes an important contribution from the temperature effect on the viscosity of the solvent. For **BODIPY**, a much higher barrier of ca. 31 kJ.mol^{-1} is found and this is difficult to cross at ambient temperature. The origin of this barrier is far from obvious but might also involve some type of ring rotation in the excited state. Note that intersystem crossing to the triplet manifold is relatively unimportant for both dyes. This point becomes significant when designing practical systems since triplet formation promotes generation[37,38] of singlet molecular oxygen.

Table 3. Derived parameters from Eqn.1 for the dyes in MTHF as a function of temperature.

Dye	k_{nrd}° / 10^7s^{-1}	k_{act}/ 10^{11}s^{-1}	E_A/kJ.mol^{-1}
ROBOD	6.2	5.2	11.0
BODIPY	2.8	110	31.1

It is worth mentioningthat all collected data were corrected before fitting by applying Equation (2) that describes changes of the solvent viscosity with temperature;$\gamma = \frac{\eta}{\rho}$ where γ is the kinematic viscosity, η is the dynamic viscosity and ρ is the density.[36] For MTHF at room temperature γ = 0.7 so η = 0.7ρ and from $\rho = 1.1 - 9.2 \times 10^{-4}T$ [39] we have:

$$\eta = 0.784 - 6 \times 10^{-4}T \qquad \text{Equation (2)}$$

2.4.2 Effect of viscosity

In principle, the barrier to internal rotation of the *meso*-phenylene ring present in **ROBOD** should increase with increasing viscosity of the surrounding solvent, although the effect might be nonlinear[25-27] and more correctly described in terms of micro-viscosity. Two experiments were made in order to assess this situation with **ROBOD** in chloroform; the change in solvent being necessitated by the need to add an inert polymer, namely poly(methyl methacrylate), PMMA. Firstly, the effects of added PMMA (molar mass = 120,000 g/mol, density = 1.185 g/cm^3) on the fluorescence yield of **ROBOD** were explored under ambient conditions. In fact, Φ_{flu} is hardly affected by the presence of high concentrations of polymer as can be seen from Figure 5. There is a small increase in Φ_{flu} with increasing PMMA content, amounting to a change from 0.03**7** to 0.048 on addition of a high concentration (i.e., 25% w/v) of PMMA. This corresponds to a decrease in k_{nrd} of ca. 20%. Within experimental limitations, this increase is linear with respect to PMMA concentration, although there is considerable spread of the data caused by the relative insensitivity. It might be noted that the presence of PMMA raises the viscosity of the solution by a significant amount (Figure 6).[40,41]

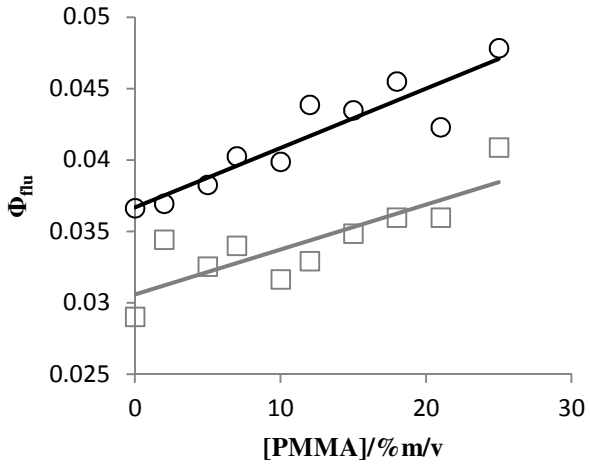

Figure 5. Effect of added PMMA on the fluorescence quantum yield for **ROBOD** (circles) and **di-ROBOD** (squares). The solid lines are least-squares fits to a linear expression.

Although it is known[25-27] that **ROBOD** responds to changes in local viscosity, as adjusted by changing the nature of the bulk solvent, this appears not to be the case when the viscosity is altered[42] by addition of a linear polymer; the shear viscosity increases from 0.563 mPa.s in the absence of polymer to 1.35 mPa.s for the highest concentration of PMMA used here. When the same change in viscosity is realised by changing the nature of the solvent, Φ_{flu} increases by 2.15-fold at 20 °C.[25]

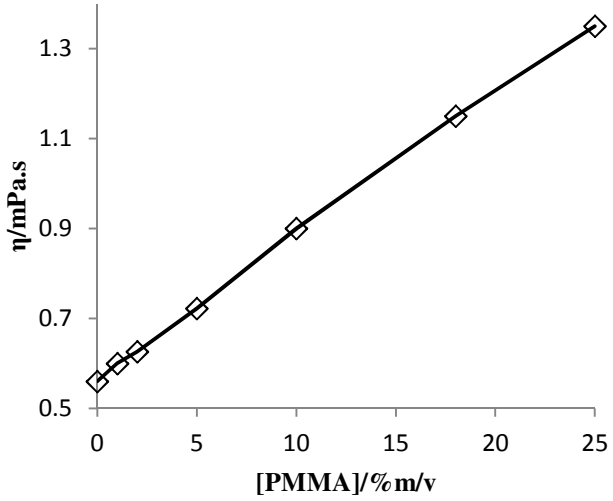

Figure 6. Illustration of how the viscosity of $CHCl_3$ is affected on adding PMMA at room temperature under atmospheric pressure.[41]

The inference to be drawn from this observation is that **ROBOD** remains in the $CHCl_3$ solvent and does not interact significantly with the polymer. As such, its fluorescence behaviour is somewhat isolated from the full rheological effects of the added PMMA. Likewise, the presence of polymer has no effect on either the absorption or fluorescence spectral profiles in $CHCl_3$ solution. Comparable behaviour was found for **BODIPY** under the same conditions where the presence of PMMA has essentially no effect on the fluorescence quantum yield or optical properties.

In the second experiment, we examined the effect of applied pressure on the fluorescence properties of **ROBOD** in $CHCl_3$ at 20 °C. Under such conditions, the density (ρ = 1.483 g/cm^3) of $CHCl_3$ increases and its freezing point, which is -63.5 °C at atmospheric pressure, is elevated to room temperature under an applied pressure of 0.6 to 0.8 GPa.[43] The magnitude of the pressure-induced change in density is easily monitored by recording the absorbance for the S_0-S_1 absorption transition (Figure 7). There is a progressive increase in absorbance with applied pressure that amounts to a factor of ca. 20% over a pressure range of 0–550 MPa. Because of this latter effect, there is also a small change in polarizability of the solvent[44] which, in turn, causes a small red shift for both absorption and fluorescence maxima recorded for **ROBOD**; these shifts amount to ca. 7 nm for a pressure increase up to 550 MPa. Over the same pressure range, there is a substantial increase in Φ_{flu} that, after correction for compression of the solvent, amounts to an increase from 0.037 at atmospheric pressure

to 0.17 at a pressure of 550 MPa (Figure 8). Before attempting analyses of these data it is prudent to consider similar experiments made for the control dye.

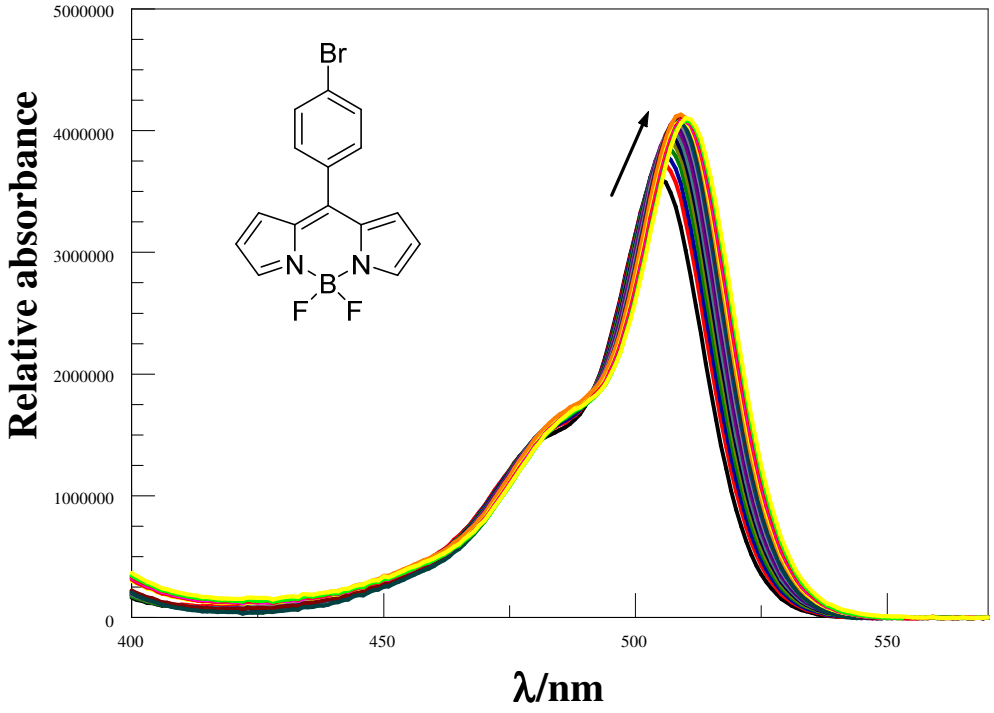

Figure 7. Effect of applied pressure on the absorption spectral profile recorded for **ROBOD** in $CHCl_3$ at room temperature.

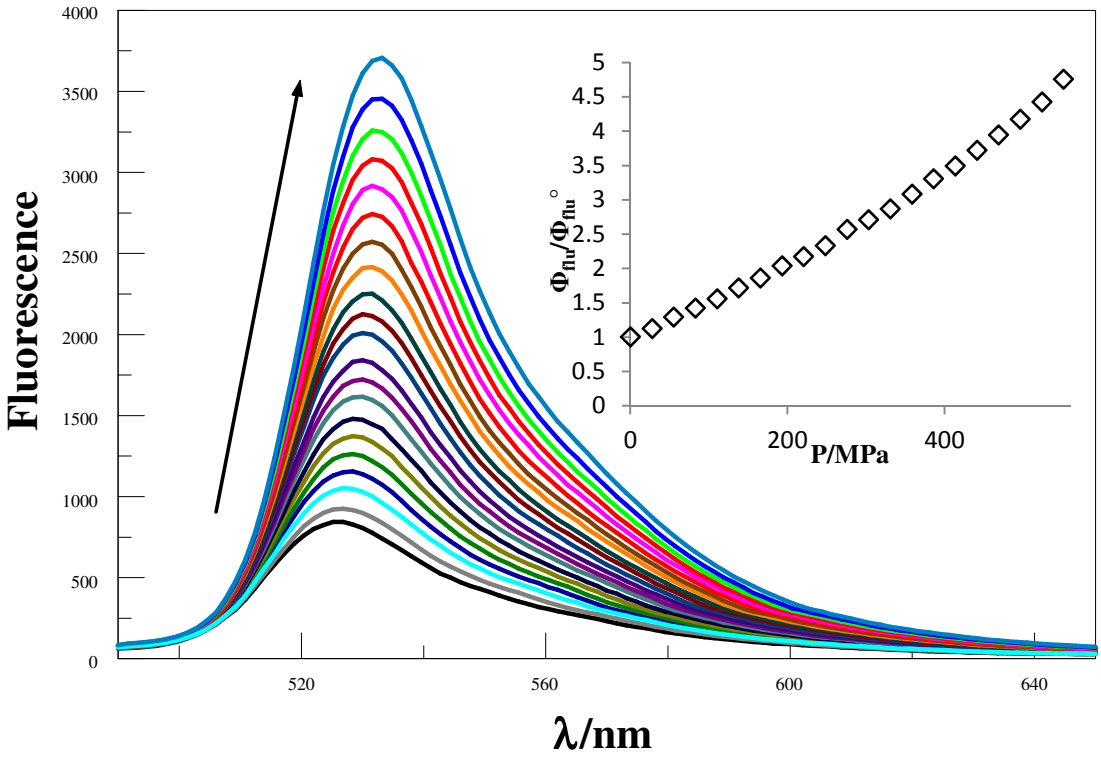

Figure 8. Effect of applied pressure on **ROBOD** fluorescence spectrum in $CHCl_3$ at room temperature. The insert shows the effect on the relative fluorescence yield.

Thus, applied pressure causes an increase in absorbance and a small red shift for the peak maximum for **BODIPY** in MTHF at room temperature; N.B. the effects of pressure on the properties of MTHF have been described earlier.[30] There is a similar red shift for the fluorescence maximum and a small increase in Φ_{flu}, after correction for the density change. This modification of Φ_{flu} is due to a pressure-induced increase in the solvent refractive index and therefore a corresponding increase in k_{rad} (Figure 9a). This conclusion is supported by the observation that the nonradiative rate constant, k_{nrd}, is insensitive to changes in applied pressure over the full range (Figure 9b). Unlike **ROBOD**, the constrained Bodipy dye is a poor molecular rotor under these conditions. To be sure on this point, a further series of control experiments was made with perylene (Φ_{flu} = 0.88 and τ_s = 5.9 ns at atmospheric pressure) in MTHF, where there is no possibility for internal rotation. The derived data are shown by way of Figure 9. Increased pressure causes a very slight increase in Φ_{flu} (Figure 9a) due to the effect on k_{rad} but no change in k_{nrd} (Figure 9b).

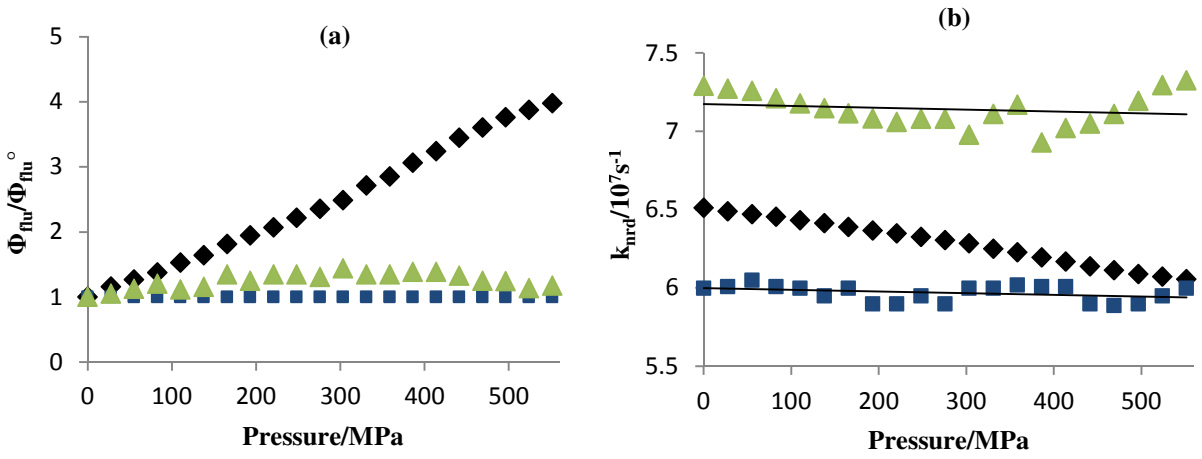

Figure 9. Effect of applied pressure on **ROBOD** (black), **BODIPY** (blue) and **perylene** (green) emission properties in MTHF at room temperature. (a) Relative fluorescence quantum yield. (b) Nonradiative decay rate constant where the values of **ROBOD** are divided by 100 and for **perylen** multiple by 0.3 for convenient comparison.

Now we return to the pressure effect on Φ_{flu} observed for **ROBOD** in $CHCl_3$ (Figure 8). The entire curve can be fitted to a power law expression of the type shown by Equation (3) where A and B are constants and C is the power coefficient. This expression implies that there is a limiting Φ_{flu} (A = 0.037) at low pressure and a pressure moderator (B = 35 x 10^{-5} MPa^{-1}). The derived value for the coefficient (C ≈ 1.0) indicates that Φ_{flu} evolves linearly with applied pressure, which is somewhat surprising in that pressure exerts an effect on both k_{rad}, because of the refractive index modulation,

and k_{nrd}. Perhaps, the apparent linearity reflects the fact that k_{nrd} dominates the deactivation process for this system. It is also to be expected that Φ_{flu} will become independent of pressure at very high pressure, or more correctly as Φ_{flu} approaches unity, but we are unable to access this range.

$$\Phi_{flu} = A + (BP)^C \qquad \text{Equation (3)}$$

For **ROBOD** in $CHCl_3$ at room temperature, pressure affects k_{nrd} in a nonlinear manner (Figure 9b). This is not so surprising because pressure has several simultaneous effects on factors affecting the fluorescence yield; e.g., increasing frictional forces, bending the dipyrrin backbone and modifying the shapes of ground- and excited-state potential energy surfaces. We attribute the general effect to inhibition of the rotary action[45] caused by closer packing of solvent molecules under pressure. At relatively high pressure (P >200 MPa), a log–log plot for k_{nrd} vs. P is linear with a gradient of -0.12. This is interesting in as much as Kramer's theory[10] predicts a corresponding linear log–log plot for k_{nrd} vs. viscosity. We do not know the precise relationship between pressure and viscosity for $CHCl_3$ but such correlations are often linear and, as such, the high-pressure behaviour illustrated for **ROBOD** on Figure 9 seems reasonable. In the low-pressure region, k_{nrd} tends towards a pressure-independent value that must correspond to a regime where viscosity no longer controls the dynamics of ring rotation. Again, this situation is fully consistent with Kramer's theory. [10]

2.4.3 Effects of applied pressure in the presence of added PMMA

It will be recalled that addition of PMMA has little effect on the absorption or emission properties of these dyes in $CHCl_3$ solution. There seems to be no real attraction between dye and polymer in this solvent under ambient conditions. Indeed, control experiments made with **BODIPY** or perylene in $CHCl_3$ containing PMMA (5% mass per volume) gave results strikingly similar to those obtained in the absence of polymer. However, on raising the pressure in the presence of PMMA fluorescence from **ROBOD** becomes more noticeable and, in particular, Φ_{flu} increases steadily with increasing pressure (Figure 10a). The rate of increase of Φ_{flu} with applied pressure is significantly more pronounced in the presence of PMMA. The net effect of pressure on Φ_{flu} can be described in terms of Equation (3),[46] although the apparent linearity seen in the absence of polymer is lost. Indeed, at high concentrations (>5% mass per volume) of PMMA the derived profiles are clearly curved. It is recognised that the specific viscosity[41,47] of the solution increases linearly with increasing mass percent of PMMA in $CHCl_3$ (Figure 6)

and throughout the range of PMMA concentrations, the value determined from the fit for the parameter A agrees well with that expected for the emission quantum yield in the presence of PMMA at atmospheric pressure (Table 4).

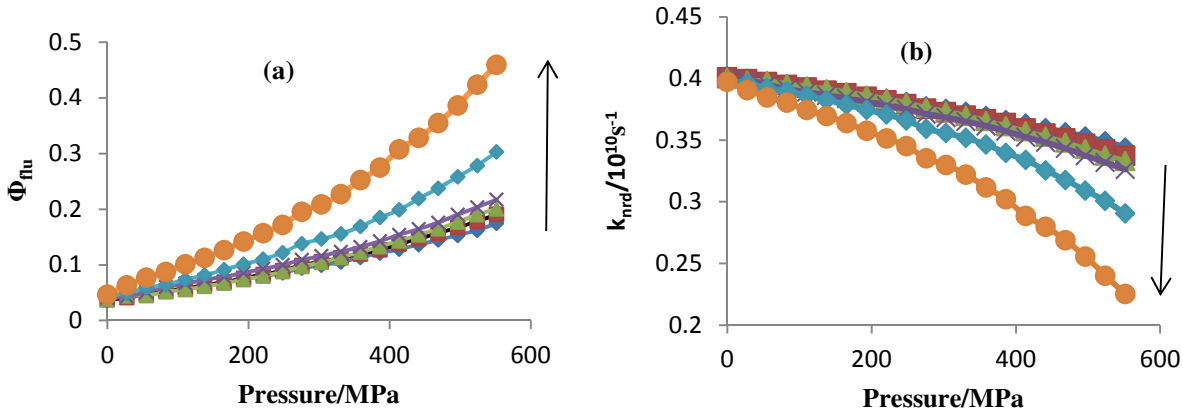

Figure 10. Effect of applied pressure for **ROBOD** in $CHCl_3$ containing PMMA ([PMMA] values are 0,2,5,10,18 and 25% m/v) at room temperature. The arrow indicates the direction of increasing [PMMA]. (a) Effect on the fluorescence quantum yield. (b) Effect on the nonradiative decay rate constant.

Table 4. Parameters derived from studying the effect of pressure on the fluorescence yield of **ROBOD** in $CHCl_3$ at room temperature.

PMMA %	A	$B/10^{-5}MPa^{-1}$	C	α
0	0.037	35	1.2	-0.12
2	0.038	42	1.3	-0.14
5	0.039	52	1.47	-0.16
10	0.041	61	1.45	-0.17
18	0.044	70	1.47	NA
25	0.047	94	1.4	NA

These data are shown in Figure 5 and lead to an improved understanding of how polymer concentration affects the fluorescence yield. As observed for the direct titration experiment, Φ_{flu} appears to evolve in a linear manner with added polymer, although the overall effect is modest and the high level of experimental uncertainty precludes close scrutiny of the fit. The two sets of data are reasonably consistent, although the fits diverge at high concentration of PMMA, and confirm that the presence of polymer does not, by itself, have much effect on the fluorescence quantum yield of the dye in $CHCl_3$ solution. The remaining terms in Equation (3),[46] namely the pressure moderator B, having units of inverse pressure, and the power coefficient C, increase systematically with increasing concentration of PMMA (Table 4). These two terms are likely correlated by the analysis but separating B from the power coefficient (i.e., $\Phi_{flu} = A + BP^C$) does not change the situation. Attempting to restrict either B or C to the value

derived without added PMMA fails to fit the experimental data; quite clearly C must increase throughout the data set to account for the observed curvature, but poor fits arise when fixing B. One feature to bear in mind is that pressure affects both k_{rad} and k_{nrd}, as mentioned earlier, but is acerbated as Φ_{flu} increases. It is also important to stress that Φ_{flu} must start to level out to a maximum value at very high pressure. This behaviour, which is not seen is our experiments, is not predicted by Equation (3).

It might be recalled that, within experimental limits, Φ_{flu} increases linearly with specific viscosity and it is known[48] that the rotational relaxation time (τ_R) of $CHCl_3$, measured by NMR or FTIR spectroscopy at 303K, increases progressively over the pressure range of interest to our studies. In turn, τ_R is expected to evolve in a first-order manner with shear viscosity divided by absolute temperature.[49,50] We can use this information to suggest that the observed pressure effect is not a simple consequence of increased shear viscosity. Rather, the evolution of Φ_{flu} seen here (Figure 10) is unique to the application of pressure in the presence of PMMA. The effect of applied pressure on k_{rad} in the presence of PMMA is unknown and therefore it is not possible to make the same kind of analysis for k_{nrd} as outlined above in the absence of polymer. At low concentrations of PMMA, log–log plots do show a linear region at high pressure when k_{rad} is taken to be that measured in pure $CHCl_3$ but the gradient (α) decreases slightly with increasing amount of polymer (Table 4). This apparent linearity disappears at high polymer concentrations.

Now, the overall effect is quite pronounced in as much as the combination of applied pressure and added PMMA restores fluorescence from **ROBOD** but not to the level found for **BODIPY**. At 550 MPa in the presence of 25% m/v PMMA, Φ_{flu} reaches 0.45 which represents an increase of almost 12-fold relative to pure $CHCl_3$ at atmospheric pressure. Under the same conditions, Φ_{flu} for **BODIPY** increases by <5%. Thus, PMMA and pressure act in synergy to enhance fluorescence from **ROBOD** and it is natural to attribute this situation to blocking of the rotary motion of the phenylene ring. The simplest explanation for this effect can be summarised as follows: Under pressure, the polymer starts to coil as a means by which to relieve the stress, most notably satisfying the need to lower the volume of the solution, and this structural change will entrap dye within the network. Close contact between polymer and dye will severely hinder rotation of the phenylene ring, cutting off nonradiative decay and restoring fluorescence. The net effect would be to coat the dye with a surrounding layer of plastic. Although attractive, this argument does not take due account of the known pressure effect on certain polymer solutions.[51,52]

It should be recognised that $CHCl_3$ is a good solvent for PMMA and, as such, the polymer will persist in a relatively extended conformation.[53,54] The fluorescent dye remains in the $CHCl_3$ such that its spectroscopic properties are insensitive to the presence of PMMA. Compression of the solution will lead to a marked escalation in PMMA concentration as the density increases but there is little evidence in the scientific literature to indicate that the radius of gyration of an added polymer changes with pressure.[55] The increased friction that accompanies the application of high pressure, therefore, is considered to arise from two complementary effects. Firstly, as the density of the solvent increases there is a concomitant increase in the concentration of the polymer and, in turn, this raises the viscosity. This situation is aided by the polymer chains serving to isolate $CHCl_3$ molecules such that there is less resistance towards compression, and at any given pressure, the density is higher in the presence of PMMA. Secondly, pressure modifies the extent of interaction between dye and polymer. In the limiting case, this could lead to the polymer coating the dye. Since pressure affects each individual part of the system (i.e., dye, solvent and polymer) to differing degrees, it is not unreasonable that the power coefficient C exceeds unity or that the moderator term B depends on the composition of the mixture.

2.5 Bichromophoric systems

2.5.1 Photophysical properties

Adding tetrahydroxybenzene as a bridge between two symmetrical **ROBOD** or **BODIPY** chromophores (Figure 1) serves to generate an unusual bichromophoric compound. The two chromophores are kept electronically isolated from each other and there are only minor alterations of the emission and absorption spectral maxima. However, the absorption spectrum recorded for **di-ROBOD** is somewhat broader than that of the simpler analogue, which suggests that the bridge causes some disturbance of the molecular system (Figure 11). This could be indicative of multiple conformations present in the ground state, although the structure seems pretty rigid, or to some level of asymmetry. A more notable effect is that fluorescence is rather low for both compounds, and looks to be somewhat comparable for the two dyes (Table 5), at least in some solvents.

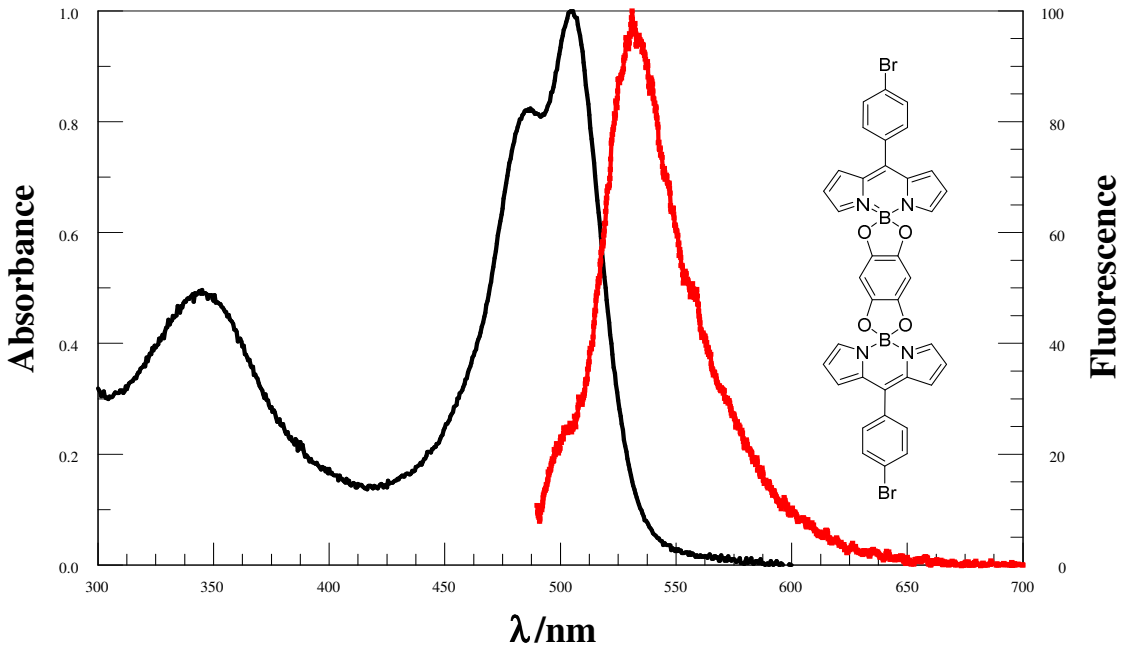

Figure 11. Normalised absorption (black) and fluorescence (red) spectra recorded for **di-ROBOD** in MTHF at room temperature.

For **di-BODIPY**, there is not much effect of solvent polarity on the measured fluorescence quantum yield while the excited-singlet state lifetime is very short in all solvents. This cannot be a consequence of internal rotation but is more likely due to intramolecular charge transfer between the Bodipy chromophore and the bridge. We can eliminate an alternative quenching step that involves electronic energy transfer since the bridge has no low-lying excited states that could operate as an acceptor and there is no obvious indication for a heavy-atom effect.[56] For **di-ROBOD**, there is more variation in the fluorescence quantum yield but without an obvious correlation with solvent dielectric constant. To further investigate this observation, emission spectra for **di-BODIPY** were recorded in toluene and cyclohexane, these being non-polar solvents where charge-transfer reactions are less likely, but to our great surprise there was no recovery of the fluorescence.

Table 5. Photophysical properties of the two bi-chromophores recorded in different solvents at room temperature. [(a)]The standard uncertainty is ±5%. [(b)]The standard uncertainty is ±10%. [(c)] Obtained from $\tau_s=\Phi_{flu}/k_{rad}$ where $k_{rad}=1.5x10^8 s^{-1}$.

Dye	Solvent	λ_{abs} /nm	λ_{flu} /nm	SS /cm^{-1}	Φ_{flu} [(a)]	τ_s /ns [(b)(c)]	$k_{nrd}/10^7 s^{-1}$ [(b)]
di-ROBOD	DCM	508	530	815	0.03	0.2	485
	MTHF	503	537	1260	0.006	0.04	2485
	EtOAc	504	527	865	0.008	0.05	1860
	$CHCl_3$	510	533	845	0.03	0.19	500
di-BODIPY	DCM	528	548	690	0.002	0.01	7485
	MTHF	524	550	900	0.009	0.06	1650
	EtOAc	524	542	635	0.002	0.01	7485
	$CHCl_3$	530	550	685	0.005	0.03	2985

Still pursuing the idea of light-induced charge transfer in these bichromophoric compounds, we recorded cyclic voltammograms for **di-BODIPY** in DCM (0.2 M tetra-butylammonium tetrafluoroborate as background electrolyte) (Figure 12). There are three reversible peaks that can be assigned on the basis of control studies. Thus, the one-electron oxidation of Bodipy occurs with a half-wave potential of 1.29 V vs Ag wire while the corresponding reduction step occurs with a half-wave potential of -1.13 V vs Ag wire. Under the same conditions, the bridge undergoes quasi-reversible, one-electron oxidation with a half-wave potential of only 0.42 V vs Ag wire. The calculated driving force $\Delta G°$ for electron transfer is -0.64 V in DCM, which means the electron transfer process is allowed thermodynamically and is likely to compete favourably with radiative decay of the first-excited singlet state.

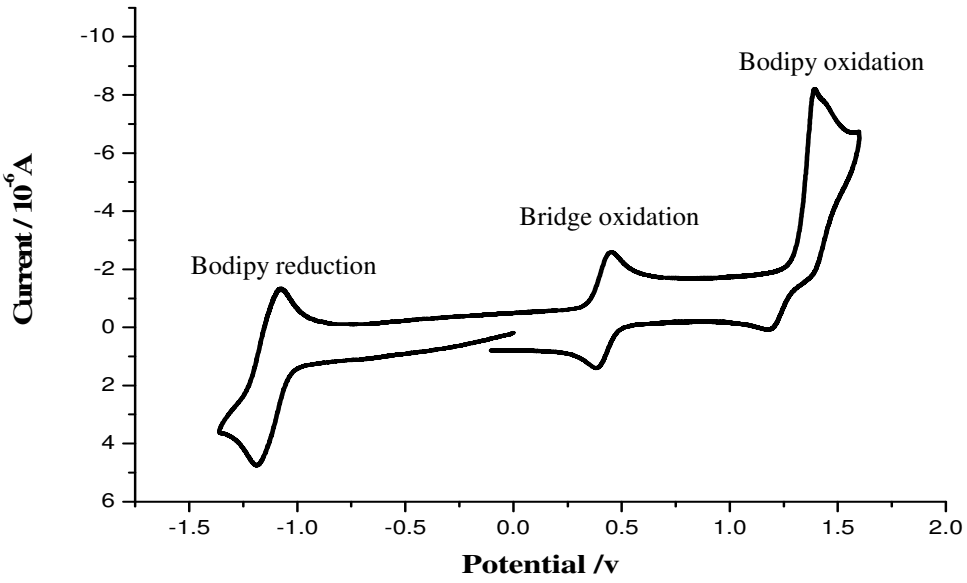

Figure 12. Cyclic voltamogram recorded for **di-BODIPY** in DCM at room temperature with an Ag wire as reference electrode, Pt wire as counter electrode and Pt as the working electrode. Scan rate 100 mV/s.

In order to obtain more insight into this system, especially in terms of the proposed light-induced electron-transfer reaction, it was decided to perform a temperature dependence study for the emission profile. On lowering the temperature, **di-BODIPY** undergoes partial recovery of the fluorescence signal. At 77K, the emission peak is blue shifted by ca. 4 nm compared to room temperature while the quantum yield is increased to 0.10 in glassy MTHF (Figure 13). Furthermore, a new peak starts to appear in the glass phase with a maximum at 622 nm; the quantum yield for this peak is ca. 0.025 at 90K. The most likely explanation for this latter peak is that it arises from charge recombination – that is to say that the observed fluorescence is due to an exciplex-type intermediate. Similar emission has been noted previously for certain Bodipy dyes equipped with weak electron donors or acceptors.[57,58] Formation of an emissive exciplex is a fine balance between the thermodynamic driving force, solvation of the charge-separated state and the solvent reorganisation energy. In the high temperature limit, we suppose that net electron transfer occurs but this process becomes less favourable at low temperature due to hindered structural rearrangements and the inherent activation energy. Under such conditions, charge transfer leads to exciplex formation but without net electron transfer.

Interestingly, the same fluorescence recovery was observed for **di-ROBOD** on cooling to the glassy region, where $\Phi_{flu} = 0.1$ (Figure 14). Above the melting point of the solvent (T = 147K), there is little variation in k_{nrd} with increasing temperature. Such behaviour is inconsistent with the rotor effect but can be well explained in terms of

solvent-controlled electron transfer. Thus, both the bichromophoric systems behave in a similar manner, despite the barrier to rotation of the *meso*-phenylene ring, and it seems that light-induced electron transfer is much faster than rotation-induced nonradiative deactivation of the excited-singlet state. Moreover, the exciplex peak can be seen under some circumstances as in the **di-BODIPY** case.

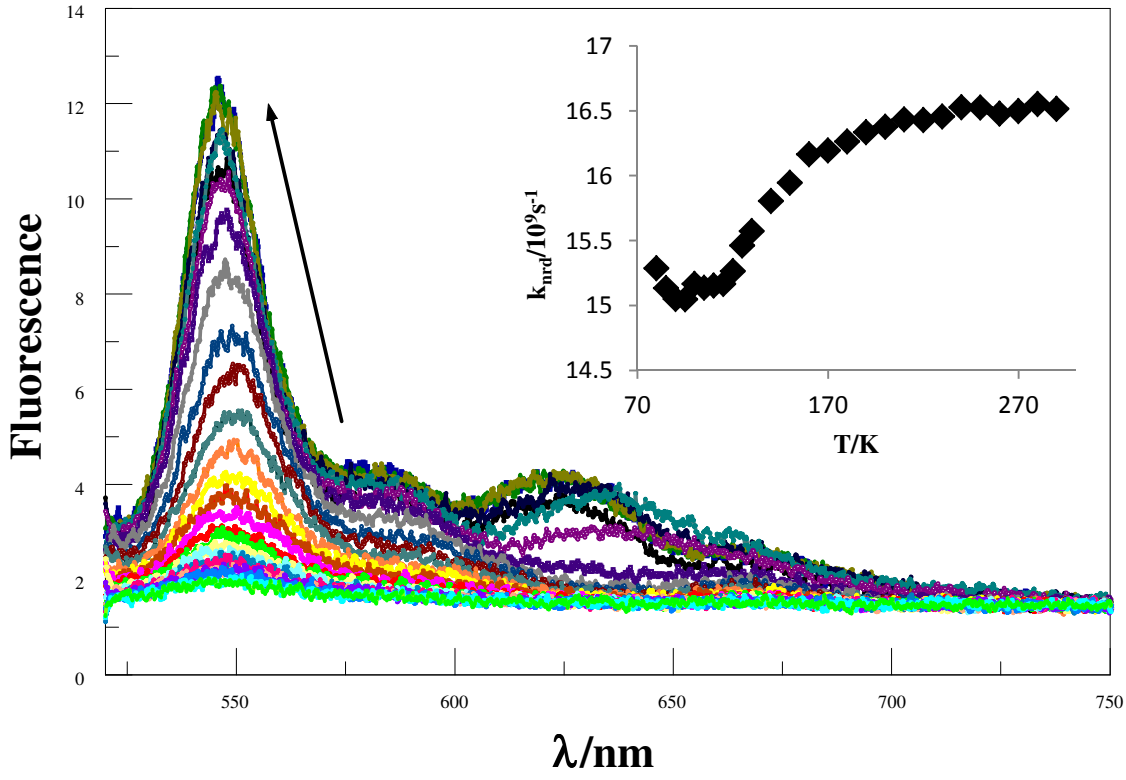

Figure 13. Temperature effect on the fluorescence spectral profile recorded for **di-BODIPY** in MTHF. The arrow indicates the direction of decreasing temperature while the insert shows the effect of temperature on the nonradiative rate constant.

In the case of **di-BODIPY**, it seems reasonable to suppose that light-induced electron transfer is solely responsible for the observed fluorescence quenching. If this really is the case we can calculate the activation energy for electron transfer in liquid solution from the temperature dependence (Eqn. 4). This approach allows estimation of ΔG^* as being 5.0 kJ.mol^{-1}; a value that is considered to be rather small. When treated in terms of conventional Marcus theory, on the basis that ΔG° = -0.64 eV, we find that the reorganisation energy (λ) accompanying charge separation is ca. 81 kJ.mol^{-1} ($\Delta G^* = (\Delta G^\circ + \lambda)^2/4\lambda$). This is a small value that suggests there is not a significant contribution from the solvent re-arrangement,[59,60] a situation that would help explain the relative insensitivity towards solvent polarity.

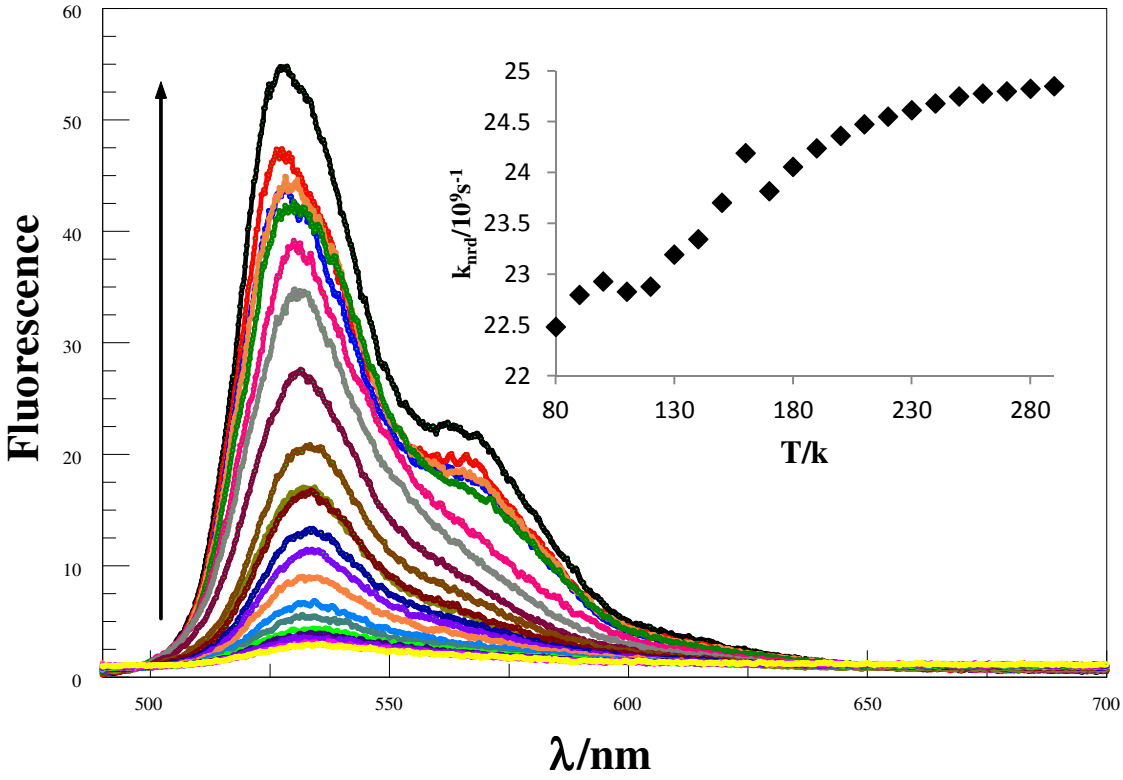

Figure 14. Temperature effect on the fluorescence spectral profile recorded for **di-ROBOD** in MTHF. The arrow indicates the direction of decreasing temperature while the insert shows the effect of temperature on the nonradiative rate constant.

Table 6 presents the derived parameters for the bichromophoric systems when analysed in terms of Equation (1). It can be argued, by comparing the results from Equations (1) and (4), that the values obtained for **di-BODIPY** indicate that the nonradiative process is due to electron transfer. But in the case of **di-ROBOD** we have to deal with the quenching rate constant as a combination of a rotation rate constant (k_{act1}) and an electron-transfer rate constant (k_{act2}).

$$k_{et} = Aexp^{\frac{-\Delta G^*}{k_B T}} \qquad \text{Equation (4)}$$

Table 6. Derived parameters from fitting to Eqn.1 for the bichromophoric systems in MTHF as a function of temperature. *These values represent the rotation effect expected on the basis of the corresponding monomer.

Compound	k°_{nrd} / $10^8 s^{-1}$	k_{act1}/ $10^{11} s^{-1}$	E_{A1}/ kJ.mol^{-1}	k_{act2}/ $10^{11} s^{-1}$	E_{A2}/ kJ.mol^{-1}
di-ROBOD	15*	9.5*	9.0*	5.2	8.0
di-BODIPY	10	1.3	5.00	NA	NA

2.5.2 Effect of increased viscosity for the bichromophoric systems

Initial experiments focussed on **di-ROBOD** in anticipation that some kind of comparison might be made with **ROBOD**. Increasing solvent viscosity by adding PMMA up to 25% in chloroform solution resulted in the fluorescence quantum yield increasing from 0.03 to 0.039, which is much the same as found for **ROBOD** (Figure 5). Varying the viscosity by changing the nature of the solvent, specifically replacing MTHF (0.6 mPa.s) with dimethylsulfoxide, DMSO, (1.99 mPa.s) resulted in further quenching of the fluorescence. This result is not too surprising since there is an accompanying increase in solvent polarity that might be expected to promote light-induced electron transfer. Incidentally, recording the degree of fluorescence quenching for **di-ROBOD** in DMSO over the temperature range from 25 to 75 °C resulted in determination of the pre-exponential factor and activation energy as being 2 x 10^{12} s^{-1} and 8.8 $kJ.mol^{-1}$, respectively. These values are comparable with the results from the corresponding low temperature experiment.

Next, we applied high pressure to a solution of **di-ROBOD** in chloroform at room temperature and recorded the changes in absorption and emission spectra. Focusing firstly on the absorption spectral properties, the bichromophoric system follows the same trend as already observed for **ROBOD**; the absorbance increases steadily with increasing pressure and there is a net red shift of 7 nm. Both effects arise from the increased density and consequent change in polarizability.[44] The same red shift appeared in the emission spectra while the fluorescence quantum yield increased from 0.03 to 0.08 over the full pressure range (Figure 15). Although qualitatively similar, **ROBOD** is more sensitive to changes in pressure (Figure 16) since the values for the pressure moderator (B) are 35 x 10^{-5} MPa^{-1} and 9 x 10^{-5} MPa^{-1} for **ROBOD** and **di-ROBOD**, respectively. This situation is probably a consequence of the competition between the rotary effect and electron transfer in the case of the latter compound.

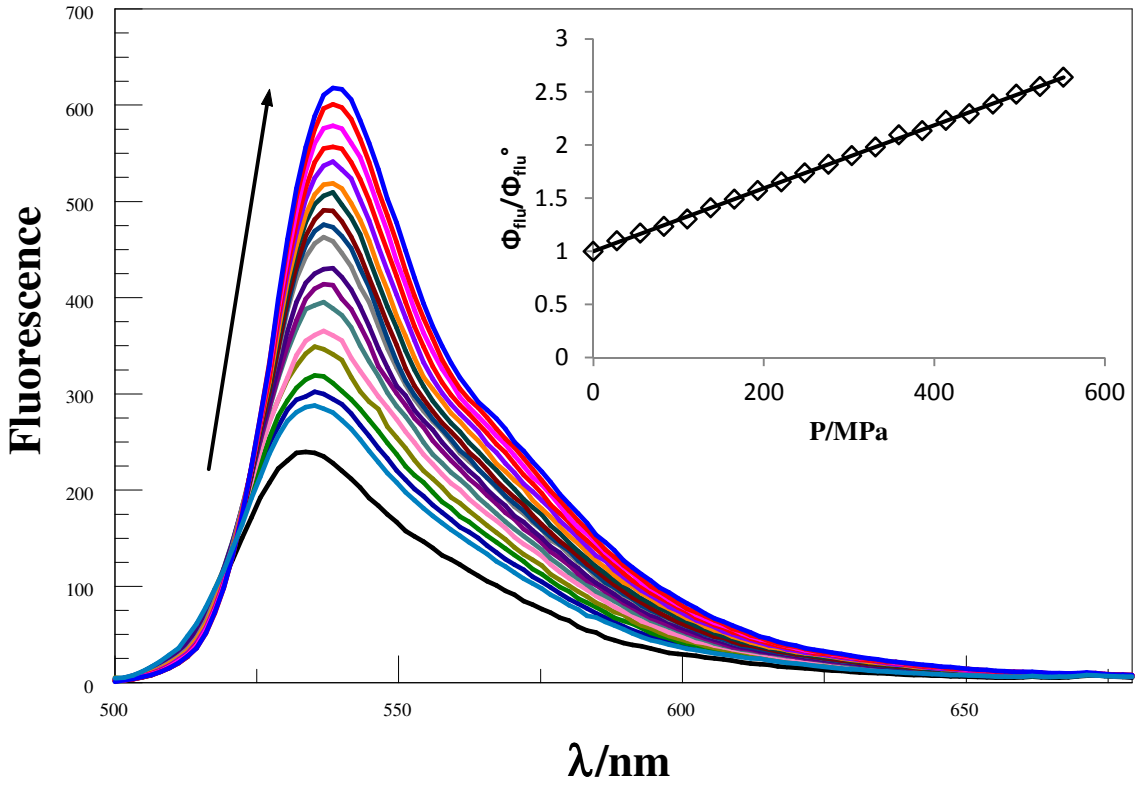

Figure 15. Effect of applied pressure on the fluorescence spectrum determined for **di-ROBOD** in $CHCl_3$ at room temperature. The arrow indicates the direction of increasing pressure. The insert shows how the relative fluorescence yield evolves with pressure.

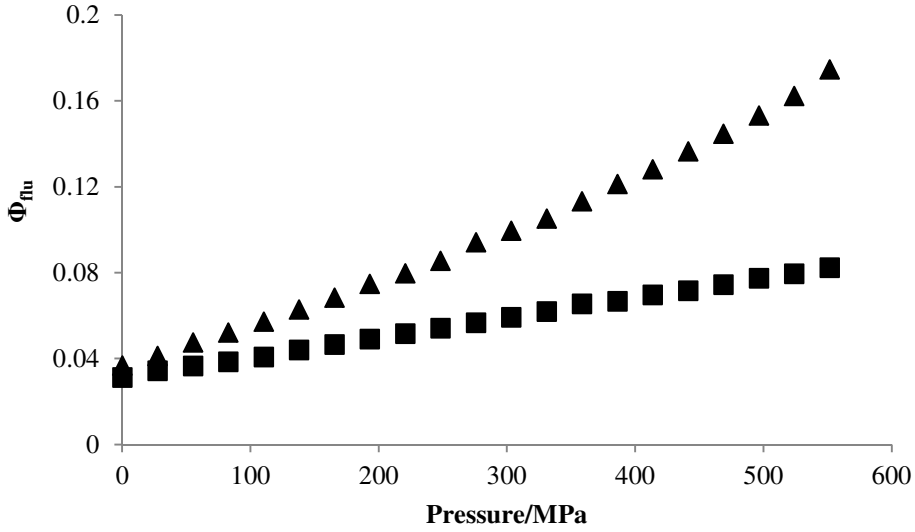

Figure 16. Fluorescence quantum yield of **ROBOD** (triangles) and **di-ROBOD** (squares) in $CHCl_3$ under applied pressure.

2.5.3 Effects of applied pressure in the presence of added PMMA

It was shown above for the simpler analogue that applying high pressure in the presence of PMMA leads to a more substantive increase in fluorescence from the dye than is observed with the pure solvent. At the simplest level, this effect is attributed to pressure forcing polymer molecules to wrap around the dye molecule and thereby increase the

local viscosity.[9] However, applying high pressure to a solution of **di-ROBOD** in the presence of PMMA at different concentrations up to 25% w/v does not show the same extent of recovery of the fluorescence. Under these conditions, the fluorescence quantum yield increases by a factor of only 3.5-fold under the most forcing conditions (i.e., 550 MPa and 25% w/v PMMA).

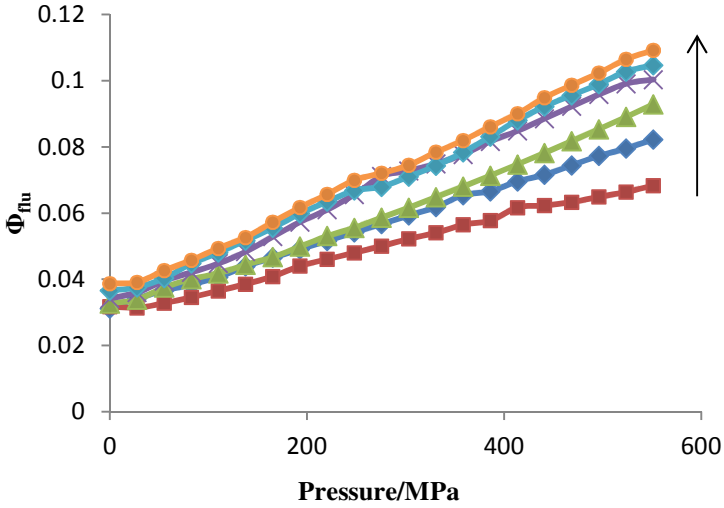

Figure 17. .Effect of applied pressure on the fluorescence quantum yield for di-**ROBOD** in $CHCl_3$ containing PMMA at room temperature. [PMMA] values are 0,2,5,10,18 and 25% m/v. The arrow indicates increasing [PMMA].

Moreover, comparing the fits to the experimental data for **ROBOD** and **di-ROBOD** exposes notable differences in the pressure moderator values (Tables 4 and 7). In general, the bichromophore responses to the pressure less than does the simpler analogue, although the overall behaviour remains much the same (Figure 17). Our understanding of this effect is that increased pressure (with polymer present) switches off the rotary behaviour and thereby leads to an increased lifetime for the excited state. However, this serves only to increase the probability of light-induced electron transfer, the rate of which is hardly affected by either pressure or the presence polymer.

Table 7. Parameters associated with the effect of applied pressure on the fluorescence of **di-ROBOD** in $CHCl_3$ at room temperature.

PMMA %	A	$B/10^{-5}MPa^{-1}$	C	α
0	0.031	9	1.0	-0.03
2	0.032	10	1.1	-0.03
5	0.033	17	1.2	-0.05
10	0.034	13	1.0	-0.05
18	0.037	16	1.1	-0.056
25	0.039	18	1.1	-0.057

2.6 Experimental note

All measurements were made as described in the experimental section given later. The compounds were supplied by our collaborators in Strasbourg and were used without further purification. All solvents were purchased as spectroscopic grade materials from Sigma-Aldrich and used as received. The reference compound employed to determine the fluorescence quantum yields was diketopyrrolopyrrol (DPP) in MTHF (Φ_{flu}=0.87).[56]

2.7 Conclusion

It might be possible to develop the molecular system described here as a simple but effective pressure sensor at ambient temperature. Such materials could be applicable for the routine detection of pressure, or accompanying viscosity changes, under hazardous or remote conditions. For example, lubrication usually involves the subjection of a polymer solution to very high pressures for extended periods under circumstances where it is difficult to make real-time measurements. Exposure to high pressures has no long-term effect on the fluorescence properties of the dyes used herein and control studies can be made with dyes unable to undergo internal rotation. The change in rheological properties of macromolecular solutions under applied pressure is a subject of considerable industrial importance but it presents severe challenges to both theory and rigorous experimental study. We consider this investigation as being a starting point for a detailed examination of the subject. A complicating issue in terms of sensor development is that the nonradiative rate constant depends on temperature. The actual relationship is complex and, at least for the present case, cannot be attributed to specific effects. There are at least three factors involved; viscosity, internal rotation, and backbone twisting. In this work, the activation studies are given only to indicate the rotor effect and the temperature dependence is treated globally. It is also important to stress that a more complete understanding of how pressure affects the rotary action of the sensor is needed. Indeed, Equation (3) should to be replaced with a version that accounts for very high pressures and for which the parameters B and C can be assigned to physical terms. This is particularly so for the interaction between polymer and rotor. At present this is not the case but, to the best of our knowledge, this is the first report of a combined (solvent and polymer) system and there are many variables that need to be examined before firm mechanistic conclusions can be drawn.

2.8 References

1. Velsko, S. P.; Waldeck, D. H.; Fleming, G. R. *J. Chem. Phys.* **1983**, *78*, 249.
2. Olivucci, M.; Ragazos, I. N.; Bernardi, F.; Robb, M. A. *J. Am. Chem. Soc.* **1993**, *115*, 3710.
3. Keirstead, W. P.; Wilson, K. R.; Hynes, J. T. *J. Chem. Phys.* **1991**, *95*, 5256.
4. Velsko, S. P.; Fleming, G. R. *J. Chem. Phys.* **1982**, *76*, 3553.
5. Hasson, K. C.; Gai, F.; Anfinrud, P. A. *Proc. Natl. Acad. Sci.* **1996**, *93*, 15124.
6. Asano, T.; Furuta, H.; Sumi, H. *J. Am. Chem. Soc.* **1994**, *116*, 5545.
7. Kim, S. K.; Courtney, S. H.; Fleming, G. R. *Chem. Phys. Lett.* **1989**, *159*, 543.
8. Haidekker, M. A.; Theodorakis, E. A. *Org. Biomol. Chem.* **2007**, *5*, 1669.
9. Kuimova, M. K.; Yahioglu, G.; Levitt, J. A.; Suhling, K. *J. Am. Chem. Soc.* **2008**, *130*, 6672.
10. Korppi-Tommola, J. E. I.; Hakkarainen, A.; Hukka, T.; Subbi, J. *J. Phys. Chem.* **1991**, *95*, 8482.
11. Rice, J. K.; Baronavski, A. P. *J. Phys. Chem.* **1992**, *96*, 3359.
12. Zhu, A.; Wang, B.; White, J. O.; Drickamer, H. G. *J. Phys. Chem. A* **2003**, *107*, 6932.
13. Shao, J.; Ji, S.; Li, X.; Zhao, J.; Zhou, F.; Guo, H. *Eur. J. Org. Chem.* **2011**, *2011*, 6100.
14. Scherer, T.; van Stokkum, I. H. M.; Brouwer, A. M.; Verhoeven, J. W. *J. Phys. Chem.* **1994**, *98*, 10539.
15. Velsko, S. P.; Fleming, G. R. *Chem. Phys.* **1982**, *65*, 59.
16. Chen, L. A.; Dale, R. E.; Roth, S.; Brand, L. *J. Biol. Chem.* **1977**, *252*, 2163.
17. Szymański, J.; Patkowski, A.; Wilk, A.; Garstecki, P.; Holyst, R. *J. Phys. Chem. B* **2006**, *110*, 25593.
18. Wang, Y.; Warshawsky, A.; Wang, C.; Kahana, N.; Chevallard, C.; Steinberg, V. *Macromol. Chem. Phys.* **2002**, *203*, 1833.
19. Levitt, J. A.; Kuimova, M. K.; Yahioglu, G.; Chung, P.-H.; Suhling, K.; Phillips, D. *J. Phys. Chem. C* **2009**, *113*, 11634.
20. Levitt, J. A.; Chung, P.-H.; Kuimova, M. K.; Yahioglu, G.; Wang, Y.; Qu, J.; Suhling, K. *ChemPhysChem* **2011**, *12*, 662.
21. Kee, H. L.; Kirmaier, C.; Yu, L.; Thamyongkit, P.; Youngblood, W. J.; Calder, M. E.; Ramos, L.; Noll, B. C.; Bocian, D. F.; Scheidt, W. R.; Birge, R. R.; Lindsey, J. S.; Holten, D. *J. Phys. Chem. B* **2005**, *109*, 20433.

22. Benniston, A. C.; Harriman, A.; Whittle, V. L.; Zelzer, M. *Eur. J. Org. Chem.* **2010**, *2010*, 523.
23. Wang, D.; Miyamoto, R.; Shiraishi, Y.; Hirai, T. *Langmuir* **2009**, *25*, 13176.
24. Yucel, B.; Sanli, B.; Akbulut, H.; Ozbey, S.; Benniston, A. C. *Org. Biomol. Chem.* **2012**, *10*, 1775.
25. Alamiry, M. A. H.; Benniston, A. C.; Copley, G.; Elliott, K. J.; Harriman, A.; Stewart, B.; Zhi, Y.-G. *Chem. Mater.* **2008**, *20*, 4024.
26. Brey, L. A.; Schuster, G. B.; Drickamer, H. G. *J. Chem. Phys.* **1977**, *67*, 2648.
27. Brey, L. A.; Schuster, G. B.; Drickamer, H. G. *J. Am. Chem. Soc.* **1979**, *101*, 129.
28. Hummer, G.; Garde, S.; García, A. E.; Paulaitis, M. E.; Pratt, L. R. *J. Phys. Chem. B* **1998**, *102*, 10469.
29. Vedam, K.; Limsuwan, P. *J. Chem. Phys.* **1978**, *69*, 4762.
30. Alamiry, M. A. H.; Hagon, J. P.; Harriman, A.; Bura, T.; Ziessel, R. *Chem. Sci.* **2012**, *3*, 1041.
31. Annable, T.; Buscall, R.; Ettelaie, R.; Whittlestone, D. *J. Rheol.* **1993**, *37*, 695.
32. Mikhalyov, I.; Gretskaya, N.; Bergstrom, F.; Johansson, L. B. A. *Phys. Chem. Chem. Phys.* **2002**, *4*, 5663.
33. Bergström, F.; Mikhalyov, I.; Hägglöf, P.; Wortmann, R.; Ny, T.; Johansson, L. B. Å. *J. Am. Chem. Soc.* **2001**, *124*, 196.
34. Zhang, D.; Martin, V.; Garcia-Moreno, I.; Costela, A.; Perez-Ojeda, M. E.; Xiao, Y. *Phys. Chem. Chem. Phys.* **2011**, *13*, 13026.
35. Qin, W.; Baruah, M.; Van der Auweraer, M.; De Schryver, F. C.; Boens, N. *J. Phys. Chem. A* **2005**, *109*, 7371.
36. Englman, R.; Jortner, J. *Mol. Phys.* **1970**, *18*, 145.
37. Bonnett, R.; McGarvey, D. J.; Harriman, A.; Land, E. J.; Truscott, T. G.; Winfield, U. J. *Photochem. Photobiol.* **1988**, *48*, 271.
38. Nicholls, D.; Sutphen, C.; Szwarc, M. *J. Phys. Chem.* **1968**, *72*, 1021.
39. Zoon, P. D.; Brouwer, A. M. *Photochem. Photobiol. Sci.* **2009**, *8*, 345.
40. Flory, P. J. *Principles of Polymer Chemistry*; Cornell University Press, Ithaca: NY, 1953.
41. Haiyang, Y.; Pingping, Z.; Feng, R.; Yuanyuan, W.; Tiao, Z. *Eur. Polym. J.* **2000**, *36*, 21.
42. Ferry, J. D. *Viscoelastic Properties of Polymers*; 3rd ed.; John Wily & Sons Inc.: New York, 1980.
43. Dziubek, K. F.; Katrusiak, A. *J. Phys. Chem. B* **2008**, *112*, 12001.

44. Neumann, B.; Pollmann, P. *Phys. Chem. Chem. Phys.* **2001**, *3*, 943.
45. Vacek, J.; Michl, J. *Proc. Natl. Acad. Sci.* **2001**, *98*, 5481.
46. Strang, G. *Introduction to Linear Algebra*; Wellesley-Cambridge Press: Boston, 1993.
47. Vinckier, I.; Moldenaers, P.; Mewis, J. *J. Rheol.* **1996**, *40*, 613.
48. Schroeder, J.; Schiemann, V. H.; Jonas, J. *J. Chem. Phys.* **1978**, *69*, 5479.
49. Fury, M.; Jonas, J. *J. Chem. Phys.* **1976**, *65*, 2206.
50. Bauer, D. R.; Brauman, J. I.; Pecora, R. *Annu. Rev. Phys. Chem.* **1976**, *27*, 443.
51. Gaeckle, D.; Patterson, D. *Macromol.* **1972**, *5*, 136.
52. Vennemann, N.; Lechner, M. D.; Oberthür, R. C. *Polym.* **1987**, *28*, 1738.
53. Roots, J.; Nystroem, B. *Macromol.* **1982**, *15*, 553.
54. Freeman, B. D.; Soane, D. S.; Denn, M. M. *Macromol.* **1990**, *23*, 245.
55. Cook, R. L.; King, H. E.; Peiffer, D. G. *Macromol.* **1992**, *25*, 2928.
56. Hablot, D.; Retailleau, P.; Ziessel, R. *Chem. Eur. J.* **2010**, *16*, 13346.
57. Benniston, A. C.; Harriman, A.; Whittle, V. L.; Zelzer, M.; Harrington, R. W.; Clegg, W. *Photochem. Photobiol. Sci.* **2010**, *9*, 1009.
58. Benniston, A. C.; Copley, G.; Lemmetyinen, H.; Tkachenko, N. V. *ChemPhysChem* **2010**, *11*, 1685.
59. Kuila, D.; Baxter, W. W.; Natan, M. J.; Hoffman, B. M. *J. Phys. Chem.* **1991**, *95*, 1.
60. Hu, L.; Farrokhnia, M.; Heimdal, J.; Shleev, S.; Rulíšek, L.; Ryde, U. *J. Phys. Chem. B* **2011**, *115*, 13111.

Chapter 3. Comparison of the probabilities of electronic energy transfer for covalently-linked and non-covalently-linked molecular dyads

3.1 Executive summary

This chapter describes two related molecular systems in an effort to explore how the binding motif affects the likelihood of electronic energy transfer (EET) between the subunits. Firstly, a covalently-linked molecular dyad is considered in which two disparate boron dipyrromethene dyes (simply referred to as "yellow" and "blue") are separated by a tolane-like spacer. Efficient EET occurs across the connector; the mechanism involves important contributions from both Förster-type coulombic interactions and Dexter-type electron exchange processes. The energy acceptor is equipped with long paraffinic chains that favour aggregation at high concentration or at low temperature. The aggregate displays red-shifted absorption and emission spectral profiles, relative to the monomer, such that EET is less efficient because of a weaker spectral overlap integral. The donor unit is insensitive to applied pressure but this is not so for the acceptor, which has extended π-conjugation associated with appended styryl groups. Here, pressure reduces the effective π-conjugation length, leading to a new absorption band at higher energy. With increasing pressure, the overall EET probability falls but this effect is nonlinear and at modest pressure there is only a small recovery of donor fluorescence. This situation likely arises from compensatory phenomena such as restricted rotation and decreased dipole screening by the solvent. However, the probability of EET falls dramatically over the regime where the π-conjugation length is reduced owing to the putative conformational exchange. It appears that the pressure-induced conformer is a poor energy acceptor.

In the second example, the same yellow and blue boron dipyrromethene dyes are equipped with opposite electronic charges such that they associate in solution to form a 1:2 complex with a stability constant of ca. $10^{17}\,M^{-2}$. The complex can be dismantled by addition of a large excess of a tetra-N-butylammonium salt. The same complex displays liquid-crystalline properties on heating from room temperature to above 150 °C, as characterized by various experimental techniques. Highly efficacious EET from the yellow to the blue dye occurs in both the initial complex and the subsequent mesomorphic state.

3.2 Structure

Figure 1 shows the molecular formulae of the various compounds studied in this chapter. Compounds **1** and **2** are (yellow) boron tetramethyl-dipyrromethene (Bodipy) dyes[1] fitted with the conventional dipyrrin backbone and with an aryl ring at the *meso*-position. In contrast, compound **3** is a Bodipy dye having extended π-conjugation that pushes the absorption profile towards the blue region.[2] In this study, the yellow and blue dyes function as donor and acceptor, respectively, in the covalently linked dyads **4** and **5**. There is a clear driving force for EET along the molecular axis from yellow to blue dyes. In the context of pressure effects, it is important to note that the blue Bodipy dye bears multiple paraffinic chains that should hinder rotation of this terminal with respect to the molecular axis. In fact, we consider this particular reagent to be fixed in space during the timescale of EET. The yellow donor lacks these fatty chains and is more likely to undergo internal rotation around the connecting spacer unit. To examine the importance of this effect on the EET dynamics, two separate yellow dyes are considered that differ according to the size of the substituents attached to the boron centre. These latter groups are selected so as to influence the rotational diffusional characteristics of the donor.

The important feature of this chapter is to compare the EET probability of the above dyads with one formed without the connecting bridge. Clearly, there needs to be some motivation for the terminals to associate into a linear dyad to make feasible such a comparison. We considered using hydrogen bonding connection points but finally opted for ionic self-association. Thus, complex **6** was formed by way of electrostatic interactions between the sodium salt of the (yellow) sulfo-Bodipy dye (**Y**) and the ammonium hexafluorophosphate salt of the (blue) distyryl-Bodipy (**B**) dye.[1] Unfortunately, there will be changes in molecular topology outside of our control such that detailed comparison of the two systems might not be warranted.

3.3 Introduction

The efficiency of intramolecular EET, usually expressed in terms of probability or quantum yield to emphasize the fact that the process must compete with other routes for deactivation of the excited state, is a complex function of the local molecular topology.[3] In certain cases, and most often with modified biological media,[4] this realization can be used to estimate distances,[5] orientations,[6] and structural heterogeneity[7] associated with the host medium.

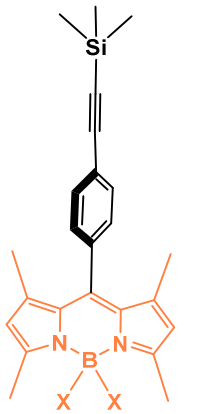

1 X=F

2 X=

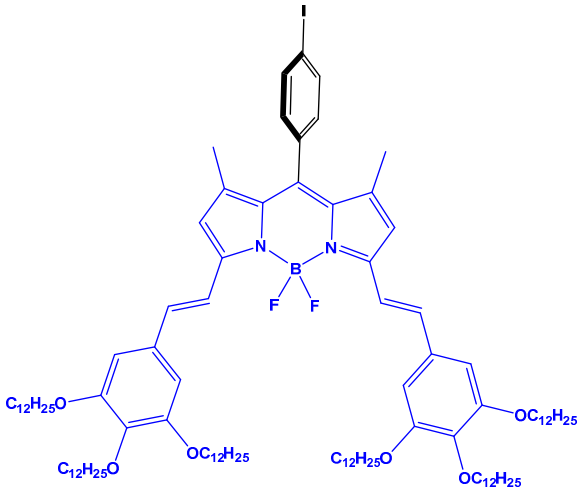

3

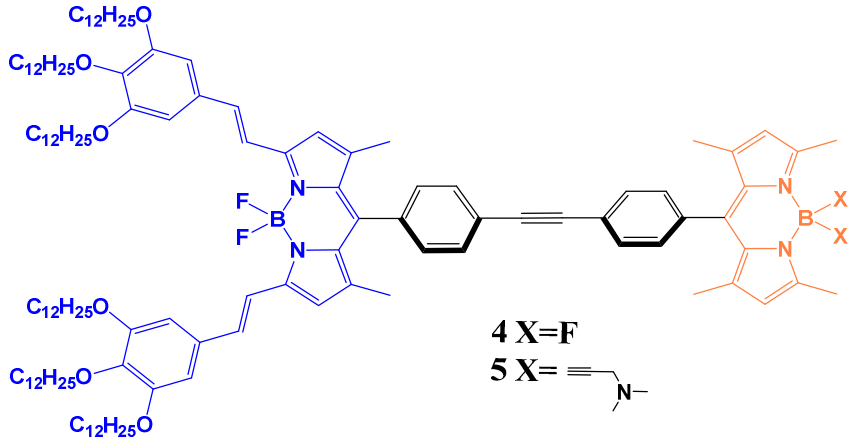

4 X=F

5 X=

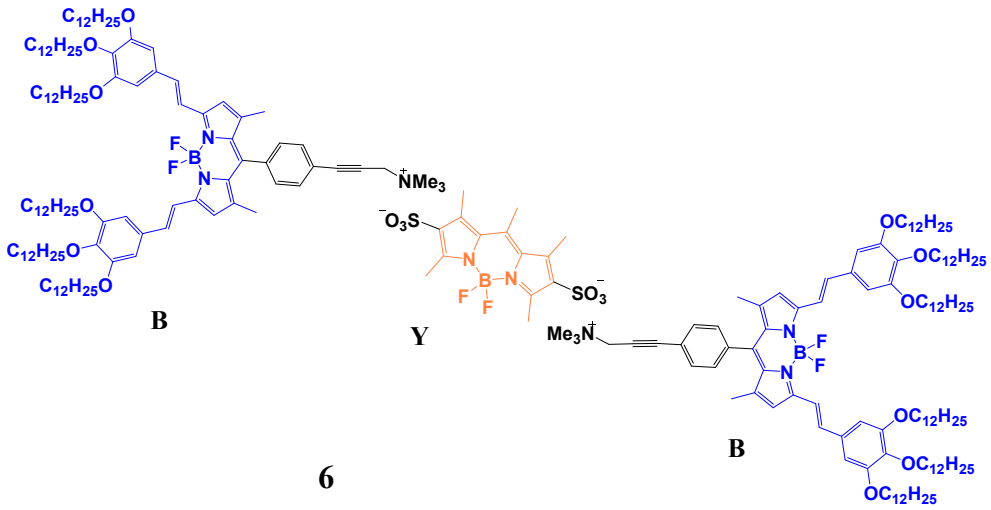

B **Y** **B**

6

Figure1. Molecular formulae of the compounds studied in this work.

Of particular interest are those examples[8] where the molecular conformation changes on a timescale comparable to the EET event because this situation provides unique information about the relative mobility of the surroundings. Such information is crucial for a better understanding of, for example, protein folding,[9] vitrification,[10] polymer mobility[11] and internal flexibility,[12] DNA melting,[13] substrate binding,[14] and the morphology of conducting polymers.[15] There are numerous constraints associated with how well EET measures molecular topology but the most important feature concerns the clarity with which the transfer mechanism is known. Indeed, three competing mechanisms underpin EET in spatially resolved molecular dyads; namely, through-space Förster (or coulombic) EET,[16] through-bond Dexter (or electron exchange) EET,[17] and bridge-mediated EET,[18] although other mechanisms might contribute at short separations.[19] The key point here is that the various mechanisms each display precise relationships between the rate of ETT and the positioning of the reactants. Thus, uncertainty in the mechanism will result in major complications for interpreting EET probabilities in terms of separation distances and mutual orientations. At short and long separations, or with particular types of linkage between donor and acceptor, it is not too difficult to assert the dominant transfer mechanism. At intermediate separations, loosely defined as being somewhere in the region of 20 Å, the situation is rather unclear and additional input is needed before the transfer mechanism can be resolved in a meaningful manner.[20]

It is also recognized that the probability of intramolecular ETT can be affected by changes in temperature,[21] solvent polarity[22] or polarizability,[23] pH,[24] viscosity,[25] the presence of adventitious species,[26] microporous media,[27] template substrates,[28] or co-solvents.[29] In the main, the effects of such perturbations are easily understood but do not help resolve the issue of the relative contribution of particular EET mechanisms. Much less is known about how applied pressure affects the rate of EET in molecular systems, despite the ubiquitous employment of pressure effects in chemistry, biology, and physics. Unlike the innumerable examples of temperature effects, there are in fact very few examples of where pressure has been used to control the likelihood of intramolecular EET in a molecular dyad.[30] This is somewhat surprising because applied pressure can be considered to affect the conformation of the dyad in a logical manner and is a component of many molecular dynamics simulation protocols.[31] Now, very recent work[32] raised the intriguing possibility that applied pressure might be a convenient tool by which to resolve individual Förster and Dexter EET contributions for a donor–acceptor pair separated by ca. 20 Å. This is the only claim to isolate these two

mechanisms by direct experimentation and, therefore, the technique deserves further examination.

Although high-pressure techniques have long been applied to spectroscopic investigations in the liquid phase, these have mostly involved infrared,[33] Raman,[34] NMR,[35] and absorption[36] spectroscopy. There are very few indications of how pressure affects the probability of EET and, in fact, research into how pressure might influence the rate of deactivation of an excited state is scant. Early work[37] showed that high pressures help to control the conformation of oligo-phenylene derivatives in solution and thereby exerted a modest influence on the rate of nonradiative decay of the first-excited singlet state. Other work[38] has explored pressure effects on the rotary action of fluorescent molecular rotors in solution. Related studies have addressed how pressure modulates the electron-transfer rates between flexibly linked donor–acceptor pairs,[39] notably using metalloporphyrin- and poly-(oxometallate)-based reagents, in homogeneous solution. Additional attention has been paid to pressure effects associated with formation of intramolecular excimers[40] and isomerization[41] of cyanine dyes in fluid solution. Several studies[42] have been concerned with the pressure dependence of "twisted charge-transfer state" formation in relatively simple donor–acceptor dyads where viscosity might play a part in controlling internal reorganization of the solute during electron transfer. The effect of solvent friction, discussed in terms of Kramer's theory,[43] on the isomerization dynamics of substituted alkenes has been treated with respect to pressure effects.[44] A common conclusion is that Kramer's theory requires modification before it can be applied to light-induced isomerization processes in liquids.

Research has shown[45] that minor structural perturbations around orthogonal linkages can have profound effects on the dynamics of intramolecular EET for closely spaced reactants. Such findings are of critical importance because they bring into question the validity of Förster-type calculations of EET rates in molecular dyads where the reactant separation is of a comparable magnitude to the sum of the lengths of the transition dipole moment vectors. Recent research[32] has raised the possibility that high pressure can freeze the conformation into the lowest-energy, i.e., the orthogonal, geometry and thereby switch off the through-space contribution to the overall EET process. Of course, this situation demands that the electron-exchange contribution is insensitive to these particular structural changes.

It should be stressed that applied pressure affects both properties of the solvent and the average conformation of the solute and that these changes are difficult to isolate. In particular, high pressure increases the density of the solvent, sometimes inducing an

unexpected isomerization[46] that helps to reduce the molar volume, and this affects secondary properties such as the refractive index, dielectric constant, viscosity, solubilization, freezing point, and polarizability. In turn, such pressure-induced perturbations of the solvent properties can affect factors controlling the likelihood of EET. For example, refractive index is important in determining fluorescence quantum yields,[47] changes in polarizability will disturb spectral overlap integrals,[48] the transition dipole moment vectors might respond to changes in dielectric constant,[49] and variations in viscosity could play important roles in biomolecular interactions.[50] These many factors must be considered when searching for the underlying reasons why applied pressure might change the EET probability in certain molecular dyads. In extreme cases, these corrections can be quite severe. The first part of this work is to consider how modest pressure influences the efficiency of EET across a fixed-distance molecular dyad dissolved in a fluid solvent at ambient temperature.

Ionic self-assembly (ISA)[51-54] is a powerful technique that employs attractive electrostatic forces to organize functionalized molecular modules into nanometer-sized materials, such as nanoparticles,[55] nanoplatelets,[56] nanoblobs,[57] nanotubes,[58] composite thin films,[59] organo-gels,[60] or liquid-crystalline phases.[61,62] In this latter case, the hierarchical superstructure that forms around oppositely charged dye molecules is favoured via secondary hydrophobic, H-bonding and/or π-π interactions which help to determine the topology of the final aggregate.[63-66] In furtherance of this field, we will describe in the second part of this chapter the self-assembly of a liquid-crystalline material that displays efficient electronic energy transfer across the emergent mesophase. This spontaneous assembly of ionic molecules into a functional liquid-crystalline phase avoids the reliance on the tedious, step-by-step evolution of covalently linked analogues and equips the aggregate with additional properties. Common building blocks are used for the two systems and, in both cases we employ EET as an analytical tool by which to assess the structure of the entity under investigation.

3.4 Covalently-linked dyads

3.4.1 Photophysical properties

The donor unit used to study the probability of intramolecular EET in the target dyads is a yellow Bodipy dye of conventional nature (Figure 1). The photophysical properties of such dyes are well known,[67] especially in fluid solution under ambient conditions, and the data collected for **1** and **2** are fully consistent with prior work. Thus, absorption (λ_{abs}) and fluorescence (λ_{flu}) maxima, respectively, are found at 500 and 520 nm in 2-

methyltetrahydrofuran (MTHF) at room temperature (Figure 2). Replacing the usual fluorine atoms attached to the boron centre with alkynylene groups has no obvious effect on these spectral features. For both compounds, the fluorescence quantum yield (Φ_{flu}) recorded in MTHF is ca. 0.72 while the excited-singlet state lifetime (τ_s) is ca. 4.8 ns under the same conditions. The radiative rate constant ($k_{rad} = 1.5 \times 10^8$ s^{-1}) lies within the range found for related Bodipy dyes, as does the Stokes' shift (SS = 600 cm^{-1}). These yellow Bodipy dyes are (photo) stable, highly emissive, monomeric, and readily soluble in common organic solvents. The acceptor unit is constructed from a bis-styryl Bodipy dye (Figure 1) where the increased π-conjugation pushes λ_{abs} and λ_{flu} to 650 and 675 nm, respectively. It is noticeable that this blue dye, **3**, possesses absorption and emission spectra that are slightly broader than those characterised for the corresponding yellow dyes (Figure 2), but this is normal for these expanded Bodipy dyes. The Stokes' shift (SS = 570 cm^{-1}) remains closely comparable to that of the yellow dye. However, the emission quantum yield (Φ_{flu} = 0.6) is somewhat decreased relative to that of the donor. Both k_{rad} (= 1.4×10^8 s^{-1}) and τ_s (= 4.2 ns) remain in the region found for many Bodipy dyes.

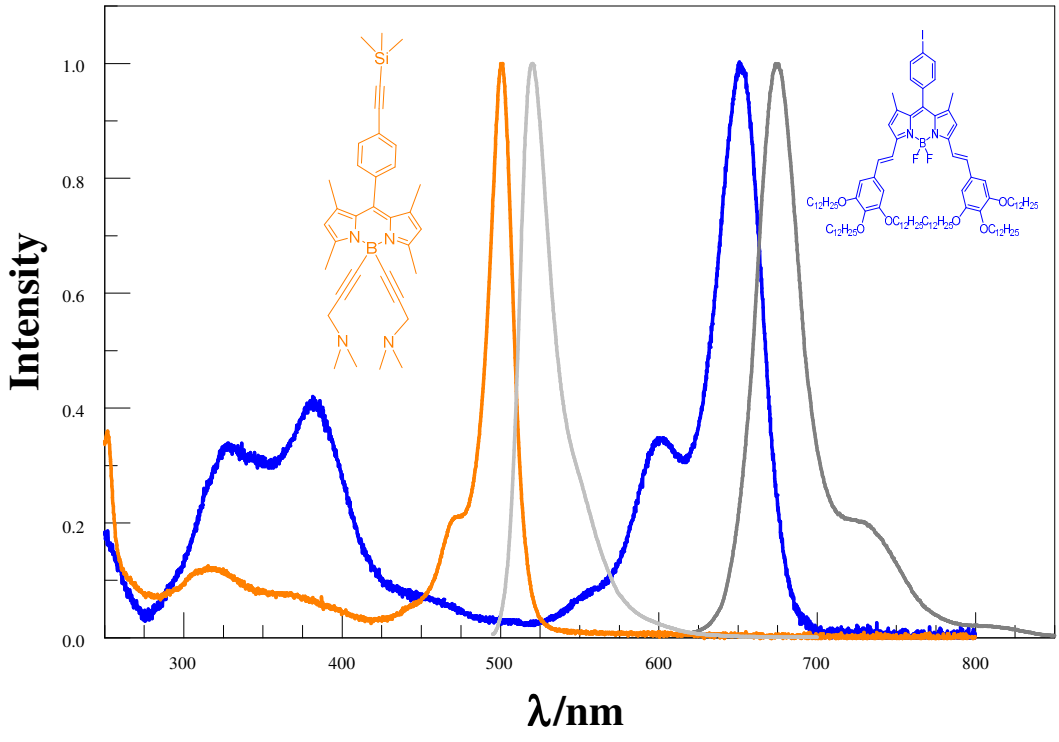

Figure 2. Normalized absorption (dark yellow and blue) and fluorescence (light grey and grey) spectra recorded for the reference compounds **2** and **3**, respectively, in MTHF at room temperature.

The paraffinic chains tend to restrict solubility of the blue dye, at least in a monomeric form, and aggregates tend to form at high concentration, high pressure or low

temperature. These aggregates display characteristic absorption (λ_{abs} = 695 nm) and emission (λ_{flu} = 720 nm) spectra with maxima at significantly lower energy than those found for the corresponding monomer. The spectral properties of the aggregate are reminiscent of those reported[68] recently for liquid-crystalline samples formed by self-association of charged monomers that will be discussed in the second part of this chapter. The former species add to the growing list of fluorescent Bodipy-based aggregates.

Overlap between emission from the yellow donor and absorption by the blue acceptor is modest (Figure 3), and the energy gap (ΔE_{SS} = 4,525 cm^{-1}) between singlet-excited states associated with these two species is sufficiently large for EET to be unidirectional at all accessible temperatures. The spectral overlap integral (J_{DA}) can be calculated from Equation (1) where ε(ν) is the molar absorption coefficient for the lowest-energy transition, including all vibrational bands, and $F(\nu)$ is the normalized emission spectral profile. In MTHF at room temperature, J_{DA} has a value of 0.0013 cm. In turn, the transition dipole moments (μ_D or μ_A) can be computed from absorption spectral measurements[69,70] made for the donor and acceptor in MTHF according to Equation (2). The derived values, again in MTHF at room temperature, are μ_D = 6.70 D and μ_A = 8.06 D, although it has to be stressed that the transition dipole moment vector for the acceptor is considered to be doubly degenerate on the basis of earlier studies[2] made with related push-pull-push Bodipy dyes. The solvent screening factor (s = 0.60) is estimated on the basis of the Onsager cavity,[71] as indicated in Equation (3) where n is the solvent refractive index. It is important to note that s is dependent on pressure and temperature because of the induced change in density of the solvent. The energy-minimized molecular structure deduced for the target dyad lacking the paraffinic chains (Figure 4) indicates that the boron-to-boron separation distance between yellow and blue dyes is 19.8 Å. This relatively close proximity, taken in conjunction with the combined lengths of the respective transition dipole moment vectors of ca. 17 Å, means that the system falls in the range where the ideal dipole approximation might not hold[72] but where the

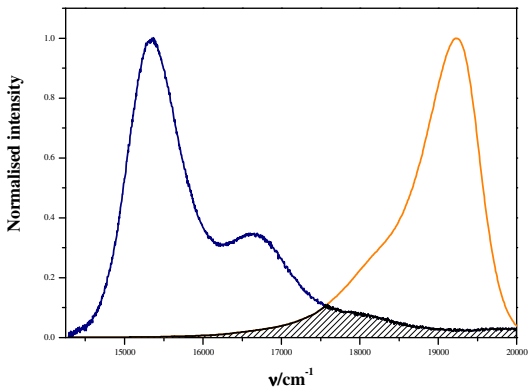

Figure 3. Illustration of spectral overlap between donor emission (dark yellow; **2**) and acceptor absorption (blue; **3**) as recorded in MTHF at room temperature.

significance of multi-pole interactions[73] is expected to be slight. Consequently, we prefer to compute the probability of coulombic EET within the dyad using the Kuhn extended dipole approach.[74]

$$J_{DA} = AB \int \frac{f_D(\nu)}{\nu^3} . \frac{\varepsilon_A(\nu)}{\nu} d\nu \qquad \text{Equation (1)}$$

$$\mu^2 = 9.186 \times 10^{-3} n \int \frac{\varepsilon}{\nu} d\nu \qquad \text{Equation (2)}$$

$$s = \frac{3}{2n^2+1} \qquad \text{Equation (3)}$$

Here, the point dipoles inherent to the ideal dipole approximation are replaced by charges assigned to each end of the transition dipole moment vectors. In reality, both the magnitude of the charge ($\pm q_D$ or $\pm q_A$) and their separation length are unknown but they are covered by the basic assumption that $q_D = \mu_D/l_D$, where l_D is taken as the molecular length of the transition dipole (l_D = 7.19 Å; l_A = 9.55 Å) as determined by quantum-chemical calculations. In turn, and allowing for the double degeneracy of the acceptor, the coulombic coupling matrix element (V_{DA}) can be calculated from Equation (4) as the sum of eight electrostatic-style interactions between the respective charges and allowing for their mutual separation (designated as "a" or "b" in the equation). In the absence of internal rotation around the connector, and using distances computed for the energy-minimized geometry in the absence of paraffinic chains (Figure 4), V_{DA} is calculated to be 7.5 cm^{-1}. In fact, rotation of the yellow dye has the effect of reducing V_{DA} and the mean value calculated on the basis of free rotation around the connector is 6.4 cm^{-1}. Finally, the rate constant (k_{XTD}) for coulombic-style EET across the molecular dyad can be calculated from Equation (5) so as to give a mean value of 2.3 x 10^{10} s^{-1}. This latter value can be compared with the experimental rate constant for EET (k_{EET}) in order to gauge the significance of through-space EET in this system.

$$V_{DA} = q_D q_A \left\{ \frac{1}{a_1} + \frac{1}{a_2} + \frac{1}{a_3} + \frac{1}{a_4} + \frac{1}{b_1} + \frac{1}{b_2} + \frac{1}{b_3} + \frac{1}{b_4} \right\} \qquad \text{Equation (4)}$$

$$k_{EET} = \frac{2\pi}{\hbar} |V_{DA} s K|^2 J_{DA} \qquad \text{Equation (5)}$$

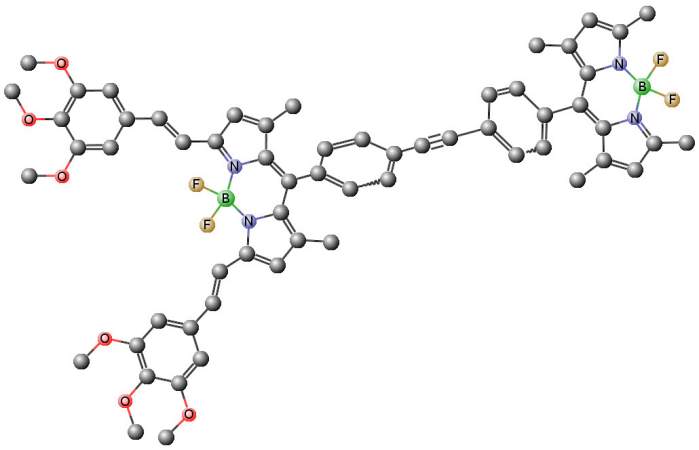

Figure 4. Energy-minimized molecular conformation computed by TD-DFT for a structural analogue of **4** lacking the paraffinic chains.

Absorption spectra recorded for the two molecular dyads, **4** and **5**, are indistinguishable and display the characteristic features of the yellow and blue terminals (Figure 5). There is no obvious sign of electronic interaction between the terminals. Excitation of these dyads at wavelengths where only the blue dye absorbs gives rise to the expected fluorescence spectral profile for that dye. For both dyads in MTHF, the derived Φ_{flu}, τ_s, and k_{rad} are in keeping with those recorded for **3** under the same conditions. In marked contrast, excitation at a wavelength where the yellow dye absorbs ca. 77 % of incident photons gives emission peaks from both yellow and blue dyes (Figure 5). It is notable that when compared to an equi-molar mixture of **2** and **3** fluorescence from the yellow dye is heavily quenched while that from the blue dye is enhanced substantially. This situation is fully consistent with efficient EET from yellow to blue dyes, and this was confirmed by excitation spectra (Figure 5). On a quantitative basis, the emission lifetime recorded for the yellow dye in **4** was found to be 29 ± 5 ps, compared to a value of 4.8 ns for the isolated dye **2**. A similar value (τ_s = 32 ± 5 ps) was recorded for the yellow dye present in **5**. In both molecular dyads, the overwhelming majority of fluorescence attributable to the blue dye grows in after the excitation pulse, as expected for highly efficacious intramolecular EET. For **5**, a small range of dilutions was studied in order to ensure the absence of intermolecular EET under these conditions. From the various lifetime studies, the average rate constant for EET can be estimated as being ca. 3.3×10^{10} s^{-1}. Interestingly, this derived value is reasonably close to that estimated for coulombic EET in this system, such that electron exchange[75] does not appear to play a dominant role in these systems.

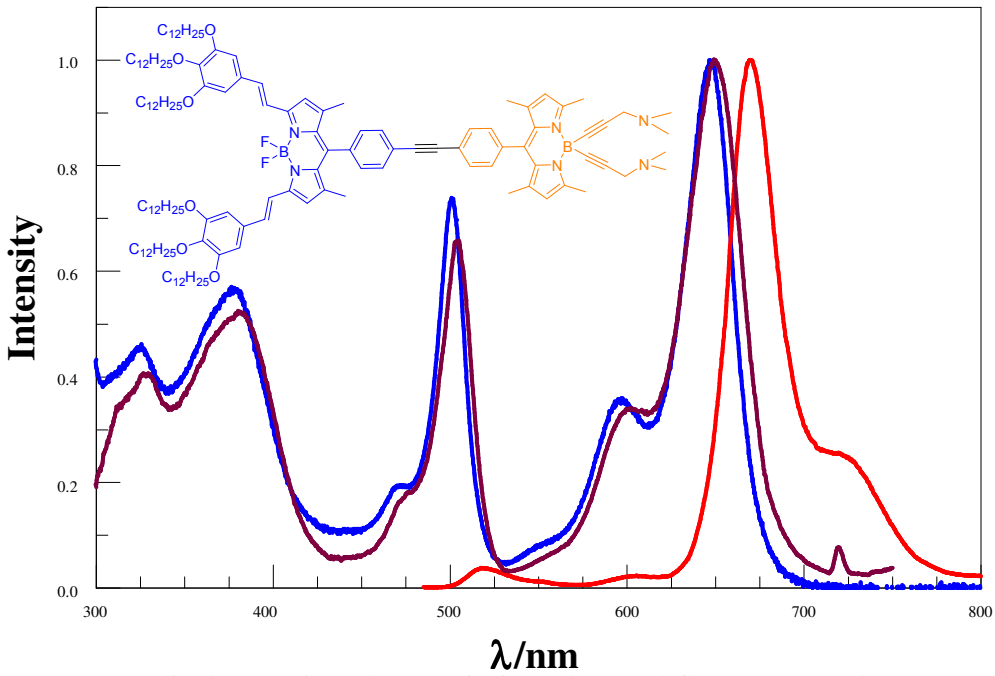

Figure 5. Normalised absorption (blue), excitation (plum) and fluorescence (red) spectra recorded for dyad **5** in MTHF at room temperature.

3.4.2 Effect of temperature

Excitation and emission spectra were collected at low temperature for **2**, **3**, **4** and **5** in MTHF. Compound **2** shows the characteristic behaviour expected for a conventional Bodipy dye[76] in as much as the fluorescence spectral profile sharpens and undergoes a 3-nm blue shift as the temperature decreases to 77K (Figure 6). No notable differences are observed in the excitation spectra as the temperature falls. However, the situation was different for **3,** where there are no apparent changes in fluorescence until 250K. Cooling below this temperature causes a pronounced red shift until the main peak at 680 nm disappears at around 190K and is replaced with a new peak that appears at about 720 nm. This latter peak grows in significance as the temperature continues to fall (Figure 7b). We assign this low-energy emission band to an aggregated form of the blue dye. Aggregation is promoted by the presence of the paraffinic chains, a fact ascertained by comparison with other blue derivatives lacking these substituents. Monitoring the excitation spectra under the same condition (Figure 7a) shows the anticipated peaks due to the blue monomer at temperature >190K and a new absorbing species evident at 695 nm at temperatures below 190K. Again, we attribute this latter spectral profile to an aggregated form of the blue dye.

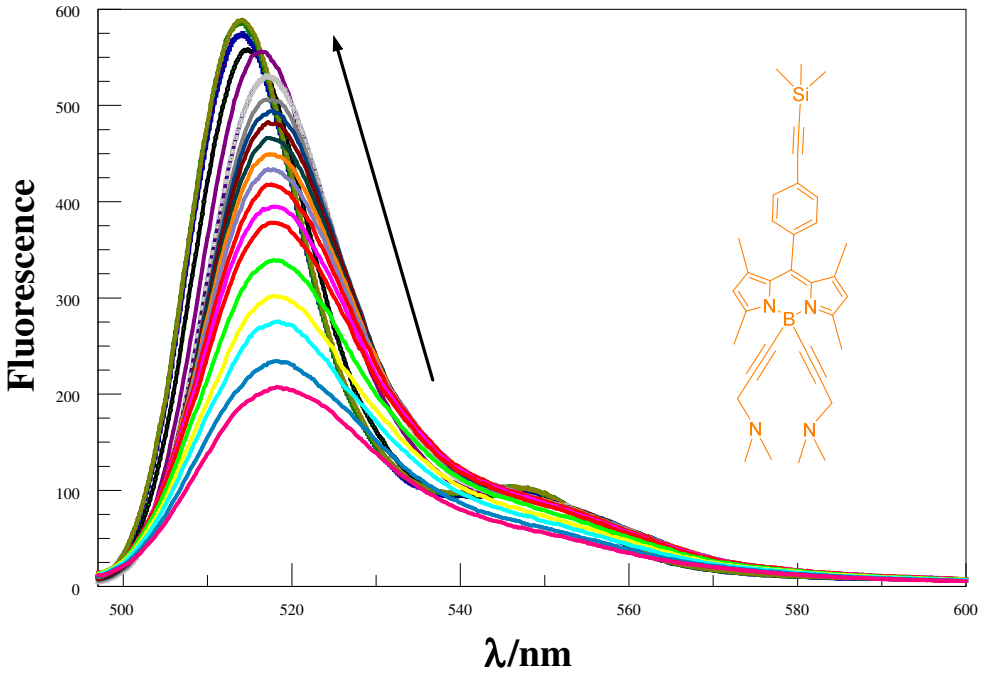

Figure 6. Effect of temperature on the emission spectral profile recorded for **2** in MTHF; the temperature ranges from 290 to 80K in the direction of the arrow.

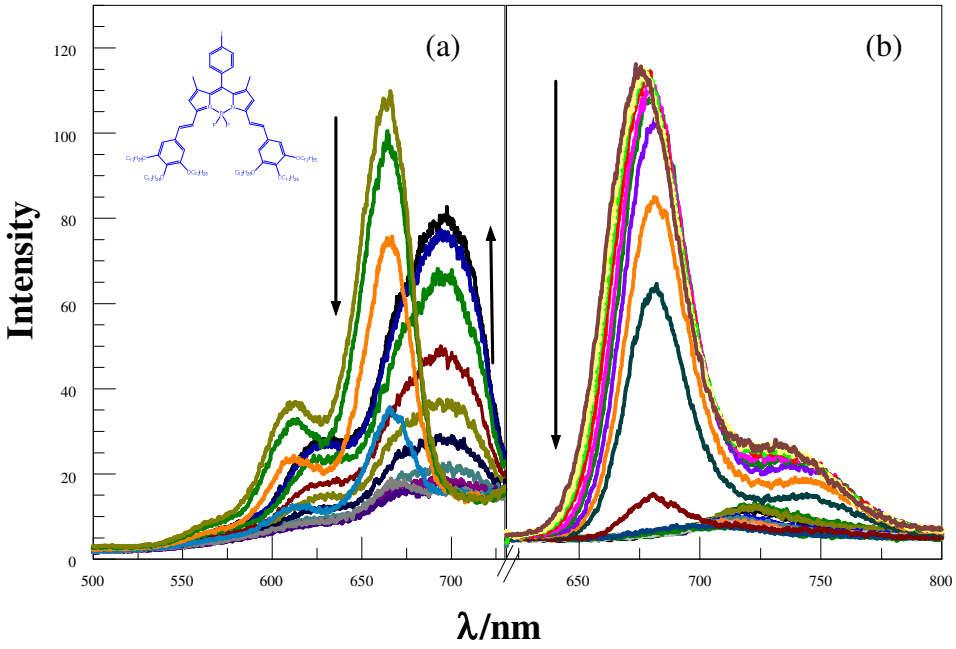

Figure 7. Effect of temperature on (a) excitation and (b) emission spectra recorded for **3** in MTHF; the arrow indicates the direction of lowering temperature.

On cooling a solution of **4** in MTHF, nothing much happens to the emission spectrum following preferential excitation into either dye until reaching ca. 250K (Figure 8). At this temperature, there is a decrease in intensity of emission from the blue dye but without a concomitant increase in fluorescence from the yellow terminal. Thus, there is no change in the probability of EET. As the temperature falls further, quenching of

emission from the blue dye becomes more pronounced, and at temperatures around 200K a new fluorescence band appears with a maximum at ca. 720 nm. This latter band, for which the excitation spectrum shows a maximum at 695 nm, is assigned to an aggregated form of the blue dye. The solvent starts to freeze at about 150K,[77] the glass-transition temperature being around 110K,[78] and at this temperature the emission maximum for the aggregate moves towards 740 nm. In the frozen solvent, there is essentially no emission from the monomeric form of the blue dye. Interestingly, the emission intensity for the yellow dye remains unperturbed, although the spectral profile shows a small blue shift, and there is no recovery of donor fluorescence. Moreover, the excitation (Figure 9) and emission spectra of **5** show exactly the same behaviour as noted above for **4**. However, the aggregation peak starts to appear at 250K in the excitation spectra while it is not detected in the emission spectrum until about 220K. This effect might be because of overlap with the more intense emission from the monomer. In addition, and following from close examination of the excitation spectra, the presence of the yellow donor enhances aggregation for the dyad (**4** and **5**) compared to the pure blue dye (**3**).

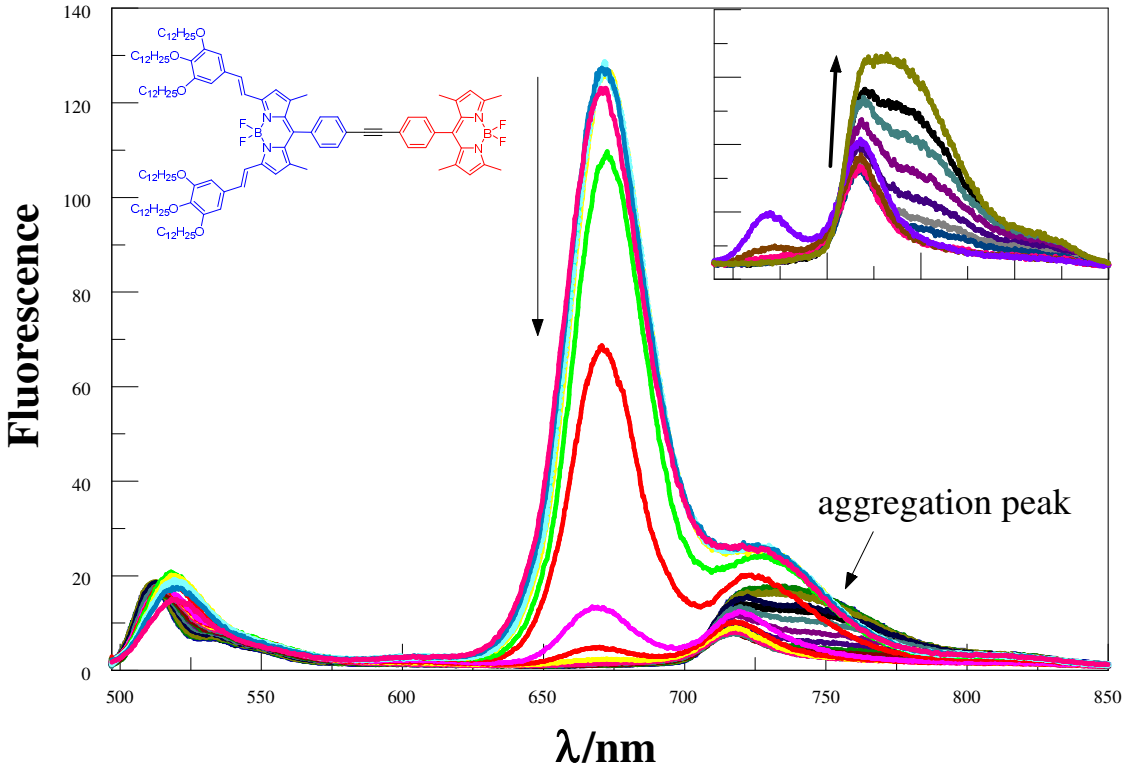

Figure 8. Temperature effect on the emission spectral behaviour noted for dyad **4** in MTHF. The insert shows formation of the aggregation peak as the temperature decreases in the direction of the arrow.

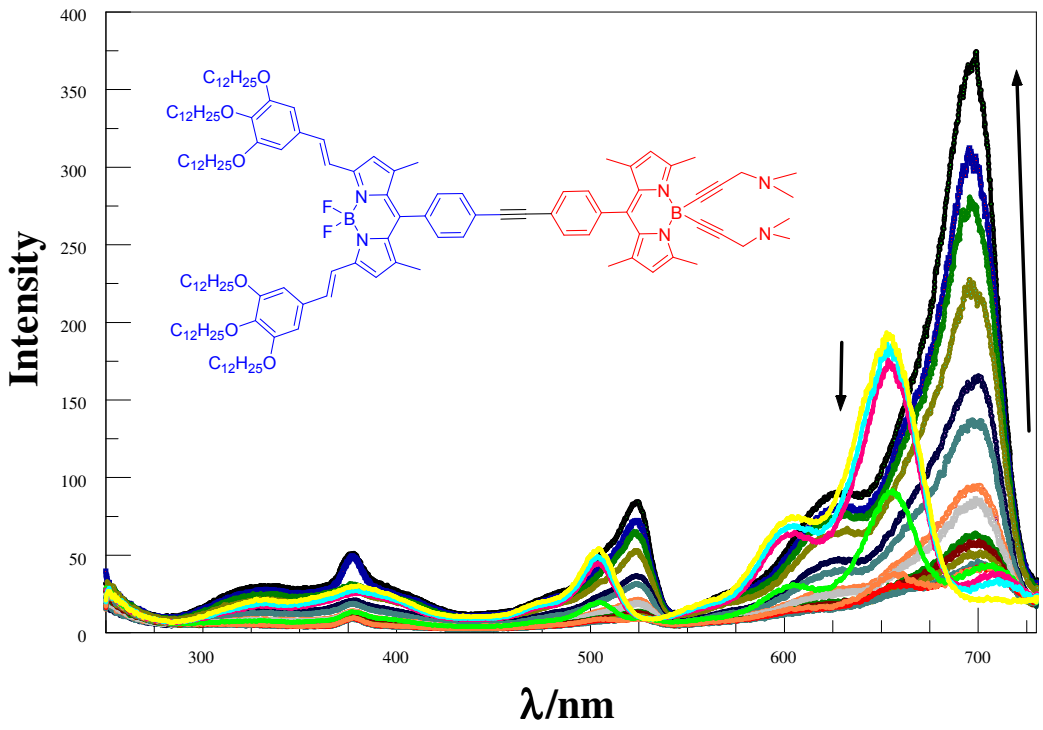

Figure 9. Temperature effect on the excitation spectra recorded for dyad **5** in MTHF. The arrow indicates the direction of decreasing temperature in equal amounts over the range from 260 to 80K.

The equilibrium constant (K) between the monomer and aggregation species in the liquid phase can be found by fitting the data to the van't Hoff expression (Eqn. 6), as is shown in Figure 10. Table 1 presents the derived changes in enthalpy and entropy, and as it can be seen from the entropy values, the aggregation of pure blue dye (**3**) is more stable than the dyad system.[79]

$$\ln K = -\frac{\Delta H}{RT} + \frac{\Delta S}{R} \qquad \text{Equation (6)}$$

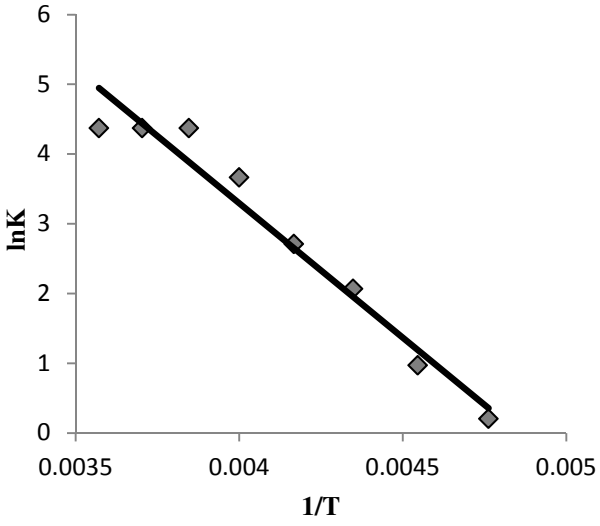

Figure 10. Relationship between the temperature and the equilibrium constant of **3**; points are experimental values and the black line is the fitted data.

Table 1. Parameters associated with aggregation of the dye as a function of temperature in MTHF.

	3	**4**	**5**
$\Delta H/kJ.mol^{-1}$	35	103	80
$\Delta S/J.K^{-1}.mol^{-1}$	160	380	290

3.4.3 Pressure dependence for the reference compounds

Earlier work[32,40] has demonstrated that the photophysical properties of conventional Bodipy dyes in liquid solution are essentially insensitive to changes in applied pressure. Of course, pressure decreases the molar volume of the solvent and thereby raises the solute concentration. In turn, the increased density modifies the polarizability of the solvent and this causes a small red shift for both λ_{abs} and λ_{flu}; this latter effect is magnified if the optical transition contains a contribution from charge-transfer interactions since pressure also tends to increase the solvent dielectric constant. For MTHF at 20 °C, the density increases by ca. 20 % at an applied pressure of 550 MPa (our upper limit!) while the lowest-energy absorption maximum shifts by ca. 5 nm for **2**. Over this pressure range, Φ_{flu} for **2** increases steadily and reaches a value of 0.77 at the highest pressure (Figure 11). The origin of this effect can be traced to the pressure-induced increase in refractive index of the solvent. Indeed, the Strickler–Berg expression[80] requires that k_{rad} scales with n^2 and the predicted effect that such a relationship has on Φ_{flu} is included as part of Figure 11. It can be concluded, therefore, that applied pressure has little effect on the accompanying rate of nonradiative relaxation of the first-allowed, excited-singlet state of the yellow Bodipy dye. It should also be noted that release of the applied pressure restores the original properties.

The situation is less clear with extended Bodipy dyes, such as the blue analogue considered here, because of the pendant styryl arms that might twist under applied pressure as a means by which to reduce the molar volume. Now, absorption spectra recorded for **3** in MTHF at room temperature indicate that the absorption maximum moves progressively towards lower energy as the pressure is raised due to the anticipated change in solvent polarizability. There is also an increase in absorbance of ca.20 % over the full pressure range, which is easily explained in terms of the increased density. At modest pressure, Φ_{flu} increases slightly after due allowance for the change in concentration but this increase is not as high as expected[80] in view of the perturbation of k_{rad} (Figure 11). As the pressure continues to mount, Φ_{flu} starts to decrease and by 550 MPa has fallen to 0.61 (c.f., Φ_{flu} = 0.60 at atmospheric pressure), whereas the projected value allowing for the change in k_{rad} is 0.67. The implication is that high pressure introduces either an important nonradiative decay route or a change in molecular conformation.

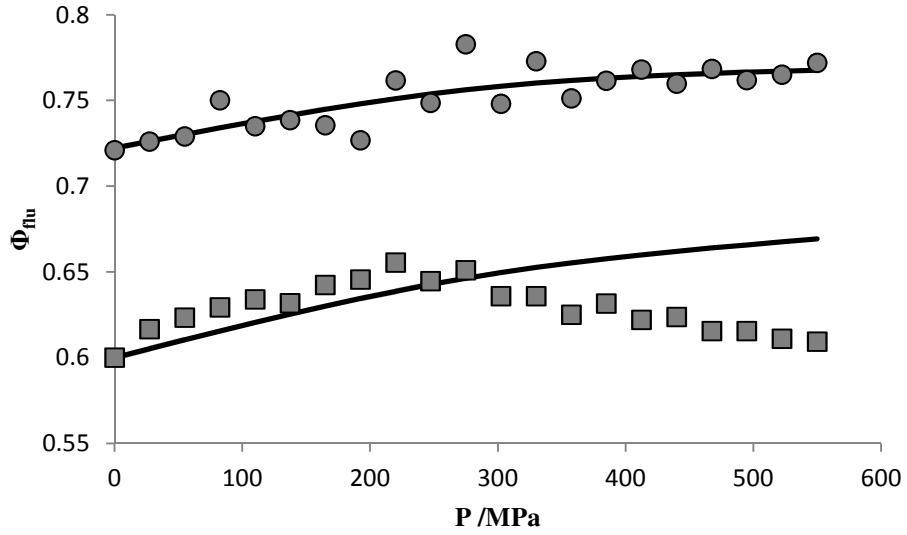

Figure 11. Effect of applied pressure on the measured fluorescence quantum yields for the control compounds **2** (circles) and **3** (squares) in MTHF at room temperature. The solid lines correspond to the anticipated pressure-induced effect on Φ_{flu} based entirely on the change in the radiative rate constant (i.e., the change in refractive index of the solvent).

Close examination of the emission spectral profiles recorded for **3** as a function of pressure shows that at ca. 200 MPa a new emission band centred at ca. 620 nm starts to evolve and grows steadily in intensity as the pressure increases (Figure 12). This is a nonlinear effect (Figure 12 insert) that is favoured at high pressure. Most likely, the effect is caused by structural distortion around one or both styryl arms that serves to decrease the effective π-conjugation length. A similar spectral shift has been reported[2] for push-pull-push Bodipy dyes bearing different appendages attached to the dipyrrin core. Unfortunately, a better assignment of this pressure-induced conformational change must await a more detailed mechanistic examination. For the moment, it is sufficient to accept that this conformational effect is responsible for the decreased Φ_{flu} observed for **3** at elevated pressure.

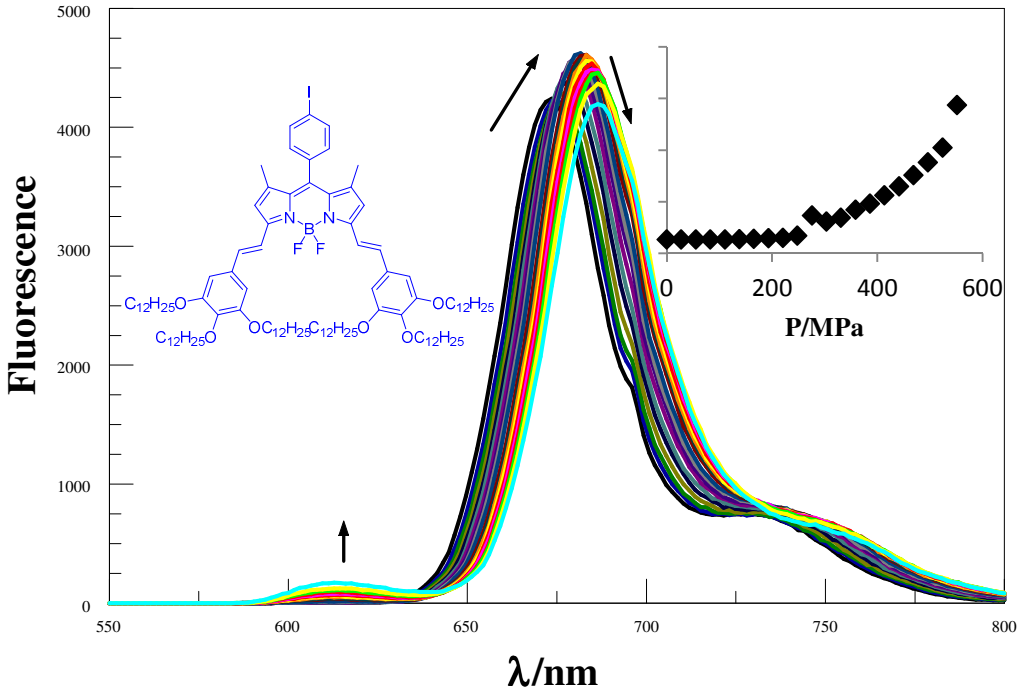

Figure 12. Effect of applied pressure on the fluorescence spectral profile recorded for compound **3** in MTHF at room temperature. Pressure increases as indicated by the arrows. The insert shows the effect of pressure on the integrated emission profile for the new peak that appears around 620 nm.

3.4.4 Effect of pressure on the probability of EET for the target dyads

Under applied pressure, the absorption spectra recorded for dyads **4** and **5** undergo changes similar to those outlined for the respective control compounds. Thus, the absorption maxima for the yellow and blue terminals are clearly evident at 500 and 652 nm, respectively. These maxima move progressively towards lower energy as the pressure is increased (Figure 13). There is a corresponding increase in absorbance of ca. 20% over the full pressure range due to compression of the solvent. No other pressure-induced spectral changes are apparent. In both qualitative and quantitative terms, these spectral perturbations are in good accord with expectations based on the control compounds. In particular, there is no sign that either dyad aggregates under these conditions, even after prolonged exposure to high pressure. Furthermore, the changes in band position and intensity are reversed on release of the pressure.

Fluorescence spectra were recorded also for dyads **4** and **5** in MTHF as a function of applied pressure. Various excitation wavelengths were used for these studies. It was noted that direct excitation into the blue dye at λ >520 nm gives rise to fluorescence characteristic of that species. Under pressure, there are changes in band position and intensity that closely mirror those observed for **3** in MTHF, including the conformational exchange seen at high pressure (Figure 14). Adding the second terminal

and accompanying connector, therefore, does not affect the sensitivity of the blue dye to changes in either solvent polarizability or density and does not hinder the conformational effect supposed to reduce the molecular volume.

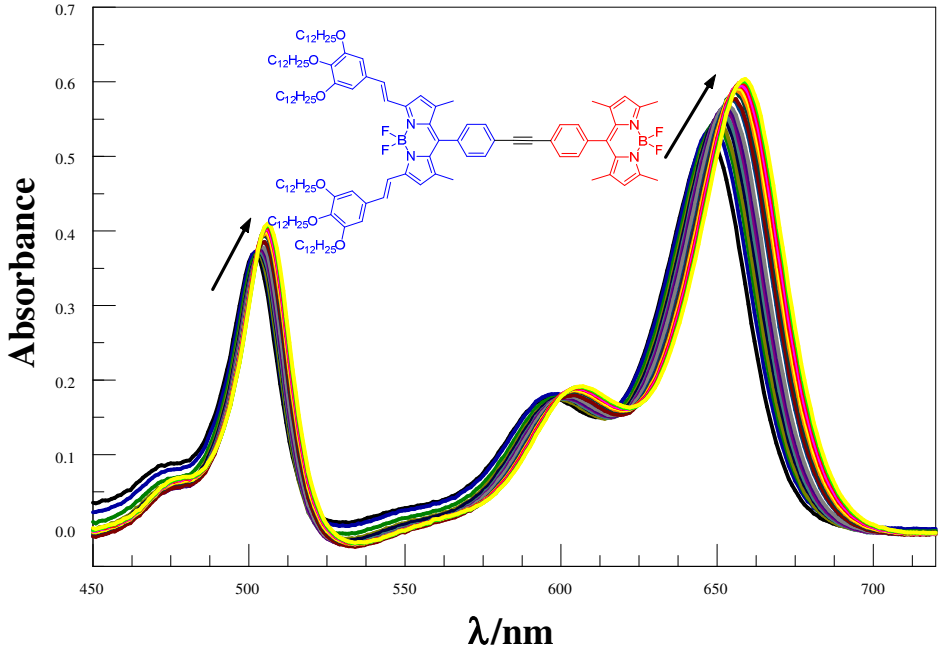

Figure 13. Effect of applied pressure on the absorption spectral profile recorded for dyad **4** in MTHF at room temperature. The arrows indicate the direction of increasing pressure.

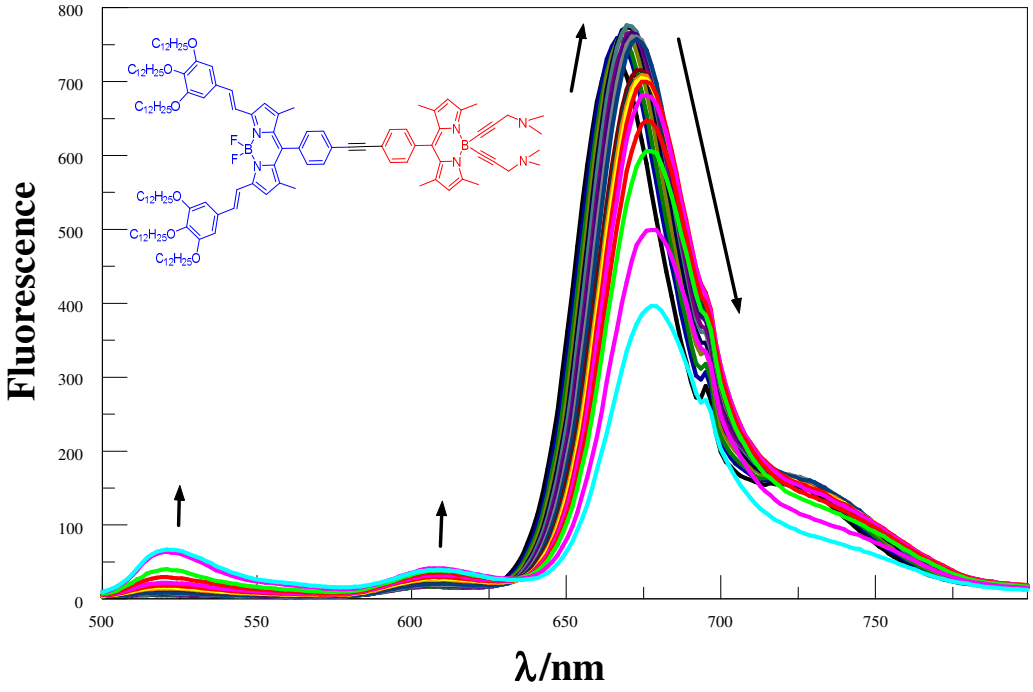

Figure 14. Effect of applied pressure on the fluorescence spectral profile recorded for dyad **5** in MTHF at room temperature. The arrows indicate the direction of increasing pressure.

These studies serve as an invaluable tool by which to calibrate changes in the acceptor emission following excitation into the donor unit. There is no excitation wavelength at which the yellow dye is the sole absorber, unlike the situation pertinent to the blue dye, and so a variety of wavelengths was used in order to assess the importance of applied pressure on the probability of EET. In all cases, there are two distinct regions of interest in the pressure-emission plots. At modest pressure (P <200 MPa), the emission intensities for both donor and acceptor tend to increase with applied pressure. At higher pressure, however, emission from the acceptor decreases significantly while there is a concomitant increase in fluorescence from the donor. This generic behaviour, which holds for both dyads and is independent of excitation wavelength, covers the pressure range where the blue dye undergoes the aforementioned conformational change. Before attempting to rationalise this behaviour, several corrections have to be applied to the experimental data. Firstly, the fluorescence signal is isolated spectrally so as to represent the yellow donor or the blue acceptor and the integral corrected for pressure-induced changes in absorbance at the excitation wavelength. The control dyes were used to indicate the relative absorbance by each dye at that wavelength. Next, the emission yields were corrected for changes in k_{rad}, as illustrated earlier. The donor signal is now fairly clean, and it is evident that applied pressure causes a nonlinear recovery of donor emission. The signal for the acceptor is distorted by the pressure-induced conformational change, which can be taken into account using a calibration curve constructed following direct excitation into the blue dye. After this critical correction, it is apparent that pressure causes a corresponding decrease in fluorescence from the acceptor. We now consider these "corrected" data (Figure 15).

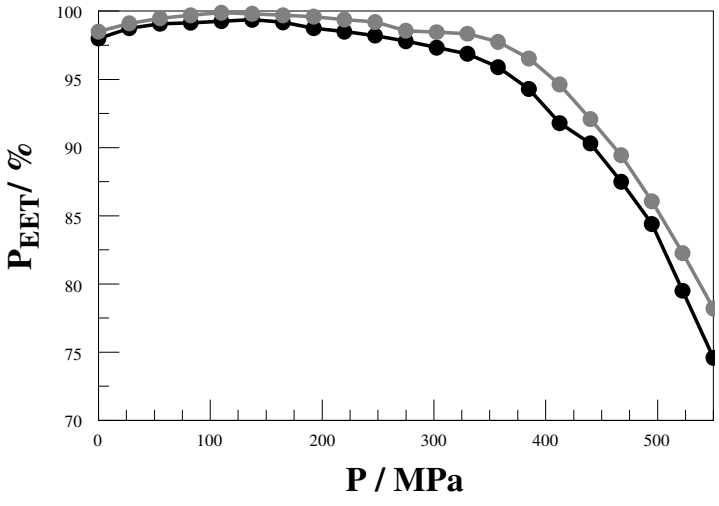

Figure 15. Effect of applied pressure on the electronic energy transfer probability (P_{EET}) across the molecular dyads **4** (black) and **5** (grey) in MTHF at room temperature.

Provided the applied pressure remains less than 200 MPa, the probability (P_{EET}) of intramolecular EET increases slightly with increasing pressure for MTHF at room temperature (Figure 15). At higher pressure, P_{EET} starts to decrease. In fact, the pressure effect is rather insignificant at low pressure but becomes increasingly more important at pressures above 300 MPa where conformational exchange takes place. The clear indication is that the pressure-induced conformer is a relatively poor energy acceptor. In the low-pressure regime, it might be considered that several pressure-induced phenomena act in a compensatory manner to minimise the effects on P_{EET}. For example, applied pressure is expected to hinder rotation of the donor around the molecular axis and this will increase P_{EET}, at least for the coulombic mechanism. Conversely, applied pressure reduces the magnitude of the dipole-screening factor, *s*, because of the increase in refractive index. These two effects each cause a 30 % change in the rate of through-space EET over the full pressure range but the effects are opposing. Within experimental limits, the pressure effect in terms of diminishing P_{EET} is roughly the same for the two dyads, although **4** requires slightly less pressure for the conformational change to become noticeable. This might point towards the importance of rotation of the yellow dye. Small changes in the molecular topology are also likely to perturb k_{EET} in this pressure region.

The main effect on P_{EET} is seen at high pressure and corresponds to the conformational change that reduces the effective π-conjugation length. Based on prior work with various synthetic Bodipy dyes,[2] the pressure-induced conformer has one styryl arm twisted out of the conjugation path: a crude estimate of the emission maximum for this hypothetical conformer, made by density functional theory (DFT) quantum-chemical calculations, is ca. 565 nm compared to the experimental value of 620 nm. From this, we can infer that the styryl group is only partially unlocked from the dipyrrin core. The most obvious reason for such a pressure-induced change is the need to reduce the molecular volume but this could also be achieved by compression of the paraffinic chains. In the absence of real information about this structural modification, it is inappropriate to speculate on why the resultant geometry is unfavourable for EET. Conformational change of this type might be expected to induce only a small modification of the rate of electron exchange but would be more significant for Förster-type coulombic interactions. In part, this is because of the change in the nature of the transition dipole moment vector for the acceptor, which would also lose its degeneracy.

It might be anticipated that high pressure will also promote aggregation of the blue dye but this situation was difficult to confirm experimentally. In most cases,

working with a relatively low concentration (i.e., <5 μM) of **4** in MTHF, there was no indication for formation of an aggregate at applied pressures less than 550 MPa. However, in one case with a dyad concentration of ca. 10 μM, the characteristic absorption spectral features of the aggregate appeared at elevated pressure (Figure 16). Thus, the usual spectrum observed at atmospheric pressure becomes distorted in the region characteristic of the blue dye at pressures above 100 MPa. The absorption band assignable to the aggregate starts to appear with a maximum at 730 nm but this moves to lower energy with increasing pressure, reaching a wavelength of ca. 740 nm at the highest pressure. Interestingly, the spectra show clear perturbation of the absorption profile due to the yellow dye as the blue dye aggregates. This latter effect helps explain why there is no recovery of emission from the yellow dye during aggregation of the blue counterpart.

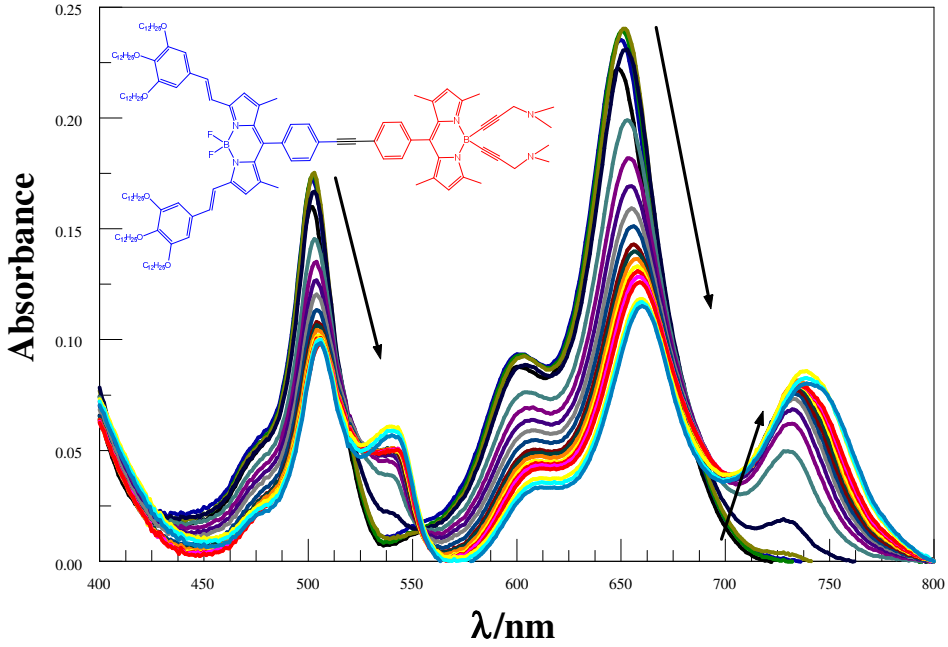

Figure 16. Effect of applied pressure on the absorption spectral profile recorded for high concentrations dyad **5** in MTHF at room temperature. The arrows indicate the direction of increasing pressure.

3.5 Ionic self-assembly

3.5.1 Photophysical properties

Figure 17 presents the absorption and fluorescence spectra of complex **6** in dry THF. Clearly, the absorption spectrum reflects the combination of yellow (λ_{abs} = 513 nm) and blue (λ_{abs} = 650 nm) dyes. Note that the main absorption band for the yellow dye is shifted from 495 in isolated solution to 513 nm in the complex whereas the absorption maximum of the blue analogue remains unchanged. Illumination at 500 nm results in

strong fluorescence centred at 670 nm and for which the emission quantum yield (Φ_{flu}) is 0.40 while the excited-singlet state lifetime (τ_s) is 4.1 ns. It is known that the isolated yellow dye emits strongly at 520 nm but almost no (i.e., ca. 2% of the total emission) such fluorescence could be detected for the complex. This is because quantitative (i.e., >98%) energy transfer occurs from the yellow dye to its blue counterpart within the complex, a situation confirmed by the fact that the excitation spectrum matches the absorption spectrum over the entire spectral window (Figure 17). These results are similar to those found earlier for the covalently linked dyads **4** and **5**.

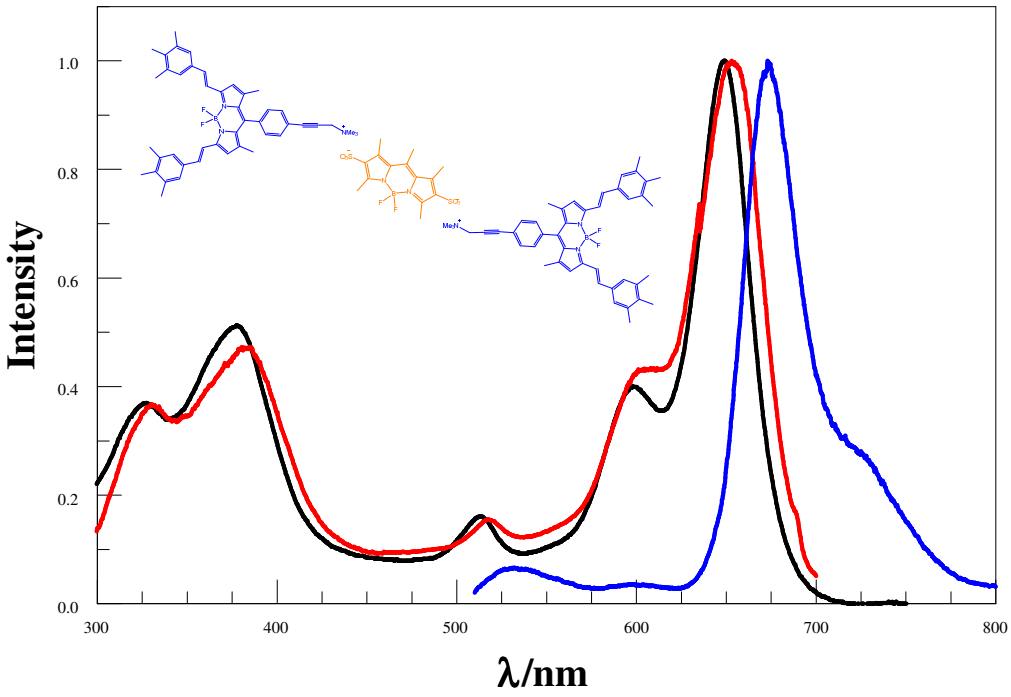

Figure 17. Normalised absorption (black), excitation (red) and emission (blue) spectra recorded for complex **6** in dry THF at room temperature.

In the absence of anionic charges on the yellow dye, the situation changes markedly. For example, mixing the blue dye and a non-charged analogue of the yellow dye in a 2:1 stoichiometry in dry THF results in an absorption spectrum resembling complex **6** (Figure 18) but excitation at 470 nm results in strong fluorescence centred at 515 nm (Φ_{flu} = 0.90: τ_s = 5.3 ns) together with the very weak emission characteristic of the blue dye at 670 nm (Φ_{flu} = 0.06). This latter emission is a consequence of the direct excitation of the blue dye since this species shows slight absorption at 470 nm. Moreover, the absence of EET under these conditions is indicated by the fact that the excitation spectrum recorded for emission from the blue dye (Figure 18) follows the absorption spectrum of that species free from contamination by that of the neutral

yellow dye. At this stage, we can conclude that formation of the 2:1 complex requires electrostatic association of the partners and is manifest by the occurrence of highly efficient EET between the assembled species.

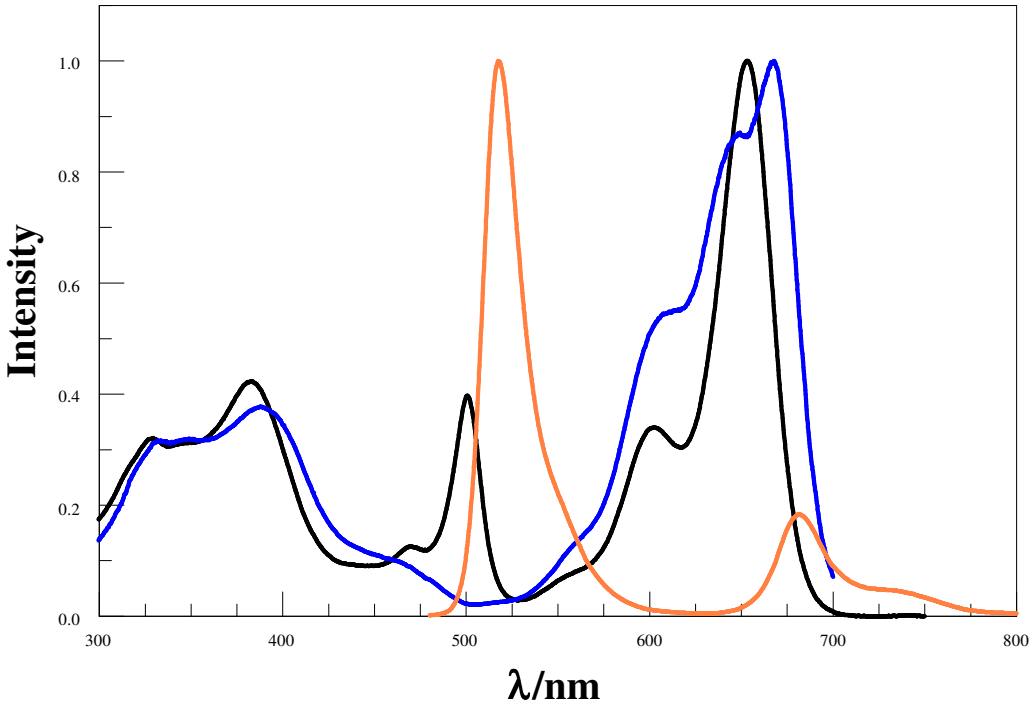

Figure 18. Normalised absorption (black), excitation (blue) and emission (dark yellow) spectra recorded for mixture of the yellow and blue dyes in dry THF at room temperature.

3.5.2 Stability constant measurements

The absorption spectrum recorded for ionic assembly **6** in tetrahydrofuran (THF) does not follow Beer's law over a wide concentration range, indicating partial dissociation of the complex during dilution in accordance with Le Chatelier's principle (Figure 19). During successive dilution with dry THF at 20 °C under stirring, the fluorescence spectral profile shows a progressive increase in fluorescence from the donor at the expense of emission from acceptor. Thus, the ratio of these individual fluorescence integrals, R_{DA}, on preferential excitation into the donor at 490 nm increases steadily with dilution over the range 15 μM to ca. 20 nM; from an initial value of ca. 0.03 to a limiting value of ca. 0.6 (Figure 20). The theoretical upper limit for R_{DA}, based on Φ_{flu} values measured for the isolated units, is ca. 15. Since fluorescence from the blue dye is relatively unperturbed in THF solution, and light scattering is minimal in this solvent, we tend to rule out the possibility that **6** undergoes aggregation under these conditions. As such, the most likely explanation for the concentration dependence is partial dissociation of the complex. Following this argument, the derived R_{DA} can be used to

determine the dissociation constants, K_1 and K_2, characteristic of the complex on the assumption that high concentrations favour formation of the 2:1 complex (Eqns. 7 and 8). The experiment was repeated several times, starting from different initial concentrations of **6**, and comparable estimates for K_1 were obtained.

$$B_2Y \rightleftharpoons BY^- + B^+ \qquad \text{Equation (7)}$$

$$BY^- \rightleftharpoons Y^{2-} + B^+ \qquad \text{Equation (8)}$$

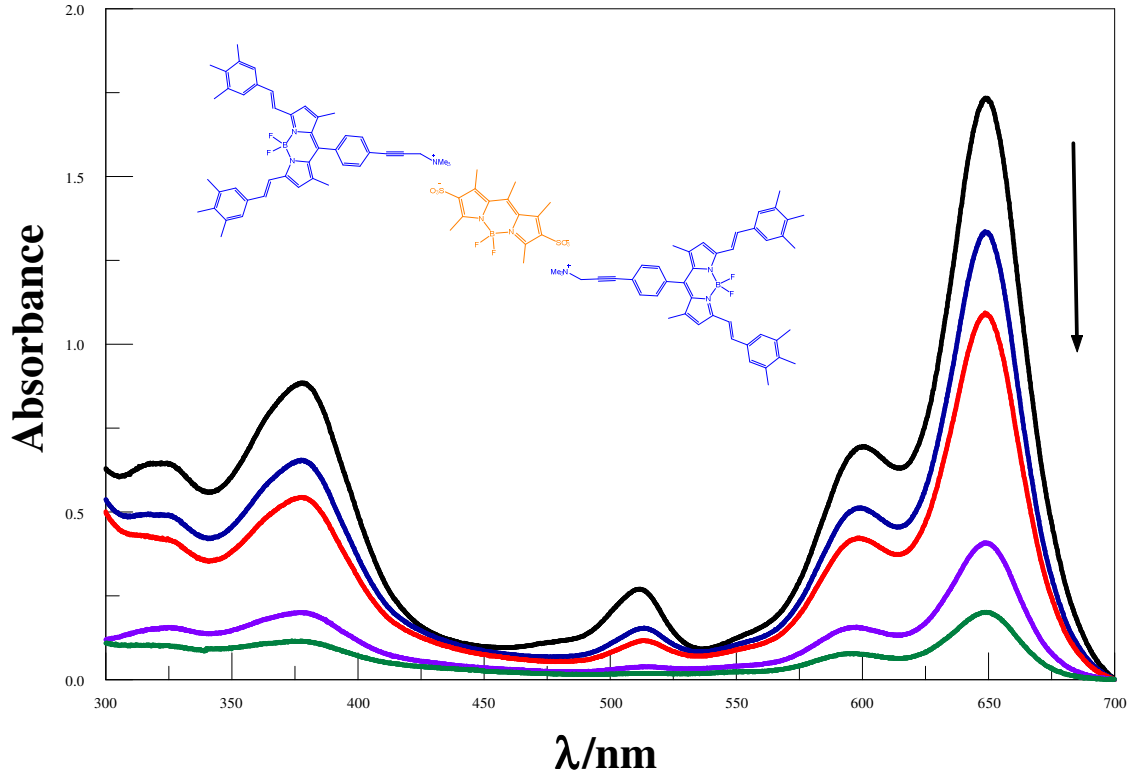

Figure 19. A few representative absorption spectra recorded for complex **6** in THF as a function of dilution. The arrow indicates the direction of dilution.

The fluorescence spectral data were analysed by standard methods[81] to give estimates for K_1 and K_2 (Figure 20). Reproducible values for K_1 (= 3.5 ± 0.8 x 10^{-7} M^{-1}) were obtained but considerably higher variation was found for K_2. The most reliable estimate places this parameter as ca. 7 x 10^{-11} M^{-1}. From the analysis, R_{DA} for the 1:1 complex, **YB**, was determined to be 0.35 ± 0.10. This is comparable to the R_{DA} found for the 2:1 complex, **B_2Y**, but significantly less than that expected for full dissociation. The fluorescence spectral titration indicates that loss of the first blue dye (**B**) is accompanied by only a slight recovery of fluorescence from the yellow counterpart (**Y**) that remains centred at 520 nm and it is the loss of the second molecule of **B** that restores the characteristic emission from the donor. Two possibilities can be raised to explain this behaviour: First, it can be argued that the tightly bound blue dye present in **BY** is a relatively poor acceptor for electronic energy transfer from the donor compared

to the second blue dye, which is held less tightly but in a more favourable orientation. Second, loss of the first blue dye might lead to restructuring within **BY** that somewhat displaces the acceptor from close contact with the donor. To help resolve this situation, competitive binding studies were undertaken as outlined below. The derived K_1 value ($\Delta G°$ = 36 kJ.mol^{-1}) compares well with the calculated change in electrostatic energy (ΔE = 42 kJ.mol^{-1}) associated with the removal of one blue dye from **6** in THF at 20 °C. Hence, the binding energy for the weakly bound blue dye is primarily electrostatic whereas that for the tightly bound blue dye is more likely derived from a combination of van der Waals, electrostatic, π,π*, and solvatophobic interactions.

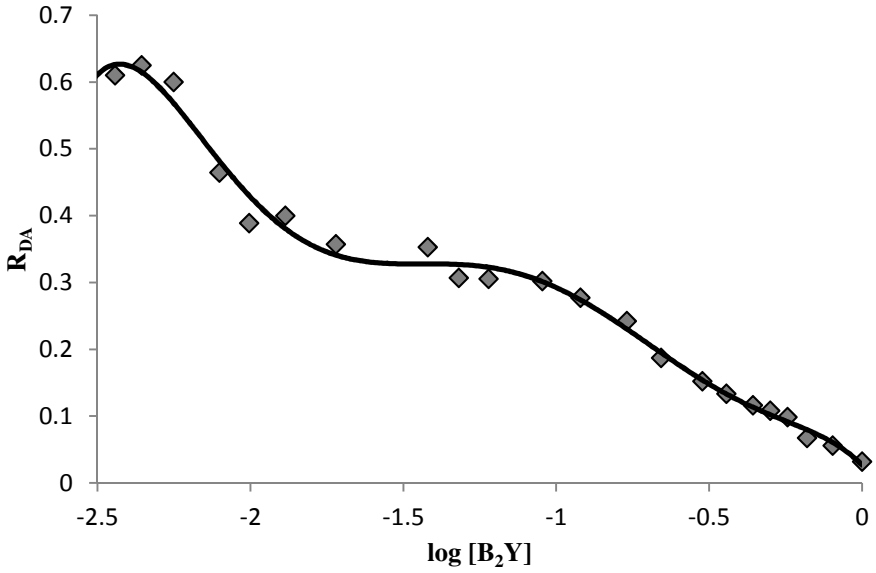

Figure 20. Typical dilution profile showing the effect of adding THF on the ratio of fluorescence yields as recorded for complex **6** at room temperature. The solid line corresponds to a nonlinear, least squares fitting.

Time-resolved fluorescence studies were carried out at various stages of the dilution experiment, focussing on emission from the yellow donor. For the bis-complex, we were not able to resolve a proper lifetime from the instrumental response function. This suggests that the donor lifetime is <30 ps under these conditions. In contrast, the emission lifetime for the yellow donor present in the mono-complex varies from 70 ps at high concentration to 150 ps at low concentration. This effect is attributed to weak intermolecular association of the complex at high concentration that brings together yellow and blue dyes from different complexes.

The first dissociation constant, K_1, derived for **6** was measured over a modest temperature range in THF solution by following the relative ratio of emission bands isolated for donor and acceptor subunits, as outlined above (Figure 21). The results are

presented in Figure 22 in the form of the van't Hoff expression (Eqn. 6) and from the linear plot the enthalpy change, ΔH, associated with loss of the weakly-bound blue dye from the complex was found to be -5.3 kJ.mol^{-1} and this can be attributed to an increase in the entropy of the surroundings. A small range of initial concentrations of the complex was used and the ΔH value is the average taken across 3 independent sets of measurements. In each case, the van't Hoff plot was reasonably linear.

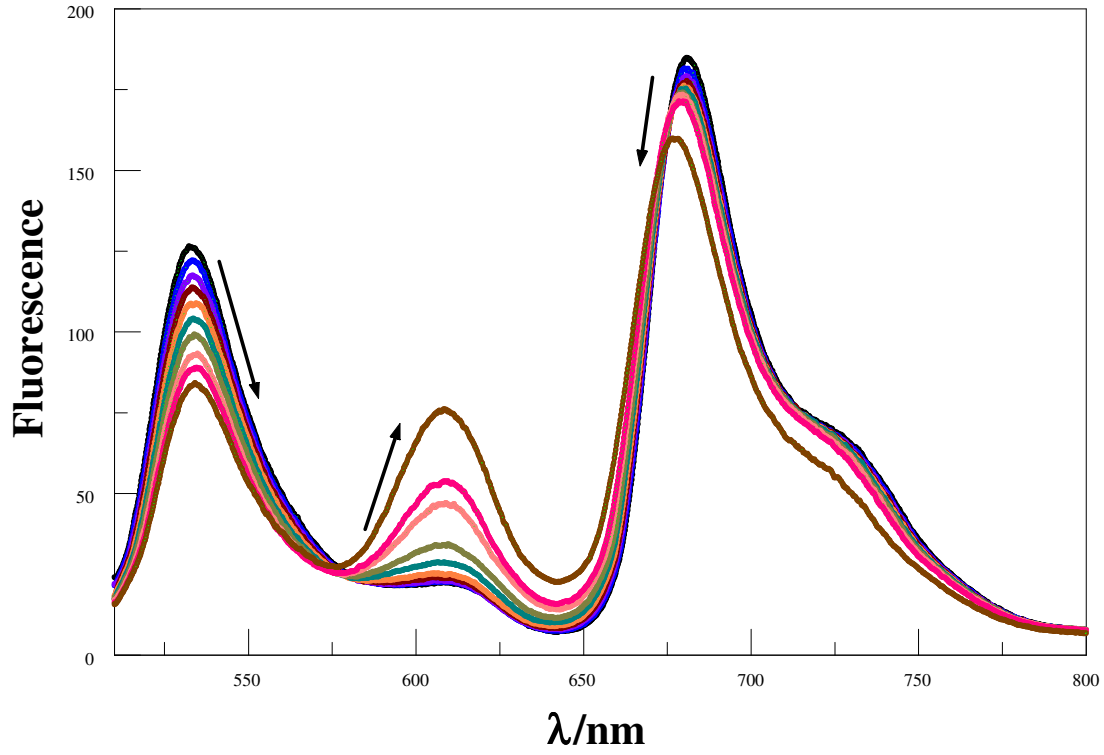

Figure 21. Effect of temperature on the fluorescence spectral profile recorded for complex **6** in THF. The arrows indicate the direction of increasing temperature.

Interestingly, a new peak starts to appear at temperatures above 30 °C around 610 nm and increases as the temperature increases further. This new peak is somewhat reminiscent of that assigned to structural distortion of the blue dye under high pressure but we cannot say that the same process occurs. Instead, we delay discussion of this point until after making careful studies of the isolated blue dye.

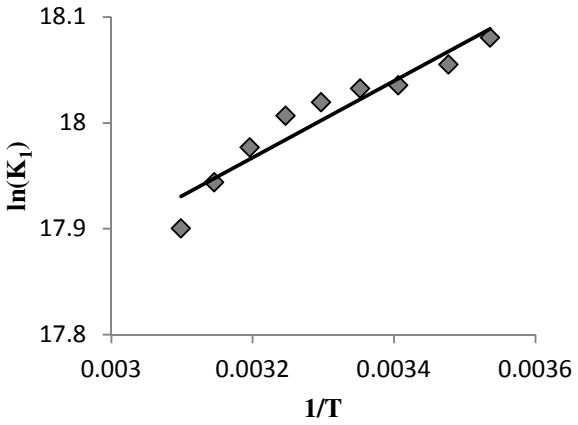

Figure 22. An example of a van't Hoff plot derived for complex **6** in THF.

Competitive binding

Absorption and fluorescence spectra recorded for **6** in THF at 20 °C were recorded as a function of added tetra-n-butylammonium perchlorate (TBAP). A small range of initial concentrations of **6** was used. An example of the fluorescence titration is given as Figure 23 following preferential excitation into the donor at 490 nm. It might be noted that TBAP is colourless and does not contribute to the recorded absorption or emission spectra. The solution was stirred and maintained at 20 °C throughout the titration. The added cation has a marked effect on the relative ratio of emission bands, R_{DA}, as illustrated via the insert to Figure 23, although a large molar excess of TBAP is needed to reach saturation. Here, the added cation competes with **B** for association to **Y** and dismantles the original complex; presumably, a new ion pair is formed by way of electrostatic binding. In THF, the first **B** molecule is readily replaced by TBA^+, but this has only a small effect on the fluorescence spectral profile. Fitting the titration data allows estimation of the relative binding constants as being ca. 17-fold in favour of **B**. The projected R_{DA} for the mixed complex, **(TBAP)YB**, is ca. 1. This is higher than that found for **BY** and might indicate a more relaxed geometry with respect to the attached blue dye and the yellow donor. Exchange of the more tightly bound **B** molecule demands a large excess of TBAP (e.g., >100 mol equiv for complete replacement) and fully restores emission from the donor with R_{DA} equal to 6.2. Data analysis is consistent with the mixed complex having a ca. 10^4-fold greater preference for **B** than TBA^+. Taking due account of the fact that TBAP is likely to form a complex by way of electrostatic interactions, it follows that complexes such as **6** are stabilized by ancillary interactions. Fitting the respective differential binding constants, K_A and K_B, involves considerable uncertainties and only approximate values could be derived from the fit. The most reproducible estimates give $K_A = 0.06$ and $K_B = 1.1 \times 10^{-4}$.

$$B_2Y + TBAP \rightleftharpoons BY(TBA) + BP \qquad \text{Equation (9)}$$

$$BY(TBA) + TBAP \rightleftharpoons Y(TBA)_2 + BP \qquad \text{Equation (10)}$$

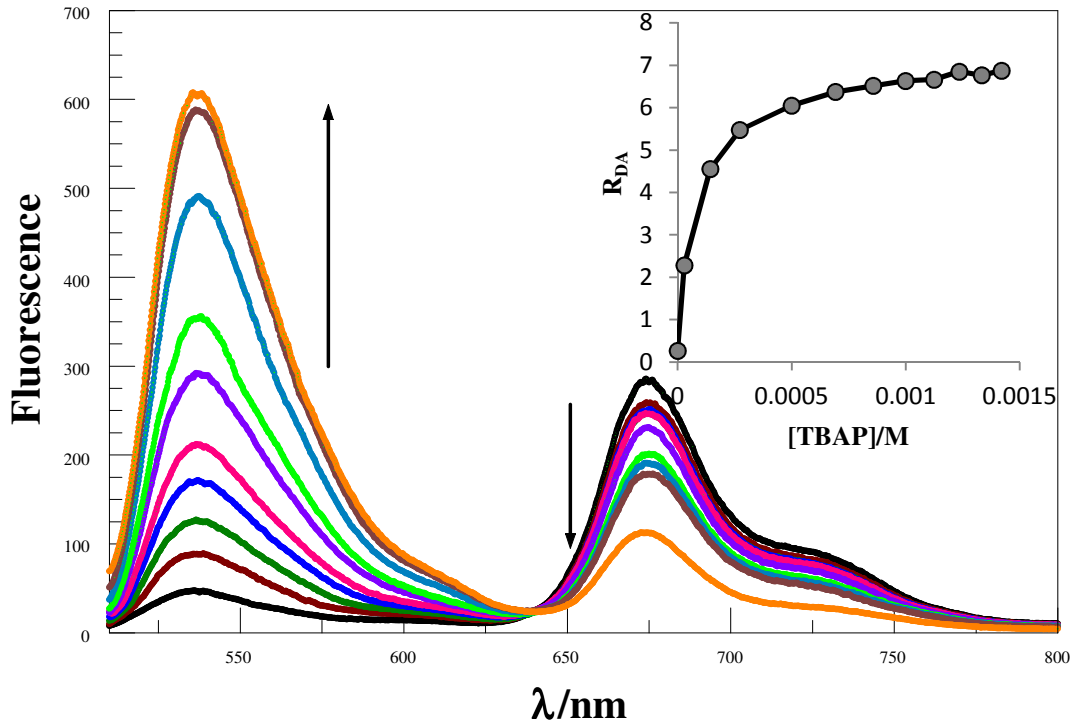

Figure 23. Effect of added TBAP on the fluorescence profile recorded for complex **6** in THF at room temperature. The arrows indicate the direction of increasing the TBAP concentration. The insert shows the relation between the cation concentration and the fluorescence ratio.

Effect of solvent polarity

The absorption and fluorescence spectral properties were recorded for complex **6** at 20 °C in a small range of solvents of differing static dielectric constant, ε_s, and the main findings are collected in Table 2.

Table 2. Effect of solvent polarity on the spectroscopic properties and the stability constant measured for **6** at room temperature. [(a)] Refers to the donor. [(b)] Refers to the acceptor. [(c)] A mixture of aggregate and monomer exists in this solvent. CCl_4 is carbon tetrachloride, C_6H_6 is benzene, Bu_2O and Et_2O are dibutyl and diethyl ether, respectively, C_6H_5Cl is chlorobenzene, THF and MTHF are tetrahydrofuran and 2-methyl substitution of it.

Solvent	ε_s	λ_{abs}/nm [(a)]	λ_{flu}/nm [(a)]	λ_{abs}/nm [(b)]	λ_{flu}/nm [(b)]	Log K_1
CCl_4	2.23	520	540	660	715	21.5
C_6H_6	2.3	510	515	650	710	23.56
Bu_2O	3.0	510	535	655	700	NA[(c)]
Et_2O	4.3	510	535	650	665	NA[(c)]
C_6H_5Cl	5.6	510	520	650	665	17.80
MTHF	6.9	500	520	650	670	15.62
THF	7.5	512	535	650	670	14.73

Selected examples of the fluorescence spectra are shown as Figure 24. In each case, emission is dominated by the contribution from the blue dye although the ratio of the isolated fluorescence integrals for yellow and blue absorbers (R_{DA}) is sensitive to the polarity of the solvent. More notable is the shift towards longer wavelength for the fluorescence band associated with the blue dye. Indeed, in non-polar solvent this emission band resembles that found for the liquid-crystalline mesophase. The indications are that **6** is self-associated in non-polar solvent in the form of large aggregates that remain suspended in solution. Light-scattering studies confirm the presence of small particles in suspension but the absorption and fluorescence spectra are stable over many hours standing in the dark. In non-cyclic ethers (Figure 25), the fluorescence spectrum appears as a mixture of monomeric and aggregated forms of **6** at 665 and 720 nm, respectively, but addition of THF restores the spectrum expected for the monomer.

The first dissociation constant, K_1, was measured for the limiting solvents at 20 °C and the derived values are given in Table 2. These values tend to increase substantially as the solvent polarity decreases in line with expectations for an electrostatic binding motif.

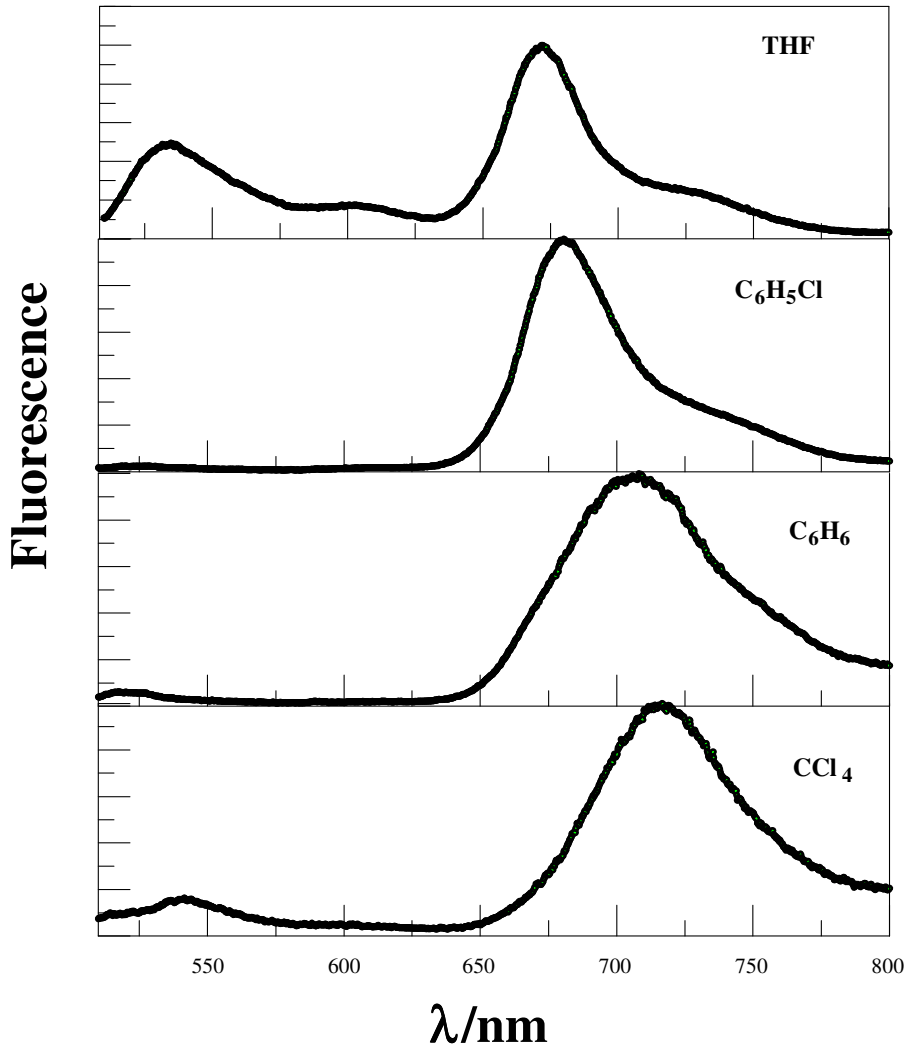

Figure 24. Selected examples of the fluorescence spectra of **6** recorded in solvents of varying polarity.

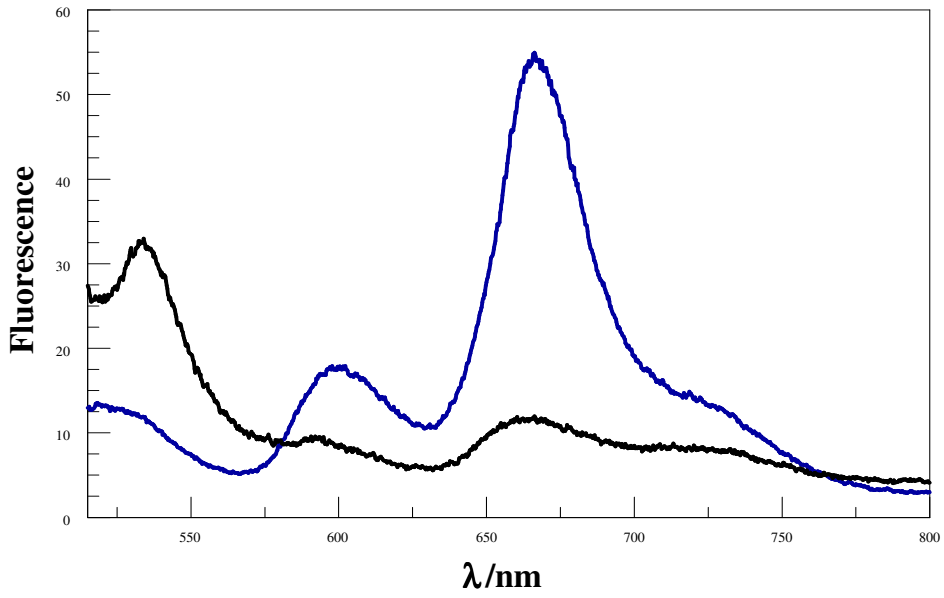

Figure 25. Recorded fluorescence spectra for complex **6** in Et_2O (black) and a mixture of Et_2O and THF (blue) at room temperature.

3.5.3 The liquid-crystalline properties

Our collaborators in Strasbourg examined the liquid-crystalline properties of **6** using polarizing optical microscopy (POM), differential scanning calorimetry (DSC), and X-ray diffraction (XRD).[82-85] The main conclusion is that complex **6** displays behaviour consistent with a 3D crystalline phase at room temperature that transforms under heating into a hexagonal columnar mesophase (Col_h), which persists on further heating to the point of thermal decomposition. On cooling, a mesomorphic glass appears that maintains the structural characteristics of the hexagonal columnar mesophase. Crystallization does not take place even on cooling to –40 °C while the covalently linked dye **5** melts directly to the isotropic liquid, which partially or totally crystallizes on cooling without passing through a mesomorphic phase. In addition, variable-temperature X-ray diffraction studies indicate that complex **6** presents a disordered, hexagonal columnar mesophase consistent with the absence of a planar aromatic core inherent to classical disk-like mesogens.[86] We emphasize that we did not participate directly in this work.

Interestingly, a broad emission profile spanning from 650 to 850 nm is observed for the columnar mesophase of **6** when dispersed on a glass slide. This latter emission is broadened significantly and red-shifted compared to that from the corresponding solution phase due to the ordering of the molecule in the thin film (Figure 26). Both the shape and intensity of the fluorescence profile depend on the temperature over the range 20–150 °C. Since there is essentially no emission from **Y** it is concluded that quantitative EET occurs in the mesophase. Indeed, mixing **B** with the neutral form of the yellow dye in a 2:1 stoichiometry and annealing at 150 °C leads to the appearance of dual emission at 550 and 750 nm when the film is examined at 100 °C in the bulk state (Figure 26). This set of experiments provides strong support for the idea that the complex is not dismantled at 150 °C and that the mesophase is stable at high temperature.

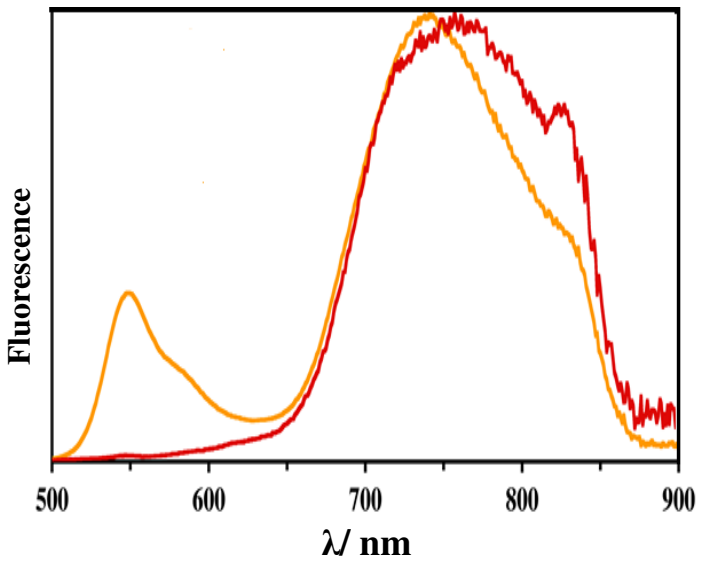

Figure 26. Fluorescence spectra recorded for complex **6** in the columnar mesophase (red) and the mixture of **Y** and **B** (dark yellow) at 100 °C.

3.6 Conclusion

One of the main themes of this chapter has been to address how applied pressure might influence the probability of intramolecular EET in a closely spaced molecular dyad. In this case, the direct effect of pressure on P_{EET} is small, perhaps because of compensatory factors, and it appears that the linear topology of the dyad does not facilitate pressure-induced structural modifications. However, at modest applied pressure the acceptor unit distorts in such a way that its electronic properties are perturbed. This leads to a substantial change in colour and serves to switch off EET from the attached donor. The process is fully reversible. It seems reasonable to suppose that such behaviour could be exploited to design novel pressure-sensitive materials. In fact, this possibility forms the basis for a later chapter where we set out to examine the pressure induced conformational exchange undertaken by certain extended Bodipy dyes in fluid media.

A second important theme revolves around the assembly of functional molecular entities by ionic self-association from solution. This approach, sometimes abbreviated in the literature as ISA, provides an attractive alternative to covalent bonding in regards to the creation of molecular entities capable of displaying highly efficacious EET. Moreover, this approach facilitates the growth of organized mesophases, under mild conditions, retaining the EET step. A further benefit of the ISA methodology is that the emergent mesophase has the potential to function as a superior light-harvesting array for silicon-based solar cells. This type of strategy might prove to be extremely useful when considering practical outlets for this type of fundamental research.

One important spin-off from this work relates to the discovery of a Bodipy derivative that exists as a viscous liquid when highly purified. This dye, prepared by our collaborators in Strasbourg, has multiple poly(ethylene glycol) chains attached to the dipyrrin nucleus. The compound dissolves in organic solvents to give optical spectra characteristic of the monomeric species and it can be readily adhered to glass slides. We anticipate that the new material might be useful as a sensitiser for solar cells but, because of time constraints, the sample will be examined by a different member of our research group.

3.7 References

1. Olivier, J.-H.; Widmaier, J.; Ziessel, R. *Chem. - Eur. J.* **2011**, *17*, 11709.
2. Ziessel, R.; Rihn, S.; Harriman, A. *Chem. - Eur. J.* **2010**, *16*, 11942.
3. Berney, C.; Danuser, G. *Biophys. J.* **2003**, *84*, 3992.
4. Piston, D. W.; Kremers, G.-J. *Trends Biochem. Sci* **2007**, *32*, 407.
5. Clapp, A. R.; Medintz, I. L.; Mauro, J. M.; Fisher, B. R.; Bawendi, M. G.; Mattoussi, H. *J. Am. Chem. Soc.* **2003**, *126*, 301.
6. Schuler, B.; Lipman, E. A.; Steinbach, P. J.; Kumke, M.; Eaton, W. A. *Proc. Natl. Acad. Sci. U.S.A.* **2005**, *102*, 2754.
7. Laurence, T. A.; Kong, X.; Jäger, M.; Weiss, S. *Proc. Natl. Acad. Sci. U.S.A.* **2005**, *102*, 17348.
8. Chung, H. S.; Louis, J. M.; Eaton, W. A. *Biophys. J.* **2010**, *98*, 696.
9. Bieri, O.; Wirz, J.; Hellrung, B.; Schutkowski, M.; Drewello, M.; Kiefhaber, T. *Proc. Natl. Acad. Sci.* **1999**, *96*, 9597.
10. Turshatov, A.; Adams, J. r.; Johannsmann, D. *Macromol.* **2008**, *41*, 5365.
11. Srinivas, G.; Bagchi, B. *PhysChemComm* **2002**, *5*, 59.
12. Beechem, J. M.; Haas, E. *Biophys. J.* **1989**, *55*, 1225.
13. De Cian, A.; Guittat, L.; Kaiser, M.; Saccà, B.; Amrane, S.; Bourdoncle, A.; Alberti, P.; Teulade-Fichou, M.-P.; Lacroix, L.; Mergny, J.-L. *Methods* **2007**, *42*, 183.
14. Zhang, C.-Y.; Yeh, H.-C.; Kuroki, M. T.; Wang, T.-H. *Nat. Mater.* **2005**, *4*, 826.
15. Fischer, M. K. R.; Kaiser, T. E.; Wurthner, F.; Bauerle, P. *J. Mater. Chem.* **2009**, *19*, 1129.
16. Forster, T. *Naturwissenschaften* **1946**, *33*, 166.
17. Dexter, D. L. *J. Chem. Phys.* **1953**, *21*, 836.
18. Kawatsu, T.; Matsuda, K.; Hasegawa, J.-y. *J. Phys. Chem. A* **2011**, *115*, 10814.
19. Ray, J.; Makri, N. *J. Phys. Chem. A* **1999**, *103*, 9417.
20. Curutchet, C.; Mennucci, B.; Scholes, G. D.; Beljonne, D. *J. Phys. Chem. B* **2008**, *112*, 3759.
21. Benniston, A. C.; Harriman, A.; Li, P.; Sams, C. A. *J. Am. Chem. Soc.* **2005**, *127*, 2553.
22. Jockusch, S.; Timpe, H. J.; Schnabel, W.; Turro, N. J. *J. Phys. Chem. A* **1997**, *101*, 440.
23. Robinson, G. W. *J. Mol. Spectrosc.* **1961**, *6*, 58.
24. Grusenmeyer, T. A.; Chen, J.; Jin, Y.; Nguyen, J.; Rack, J. J.; Schmehl, R. H. *J. Am. Chem. Soc.* **2012**, *134*, 7497.

25. Andreasson, J.; Kyrychenko, A.; Martensson, J.; Albinsson, B. *Photochem. Photobiol. Sci.* **2002**, *1*, 111.
26. Yu, J.; Hu, D.; Barbara, P. F. *Science* **2000**, *289*, 1327.
27. Chatterjee, S.; Nandi, S.; Bhattacharya, S. C. *J. Photochem. Photobiol., A* **2005**, *173*, 221.
28. Brun, A. M.; Harriman, A. *J. Am. Chem. Soc.* **1994**, *116*, 10383.
29. Fiedor, J.; Pilch, M.; Fiedor, L. *J. Phys. Chem. B* **2009**, *113*, 12831.
30. Schuler, B. *Methods in Molecular Biology: Protein Folding Protocols*; Humana Press Inc.: Totowa, NJ, 2007; Vol. 350.
31. Merchant, K. A.; Best, R. B.; Louis, J. M.; Gopich, I. V.; Eaton, W. A. *Proc. Natl. Acad. Sci.* **2007**, *104*, 1528.
32. Alamiry, M. A. H.; Hagon, J. P.; Harriman, A.; Bura, T.; Ziessel, R. *Chem. Sci.* **2012**, *3*, 1041.
33. Kato, M.; Taniguchi, Y. *J. Chem. Phys.* **1991**, *94*, 4440.
34. Sabharwal, R. J.; Huang, Y.; Song, Y. *J. Phys. Chem. B* **2007**, *111*, 7267.
35. Adamy, S. T.; Kerrick, S. T.; Jonas, J. *Z. Phys. Chem. Int. J. Res. Phys. Chem. Chem. Phys.* **1994**, *184*, 185.
36. Herberhold, H.; Marchal, S.; Lange, R.; Scheyhing, C. H.; Vogel, R. F.; Winter, R. *J. Mol. Biol.* **2003**, *330*, 1153.
37. Webster, S.; Batchelder, D. N. *Polym.* **1996**, *37*, 4961.
38. Dreger, Z. A.; Lang, J. M.; Drickamer, H. G. *Chem. Phys.* **1993**, *169*, 351.
39. Harriman, A.; Elliott, K. J.; Alamiry, M. A. H.; Pleux, L. c. L.; Séverac, M.; Pellegrin, Y.; Blart, E.; Fosse, C. l.; Cannizzo, C.; Mayer, C. d. R.; Odobel, F. *J. Phys. Chem. C* **2009**, *113*, 5834.
40. Alamiry, M. A. H.; Benniston, A. C.; Copley, G.; Harriman, A.; Howgego, D. *J. Phys. Chem. A* **2011**, *115*, 12111.
41. Murphy, S.; Sauerwein, B.; Drickamer, H. G.; Schuster, G. B. *J. Phys. Chem.* **1994**, *98*, 13476.
42. Zhu, A.; Wang, B.; White, J. O.; Drickamer, H. G. *J. Phys. Chem. A* **2003**, *107*, 6932.
43. Korppi-Tommola, J. E. I.; Hakkarainen, A.; Hukka, T.; Subbi, J. *J. Phys. Chem.* **1991**, *95*, 8482.
44. Hara, K. k. *High Press. Res.* **2003**, *23*, 225.
45. Madjet, M. E.-A.; Müh, F.; Renger, T. *J. Phys. Chem. B* **2009**, *113*, 12603.

46. Alamiry, M. A. H.; Benniston, A. C.; Copley, G.; Harriman, A. *RSC Adv.* **2012**, *2*, 1936.
47. Magde, D.; Wong, R.; Seybold, P. G. *Photochem. Photobiol.* **2002**, *75*, 327.
48. Bublitz, G. U.; Boxer, S. G. *Annu. Rev. Phys. Chem.* **1997**, *48*, 213.
49. Lockhart, D. J.; Boxer, S. G. *Biochem.* **1987**, *26*, 664.
50. Crane, D. R.; Ford, P. C. *J. Am. Chem. Soc.* **1991**, *113*, 8510.
51. Faul, C. F. J.; Antonietti, M. *Adv. Mater.* **2003**, *15*, 673.
52. Wu, D.; Pisula, W.; Enkelmann, V.; Feng, X.; Müllen, K. *J. Am. Chem. Soc.* **2009**, *131*, 9620.
53. Tian, Y.; Martin, K. E.; Shelnutt, J. Y. T.; Evans, L.; Busani, T.; Miller, J. E.; Medforth, C. J.; Shelnutt, J. A. *Chem. Commun.* **2011**, *47*, 6069.
54. Ahmed, R.; Hsiao, M.-S.; Matsuura, Y.; Houbenov, N.; Faul, C. F. J.; Manners, I. *Soft Matter* **2011**, *7*, 10462.
55. Caruso, F.; Caruso, R. A.; Möhwald, H. *Science* **1998**, *282*, 1111.
56. Cassagneau, T.; Fendler, J. H.; Mallouk, T. E. *Langmuir* **1999**, *16*, 241.
57. Cini, N.; Tulun, T.; Decher, G.; Ball, V. *J. Am. Chem. Soc.* **2010**, *132*, 8264.
58. Wang, Z.; Medforth, C. J.; Shelnutt, J. A. *J. Am. Chem. Soc.* **2004**, *126*, 15954.
59. Rosidian, A.; Liu, Y.; Claus, R. O. *Adv. Mater.* **1998**, *10*, 1087.
60. Zakrevskyy, Y.; Faul, C. F. J.; Guan, Y.; Stumpe, J. *Adv. Funct. Mater.* **2004**, *14*, 835.
61. Zhang, T.; Spitz, C.; Antonietti, M.; Faul, C. F. J. *Chem. - Eur. J.* **2005**, *11*, 1001.
62. Kato, T.; Mizoshita, N.; Kishimoto, K. *Angew. Chem. Int. Ed.* **2006**, *45*, 38.
63. Camerel, F.; Ulrich, G.; Barberá, J.; Ziessel, R. *Chem. - Eur. J.* **2007**, *13*, 2189.
64. Olivier, J.-H.; Camerel, F.; Barberá, J.; Retailleau, P.; Ziessel, R. *Chem. - Eur. J.* **2009**, *15*, 8163.
65. Olivier, J. H.; Camerel, F.; Ulrich, G.; Barbera, J.; Ziessel, R. *Chem. Eur. J.* **2010**, *16*, 7134.
66. Huang, Y.; Yan, Y.; Smarsly, B. M.; Wei, Z.; Faul, C. F. J. *J. Mater. Chem.* **2009**, *19*, 2356.
67. Ziessel, R.; Harriman, A. *Chem. Commun.* **2011**, *47*, 611.
68. Olivier, J.-H.; Barberá, J.; Bahaidarah, E.; Harriman, A.; Ziessel, R. *J. Am. Chem. Soc.* **2012**, *134*, 6100.
69. Georgakopoulou, S.; Cogdell, R. J.; van Grondelle, R.; van Amerongen, H. *J. Phys. Chem. B* **2002**, *107*, 655.
70. Knox, R. S.; van Amerongen, H. *J. Phys. Chem. B* **2002**, *106*, 5289.

71. Scholes, G. D.; Jordanides, X. J.; Fleming, G. R. *J. Phys. Chem. B* **2001**, *105*, 1640.
72. Wong, K. F.; Bagchi, B.; Rossky, P. J. *J. Phys. Chem. A* **2004**, *108*, 5752.
73. Andrews, D. L. *Phys. Rev. A* **2010**, *81*, 033825.
74. Czikklely, V.; Forsterling, H. D.; Kuhn, H. *Chem. Phys. Lett.* **1970**, *6*, 207.
75. Harriman, A.; Mallon, L. J.; Elliot, K. J.; Haefele, A.; Ulrich, G.; Ziessel, R. *J. Am. Chem. Soc.* **2009**, *131*, 13375.
76. Benniston, A. C.; Harriman, A.; Whittle, V. L.; Zelzer, M. *Eur. J. Org. Chem.* **2010**, *2010*, 523.
77. McIntosh, A. R.; Siemiarczuk, A.; Bolton, J. R.; Stillman, M. J.; Ho, T. F.; Weedon, A. C. *J. Am. Chem. Soc.* **1983**, *105*, 7215.
78. Xu, Q.-H.; Fayer, M. D. *J. Chem. Phys.* **2002**, *117*, 2732.
79. Pohl, G.; Jakli, I.; Csizmadia, I. G.; Papp, D.; Matias, G. F.; Perczel, A. *Phys. Chem. Chem. Phys.* **2012**, *14*, 1507.
80. Strickler, S. J.; Berg, R. A. *J. Chem. Phys.* **1962**, *37*, 814.
81. Wang, Z.-X.; Ravi Kumar, N.; Srivastava, D. K. *Anal. Biochem.* **1992**, *206*, 376.
82. Yoshio, M.; Kagata, T.; Hoshino, K.; Mukai, T.; Ohno, H.; Kato, T. *J. Am. Chem. Soc.* **2006**, *128*, 5570.
83. Stępień, M.; Donnio, B.; Sessler, J. L. *Angew. Chem. Int. Ed.* **2007**, *46*, 1431.
84. Laschat, S.; Baro, A.; Steinke, N.; Giesselmann, F.; Hägele, C.; Scalia, G.; Judele, R.; Kapatsina, E.; Sauer, S.; Schreivogel, A.; Tosoni, M. *Angew. Chem. Int. Ed.* **2007**, *46*, 4832.
85. Santoro, A.; Prokhorov, A. M.; Kozhevnikov, V. N.; Whitwood, A. C.; Donnio, B.; Williams, J. A. G.; Bruce, D. W. *J. Am. Chem. Soc.* **2011**, *133*, 5248.
86. Kumar, S. *Chem. Soc. Rev.* **2006**, *35*, 83.

Chapter 4. Nanomechanical properties of molecular-scale bridges as visualised by intramolecular electronic energy transfer

4.1 Executive summery

A series of molecular dyads has been synthesized and fully characterised. These linear, donor–spacer–acceptor compounds comprise terminal dyes selected to exhibit intramolecular electronic energy transfer (EET) along the molecular axis. The spacer is built by accretion of ethynylene–carborane units that give centre-to-centre separation distances of 38, 57, 76, 96, and 115Å respectively along the series. The probability of one-way EET between the terminals depends on the length of the spacer but also on temperature and applied pressure. Throughout the series, the derived EET parameters are well explained in terms of through-space interactions but the probability of EET is higher than predicted for the fully extended conformation except in a glassy matrix at low temperature. The implication is that these spacers contract under ambient conditions, with the extent of longitudinal contraction increasing under pressure but decreasing as the temperature is lowered. Longer bridges are more susceptible to such distortions, which are considered to resemble a concertina effect caused by out-of-plane bending of individual subunits. The dynamics of EET can be used to estimate the strain energy associated with molecular contraction, the amount of work done in effecting the structural change, and the apparent Young's modulus for the bridge.

4.2 Structure

The compounds of interest here (Figure 1), **B-C$_n$-DPP**, comprise a linear molecular wire of variable length formed by linking together *para*-ethynylene–carborane (**C**) fitted with terminal chromophores; the latter are blue Bodipy (**B**)[1-4] and dipyrrolopyrrole (**DPP**).[5] The corresponding **B-C$_n$-TES** derivatives were used as reference compounds to investigate the effect of the carborane unit on the properties of the blue Bodipy.

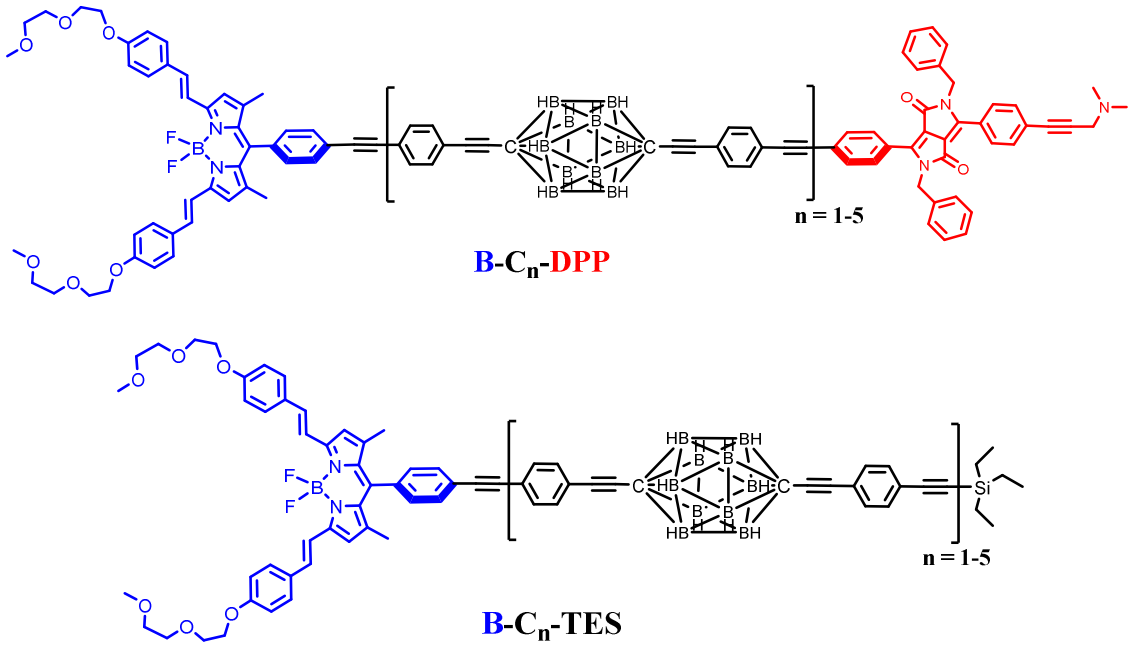

Figure 1. Structures of the compounds under study. **B** refers to blue Bodipy, **C** refers to carborane, **n** is the number of carborane units, **DPP** refers to diketopyrrolopyrrol, and **TES** is triethylsilane.

4.3 Introduction

Electronic energy transfer (EET) is of major importance in biology, notably photosynthesis[6] and photolyase enzymes,[7,8] and in modern opto-electronic devices such as OLEDs.[9] The original theoretical frameworks were developed[10,11] more than 50 years ago but have been subjected to considerable modification and extension over the past few decades.[12-14] With specific consideration of intramolecular EET, there are three primary mechanisms that combine to cover most cases. These include electron exchange (or through-bond EET), coulombic interactions (or through-space EET), and bridge-mediated EET.[15] The latter[16-18] applies to systems where the donor and acceptor are bridged by a conjugated spacer in such a way that the identities of the three components become somewhat blurred in electronic terms. Electron exchange[19] demands orbital overlap between donor and acceptor, often facilitated by super-exchange interactions, where the rate is attenuated exponentially with increasing separation between the

reactants.[20,21] This mechanism is important for triplet-excited states[22,23] and for EET in conducting polymers.[24,25] A special situation might arise, however, when the reactants share a common connecting vibrational mode.[26]

Through-space EET, as first formulated by Förster,[11] is most often explained within the confines of the ideal dipole approximation but this might not hold at short (<30 Å) separations unless the transition dipole moment vectors are of uncommonly short length.[27] This process has been used widely in biology to measure distances and/or orientations[28,29] and does not require orbital contact. It can occur over separations exceeding 100 Å. The requirements for efficient Förster-type EET include good spectral overlap between fluorescence from the donor and absorption by the acceptor, and a high radiative rate constant for the donor.[30] Additional requisites relate to an appropriate alignment of transition dipole moment vectors[31-33] and to the screening factor imposed by the surrounding medium.[34] This latter term is likely to be distance dependent for short (<20 Å) separations,[35] where higher-order multi-poles have to be considered,[36] and where the spatial distribution of the transition moment should be taken into account. There are the additional challenges of dealing with reactants subjected to Brownian motion that perturbs the overall orientation factor[37] and in handling cases where the transition dipole moment vectors are degenerate.[38]

Many experimental and theoretical studies have addressed the basic premise of how separation distance affects the dynamics of EET[39,40] while other research has used the ideal distance dependence to estimate molecular topology.[41,42] Such work is most likely to succeed over modest separations but to become increasingly less reliable as the reactants approach each other. The opposite trend, namely increasing the molecular separation, introduces severe problems in terms of establishing the actual distance between the reactants. Early work in this subject relied on random distributions of donors and acceptors where the mean separation is determined by concentration.[43,44] This situation was improved by attaching the reactants to biomolecules, such as helical proteins[45,46] or DNA,[47-49] thereby allowing the distance to be better defined. Related studies have used polymers[50-52] to bind the reactants but suffer badly from structural heterogeneity.[53] In attempting to design new molecular dyads that overcome these structural problems, we consider here the possible use of carboranes as building blocks by which to assemble linear molecules of unusual length but structural integrity and this chapter will investigate these compounds.

Carboranes are polyhedral clusters built with skeletal boron and carbon atoms terminated by hydrogen atoms which are used extensively as templates for the

preparation of soft matter,[54,55] polymers,[56] non-linear materials,[57] rigid rods[58] and self-assembled molecular structures.[59] Notably, *closo-para*-carborane ($C_2B_{10}H_{12}$) is an electronically closed structure stabilised with 26 electrons. This electronic and geometric shell closure makes carboranes electronically, chemically and thermodynamically rather robust.[60] Furthermore, these caged clusters are transparent to visible light and do not exhibit redox activity at normally accessible potentials.[61] This realisation prompted us to use *closo-para*-carborane as a platform through which to link photoactive modules in a rod-like manner (Figure 1).[62] Note that the blue dye has been chosen from the distyryl-boron dipyrromethene (Bodipy) family[1-4] while the dipyrrolopyrrole (**DPP**) donor is known for its exceptional stability, ease of chemical modification and well-defined structure.[5] For both dyes, the presence of ancillary functions (BF_2 in the acceptor and dimethylamino-propyne in the donor) help to prevent aggregation.

4.4 Photophysical properties in fluid solution

Absorption spectra recorded for the compounds in 2-methyltetrahydrofuran (MTHF) exhibit the expected features characteristic of each chromophore (Figure 2). In particular, the blue Bodipy dye (**B**) exhibits a strong absorption transition centred at 645 nm ($\varepsilon_{max} \approx 123{,}000\ M^{-1}cm^{-1}$), with a set of vibronic bands stretching to higher energies.[63,64] The corresponding absorption transition for **DPP** is easily recognised[65,66] as a series of weaker bands starting at around 497 nm ($\varepsilon_{max} \approx 30{,}500\ M^{-1}cm^{-1}$). The carborane-based bridge, **C**, absorbs only in the near-UV region, with bands centred in the 300–350 nm region. Band maxima, half-widths and molar absorption coefficients (ε_{max}) recorded for both **B** and **DPP** are insensitive to the molecular length but there is a progressive increase in ε_{max} for **C** with increasing number of repeat units. Absorption spectra recorded for the reference compounds **B-C$_n$-TES** in MTHF show the same behaviour but with the absence of the **DPP** peak (Figure 3). It is notable that adding the **DPP** chromophore does not affect the properties of **B**, a finding that confirms the absence of electronic interaction between the terminals. Fluorescence spectra (Figure 4) recorded for **B-C$_n$-DPP** in MTHF after illumination into the **DPP** donor at 490 nm show emission bands characteristic of **B**[63,64] (λ_{flu} = 662 nm) and **DPP**[65,66] (λ_{flu} = 570 nm). The blue dye can be excited selectively at 620 nm while the optimal excitation wavelength for **DPP** is 490 nm, where **B** absorbs ca. 5% of incident photons. No

fluorescence is observed from **C** following excitation at 300 nm. Throughout this work, comparison is made to control compounds for both **DPP** and **B**.[67]

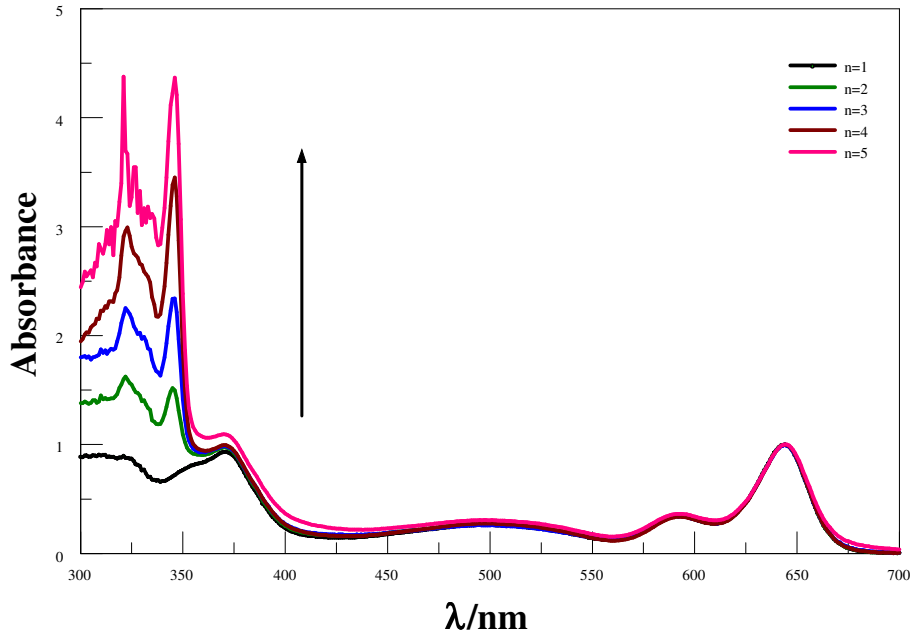

Figure 2. Recorded absorption spectra for **B-C$_n$-DPP** in MTHF at room temperature. The spectra are normalized at the lowest-energy peak for **B**. The arrow indicates increasing molecular length.

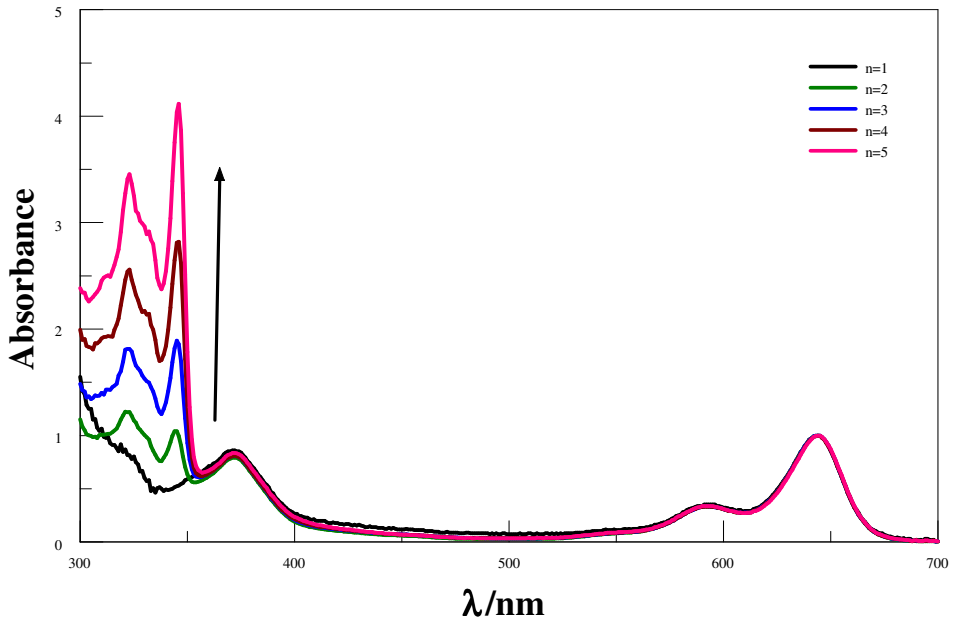

Figure 3. Recorded absorption spectra for **B-C$_n$-TES** in MTHF at room temperature. The spectra are normalized as above for **B.** The arrow indicates increasing molecular length.

Fluorescence quantum yields (Φ_{flu}) and excited-singlet state lifetimes (τ_s) recorded for the **B** and **DPP** units present in the assembled dyads were compared with those recorded for the isolated control compounds in MTHF at room temperature. The main results are listed in Table 1. In each case, direct excitation into **B** gives fluorescence characteristic of that unit with Φ_{flu} and τ_s being essentially unperturbed

relative to those of the relevant control compound. In contrast, preferential excitation into **DPP** gives a mixture of fluorescence characteristic of **DPP** and **B**, which can be deconstructed spectrally to allow calculation of the individual Φ_{flu} and τ_s values.

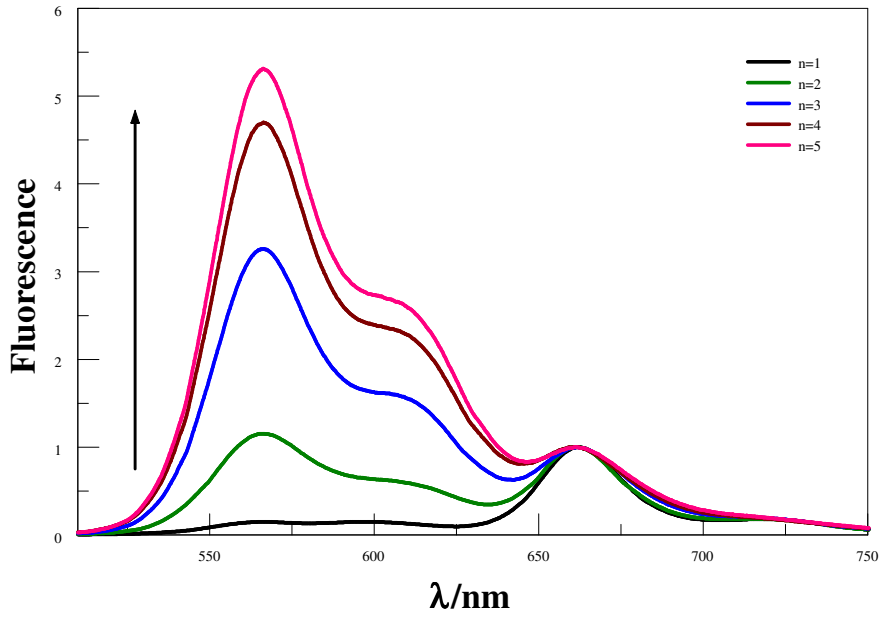

Figure 4. Fluorescence spectra recorded for the **B-C$_n$-DPP** compounds in MTHF at room temperature following selective excitation into **DPP.** The spectra are normalized at the peak of **B.** The arrow indicates the direction of increasing molecular length.

Table 1. Selected photophysical properties recorded for the compounds in MTHF at room temperature. [(a)] photophysical data refer to the **DPP** unit following excitation at 490nm. [(b)] Photophysical data refer to the **B** unit following excitation at 590 nm. The standard uncertainty for Φ_{flu} and τ_s are ±5% and ±10%, respectively.

Compound	Φ_{flu} [(a)]	τ_s /ns[(a)]	Φ_{flu} [(b)]	τ_s /ns[(b)]
B-C$_1$-DPP	0.096	0.49	0.55	4.3
B-C$_2$-DPP	0.44	2.48	0.55	4.3
B-C$_3$-DPP	0.73	4.18	0.52	4.2
B-C$_4$-DPP	0.81	4.65	0.56	4.4
B-C$_5$-DPP	0.84	4.75	0.54	4.3
B-C$_1$-TES	NA	NA	0.56	4.2
DPP	0.87	4.85	NA	NA

It is seen that, in each case, emission from **DPP** is decreased relative to that recorded for the control compound under identical conditions (taking due account of the 5% photon loss) while emission from **B** is increased compared to what could be expected on account of the respective absorption spectral profiles. This feature was confirmed by comparison to an equi-molar mixture of **DPP** and **B** in MTHF. The disparity in Φ_{flu} and τ_s values measured for dyad and control compound in the equi-molar mixture increases markedly as the molecular length decreases but becomes

difficult to assess with real accuracy for the longest dyad. Indeed, it is more meaningful, at least for the longer analogues, to report the ratio (R_{DA}) of deconstructed Φ_{flu} values measured for **DPP** relative to **B**. There is acceptable agreement between the variation in Φ_{flu} and τ_s values along the series, while the time-resolved emission decay curves are well described in terms of mono-exponential fits in each case. Excitation spectra (Figure 5) confirm that quenching of donor emission is due to intramolecular EET from **DPP** to **B** under these conditions. The photophysical properties of the acceptor moiety are unaffected by the presence of the donor while the large energy gap between donor and acceptor excited-singlet states (ΔE_{SS} = 2,400 cm^{-1}) points to unidirectional EET. Rate constants (k_{EET}) and probabilities (P_{EET}) for this step, as derived from the steady-state yields and time-resolved decay profiles by applying Equations (1) and (2) are collected in Table 2. The two sets of data are in good agreement, as are the P_{EET} values determined from the ratio (R_{DA}), the donor lifetimes or the fluorescence quantum yields (Eqns. 3, 4, 5). For the sake of consistency throughout the different sets of experimental results to follow, we have opted to rely on these latter P_{EET} values, which are seen to decrease with increasing molecular length (Table 2).

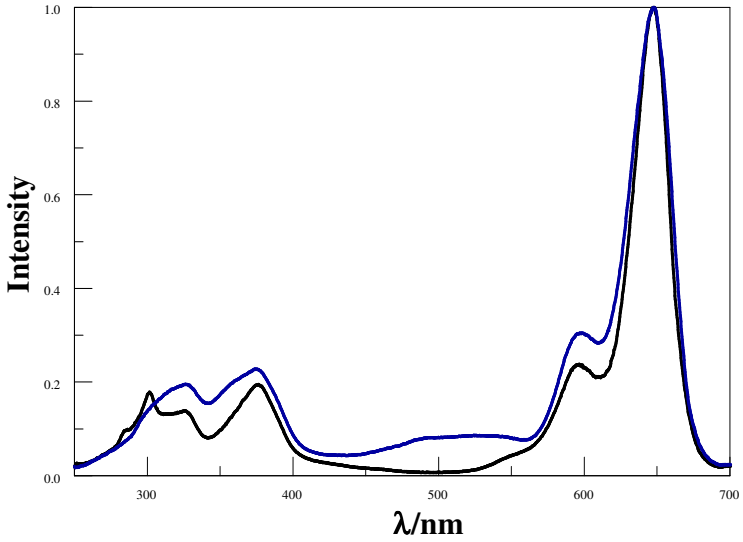

Figure 5. Normalized excitation spectra for **B-C_1-TES** (black) and **B-C_1-DPP** (blue) in MTHF at room temperature. The emission wavelength is 725 nm.

$$k_{EET} = \frac{9000(ln10)K^2\Phi_D}{128\pi^5 n^4 N d_{EFF}^6} J_{DA} \qquad \text{Equation (1)}$$

$$P_{EET} = \frac{D_{CD}^6}{D_{CD}^6 + d_{EFF}^6} \qquad \text{Equation (2)}$$

$$P_{EET} = \left(\frac{0.95\Phi_D - 0.05R_{DA}\Phi_A}{R_{DA}\Phi_A + \Phi_D}\right)/0.95 \qquad \text{Equation (3)}$$

$$P_{EET} = 1 - \frac{\tau_{DA}}{\tau_D} \qquad \text{Equation (4)}$$

$$P_{EET} = 1 - \frac{\Phi_{DA}}{\Phi_D} \qquad \text{Equation (5)}$$

Here J_{DA} is the spectral overlap integral between the donor emission and acceptor absorption, K is the orientation factor, Φ_D and τ_D are the fluorescence quantum yield and lifetime, respectively, of the isolated donor (D) while Φ_{DA} and τ_{DA} are similar parameters for the donor in presence of acceptor (A). Here, 0.95 and 0.05 are the percentage of absorbed photons at the excitation wavelength (490 nm) for the donor (**DPP**) and the acceptor (**B**), respectively.

Table 2. Derived parameters relating to fluorescence quenching in the various dyads as a consequence of EET in MTHF at room temperature. [(a)]Probability of EET calculated on the basis of the IDA and Förster theory (Eqn.2). [(b)]Calculated from the measured R_{DA} values (Eqn.3). [(c)] Calculated from the measured lifetime values (Eqn.4). [(d)] Calculated from the experimental fluorescence quantum yields (Eqn.5). [(e)] Calculated on the basis that IDA is valid for these molecular dyads.

Compound	D_{CC}/Å	$P_{EET}^{(a)}$	$P_{EET}^{(b)}$	$P_{EET}^{(c)}$	$P_{EET}^{(d)}$	$k_{EET}/10^7 s^{-1}$	$d_{EFF}^{(b,e)}$/Å
B-C_1-DPP	38	0.90	0.910	0.90	0.89	205	37
B-C_2-DPP	57	0.43	0.485	0.49	0.48	19	55
B-C_3-DPP	76	0.12	0.166	0.14	0.16	4.1	71
B-C_4-DPP	96	0.032	0.064	0.060	0.073	1.4	85
B-C_5-DPP	115	0.011	0.020	0.022	0.025	0.42	104

The critical molecular dimensions were assessed by quantum chemical computations that confirm the fully extended conformations to be the lowest-energy species in each case. In particular, the distances (D_{CC}) between the centres of the terminal fluorophores for the energy-minimised structures are listed in Table 2. For the isolated control compounds, the Förster critical distance[68,69] (D_{CD}) is estimated to be 54.4 Å for MTHF at room temperature on the basis of the ideal dipole approximation (IDA) being valid for these reactants by using Equation (6). Now, the effective separation distance (d_{EFF}) between the centres of the reactants can be obtained from Equation (2) and the derived values are given in Table 2. It is apparent that the probability of Förster-style EET is somewhat higher than expected at the longer separations, although it has to be realised that the experimental uncertainty increases with decreasing extent of fluorescence quenching. Nonetheless, all three estimates of P_{EET} indicate that the effective separation distance is less than that predicted for the fully extended geometries, except for n = 1. These fluorescence experiments were repeated as a function of concentration in order to eliminate any effects due to intermolecular EET, which could be a particular problem for the longer bridges where solubility is limited and neighbouring molecules are necessarily in close contact at

modest concentration. However, a 20-fold dilution (from an initial concentration of 2 μM) had no obvious effect on the results.

$$D_{CD}^{6} = 5.86 \times 10^{-25} \frac{\Phi_D}{n^4} J_{DA} \qquad \text{Equation (6)}$$

It can be seen that the IDA allows rather good estimation of the molecular length (i.e., d_{EFF} = 37 Å compared to D_{CC} = 38 Å) for the shortest bridge, thereby confirming an earlier report[62] relating to EET across the same bridge but with different terminals. As the molecular length increases, however, d_{EFF} becomes progressively shorter than D_{CC} (Table 2). There are, in fact, several reports[70,71] in the scientific literature to indicate that the reliability of the IDA depends on the distance separating the reactants. Normally it is considered that Förster theory works well at large separations but becomes suspect when the distance between the reactants is comparable to the sum of the lengths of the transition dipole moment vectors. The carborane-based system, which spans an unusually wide variation in separation distance, appears to behave in the opposite sense! The most likely cause of this effect is that the molecular bridges are susceptible to out-of-plane bending that provides access to molecules with decreased D_{CC}.

4.5 Effect of low temperature

It has been demonstrated experimentally that the bending rigidity of molecular surfaces is temperature dependent.[72] We might expect similar behaviour for the carborane-bridged molecular dyads under investigation here. As such, fluorescence spectra were recorded in MTHF as a function of temperature. On cooling the solution (Figure 6), the emission maxima recorded for **DPP** and **B** undergo modest red shifts due to the temperature-induced change in polarizability of MTHF.[73] This effect is more pronounced for **B** than for **DPP** because of the increased charge-transfer character inherent to the former chromophore. As a consequence, there is a progressive decrease in the spectral overlap integral associated with intramolecular EET from **DPP** to **B**, but this remains a small effect for fluid solution. On approaching the freezing point of MTHF (i.e., 140K), the emission maximum observed for **B** continues to be red shifted but that for **DPP** undergoes a blue shift. This reversal in the hypsochromicity has a marked effect on the spectral overlap integral in the frozen state, which is reduced with decreasing temperature. Lowering the temperature also causes a significant increase in the solvent refractive index,[74] which is also a factor involved in controlling k_{EET}. These

various changes combine to affect the magnitude of the Förster critical distance, which falls from 54.4 Å at room temperature to 52.8 Å at 77K.

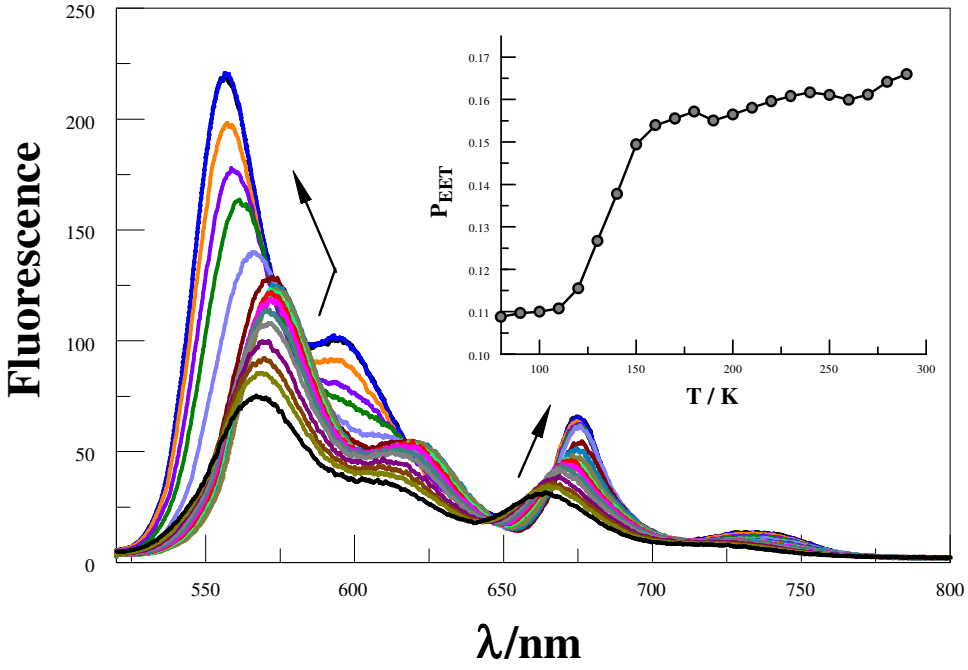

Figure 6. Effect of temperature on the emission spectrum recorded for **B-C_3-DPP** in MTHF following excitation into **DPP**. The temperature ranges from 293 to 77K while the overall intensity increases steadily with decreasing temperature. The arrows indicate the direction of decreasing temperature. The insert shows the temperature effect on the EET probability for the same system.

Apart from the above-mentioned spectral shifts, lowering the temperature also affects the relative ratio of the areas of the two emission bands following preferential excitation into **DPP**. Indeed, R_{DA} tends to increase in favour of emission from **DPP** as the temperature decreases. Consequently, as shown in Figure 7, there is a progressive decrease in P_{EET} on lowering the temperature. The longest bridge, n = 5, suffers from limited solubility at low temperature and, in this case, the results should be treated cautiously. The shortest analogue, n = 1, is insensitive to temperature; P_{EET} falls from 91% at room temperature to 88% at 77K (Table 3). On the basis of EET occurring via

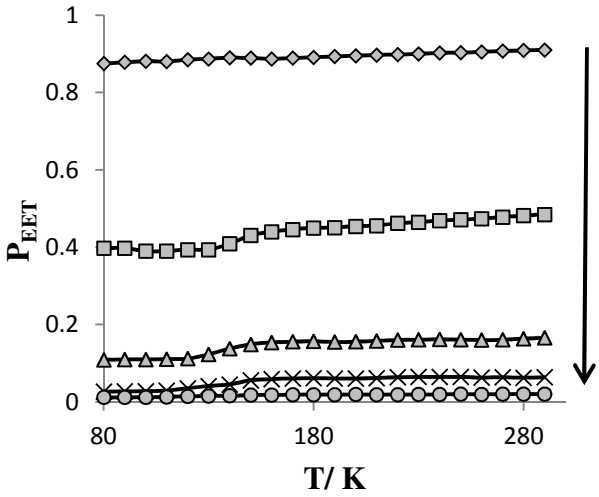

Figure 7. Effect of temperature on the EET probability for each of the dyads in MTHF. The arrow indicates the direction of increasing molecular length (140K is the melting point of MTHF).

the Förster IDA mechanism, this drop in efficacy could be explained in terms of d_{EFF} increasing from 37Å at room temperature to 38Å at 77K. The longer bridges display more significant temperature effects in respect of their P_{EET} values, before approaching a near constant value in the glass at around 100K (Table 3). One possible explanation for this behaviour is that the average separation distance increases as the temperature falls, perhaps reaching the fully extended conformation in the glassy matrix. We return to this point later in the chapter.

Table 3. EET probability and the effective distance associated with the molecular dyads in glassy MTHF. [(a)] P_{EET} measured at 77K using R_{DA} values (Eqn.3). [(b)] Centre-to-centre distance at 77K as calculated from the IDA (Eqn.2).

Compound	P_{EET} [(a)]	d_{77}/Å [(b)]
B-C_1-DPP	0.88	38
B-C_2-DPP	0.40	56.5
B-C_3-DPP	0.11	75
B-C_4-DPP	0.027	96
B-C_5-DPP	0.012	110

4.6 Effect of applied pressure

In this experiment, emission spectra were recorded for the various dyads in MTHF at 20 °C as a function of increasing pressure. It is known[75] that pressure raises the density of the solvent and has a small effect on the polarizability of MTHF. This latter effect causes a slight red shift for the fluorescence maxima of both emitters (Figure 8) but the spectral overlap term does not change significantly at pressures below 550 MPa. These spectral shifts are independent of molecular length. Close scrutiny of these latter results indicates that both **DPP** and **B** undergo red shifts of ca. 350 cm^{-1} over the full pressure range; the shift increasing in an almost linear manner with applied pressure.[73] In each case, the original fluorescence profile is restored on release of the pressure.

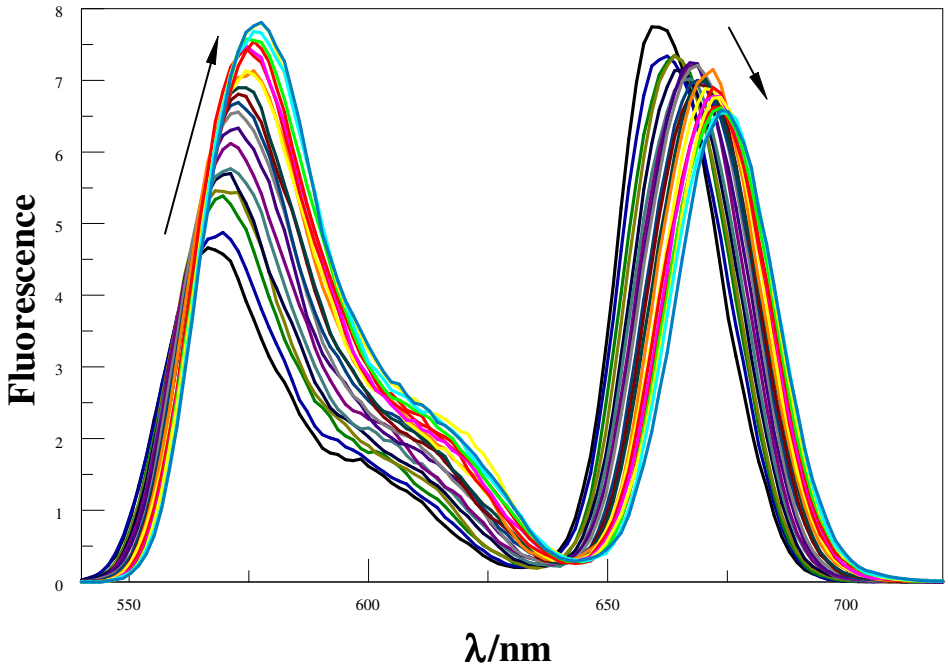

Figure 8. Effect of applied pressure on the fluorescence spectrum recorded for **B-C_2-DPP** in MTHF at room temperature. The pressure increases systematically in the direction of the arrows.

On applying pressure to a solution of the carborane-bridged molecular dyads in MTHF at 293K there is a progressive increase in emission from **DPP** and a concomitant decrease in fluorescence from **B** (Figure 8). As such, we can conclude that the mean P_{EET} decreases under pressure. The origin of this effect can be traced to several factors; the best way to correct for these factors is to focus on the coulombic coupling matrix element V_{DA} rather than simply comparing P_{EET} values. This particular term can be determined from Equation (7) where J_{DA} is the spectral overlap integral and s is the solvent screening factor computed from Equation (8). Now, increased pressure causes a small reduction in J_{DA} and a minor change in absorbance at the excitation wavelength due to compression of the solvent.[75] Such corrections are trivial, however, and change the derived V_{DA} values by less than 5%. Elevated pressure also serves to increase the refractive index of MTHF,[75] which affects the magnitude of P_{EET} by way of altering s. This requires a more significant correction. Indeed, after taking due account of the pressure-induced decrease in s, it becomes clear that increasing pressure causes V_{DA} to increase steadily, regardless of the length of the connection. The rise in V_{DA} is of the order of 6, 20, 21, 13 and 8% for n = 1, 2, 3, 4 and 5, respectively, as measured over the full pressure range. In each case, the rate of change of V_{DA} with pressure is almost linear and does not tend towards a plateau (Figure 9). Having applied the obvious correction factors, the most reasonable explanation of these results is that high pressure causes the bridge to contract so as to bring the terminals into closer proximity (*vide infra*).

The IDA model [69,70] allows the derived V_{DA} terms to be converted into d_{EFF} values on the basis of Equation (9). Here, μ_D (μ_A) is the transition dipole moment of the donor (acceptor), as determined[76,77] from absorption spectroscopy in MTHF at that pressure (Eqn. 10). In fact, pressure has only a minor effect on these latter values. The available data can be interpreted in terms of the molecular length contracting steadily with increasing pressure, with the significance of the effect increasing with the length of the bridge. For example, the shortest bridge is not much affected by applied pressure and undergoes a minor contraction of ca. 1.6 Å. In contrast, n = 4 shows the largest contraction of 6.2 Å over the same pressure range.

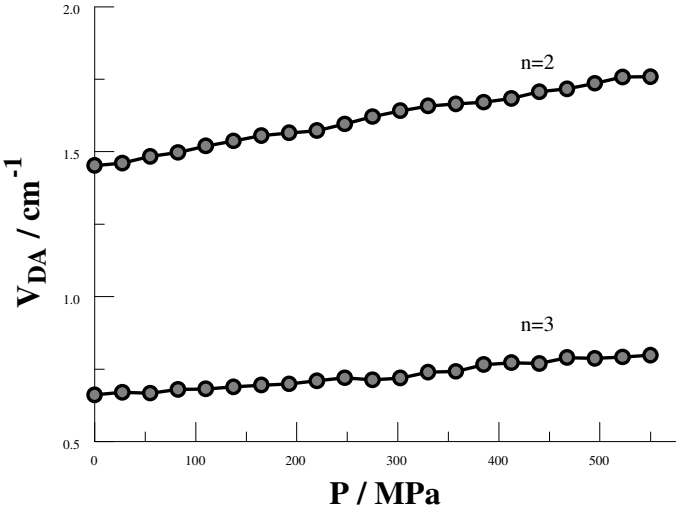

Figure 9. Effect of applied pressure on the electronic coupling matrix element for EET across the dyad as derived in MTHF at room temperature.

$$k_{EET} = \frac{2\pi}{\hbar}|V_{DA}sK|^2 J_{DA} \qquad \text{Equation (7)}$$

$$s = \frac{3}{2n^2+1} \qquad \text{Equation (8)}$$

$$V_{DA} = \frac{\mu_D \mu_A}{d_{EFF}^3(4\pi\varepsilon_\circ)} \qquad \text{Equation (9)}$$

$$\mu^2 = 9.186 \times 10^{-3} n \int \frac{\varepsilon}{\nu} d\nu \qquad \text{Equation (10)}$$

4.7 Refining the molecular length

With the exception of n = 5, where experimental uncertainty makes the results unreliable, the emission studies can be used to determine the molecular length on the assumption that low temperature favours the fully extended conformation while applied pressure causes the terminals to approach each other. As such, the effective separation distances (d_{77}), calculated at 77K on the basis that the IDA[69,70] holds for this system, are listed in Table 3. Before attempting to rationalise the variations in molecular length associated with temperature or pressure effects it should be noted that there is excellent agreement between d_{77} and D_{CC} for n = 1. It is also important to recognise the possible limitations of the IDA approach at distances less than ca. 50Å.

Many of these problems can be overcome by replacing the IDA with the extended dipole method introduced by Kuhn[78] and applied by other groups.[79] This was not the case here, however, since (essentially) the same values were derived by both methods. The variation of d_{EFF} with temperature has the appearance of two separate effects (Figure 10). Thus, the molecular length is reasonably constant over the temperature range where the solvent is frozen but decreases by a significant amount near the melting point. This ''spring-like'' effect is suggestive of the molecular geometry being somewhat strained in the solid state but becoming more relaxed in the fluid as shown in Chart 1. In each case, the effect occurs at ca. 140K; this is not the glass transition temperature, believed to be around 90–110K, but is in agreement with estimates (e.g., 137K)[80] of the melting point of MTHF. The magnitude of this strain, S_T, can be computed from Equation (11) and, apart from n = 5, is seen to increase with increasing molecular length (Table 4).

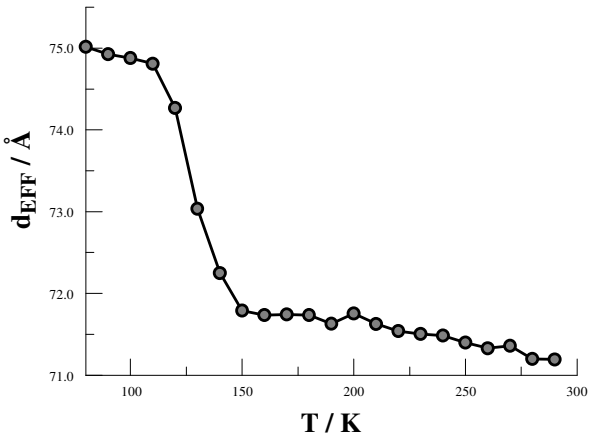

Figure 10. Effect of temperature on the effective molecular length for n=3 in MTHF.

In principle, the strain energy per carborane, U_S/n, can be calculated from Equation (12) on the basis of elastic behaviour but this requires knowledge of the spring constant, K, associated with the geometry relaxation at each carborane unit. We have no information on this latter term but, from comparison of the total strain energy (i.e., the product of U_S and n), it appears that it is not constant across the series. Rather, ΔL increases as the bridge becomes longer. By partitioning the total strain energy into spring constants related to the carborane-to-terminal units (K_{END}) and to the inter-carborane units (K_{MID}), it becomes clear that the latter are more flexible.

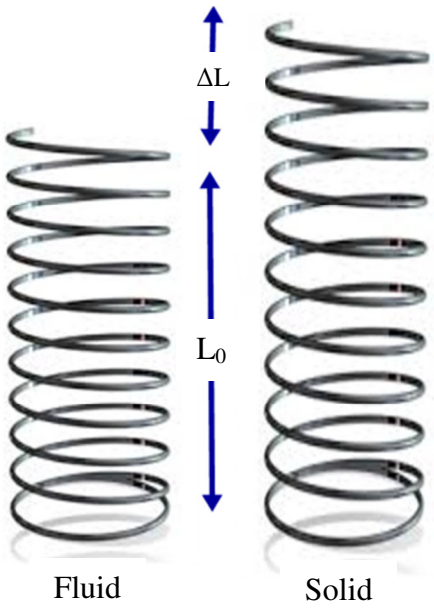

Chart 1. Simple illustration of the elastic behaviour of carborane bridges at different temperatures.

Furthermore, these units act cooperatively to increase the total stretching length (Table 4). In order words, these internal linkages are primarily responsible for the geometry relaxation accompanying melting of the solvent.

$$S_T = \frac{\Delta L}{L_0} \qquad \text{Equation (11)}$$

$$U_S = \frac{K}{2}\left(\frac{\Delta L}{L_0}\right)^2 \qquad \text{Equation (12)}$$

Table 4. Various parameters associated with the molecular dyads in frozen MTHF or as a consequence of melting the solvent at 140K. [(a)] Crude ratio of the spring constant estimated for the "end" and "middle" components of the bridge.

Compound	ΔL/Å	S_T	(U_S/nK)/Å^2	K_{MID} / K_{END} [(a)]
B-C_1-DPP	0.6	0.016	0.18	NA
B-C_2-DPP	1.5	0.027	0.28	3.8
B-C_3-DPP	2.6	0.035	0.38	5.3
B-C_4-DPP	4.0	0.042	0.50	6.8
B-C_5-DPP	4.0	0.036	0.32	3.9

A more gradual contraction is seen as the temperature continues to rise and this is consistent with out-of-plane bending modes that have vibrational transition energies comparable to k_BT.[81] Since the carborane unit is unlikely to distort, compression of the molecular length must be confined to the tolane-like linkages, which are known[82] to distort under ambient conditions (Chart 2). The extent of molecular contraction in the liquid phase as a function of temperature can be considered in terms of Equation (13), which is a modified form of expressions employed to account for the bending rigidity of graphene[72] and related materials.[83,84] Here, L_{LIQ} refers to the projected molecular length in the liquid phase at 0K and F is a parameter that depends on bridge composition and length; F has units equivalent to force such that the product ($W = F \times L_{LIQ}$; $\Delta L_{LIQ} = L_{LIQ} - L$) corresponds to the total amount of work done in bringing about the structural change and this remains surprisingly constant across the series. Expansion of Equation (13) into a Taylor series allows further refinement of F and shows that this term decreases markedly with increasing n (Table 5). As such, we can conclude that the inherent stiffness, and in particular its sensitivity towards changes in temperature, decreases as the bridge gets longer. Similar behaviour[72] has been noted for certain surfactant molecules packed into a lipid membrane.

$$L = L_{LIQ} exp\left(-\frac{k_BT}{FL_{LIQ}}\right) \qquad \text{Equation (13)}$$

Table 5. Derived parameters relating to the temperature dependence for EET in the liquid phase. [(a)] Center-to-center separation distance extrapolated for the liquid phase to 0K as calculated from the IDA. [(b)] Contraction of the molecular length on heating from 0 to 295K in the liquid phase.

compound	L_{LIQ} / Å[(a)]	ΔL /Å[(b)]	F/pN	W/ perg
B-C_1-DPP	38.1	1.2	33.4	0.040
B-C_2-DPP	57.1	2.2	18.2	0.040
B-C_3-DPP	75.0	4.8	8.2	0.039
B-C_4-DPP	97.0	10.7	3.6	0.038
B-C_5-DPP	109.6	11.0	3.5	0.039

The same approach can be applied to the pressure effect at ambient temperature (Table 6). From the experimental results highlighted above, it appears that pressure distorts the bridge so as to bring the terminals into closer proximity. It is considered that, under high pressure, the terminals are locked into the contracted geometry – as opposed to sampling a wide distribution of molecular lengths as might be expected at atmospheric pressure.[85] Other studies have shown that the photophysical properties of the **DPP** donor are insensitive to applied pressure, at least in MTHF. Using the IDA approach,[69,70] the pressure-induced changes in d_{EFF} (from atmospheric pressure to 550 MPa) are on the order of 1–7 Å and tend to increase progressively with increasing molecular length (Table 6). The driving force for this effect arises from the need to minimise the molecular volume and this is best achieved by compressing the bridge in a "zigzag" fashion (i.e., an accordion- or concertina-type compression).

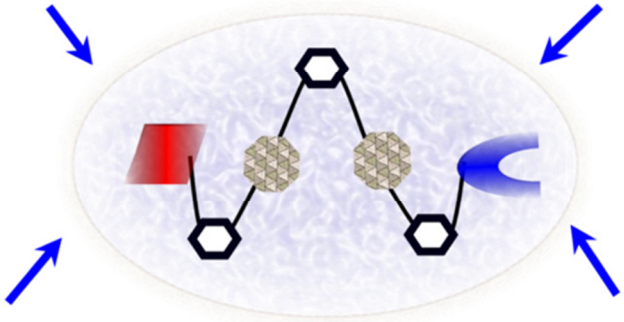

Chart 2. Illustrated picture of out-of-plane bending.

Table 6. Summary of the parameters derived from the pressure dependence recorded for the compounds in MTHF solution at room temperature. [(a)] Length contraction measured over the full pressure range from atmospheric pressure to an applied pressure of 550 MPa. [(b)] Radius derived from the cross-sectional area assuming the latter is circular.

Compound	L_p/ Å	ΔL/Å[(a)]	E/GPa	R_C/ Å[(b)]
B-C_1-DPP	37.0	1.6	12.48	1.4
B-C_2-DPP	55.4	3.5	8.52	1.0
B-C_3-DPP	72.8	4.7	8.34	0.7
B-C_4-DPP	84.8	6.2	7.42	0.5
B-C_5-DPP	105.0	4.7	12.05	0.5

Applied pressure causes stress on the molecule; stress is normally considered as being "force per unit area" and has the same units as pressure. It can also be described in terms of the Young's modulus, *E*, of the compressible material,[86,87] although the relationship is often nonlinear.[88] For the various dyads studied here, the isothermal compressibility data are well accounted for by Equation (14) where L_P is the molecular length at atmospheric pressure; again the significance of n = 5 is marginal because of experimental limitations. Now, we see that the Young's modulus for a carborane bridge is estimated as being on the order of ca. 10 GPa but that the actual value decreases somewhat with increasing length of the bridge (Table 6). This is clear indication that longer bridges are more amenable to longitudinal distortion under pressure. There is also a significant increase in bulk viscosity of MTHF over this pressure range[75] and this is likely to minimize large fluctuations in d_{EFF}. Information on how applied pressure affects the length of semi-rigid molecules, in contrast to flexible polymers,[89,90] is scarce but recent work serves to illustrate that large-scale torsional motions are dampened at high pressure.[75] We are unaware of any prior attempts to record *E* for organic-based molecular bridges, although an *E* value of ca. 130 GPa has been reported[84] for β-SiC nanowires. This same work reports that *E* increases with decreasing temperature, which is the same general trend as observed in our work.

$$\frac{\Delta L}{L_P} = \frac{P}{E} \qquad \text{Equation (14)}$$

These results can be tested for self-consistency by reference to the fact that Young's modulus can be expressed in terms of stress divided by strain. This leads to Equation (15) where the force, *F*, is taken from the temperature-dependent studies described earlier and *A* is the cross-sectional area of the contractor. Taking the latter as a circle, the radius of the contractor, R_C, can be estimated from the experimental data (Table 6). It appears that this term has the appropriate dimensions (i.e., R_C = 0.86 Å) for a nanowire as might be formed from the carborane bridge.

$$E = \frac{stress}{strain} = \frac{FL_P}{A(\Delta L)} \qquad \text{Equation (15)}$$

4.8 Conclusion

Molecular surfaces, often represented as flat and smooth plates of well-defined area, appear curved or distorted under closer scrutiny. Such behaviour has been recognised for graphene,[91] where curvature is a prerequisite for formation of carbon nanotubes, and

for lipid bilayers.[92] In the latter case, X-ray scattering[93,94] shows severe bumps and crevices in the surface. It follows that long, linear molecules will also distort in solution at ambient temperature and pressure. This is certainly the case for duplex DNA[95,96] and for conjugated polymers,[97] where the importance of cooperative domains has been stressed. Other supposedly rigid, rod-like molecules can distort to such a degree that their orientation in solution might differ dramatically from that of the fully extended species. Molecular dynamic simulations[98] offer a means by which to inspect possible torsional motions but do not provide experimental support for a dynamic molecular topology. High-field NMR spectroscopy can give meaningful structural information about molecular rigidity in solution[82] but is time consuming and requires careful calibration. Here, we apply fluorescence spectroscopy to probe the effective length of ''stiff'' molecular dyads equipped with terminal fluorophores. It has been shown that, in the extreme case, a molecular dyad with an extended molecular length of ca. 85Å contracts by as much as 6Å under applied pressure at ambient temperature. There is a corresponding extension of ca. 10Å on cooling to 0K. A direct consequence of this situation is that the probability of EET between terminal groups depends markedly on the local environment even for seemingly rigid bridges.

The molecular dyads examined in this chapter have the crude appearance of plate-like terminals separated by a semi-rigid cylindrical rod (Chart 3) and such topologies might be particularly sensitive to pressure effects. Indeed, we consider the overall pressure and temperature effects in terms of force applied to the flat terminals causing structural distortion (i.e., compression) at the centre of the connector. An interesting feature to emerge from our analysis is that the carborane-based linkages comprising the connector act in a cooperative manner. Thus, the carborane-terminal linkages are robust and possess relatively small spring constants. The carborane–carborane connections, however, take up more strain and the corresponding spring constant increases with increasing number of accreted units. As such, the amount of work needed to compress the molecule decreases substantially with increasing number of carboranes. This might be an important finding but we have no literature comparisons by which to test the generality of our ideas.

Chart 3. Imaginary design for the system under study in this chapter.

4.9 References

1. Ulrich, G.; Ziessel, R.; Harriman, A. *Angew. Chem. Int. Ed.* **2008**, *47*, 1184.
2. Loudet, A.; Burgess, K. *Chem. Rev.* **2007**, *107*, 4891.
3. Boens, N.; Leen, V.; Dehaen, W. *Chem. Soc. Rev.* **2012**, *41*, 1130.
4. Ziessel, R.; Retailleau, P.; Elliott, K. J.; Harriman, A. *Chem. - Eur. J.* **2009**, *15*, 10369.
5. Hablot, D.; Retailleau, P.; Ziessel, R. *Chem. - Eur. J.* **2010**, *16*, 13346.
6. Blankenship, R. E. *Molecular Mechanism of Photosynthesis*; Blackwell Science: Oxford, 2002.
7. Sancar, A. *Chem. Rev.* **2003**, *103*, 2203.
8. Brettel, K.; Byrdin, M. *Curr. Opin. Struct. Biol.* **2010**, *20*, 693.
9. Hong, K.; Lee, J.-L. *Electron. Mater. Lett.* **2011**, *7*, 77.
10. Dexter, D. L. *J. Chem. Phys.* **1953**, *21*, 836.
11. Forster, T. *Disc. Faraday Soc.* **1959**, *27*, 7.
12. Jang, S.; Newton, M. D.; Silbey, R. J. *Phys. Rev. Lett.* **2004**, *92*, 218301.
13. Sumi, H. *J. Phys. Chem. B* **1998**, *103*, 252.
14. Beljonne, D.; Curutchet, C.; Scholes, G. D.; Silbey, R. J. *J. Phys. Chem. B* **2009**, *113*, 6583.
15. Fückel, B.; Köhn, A.; Harding, M. E.; Diezemann, G.; Hinze, G.; Basché, T.; Gauss, J. *J. Chem. Phys.* **2008**, *128*.
16. Seth, J.; Palaniappan, V.; Johnson, T. E.; Prathapan, S.; Lindsey, J. S.; Bocian, D. F. *J. Am. Chem. Soc.* **1994**, *116*, 10578.
17. Kilså, K.; Kajanus, J.; Mårtensson, J.; Albinsson, B. *J. Phys. Chem. B* **1999**, *103*, 7329.
18. Eng, M. P.; Albinsson, B. *Angew. Chem. Int. Ed.* **2006**, *45*, 5626.
19. May, V. *Dalton Trans.* **2009**, 10086.
20. Schlicke, B.; Belser, P.; De Cola, L.; Sabbioni, E.; Balzani, V. *J. Am. Chem. Soc.* **1999**, *121*, 4207.
21. Lammi, R. K.; Wagner, R. W.; Ambroise, A.; Diers, J. R.; Bocian, D. F.; Holten, D.; Lindsey, J. S. *J. Phys. Chem. B* **2001**, *105*, 5341.
22. Guldi, D. M. *Chem. Soc. Rev.* **2002**, *31*, 22.
23. Harriman, A.; Ziessel, R. *Chem. Commun.* **1996**, 1707.
24. Schwartz, B. J. *Annu. Rev. Phys. Chem.* **2003**, *54*, 141.
25. Collini, E.; Scholes, G. D. *Science* **2009**, *323*, 369.

26. Hennebicq, E.; Beljonne, D.; Curutchet, C.; Scholes, G. D.; Silbey, R. J. *J. Chem. Phys.* **2009**, *130,* 214505.
27. Sahoo, H.; Roccatano, D.; Hennig, A.; Nau, W. M. *J. Am. Chem. Soc.* **2007**, *129*, 9762.
28. Schuler, B.; Lipman, E. A.; Steinbach, P. J.; Kumke, M.; Eaton, W. A. *Proc. Natl. Acad. Sci. U.S.A.* **2005**, *102*, 2754.
29. VanBeek, D. B.; Zwier, M. C.; Shorb, J. M.; Krueger, B. P. *Biophys. J.* **2007**, *92*, 4168.
30. Li, F.; Yang, S. I.; Ciringh, Y.; Seth, J.; Martin, C. H.; Singh, D. L.; Kim, D.; Birge, R. R.; Bocian, D. F.; Holten, D.; Lindsey, J. S. *J. Am. Chem. Soc.* **1998**, *120*, 10001.
31. Wong, K. F.; Bagchi, B.; Rossky, P. J. *J. Phys. Chem. A* **2004**, *108*, 5752.
32. Dolan, P. M.; Miller, D.; Cogdell, R. J.; Birge, R. R.; Frank, H. A. *J. Phys. Chem. B* **2001**, *105*, 12134.
33. Harriman, A.; Mallon, L.; Ziessel, R. *Chem. - Eur. J.* **2008**, *14*, 11461.
34. Curutchet, C.; Scholes, G. D.; Mennucci, B.; Cammi, R. *J. Phys. Chem. B* **2007**, *111*, 13253.
35. Scholes, G. D.; Curutchet, C.; Mennucci, B.; Cammi, R.; Tomasi, J. *J. Phys. Chem. B* **2007**, *111*, 6978.
36. Challacombe, M.; Schwegler, E.; Almlöf, J. *Chem. Phys. Lett.* **1995**, *241*, 67.
37. Dale, R. E.; Eisinger, J.; Blumberg, W. E. *Biophys. J.* **1979**, *26*, 161.
38. Mårtensson, J. *Chem. Phys. Lett.* **1994**, *229*, 449.
39. Lu, H.; Schöps, O.; Woggon, U.; Niemeyer, C. M. *J. Am. Chem. Soc.* **2008**, *130*, 4815.
40. Zhang, J.; Fu, Y.; Chowdhury, M. H.; Lakowicz, J. R. *J. Phys. Chem. C* **2007**, *111*, 11784.
41. Sapsford, K. E.; Berti, L.; Medintz, I. L. *Angew. Chem. Int. Ed.* **2006**, *45*, 4562.
42. Wilson, M. C.; Meredith, D.; Halestrap, A. P. *J. Biol. Chem.* **2002**, *277*, 3666.
43. Balzani, V.; Juris, A. *Coord. Chem. Rev.* **2001**, *211*, 97.
44. Gösele, U. *Chem. Phys. Lett.* **1976**, *43*, 61.
45. Brouillette, C. G.; Dong, W. J.; Yang, Z. W.; Ray, M. J.; Protasevich, II; Cheung, H. C.; Engler, J. A. *Biochem.* **2005**, *44*, 16413.
46. Karasawa, S.; Araki, T.; Nagai, T.; Mizuno, H.; Miyawaki, A. *Biochem. J.* **2004**, *381*, 307.
47. Brun, A. M.; Harriman, A. *J. Am. Chem. Soc.* **1994**, *116*, 10383.

48. Kumar, C. V.; Asuncion, E. H. *J. Am. Chem. Soc.* **1993**, *115*, 8547.
49. Yun, B. H.; Kim, J.-O.; Lee, B. W.; Lincoln, P.; Nordén, B.; Kim, J.-M.; Kim, S. K. *J. Phys. Chem. B* **2003**, *107*, 9858.
50. Wang, S.; Gaylord, B. S.; Bazan, G. C. *J. Am. Chem. Soc.* **2004**, *126*, 5446.
51. Kuzmenkina, E. V.; Heyes, C. D.; Nienhaus, G. U. *Proc. Natl. Acad. Sci. U.S.A.* **2005**, *102*, 15471.
52. Lee, B.-C.; Zuckermann, R. N.; Dill, K. A. *J. Am. Chem. Soc.* **2005**, *127*, 10999.
53. Makarov, D. E.; Plaxco, K. W. *J. Chem. Phys.* **2009**, *131*, 085105.
54. Kaszynski, P.; Pakhomov, S.; Tesh, K. F.; Young, V. G. *Inorg. Chem.* **2001**, *40*, 6622.
55. Kaszynski, P.; G. Douglass, A. *J. Organomet. Chem.* **1999**, *581*, 28.
56. Fox, M. A.; Wade, K. *J. Mater. Chem.* **2002**, *12*, 1301.
57. Taylor, J.; Caruso, J.; Newlon, A.; Englich, U.; Ruhlandt-Senge, K.; Spencer, J. T. *Inorg. Chem.* **2001**, *40*, 3381.
58. Vicente, J.; Chicote, M.-T.; Alvarez-Falcón, M. M.; Fox, M. A.; Bautista, D. *Organometallics* **2003**, *22*, 4792.
59. Jude, H.; Disteldorf, H.; Fischer, S.; Wedge, T.; Hawkridge, A. M.; Arif, A. M.; Hawthorne, M. F.; Muddiman, D. C.; Stang, P. J. *J. Am. Chem. Soc.* **2005**, *127*, 12131.
60. Williams, R. E. *Chem. Rev.* **1992**, *92*, 177.
61. Plesek, J. *Chem. Rev.* **1992**, *92*, 269.
62. Ziessel, R.; Ulrich, G.; Olivier, J. H.; Bura, T.; Sutter, A. *Chem. Commun.* **2010**, *46*, 7978.
63. Rousseau, T.; Cravino, A.; Bura, T.; Ulrich, G.; Ziessel, R.; Roncali, J. *Chem. Commun.* **2009**, 1673.
64. Olivier, J.-H.; Haefele, A.; Retailleau, P.; Ziessel, R. *Org. Lett.* **2009**, *12*, 408.
65. Bürgi, L.; Turbiez, M.; Pfeiffer, R.; Bienewald, F.; Kirner, H.-J.; Winnewisser, C. *Adv. Mater.* **2008**, *20*, 2217.
66. Tamayo, A. B.; Walker, B.; Nguyen*, T.-Q. *J. Phys. Chem. C* **2008**, *112*, 11545.
67. Hablot, D.; Harriman, A.; Ziessel, R. *Angew. Chem. Int. Ed. Engl.* **2011**, *50*, 7833.
68. Saini, S.; Singh, H.; Bagchi, B. *J Chem Sci* **2006**, *118*, 23.
69. Claudio, G. C.; Bittner, E. R. *J. Phys. Chem. A* **2003**, *107*, 7092.
70. Muñoz-Losa, A.; Curutchet, C.; Krueger, B. P.; Hartsell, L. R.; Mennucci, B. *Biophys. J.* **2009**, *96*, 4779.

71. Dolghih, E.; Ortiz, W.; Kim, S.; Krueger, B. P.; Krause, J. L.; Roitberg, A. E. *J. Phys. Chem. A* **2009**, *113*, 4639.
72. Liu, P.; Zhang, Y. W. *Appl. Phys. Lett.* **2009**, *94,* 231912.
73. Renge, I. *J. Phys. Chem. A* **2000**, *104*, 7452.
74. Zoon, P. D.; Brouwer, A. M. *Photochem. Photobiol. Sci.* **2009**, *8*, 345.
75. Alamiry, M. A. H.; Hagon, J. P.; Harriman, A.; Bura, T.; Ziessel, R. *Chem. Sci.* **2012**, *3*, 1041.
76. Andersson, P. O.; Gillbro, T.; Ferguson, L.; Cogdell, R. J. *Photochem. Photobiol.* **1991**, *54*, 353.
77. Knox, R. S.; van Amerongen, H. *J. Phys. Chem. B* **2002**, *106*, 5289.
78. Czikklely, V.; Forsterling, H. D.; Kuhn, H. *Chem. Phys. Lett.* **1970**, *6*, 207.
79. Markovitsi, D.; Marguet, S.; Gallos, L. K.; Sigal, H.; Millié, P.; Argyrakis, P.; Ringsdorf, H.; Kumar, S. *Chem. Phys. Lett.* **1999**, *306*, 163.
80. Zimdars, D.; Tokmakoff, A.; Chen, S.; Greenfield, S. R.; Fayer, M. D.; Smith, T. I.; Schwettman, H. A. *Phys. Rev. Lett.* **1993**, *70*, 2718.
81. Tsuda, Y.; Yasutake, H.; Ishijima, A.; Yanagida, T. *Proc. Natl. Acad. Sci.* **1996**, *93*, 12937.
82. Bothner-By, A. A.; Dadok, J.; Johnson, T. E.; Lindsey, J. S. *J. Phys. Chem.* **1996**, *100*, 17551.
83. Kurtisovski, E.; Taulier, N.; Ober, R.; Waks, M.; Urbach, W. *Phys. Rev. Lett.* **2007**, *98*, 258103.
84. Kim, T. Y.; Han, S. S.; Lee, H. M. *Mater. Trans.* **2004**, *45*, 1442.
85. Badali, D.; Gradinaru, C. C. *J. Chem. Phys.* **2011**, *134*.
86. Dobrynin, A. V.; Carrillo, J.-M. Y.; Rubinstein, M. *Macromol.* **2010**, *43*, 9181.
87. Strick, T. R.; Allemand, J. F.; Bensimon, D.; Bensimon, A.; Croquette, V. *Science* **1996**, *271*, 1835.
88. Schwarzer, N. *Philos. Mag.* **2012**, *92*, 1631.
89. Casalini, R.; Roland, C. M. *Macromol.* **2005**, *38*, 1779.
90. Liu, J.; Wu, S.; Cao, D.; Zhang, L. *J. Chem. Phys.* **2008**, *129,*154905.
91. Frank, O.; Tsoukleri, G.; Parthenios, J.; Papagelis, K.; Riaz, I.; Jalil, R.; Novoselov, K. S.; Galiotis, C. *ACS Nano* **2010**, *4*, 3131.
92. Unwin, N. *J. Mol. Biol.* **1993**, *229*, 1101.
93. Rawicz, W.; Olbrich, K. C.; McIntosh, T.; Needham, D.; Evans, E. *Biophys. J.* **2000**, *79*, 328.
94. Fuller, N.; Rand, R. P. *Biophys. J.* **2001**, *81*, 243.

95. Smith, S. B.; Finzi, L.; Bustamante, C. *Science* **1992**, *258*, 1122.
96. Strauss, J. K.; Maher, L. J. *Science* **1994**, *266*, 1829.
97. Smela, E.; Inganäs, O.; Lundström, I. *Science* **1995**, *268*, 1735.
98. Fernandez-Alberti, S.; Kleiman, V. D.; Tretiak, S.; Roitberg, A. E. *J. Phys. Chem. A* **2009**, *113*, 7535.

Chapter 5. Intramolecular electronic energy transfer in a Bodipy-terminated molecular triad

5.1 Executive summary

A new molecular triad, constructed from a soluble diketopyrrolopyrrole (**DPP**) unit linked to two disparate boron dipyrromethene (Bodipy) fluorophores, has been subjected to photophysical examination. The terminal Bodipy dyes differ by virtue of the strength of the donor group situated at the outer periphery of the conjugated pathway, which causes a marked variation in colour, this varying from blue (**B**) to green (**G**), with the latter dye being susceptible to protonation. In the symmetrical dyes **B(DPP)B** and **G(DPP)G**, the photophysical properties of the Bodipy dyes remain closely comparable to those of the isolated terminals, confirming that each module remains electronically isolated. However, illumination into the **DPP** unit results in almost quantitative intramolecular electronic energy transfer (EET) to the terminal Bodipy. Due to more favourable spectral overlap, EET occurs preferentially from **DPP** to the blue Bodipy dye (k_{EET} = 11.5 x 10^{11} s^{-1}), followed by long-range EET from the blue dye to the green subunit (k_{EET} = 1.2 x 10^{10} s^{-1}). Protonation of the green Bodipy dye increases the spectral overlap term and switches the direction of EET, first to the protonated dye (k_{EET} = 17.0 x $10^{11}s^{-1}$) and then to the distal blue terminal (k_{EET} = 3.0 x 10^{10} s^{-1}). The EET probability decreases in polar solvent but remains very high (>90%). In addition, EET takes place with high efficacy (99%) in glassy MTHF at 77K but decreases under applied pressure.

5.2 Structure

Figure 1 presents molecular formulae for all the compounds under study in this chapter; where the reference compounds are 1,4-diketo-3,6-diphenylpyrrolo[3,4-c]pyrrole (**DPP**) and the styryl-expanded Bodipy dyes (**B**) and (**G**). In the triad systems, blue (**B**) and green (**G**) Bodipy units are attached to a central **DPP** spacer function so as to expand the absorption spectral window. Included in this work are both the symmetric systems, **B(DPP)B** and **G(DPP)G**, and the asymmetric system **B(DPP)G**. These compounds were supplied by Dr Raymond Ziessel (Université Louis Pasteur, Strasbourg) and were used as received.

5.3 Introduction

Chlorophylls are recognised as being the most popular light-harvesting antennae; in Nature, the various chlorophylls are used to collect and convert solar energy via the well-known photosynthetic process. Chlorophylls absorb light in the blue and red regions but they are poor absorbers in the green region (500-600 nm) since the main absorption peaks appear around 450 and 650 nm, according to the type of chlorophyll substitution pattern, but with little absorption in the region between (Figure 2). The collected energy reappears as fluorescence at around 700 nm but under normal circumstances this excitation energy is transferred to a reaction centre.[1-3] Porphyrin, a synthetic analogue of chlorophyll, has been used to mimic the natural pigments in the form of artificial light harvesters.[4-6] Many imaginative systems have been reported. In seeking to design artificial light-harvesting arrays with advanced functionality, it has to be recognised that robust, synthetically amenable dyes are needed that absorb and emit at desirable wavelengths. In this respect, 4,4-difluoro-4-bora-3a,4a-diaza-s-indacene (Bodipy; the so-called little sister of porphyrin) dyes have been studied extensively.[7-9] The upsurge of interest in this class of dye can be traced to their high absorption coefficients, narrow emission profiles and impressive fluorescence quantum yields.[7-10] Furthermore, they are quite resistant to triplet formation but readily undergo both oxidation and reduction at accessible potentials.

Our attention has also been drawn to 1,4-diketo-3,6-diphenylpyrrolo[3,4-c]pyrrole (**DPP**) as representing a class of brilliant red pigments with exceptional photo- and thermal stability.[11,12] The main attributes of these latter dyes are their ready adaptability in terms of solubility, functionality and absorptivity, and their high fluorescence quantum yields. Indeed, such materials have recently been used in polymeric solar cells,[13-16] field-effect transistors,[17] OLEDs[18] and two-photon absorption

devices.[19,20] These two classes of highly fluorescent dye provide the basic building blocks with which to construct next-generation optical devices as outlined in the following discussion.

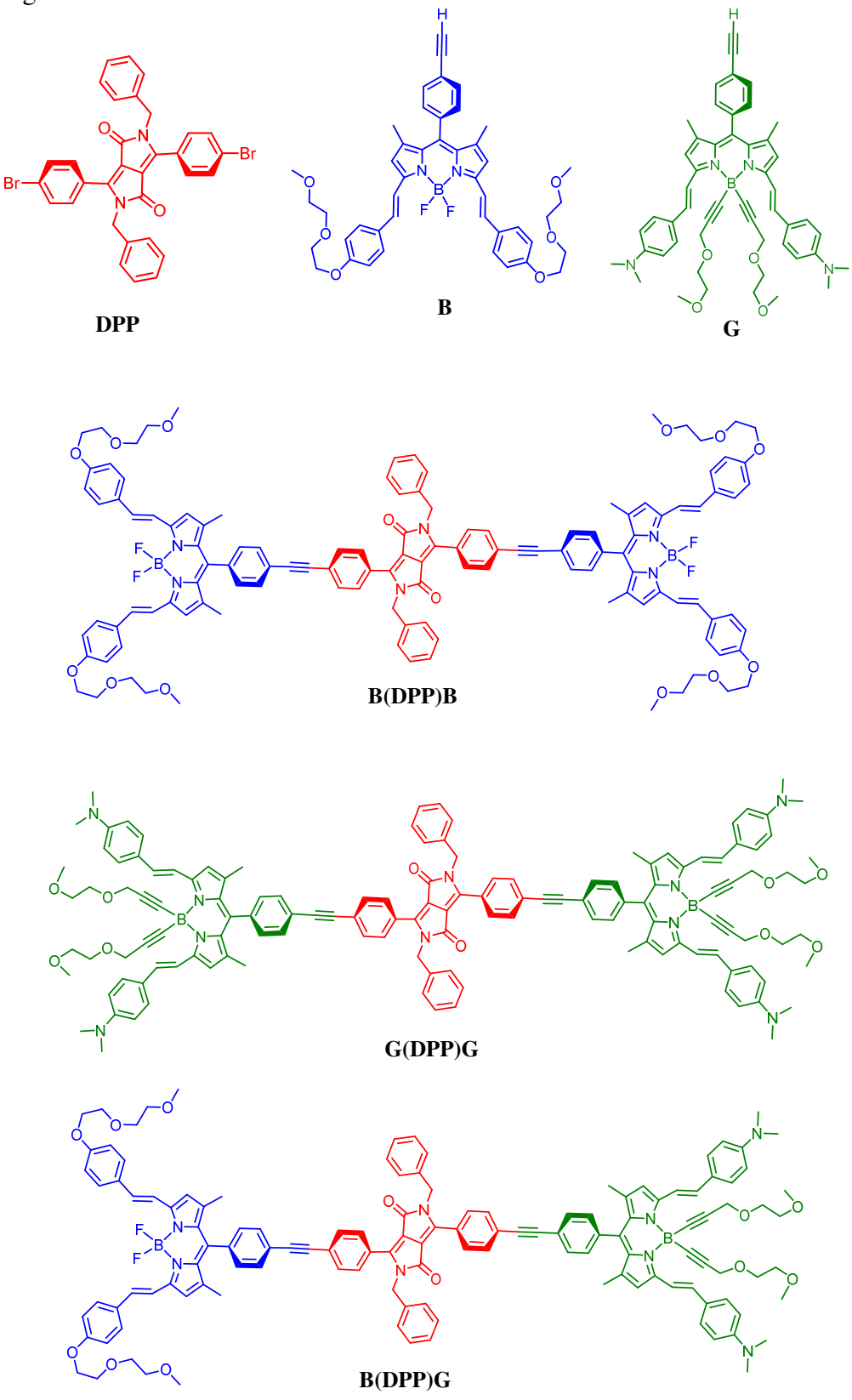

Figure 1. Molecular formulae of the reference compounds and triad systems examined in this chapter.

Moving now to the generic concept of directed EET in artificial arrays, we acknowledge that a wide range of molecular systems have been described already.[21-31] Many of these arrays display a cascade effect in which photonic energy is transferred along a logical gradient of chromophores such that EET is driven by modest thermodynamic factors. An obvious extension for these materials is to devise a simple means by which the EET flow can be reversed, while maintaining unusually high efficiency. The basic approach is sketched in Chart 1, where selective illumination of the central donor leads to non-equivalent partitioning of the subsequent EET events between attached units A1 and A2. The process is completed by long-range EET from A1 to A2 such that all absorbed photons ultimately reach A2. Reversible chemical modification of A2, for example, switches the EET direction, with excitons moving firstly to A2' and then to A1, again in quantitative yield. We now demonstrate this principle using a new molecular triad built from **DPP** and two different Bodipy units.

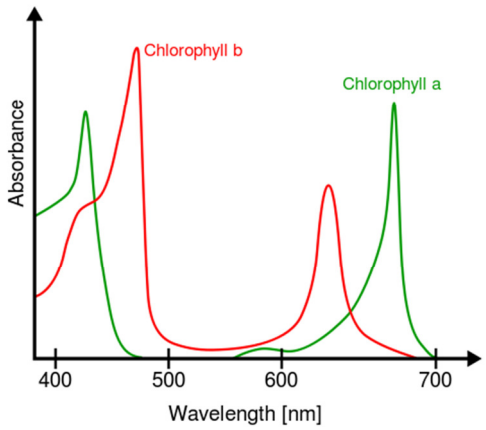

Figure 2. Chlorophyll absorption spectra.[1]

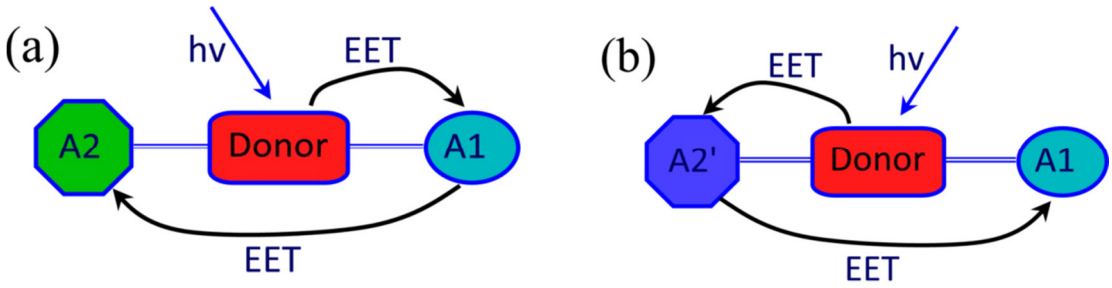

Chart 1. Principal of switching the EET direction in a triad system by chemical modification.

5.4 Photophysical properties of the reference compounds

The photophysical properties of all the target compounds were measured in toluene at room temperature. As a starting point, absorption spectra were recorded for the reference compounds, **DPP**, **B** and **G** (Figure 3). Both **B** and **G** dyes show similar optical behaviour to related Bodipy dyes;[32-35] most notably a narrow and high intensity absorption peak at 650 nm and 700 nm, respectively, due to the $S_0 \rightarrow S_1$ transition. In terms of the molar absorption coefficient, it is noted that the blue dye has a significantly

higher value at the respective peak maxima but that the green dye has a far broader absorption profile. At higher energy, many overlapping peaks appear as a result of $S_0 \rightarrow S_n$ transitions such as $S_0 \rightarrow S_3$ that appears around 360 nm and 410 nm in **B** and **G**, respectively. The green Bodipy dye shows a charge-transfer (CT) absorption transition at around 490 nm as a result of the amine group, which enhances the bathochromic shift and acid sensitivity.[36,37] Regarding **DPP**, the absorption spectrum (Figure 3) shows a main peak at 482 nm that does not correspond to a single transition but can be attributed to overlap between two transitions.[38] Adding **DPP** as a spacer residue between two symmetrical Bodipy dyes does not affect the spectroscopic properties of **DPP** or Bodipy. Indeed, absorption spectra of the composite molecules show all the anticipated transitions in the expected wavelength regions; i.e., 482 nm corresponding to **DPP**, 650 nm for **B** present in **B(DPP)B** while in **G(DPP)G** there is peak appearing at around 700 nm due to **G** which overlaps with **DPP** absorption at around 480 nm (Figure 4).

High fluorescence quantum yields (0.54 and 0.34, respectively) were found for both **B** and **G** reference dyes in toluene solution and the observed spectra were well defined, with peak maxima at 666 and 730 nm, respectively (Figure 3). The Stokes' shifts lie in the same range as found for regular Bodipy dyes; values being 345 and 650 cm^{-1} for **B** and **G**, respectively.[36,38] For **DPP**, an intensely fluorescent peak appears at 546 nm with the unusually large Stokes' shift of 2,430 cm^{-1}, which gives an indication of charge-transfer character in the excited state.[38] The rate constants for radiative and nonradiative deactivation (Table 1) were calculated from the measured fluorescence quantum yields (Φ_{flu}) and lifetimes (τ_s) according to Equations 1 and 2.

$$k_{rad} = \Phi_{flu}/\tau_s \qquad \text{Equation (1)}$$

$$k_{nrd} = (1 - \Phi_{flu})/\tau_s \qquad \text{Equation (2)}$$

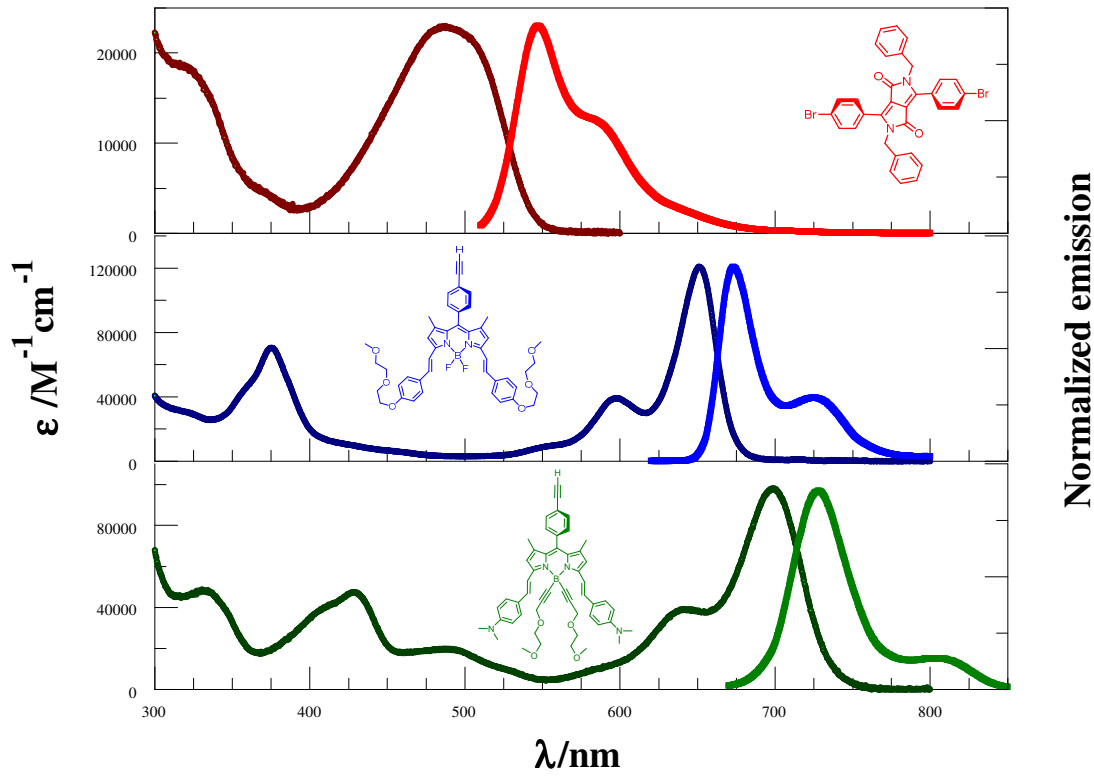

Figure 3. Recorded absorption and fluorescence spectra for the isolated dyes in toluene at room temperature; **DPP** (red), **B** (blue) and **G** (green). The excitation wavelengths were 480, 600 and 640 nm, respectively.

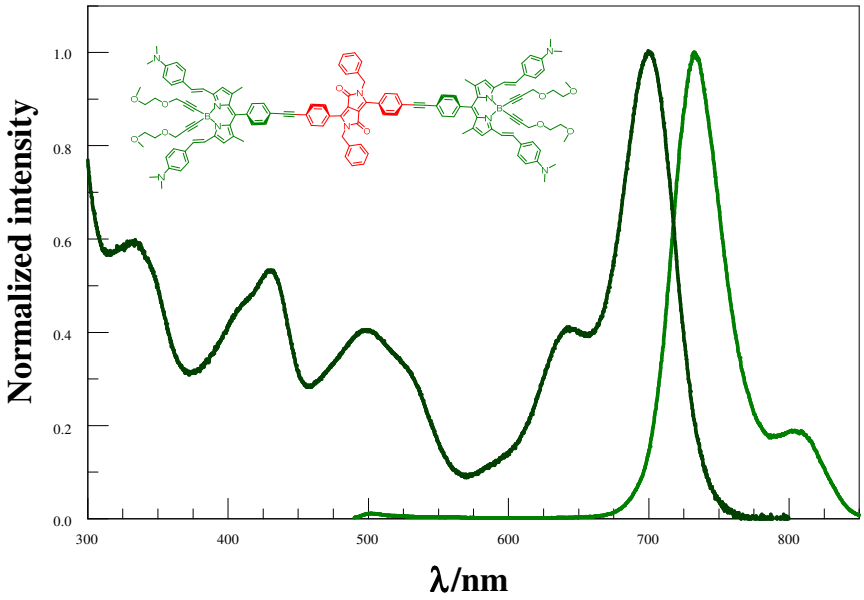

Figure 4. Normalized absorption (dark green) and fluorescence (bright green) spectra recorded for **G(DPP)G** in toluene at room temperature. The excitation wavelength was 480 nm.

In the symmetrical triad systems it is noted that direct excitation into **DPP** at 480 nm leads to strong fluorescence from either **B** or **G** according to the nature of the compound (Figure 4). Since the terminal Bodipy dyes do not absorb significantly at 480

nm we can safely conclude that electronic energy transfer takes place in these cases (this will be discussed latter). It is important to emphasize that the **B** and **G** terminals have the same emission properties as those of the reference compounds. Table 1 contains the photophysical properties recorded for these dyes measured in dilute toluene solution.

Table 1. Photophysical properties of the target dyes in toluene at room temperature. (a) ±5% ; (b) ± 0.1ns; (c) $\pm 0.05 \times 10^8$; (d) calculated from crossover point between absorption and fluorescence peaks.

Property	**DPP**	**B**	**B(DPP)B**	**G**	**G(DPP)G**
Φ_{flu} [(a)]	0.77	0.54	0.57	0.34	0.31
τ_s/ns [(b)]	6.1	7.0	7.0	3.3	3.2
k_{rad}/ 10^8 s^{-1} [(c)]	1.25	0.8	0.85	1.0	1.0
k_{nrd}/ $10^8 s^{-1}$ [(c)]	0.4	0.7	0.65	2.0	2.2
SS/cm^{-1}	2430	345	390	650	610
E_s/eV [(d)]	2.35	1.88	1.87	1.73	1.73

The most interesting, and more challenging, compound is the asymmetrical triad **B(DPP)G** which contains all three chromophores linked in a logical fashion. Again, the absorption spectrum is much as might be expected (Figure 5). There are three main absorption bands at 500, 650 nm and 700 nm that can be attributed to $S_0 \rightarrow S_1$ transitions localised on **DPP**, **B** and **G**, respectively. These absorption bands closely resemble those found for the corresponding reference dyes, or mixtures thereof. Regarding the emission spectrum, at first sight it appears that only the green dye emits regardless of excitation wavelength. Thus, fluorescence centred at 727 nm appears whether excitation is made into **DPP**, **B** or **G** (Figure 5). We consider this situation to arise because of efficient intramolecular EET. However, on closer inspection there is a weak (up to 5% of the total emission intensity) emission band corresponding to fluorescence from the blue dye at 667 nm. This suggests that EET is not quite complete. Table 2 summarizes the measured photophysical properties of the Bodipy terminals in the triad.

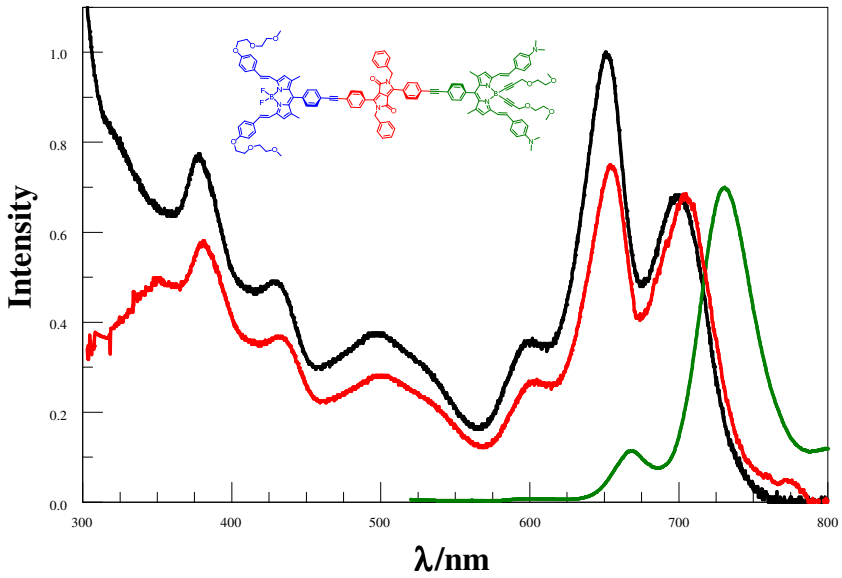

Figure 5. Normalized absorption (black), fluorescence (green) and excitation (red) spectra for **B(DPP)G** in toluene at room temperature. The excitation and emission wavelengths were 480 and 790 nm, respectively.

Table 2. Photophysical properties of asymmetrical system in toluene at room temperature. [(a)] Dioxane solution.

Compound	λ_{abs}/nm	ε_{max}/ $M^{-1}cm^{-1}$[(a)]	λ_{flu}/nm	τ_s/ns	Φ_{flu}
B(DPP)G	651	162 181	667	0.06	0.025
	698	109 647	727	3.2	0.26

5.5 Electronic energy transfer in the target compounds

We now present results pertaining to EET in the various symmetrical and asymmetrical systems as recorded in toluene solution at room temperature. In the simpler case of the symmetrical systems, **B(DPP)B** and **G(DPP)G**, direct illumination into **DPP** leads to strong emission from the Bodipy terminals with no notable fluorescence from **DPP**; i.e., illumination of the triad at 480 nm, where **DPP** absorbs more than 95% of incident photons, leads to strong emission centred at 668 nm or 730 nm depending on the type of acceptor, **B** or **G,** terminal (Figure 4). On the other hand, illumination into **DPP** present in **B(DPP)G** results in two emission peaks; a relatively weak (i.e., 5%) emission centred at 667 nm – which we know corresponds to the **B** terminal - and strong emission centred at 727 nm – which is known to correspond to the **G** terminal. There is no obvious emission from the **DPP** spacer. Moreover, the excitation spectrum recorded for **B(DPP)G** confirms efficient EET from both **DPP** and **B** moieties to the **G** terminal (Figure 5). All these observations are indicators for highly efficient intramolecular EET in these molecular systems. The Förster mechanism seems to be most likely in this case where the donors and acceptors are in weak electronic interaction.[38] In addition, the **B**-

G separation distance (R_{DA}) computed from molecular modelling is ca. 31 Å (Figure 6), which makes the Förster mechanism the only likely way for electronic energy to move along the molecular axis.[39] Taking due account of the spectral overlap integral[40] (J_{DA}) between donor emission and acceptor absorption (Figure 7), calculations according to Equation (3) have been completed and the main results are shown in Table 3. The electronic coupling matrix element (V_{DA}) between donor and acceptor is calculated from Equation (4), where μ is the transition dipole moment calculated by applying Equation (5)[41] and is found to be 7.6, 5.4 and 5.8 D for **DPP**, **B** and **G**, respectively.

$$k_{EET} = \frac{2\pi}{\hbar}|V_{DA}sK|^2 J_{DA} \qquad \text{Equation (3)}$$

$$V_{DA} = \frac{\mu_D \mu_A}{R_{DA}^3(4\pi\varepsilon_\circ)} \qquad \text{Equation (4)}$$

$$\mu^2 = 9.186 \times 10^{-3} n \int \frac{\varepsilon}{\nu} d\nu \qquad \text{Equation (5)}$$

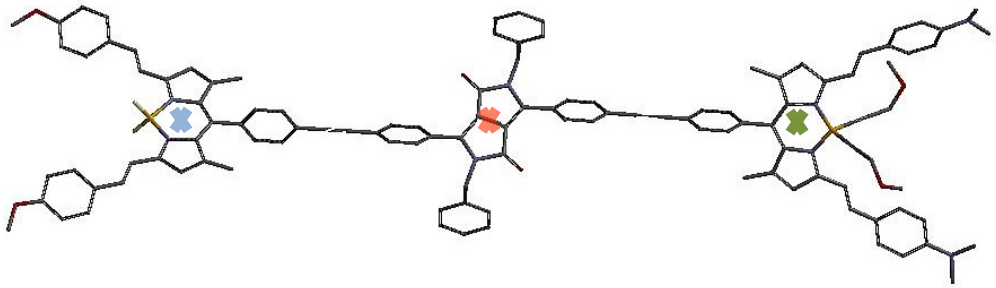

Figure 6. Energy-minimized molecular conformation computed by the semi-empirical AM1 method for **B(DPP)G** lacking the paraffinic chains. The cross signs show the centre of each chromophore.

Table 3. Parameters derived for EET in toluene solution at room temperature. [(a)] MTHF.

Donor	Acceptor	J_{DA}/ 10^{-3} cm	R_{DA}/Å	k_{EET}/ 10^{11} s^{-1}
DPP	**B**	4.2	16	11.5
DPP	**G**	1.8	16	5.7
DPP[(a)]	**GH**$^{+}$[(a)]	6.3	16	17.0
B	**G**	4.0	31	0.12
GH^{+}[(a)]	**B**[(a)]	12.0	31	0.30

In the symmetrical system, direct EET takes place from excited **DPP** to the Bodipy terminals; note that for triad **B(DPP)B** EET is faster by some 2-fold than for **G(DPP)G** because of the larger spectral overlap integral (Figure 7a,b).

In the asymmetrical system, it is necessary to consider a minimum of two EET steps following selective illumination into **DPP**. Thus, EET is expected to take place from **DPP** to the nearby **B** terminal, since this has the most favourable spectral overlap integral, followed by EET from **B** to the distal **G** terminal. Of course, it is likely that there will be a contribution from direct EET from **DPP** to **G**, since the spectral overlap integral is far from zero. According to Equation (6), the overall probability of EET from **DPP** to one of the **B** or **G** terminals has been found to be about 99%, with the relative fraction being two thirds in favour of the **B** terminal. Then, this is followed by 95% of blue fluorescence being transferred to the green terminal as a result of the large overlap integral between blue emission and green absorption (Figure 7c).

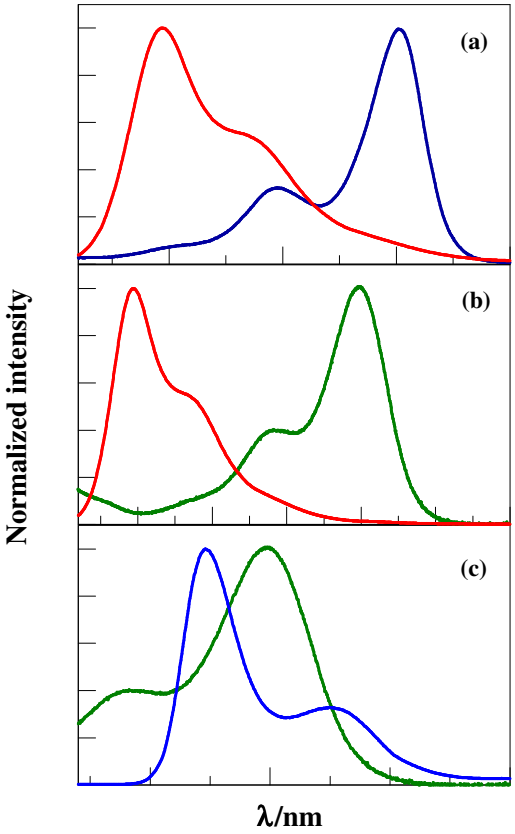

Figure 7. Illustration of the spectral overlap between donor emission and acceptor absorption; (a) **DPP** and **B**, (b) **DPP** and **G**, (c) **B** and **G**.

$$P_{EET} = 1 - (\Phi_{DA}/\Phi_D) \qquad \text{Equation (6)}$$

where, Φ_{DA} and Φ_D are the fluorescence quantum yields of the donor in presence and absence the acceptor.

5.6 Effect of acid

Over the past five years or so, the idea of using Bodipy-based dyes as the generic platform for fluorescent chemical sensors has grown steadily in significance. Such dyes have been employed in quantitative analysis of heavy metals and transition metal species and as a detector for acidity levels in organic solvents.[42-45] A modest variety of experimental protocols have been advocated as the means by which to follow the sensory behaviour; for example, recovery or quenching of the inherent fluorescence signal, forming a new fluorescent state,[46] and well-defined colour changes that can be followed by the ratiometric method.[37] As a direct consequence of inserting an amino group into the conjugation pathway, as in the case of the green Bodipy chromophore under study here, the fluorophore takes on a certain degree of sensitivity towards acidic

impurities. For example, acidification of an organic solution by adding a few drops of trifluoroacetic acid (CF_3COOH) to a solution of the dye in MTHF causes marked changes in both absorption and emission profiles (and also quantum yields and excited-state lifetimes). The main observation is a substantial blue shift for each of the green dyes, the solution turning from green to blue. Moreover, the blue moiety present in **B**, **B(DPP)B** and **B(DPP)G** does not show any spectral perturbation under these conditions.

The blue shift mentioned above is a result of protonation of the amino group, which leads to removal of the nitrogen lone-pair from delocalization.[36,37] An example of the magnitude of this blue shift is given in Figure 8 and amounts to about 65 nm. There is an accompanying decrease in the half-width of the lowest-energy absorption transition and an increase in the molar absorption coefficient at the peak. It is interesting to note that acidification tends to eliminate the charge-transfer absorption transition seen for **G** and **G(DPP)G**, while in **B(DPP)G** the absorption band associated with the protonated species overlaps with the blue absorption bands (Figure 9a). A more substantial blue shift (i.e., ~85 nm) is seen in the case of the emission spectra, with the fluorescence quantum yield increasing upon protonation.[39] Table 4 summarizes the general behaviour associated with protonation of the green dyes.

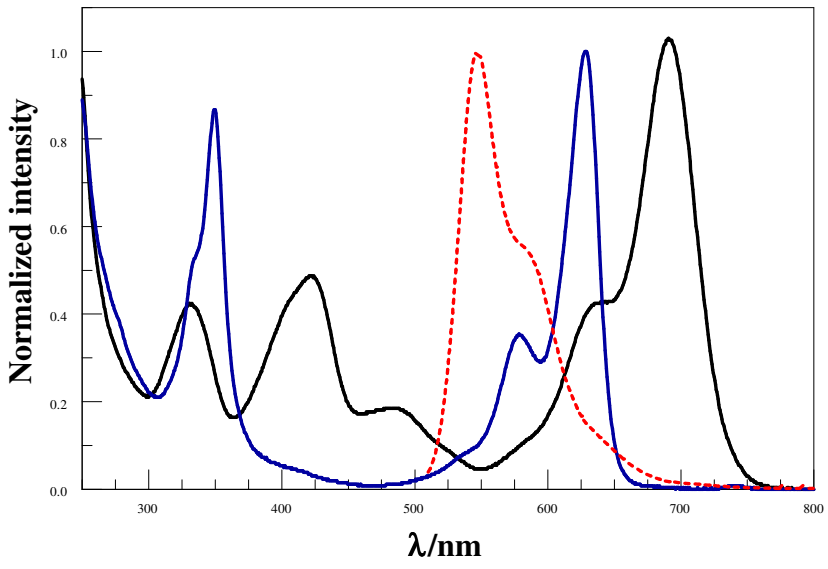

Figure 8. Normalized absorption spectra of green Bodipy before (black) and after (blue) acidification in MTHF solution. Also shown is the **DPP** fluorescence spectrum (red).

Table 4. Effect of acidification on the photophysical properties of the green moiety in MTHF at room temperature. NA refers to non-applicable data because the green peak overlaps with the blue peak.

	Before adding acid				After adding acid			
Compound	λ_{abs}/nm	λ_{flu}/nm	Φ_{flu}	E_S/eV	λ_{abs}/nm	λ_{flu}/nm	Φ_{flu}	E_S/eV
G	690	730	0.28	1.74	628	645	0.39	1.94
G(DPP)G	691	730	0.034	1.74	629	644	0.25	1.94
B(DPP)G	693	727	0.08	1.74	NA	NA	NA	NA

In the protonated asymmetrical system, preferential illumination into the **DPP** unit leads to one principal emission peak at 660 nm (Figure 9). This emission band is attributed to the blue terminal (by comparison with the pure chromophores) since the excited state of the protonated green dye is shifted to higher energy (E_S = 1.94 eV) than that of the blue dye (E_S = 1.88 eV). Now, we have the possibility for preferential electronic energy transfer from the **DPP** donor to the protonated green terminal (60%) relative to ETT to the opposite blue dye (40%). This is a simple consequence of the increased spectral overlap integral (J_{DA} = 6.3 x 10^{-3} cm^{-1}) and the slightly elevated transition dipole moment (μ = 5.35 D). This initial energy redistribution is followed by slower EET from the protonated green dye to the distal blue terminal (k_{EET} = 3.0 x 10^{10} s^{-1}).

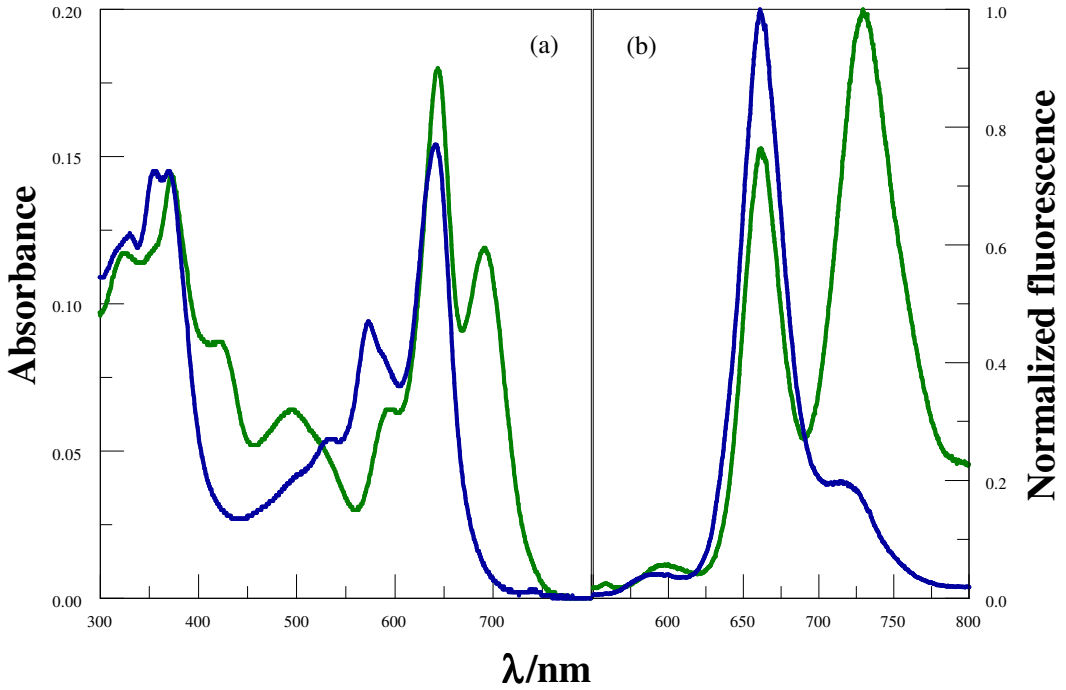

Figure 9. Absorption (a) and normalized fluorescence (b) spectra recorded for **B(DPP)G** in MTHF before (green) and after (blue) acidification.

5.7 Effect of solvent

A substantial volume of published work has been directed towards understanding the general effects of solvent polarity on the photophysical properties of neutral dyes in solution.[47,48] Here, we simply examine how the molecular triads respond to changes in the nature of the solvent in order to confirm the validity of the EET schemes proposed above; we are not intending to add to the depth of knowledge about how solvent properties affect the absorption or emission energies of the dyes. In the first instance, the photophysical behaviour of **B** and **B(DPP)B** was studied in order to expose to what degree the solvent polarizability[49] controls the position and/or band shape of the absorption and emission peaks. By changing the solvent at room temperature, we note for **B** that the absorption maximum undergoes a small red shift with increasing solvent polarizability; for example changing the solvent polarizability from 0.2 to 0.22 shifts the maximum peak by 6 nm towards lower energy. Furthermore, the emission peak maximum also tends to vary with a comparable dependence on the magnitude of the solvent polarizability (showing an 8-nm red shift as the polarizability increases from 0.17 to 0.22). In other words, increasing solvent polarizability decreases the HOMO-LUMO energy gap as it appears from the energy values of the singlet-excited state (E_S) in Table 5.[50] We also note that the fluorescence quantum yield (Φ_{flu}) decreases by 10% with increasing solvent polarizability over the same range.[51,52] Table 5 summarizes the effect of solvent polarizability found for **B**. (N.B. Solvent polarizability is an electrical property of the solvent which can be quantified in term of the refractive index and the density according to Lorentz-Lorentz equation.[53] It is used to describe non-specific interactions, both repulsive and attractive, between solute and solvent and, in some cases, is able to describe solvatochromic behaviour more accurately than many single parameter functions.[49] Polarizability varies with temperature and applied pressure and is considered to be a short-range effect. There are, however, very few examples where the solvatochromic properties of a large molecular dye can be adequately described in term of solvent polarizability and this has led to the introduction on numerous empirical functions intended to better report on solvent dependent spectral shifts. The situation is complicated by the fact that the molecular dipole moment tends to change under excitation. A further difficulty lies with establishing the size and shape of the cavity housing the solute. Our molecules are often large and dipolar and, as a consequence, not readily amenable to detailed examination in term of solvent-induced spectral shifts. We rely, therefore, on a cursory comparison with the polarizability function).

Table 5. Photophysical properties of pure blue dye (**B**) in different solvents. PC is propylene carbonate, MTHF is 2-methyletetrahydrofuran, BuCN is butyronitrile and AcCN is acetonitrile.

Solvent	Polarizability	λ_{abs} /nm	λ_{flu} /nm	Φ_{flu}	SS /cm^{-1}	E_S/eV
Toluene	0.22	651	666	0.54	345	1.88
PC	0.2	645	666	0.49	490	1.89
MTHF	0.19	643	659	0.60	380	1.9
BuCN	0.18	642	661	0.60	445	1.91
AcCN	0.17	639	658	0.65	450	1.91

Similar behaviour was observed for the blue terminal present in **B(DPP)B**. The linearity of plots of both ν_{abs} and ν_{flu} vs the solvent polarizability term (Figure 10) confirms that van der Waals interactions with polarizable solvent molecules can rationalize the solvent dependence of the excitation energy.[54] Comparison of this system with the isolated blue dye indicates that there is no special effect attributable to the **DPP** spacer. A related study was put into place to examine the effect of solvent polarity on the spectral properties of **G** and the green terminal present in **G(DPP)G**. Table 6 gives a summary of the main findings observed for isolated **G**.

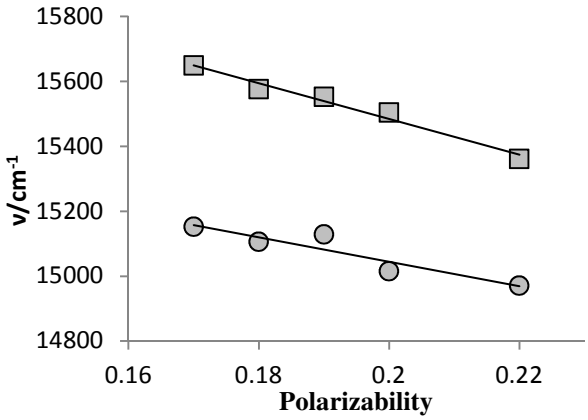

Figure 10. Effect of solvent polarizability on the absorption (squares) and emission (circles) maxima of **B(DPP)B.**

Table 6. Photophysical properties of the isolated green dye (**G**) in different solvents. ε_s refers to the dielectric constant of the solvents.

Solvent	ε_s	λ_{abs}/nm	λ_{flu}/nm	SS/cm^{-1}	Φ_{flu}	E_s/eV	FWHM /nm
Toluene	2.38	697	730	650	0.34	1.73	50
MTHF	6.97	690	730	795	0.28	1.74	55
BuCN	24.8	694	745	985	0.11	1.72	65
AcCN	37.5	694	750	1075	0.06	1.71	70
PC	64.7	703	767	1185	0.02	1.69	75

In general, the main absorption band observed at around 690 nm becomes broader (by up to 25 nm) as the solvent polarity increases, which we attribute to an enhancement of the intramolecular charge-transfer character.[48] The red shift of the emission peak and the decreasing Φ_{flu} seen as the solvent polarity increases are indirect indications of the extent of intramolecular charge transfer along the molecular axis of the green dye. Moreover, changing the solvent from toluene to acetonitrile leads to a fall in the fluorescence quantum yield from 0.34 to 0.06 with an accompanying 20-nm bathochromic shift. In addition, solvent polarity tends to increase the magnitude of the Stokes' shift for both **G** and **G(DPP)G** as it becomes twice larger in the polar solvent. The increased Stokes' shift is taken to indicate an increase in the size of the dipole moment upon excitation.[37] Again, there are no notable effects arising from adding **DPP** as a spacer in the triad system.

Moving now to **B(DPP)G**, as can be seen from Figure 11, the position of the **DDP** absorption peak does not show a notable dependence on solvent polarity. Otherwise, the blue and green absorption peaks are affected by solvent polarizability and polarity, respectively, in the same way as outlined for the isolated compounds, **B** and **G**.

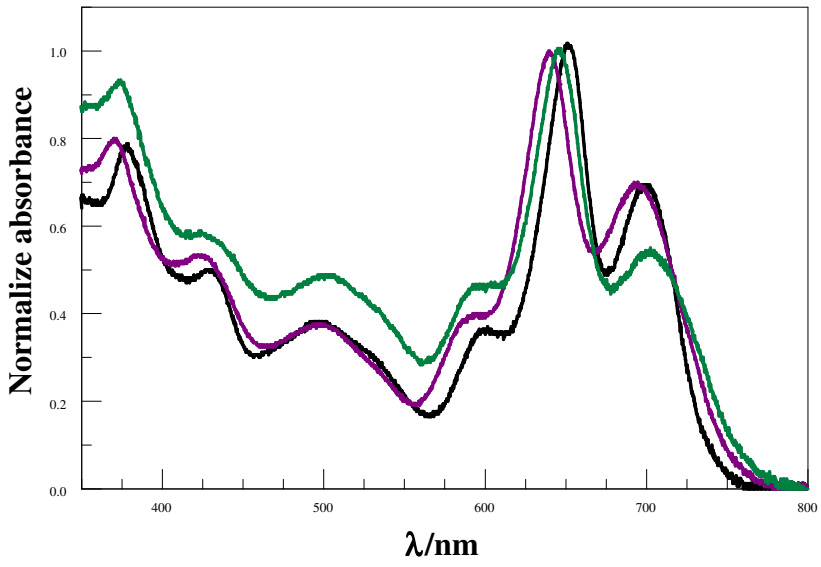

Figure 11. Normalized absorption spectra recorded for **B(DPP)G** in different solvents; toluene (black), acetonitrile (plum) and propylene carbonate (green).

Figure 12 shows the normalized emission spectra recorded for **B(DPP)G** in a few solvents of differing dielectric constant. It can be seen that the more polar solvents tend to shift the emission peak of the green dye towards lower energy while also decreasing the fluorescence quantum yield from 0.26 (toluene) to 0.004 (propylene carbonate). This, we believe, is a consequence of increased charge-transfer character in

the green dye that serves to raise the level of π-electron conjunction running along the molecular backbone. As the energy of the excited state drops, the Englman-Jortner energy-gap law dictates that the rate of accompanying nonradiative decay will increase and thereby reduce the emission quantum yield.[55] There is a secondary effect on the probability of EET along the molecular axis (Table 7), probably because of solvent-induced changes in spectral overlap integral and/or transition dipole moments, which restores some emission (up to 0.07) from the blue dye in the most polar solvent. Interestingly, in polar solvents there is a new emission peak at 535 nm, with Φ_{flu} = 0.02 that can be attributed to **DPP** depending on the comparison with pure DPP. However, the variation in the EET probability is around 3% in case of **DPP** and up to 5% in the **B**.

Table 7. Solvent effect on the fluorescence quantum yields of each subunit and the total EET probability in **B(DPP)G** triad.

Solvent	Φ_{flu} **DPP**	Φ_{flu} **B**	Φ_{flu} **G**	P_{EET} **DPP**	P_{EET} **B**
Toluene	0.0009	0.025	0.26	0.99	0.95
MTHF	0.0005	0.037	0.08	0.99	0.93
BuCN	0.0112	0.066	0.014	0.98	0.89
AcCN	0.0190	0.060	0.017	0.97	0.90
PC	0.0194	0.033	0.0038	0.97	0.93

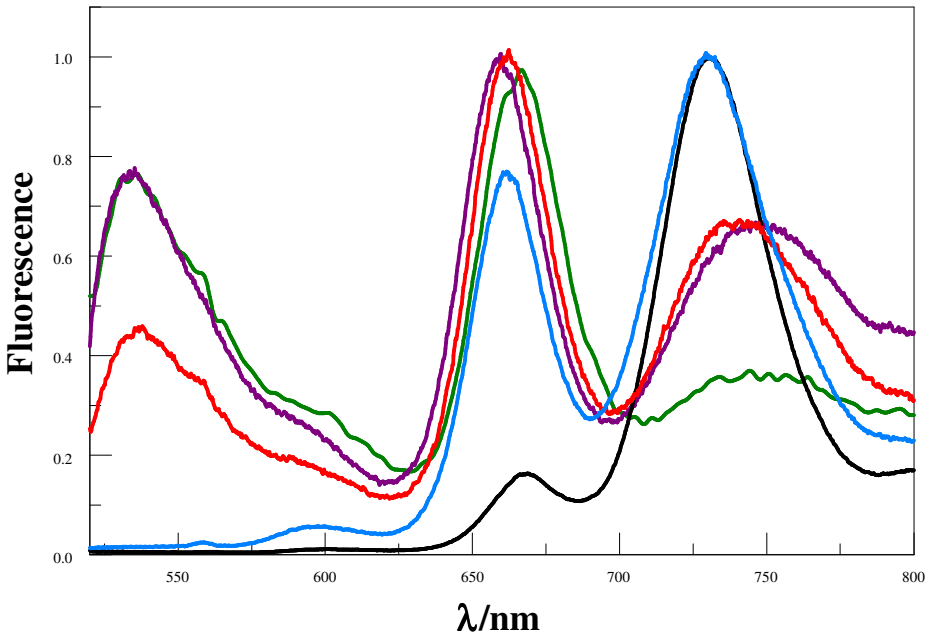

Figure 12. Normalized fluorescence spectra recorded for **B(DPP)G** in different solvents; toluene (black), MTHF (blue), AcCN (plum), BuCN (red) and PC (green). The excitation wavelength was 480 nm.

5.8 Annealing process

The energy-minimised structures are readily computed, at least for the ground state, but we were unable to obtain crystal structures for the dyes under consideration here. One particular geometrical feature of some concern relates to the extent to which the vinyl arms fall into conjugation with the central dipyrrin core since this will determine the conjugation length. To examine this situation, a limited amount of computational simulated annealing was done using HyperChem. Figure 13 presents a few selected geometries accessed during the runs for the blue dye **B** dye as an example.

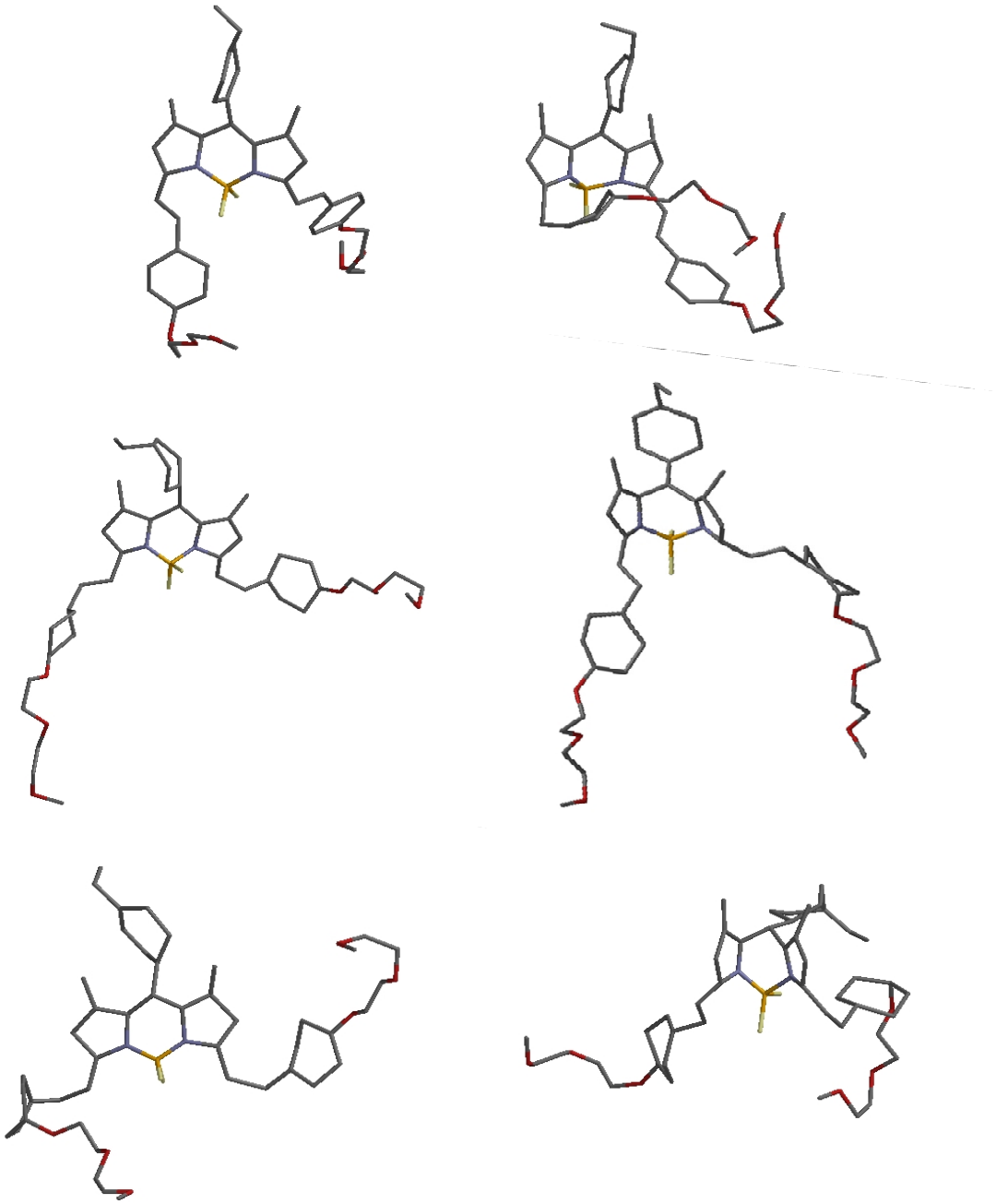

Figure 13. Examples of the suggested distorted geometries computed for **B** during simulated annealing runs made with HyperChem.

It appears there are notable changes in the geometry at the *meso*-phenyl ring, the substituents at positions 3 and 5, and in the dipyrrin core itself. In some cases, the conjugation is broken and that could lead to a blue shift in the spectra while the observed distortion of the dipyrrin core could alter the excited-state properties. This theoretical study indicates the non-rigidity of this type of molecule and gives some support for geometry changes occurring during certain experiments, such as under conditions of high temperature or applied pressure. There is no evidence for the interconversion between two groups of conformers but rather a general structural distortion at elevated temperature. It needs to be emphasised that this is just a computational study and might not correspond to the behaviour of a real system.

5.9 Effect of temperature

At temperatures below about 110K, MTHF forms a rigid, optical glass but over the range 110 to 140K there is an amorphous phase that is difficult to characterise.[56] The melting point of MTHF is usually taken as 137K. In our work we have recorded emission spectra over the range 80 to 290K. The blue chromophore present in both **B** and **B(DPP)B** exhibits a sensitivity towards temperature over this range, as illustrated in Figure 14. The insert to Figure 14 shows the effect of slowly increasing the temperature on the emission maximum, as given in units of wavenumber, ν_{flu}. It can be seen that there are three phases (or stages) of behaviour: Firstly, there is no discernible change in peak position in the glassy matrix between 80 and 110K.[57] Throughout the amorphous region, 110 to 150K, there is a modest red shift.[56] Finally, for the liquid phase that appears at above 150K, temperature induces a small blue shift. Over the entire temperature range, the emission maximum is subjected to a blue shift of ca. 200 cm^{-1}. The most likely explanation for this behaviour is that, at low temperature, the molecule adopts the fully extended conformation that tends to maximise the conjugation length. There will be small adjustments of the solvation character as the solvent changes from glass to molten state. Further heating of the solution, thereby melting the amorphous phase, will introduce heterogeneity into the conformational balance and this will push the emission peak towards higher energy.[58] The blue shift is accompanied by an increase in the band half-width of ca. 13 nm, which is taken as further indication for the existence of a multitude of conformers.

In general, Φ_{flu} for the blue chromophore increases gradually from 0.15 at 80K to 0.6 at 290K in both systems. This situation is somewhat unusual in that most systems tend to be more emissive at lower temperature. The explanation for this effect is not so

obvious but might indicate that the radiative rate constant is temperature dependent because of the change in geometry. It is important to recall that there will be a marked change in polarity (as indicated by the static dielectric constant) of the solvent over this temperature range and we know that the photophysical properties of the dye are somewhat sensitive to this term.

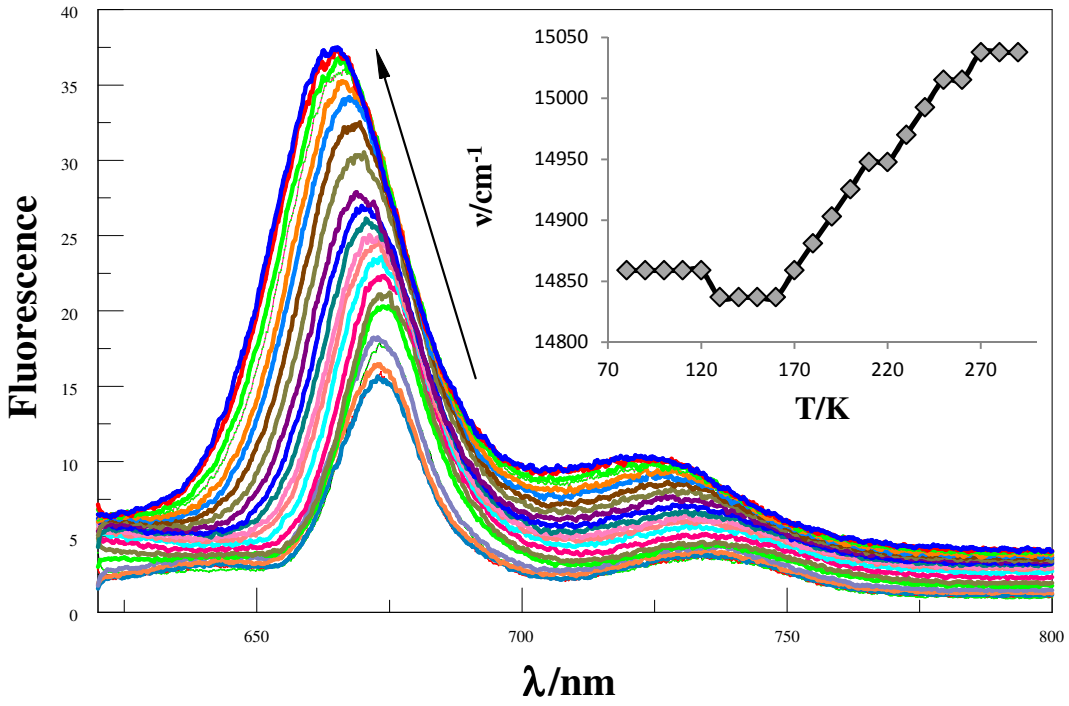

Figure 14. Effect of temperature on the emission spectrum of the blue Bodipy (**B**) in MTHF solution. The insert shows the effect on the peak position. The arrow indicates the direction of rising temperature. The excitation wavelength was 580 nm. (The change in the baseline is due to the temperature effect on the solvent refractive index)

Similarly, fluorescence spectra recorded for the green chromophore present in both **G** and **G(DPP)G** show three stages of behaviour over the same temperature range. Overall, there is a 9-nm blue shift but the same individual pattern as described above is observed. As the temperature increases, the emission maximum shifts towards lower energy by 15 nm as the glassy matrix becomes vitrified before undergoing a blue shift of 24 nm in the liquid phase. The same generic trend have been found in MTHF for a different compound.[59] It is, however, difficult to fully rationalise this behaviour because of the many factors that change as the solvent moves through the various phases. In fact, the temperature dependence of MTHF is still quite poorly understood.[59]

The effect of temperature on the fluorescence quantum yield is rather complex for the green dye. Thus, in the case of the isolated green (**G**), Φ_{flu} , which is 0.2 at 77K, increases with increasing temperature in the solid state but decreases slightly to 0.18 over the amorphous region. Once the liquid phase is reached, the quantum yield

continues to increase to reach 0.26. In contrast, for **G(DPP)G**, Φ_{flu} reaches a maximum value of 0.15 at 140K but begins to decrease at higher temperature to end up with 0.034 (Figures 15 and 16).

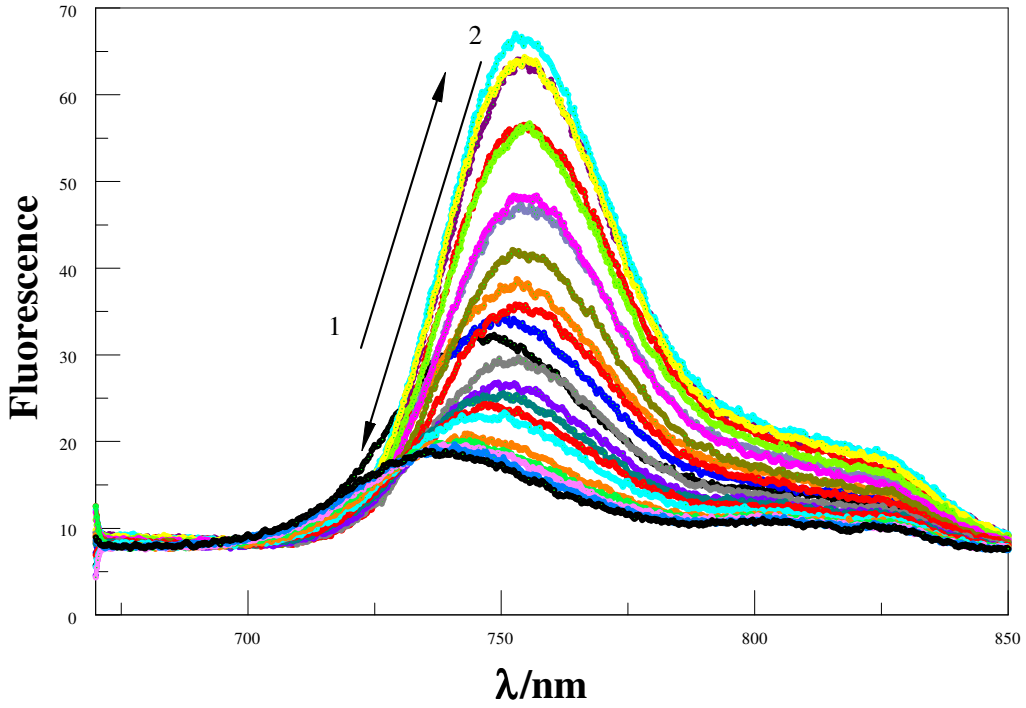

Figure 15. Temperature effect on the emission spectrum of **G(DPP)G** in MTHF. The arrows (1) and (2) indicate the temperature increasing from 80 to 140 K and then from 140 to 290 K, respectively. The excitation wavelength was 660 nm.

Turning our attention now to the asymmetrical system, we know that increasing the temperature from 80 K causes the glassy matrix to evolve into an amorphous region before melting at around 140K to give the liquid phase. There is a change in polarity over this region. Interestingly, for the mixed system, the effect of temperature on the emission peak positions follows precisely the same behaviour as found for the isolated terminals. It can be seen from Figure 17 that the fluorescence bands are narrow in the glassy matrix but begin to broaden as the temperature is raised. In fluid solution, we note that the emission peak associated with the green dye has moved by 17 nm towards higher energy relative to the glassy matrix and this is the same behaviour as noted for the isolated terminal. In fact, the identical

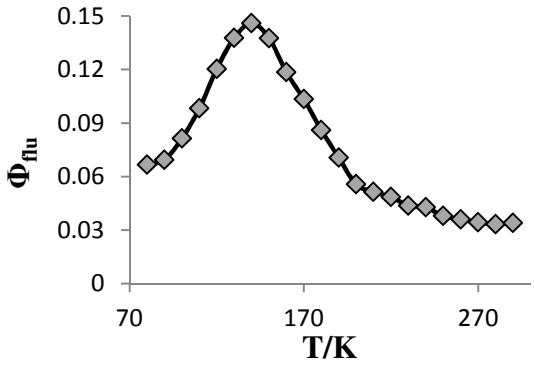

Figure 16. Temperature effect on Φ_{flu} for **G(DPP)G** in MTHF solution. The excitation wavelength was 660 nm.

behaviour is observed for the isolated green dye by decreasing the dielectric constant of the solvent.[60] We recall that whereas Φ_{flu} for the green dye undergoes a marked drop from 0.33 to 0.08 with increasing temperature, there is no significant change for the blue dye. An interesting observation is that EET still takes place at low temperature; indeed the probability of net EET reaches about 99% even at low temperature.

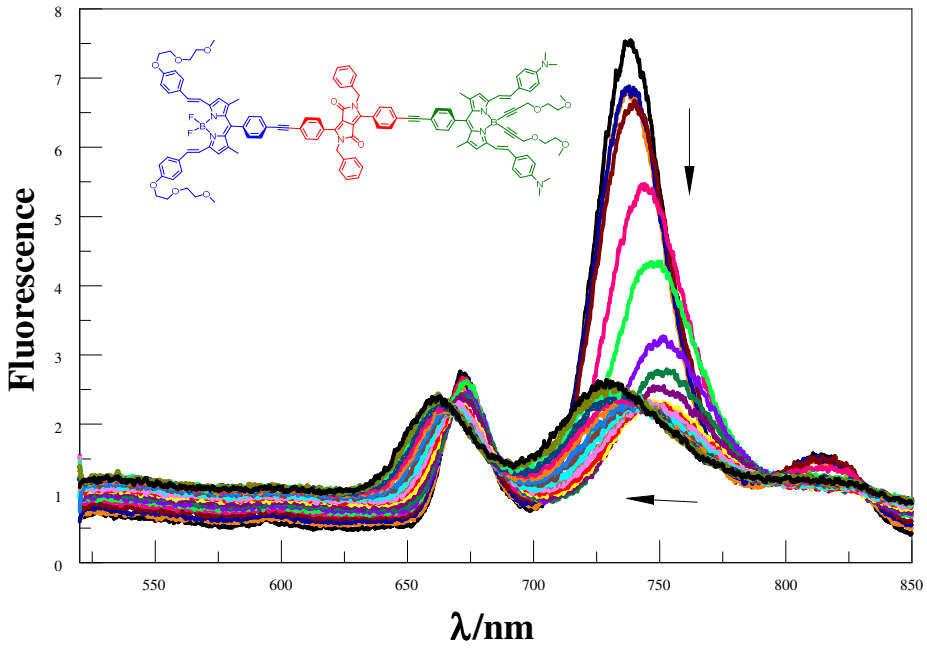

Figure 17. Recorded fluorescence spectra of **B(DPP)G** in MTHF solution as the temperature increases gradually from 80 to 290 K. The arrows indicate the direction of increasing temperature. The excitation wavelength was 480 nm. (The change in the baseline is due to the temperature effect on the solvent refractive index)

5.10 Effect of pressure

In order to extend this work, we examined the effect of applied pressure on the fluorescence properties of the dyes in MTHF at room temperature. It is recognised that pressure will increase the density of the solution and thereby affect the solvent properties such as viscosity, polarity and refractive index.[61] Of particular interest is the possible influence of pressure on the probability of EET in solution phase. It might be noted that there have been very few reports of how pressure might affect EET.

5.10.1 Absorption spectra

As a starting point for this part of the investigation, absorption spectra were recorded for each of the target compounds in MTHF under applied pressure. Although the apparatus is capable of reaching higher pressure, we restricted the system to 550 MPa for safety reasons. Absorbance values were corrected for changes in density of the solution. This same change in density, which is responsible for the apparent increase in solute

concentration, also modifies the solvent polarizability and causes a red shift of ca. 10 nm for the respective absorption maxima.

Indeed, Figure 18 shows the shift in the absorption maximum for the blue and green moieties in the isolated and symmetrical systems as a function of applied pressure. The observed effect is attributed to the anticipated change in polarizability. The intriguing aspect of this part of the work is the possibility that applied pressure will affect the molecular conformation of the solute, in addition to perturbing the solvent. In turn, this could modulate the degree of intramolecular EET. This issue will be discussed later in the chapter.

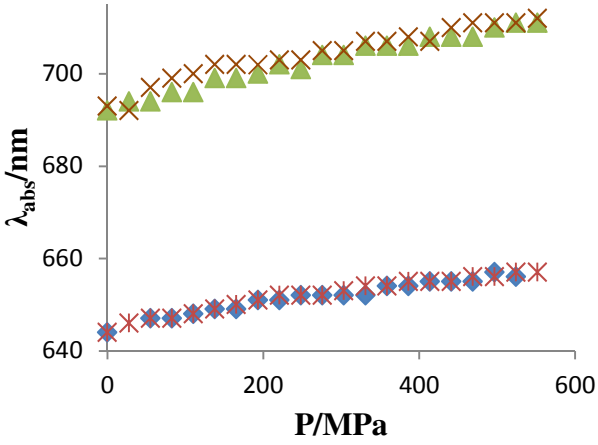

Figure 18. Effect of applied pressure on the absorption peak position for **B** (blue), **B(DPP)B** (red), **G** (green) and **G(DPP)G** (brown) in MTHF.

5.10.2 Emission spectra

Looking now at the emission behaviour, Figure 19 shows the fluorescence spectra of the isolated blue dye (**B**) as a function of applied pressure. It is apparent that the emission maximum that appears at 660 nm and has Φ_{flu} around 0.6 before application of the pressure undergoes a small red shift with increasing pressure until 275 MPa. At higher pressure, the peak position remains unaffected but there is a significant decrease in the emission intensity, whereby the fluorescence quantum yield drops from 0.7 at 275 MPa to 0.03 at 550 MPa. At the same time, new emission peaks appear at 535 and 600 nm. A possible explanation for this observation might be that pressure modifies the dye structure and forces it to become less conjugated. This feat could be achieved by bending the appended arms out of the plane of the dipyrrin nucleus (refer to Figure 13) in order to reduce the molar volume of the solute. This is a most unusual and rather exciting situation, opening the possibility to construct new types of pressure sensitive materials.[62,63]

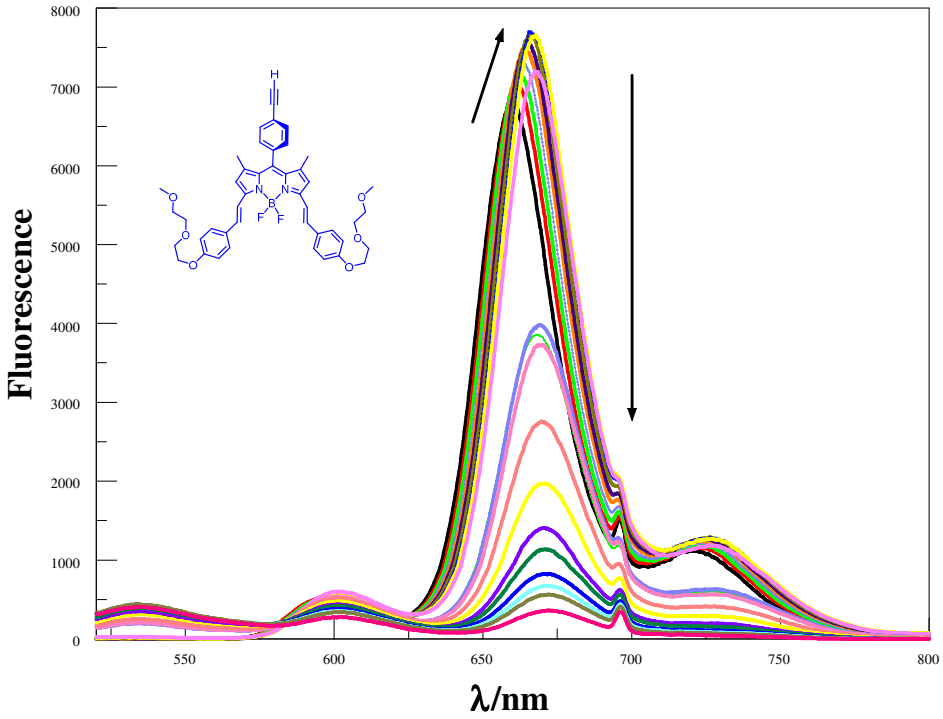

Figure 19. Recorded fluorescence spectra for pure **B** solution in MTHF under applied pressure at room temperature. The arrows indicate the direction of increasing pressure.

In much the same way, it was found that the blue dye present in both **B(DPP)B** and **B(DPP)G** shows a comparable effect under applied pressure. There is a progressive red shift at moderate applied pressure that tends to saturate at around 300 MPa. Probably, this is a reflection of the pressure-induced change in solvent polarizability (Figure 20). In the symmetrical triad, pressure causes a drop in the emission yield from 0.65 to 0.026 as described for the isolated blue chromophore. This situation confirms that pressure is an interesting experimental variable for these dyes that could lead to useful exploitation in the form of new "smart" materials.

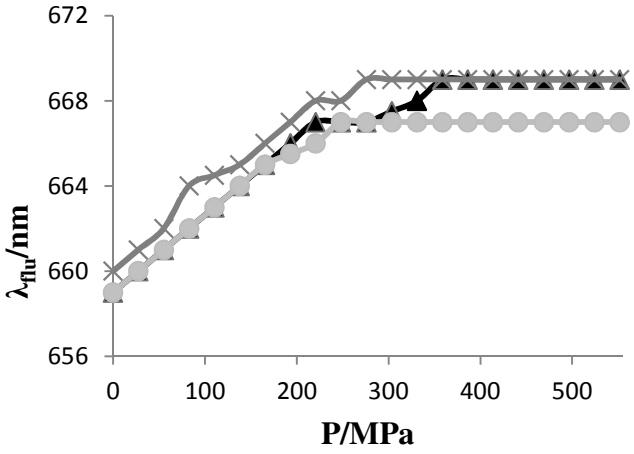

Figure 20. Pressure applying effect on the fluorescence blue peak position in **B** (black), **B(DPP)B** (grey) and **B(DPP)G** (light grey) solutions in MTHF.

Continuing this approach to include the green chromophore, it is noted that this dye behaves identically in all three molecular systems. That is to say, pressure affects the emission properties of the green dye in the same way regardless of the composition

of the molecule. It is also important to stress that the original properties are not fully recovered on release of the pressure, although there is partial (i.e., >80%) recovery of the fluorescence yield and the peak position returns precisely to its original value. We deduce from these findings that the peak position reflects the solvent polarizability, this being set by the density, while the intensity is a consequence of dye concentration and conformation. As above, a progressive bathochromic shift occurs at pressures up to 275 MPa but saturates at this level so the total shift of the green peak is around 15 nm towards lower energy in all systems. The emission intensity falls rather dramatically with increasing pressure (Figure 21) and reaches a level corresponding to about 5% of the atmospheric pressure value at the maximum applied pressure. It might be expected that, because of the terminal amino donor, the green dye possesses more charge-transfer character than does the blue analogue. This would make the emission properties more sensitive to changes in solvent polarity. Thus, although the pressure effect on the blue and green dyes is similar, the latter is much more pronounced. In addition, new emission peaks start to appear at 535 and 600 nm during the pressure cycle as the main emission band loses intensity and this is more obvious in **B(DPP)G** system as appears in Figure 22.

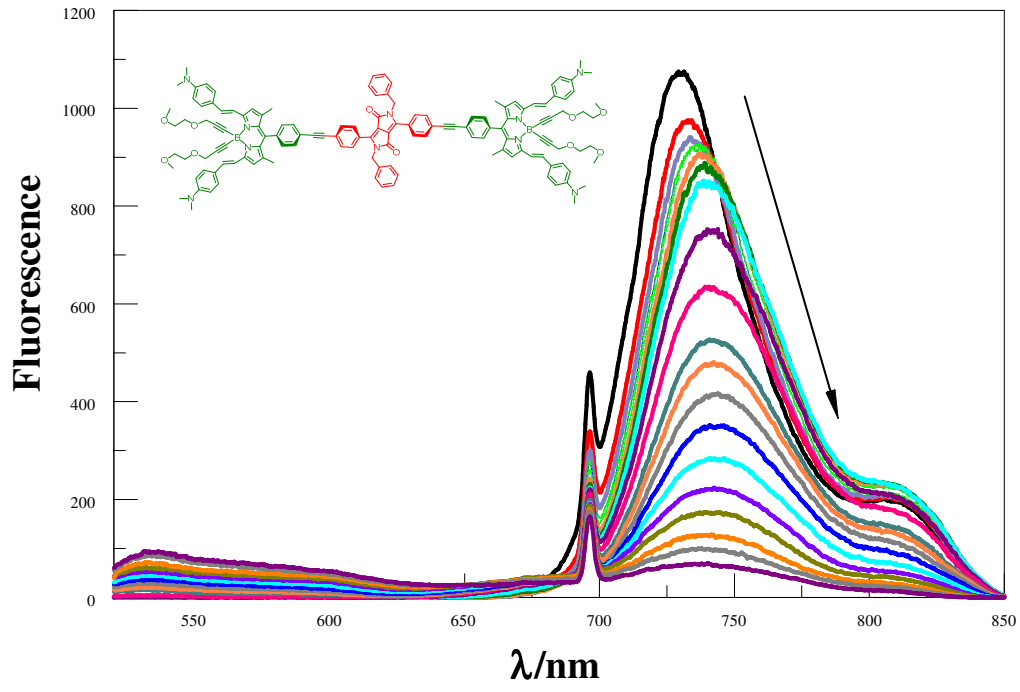

Figure 21. Recorded fluorescence spectra for **G(DPP)G** solution in MTHF under applied pressure at room temperature. The arrow indicates the direction of increasing pressure.

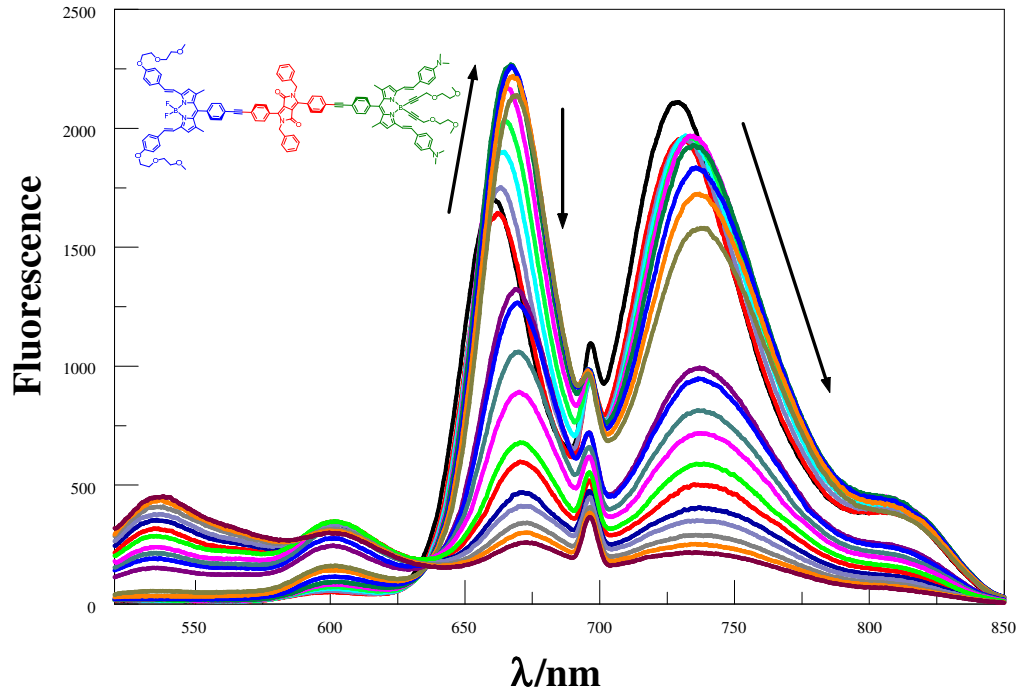

Figure 22. Recorded fluorescence spectra for **B(DPP)G** solution in MTHF under applied pressure at room temperature. The arrows indicate the direction of increasing pressure.

Figure 23 illustrates the partial recovery of the system on release of the applied pressure. It is informative to note that most of the fluorescence due to the blue dye is recovered quickly but there is still a high fraction of the green dye present in one of the high-energy conformers. In order to explore this behaviour in more detail, additional studies were made with the green dye (**G**) in a few other solvents. Similar behaviour was observed in all solvents and Figure 24 provides an example of this trend in a polar solvent (BuCN) and as it appears, there is an obvious red shift by 17 nm and progressive decrease in the emission intensity which give an indication that the solvent polarity itself does not cause the molecular response towards applied pressure.

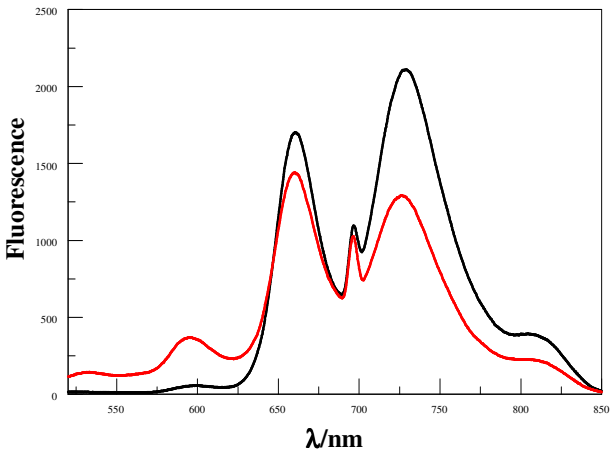

Figure 23. Recorded emission spectra before (black) and on release (red) of high pressure for **B(DPP)G** in MTHF at room temperature.

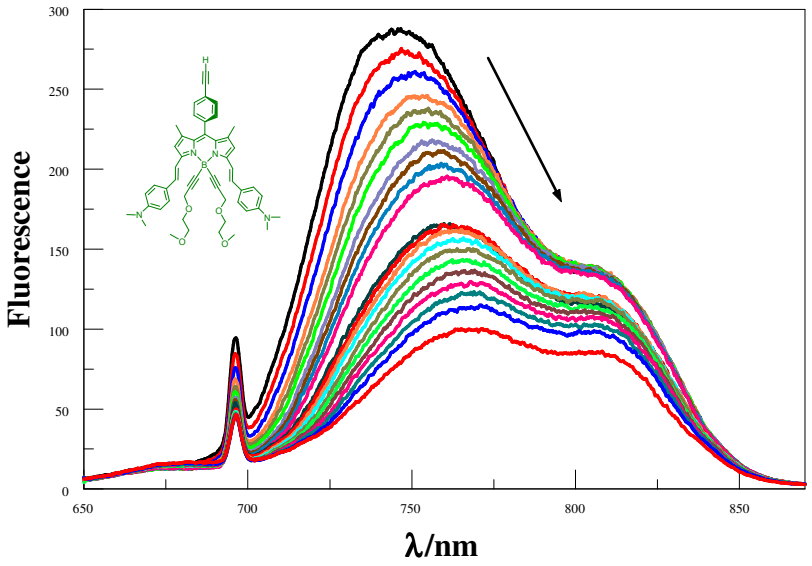

Figure 24. Recorded fluorescence spectra for pure **G** solution in BuCN under applied pressure at room temperature. The arrow indicates the direction of increasing pressure.

One unfortunate consequence of these pressure effects is that they tend to obscure the EET process occurring in the mixed dye. Thus, applied pressure introduces quite severe complications due to changes in solvent properties and molecular geometry. Many corrections need to be taken into consideration when attempting to determine emission quantum yields, or even ratios, which add more uncertainty to the derived EET probability. Moreover, changing the geometry by distortion under high pressure could affect the calculated transition dipole moment and subsequently affect the electronic coupling term. As such, discussion of the pressure effect on the probability of EET will be deferred until a full understanding of the geometry changes has been achieved.

5.11 Conclusion

This work has verified the basic concept of switching the direction of intramolecular EET by protonation of one chromophore in a multiple dye package. The switch is reversible, at least to a high degree. In the case of **B(DPP)G**, the state of the switch can be read by fluorescence and/or absorption spectroscopy. Further modification of this approach could involve using a photo-acid generator (**PAG**) rather than changing the pH by manual methods. Such protocols might be developed as a means for designing rapid switching systems. Fast, reversible switches might become possible by employing proton transfer strategies involving covalently attached chromophores that deprotonate under illumination, such as 2-naphthol.[64] It has also been shown[65] that certain green Bodipy-based dyes can be appended to porous microspheres in such a way that

reversible protonation still takes place. It is reasonable to suppose that **B(DPP)G** could likewise be anchored to polystyrene spheres preloaded with **PAG**. Such materials could be studied at the single bead level and developed as advanced probes for chemical pollutants (e.g., phosgene) and/or acidic contaminants. It should also be stressed that, while this work has focussed on photo-acids, companion studies could be conducted with photo-bases. New personnel joining the research group will try to take these ideas to a more advanced stage.

5.12 References

1. Li, Y.; Cai, Z.-L.; Chen, M. *J. Phys. Chem. B* **2013**, *117*, 11309.
2. Mackinney, G. *J. Biol. Chem.* **1941**, *140*, 315.
3. Niedzwiedzki, D.; Blankenship, R. *Photosynth. Res.* **2010**, *106*, 227.
4. Yella, A.; Lee, H.-W.; Tsao, H. N.; Yi, C.; Chandiran, A. K.; Nazeeruddin, M. K.; Diau, E. W.-G.; Yeh, C.-Y.; Zakeeruddin, S. M.; Grätzel, M. *Science* **2011**, *334*, 629.
5. Li, L.-L.; Diau, E. W.-G. *Chem. Soc. Rev.* **2013**, *42*, 291.
6. Hasobe, T.; Imahori, H.; Kamat, P. V.; Ahn, T. K.; Kim, S. K.; Kim, D.; Fujimoto, A.; Hirakawa, T.; Fukuzumi, S. *J. Am. Chem. Soc.* **2004**, *127*, 1216.
7. Ziessel, R.; Ulrich, G.; Harriman, A. *New J. Chem.* **2007**, *31*, 496.
8. Loudet, A.; Burgess, K. *Chem. Rev.* **2007**, *107*, 4891.
9. Ulrich, G.; Ziessel, R.; Harriman, A. *Angew. Chem. Int. Ed.* **2008**, *47*, 1184.
10. Haughland, R. P. *In Handbook of Fluorescent Probes and Research Products*; 9 ed.; Molecular Probes Inc: Eugene, OR, 2002.
11. Farnum, D. G.; Mehta, G.; Moore, G. G. I.; Siegal, F. P. *Tetrahedron Lett.* **1974**, 2549.
12. Hao, Z. M.; Iqbal, A. *Chem. Soc. Rev.* **1997**, *26*, 203.
13. Thompson, B. C.; Frechet, J. M. J. *Angew. Chem. Int. Ed.* **2008**, *47*, 58.
14. Wienk, M. M.; Turbiez, M.; Gilot, J.; Janssen, R. A. J. *Adv. Mater.* **2008**, *20*, 2556.
15. Tamayo, A. B.; Walker, B.; Nguyen, T. Q. *J. Phys. Chem. C* **2008**, *112*, 11545.
16. Tamayo, A. B.; Dang, X. D.; Walker, B.; Seo, J.; Kent, T.; Nguyen, T. Q. *Appl. Phys. Lett.* **2009**, *94*.
17. Yanagisawa, H.; Mizuguchi, J.; Aramaki, S.; Sakai, Y. *Jpn. J. Appl. Phys.* **2008**, *47*, 4728.
18. Zhu, Y.; Rabindranath, A. R.; Beyerlein, T.; Tieke, B. *Macromol.* **2007**, *40*, 6981.
19. Jiang, Y. H.; Wang, Y. C.; Hua, J. L.; Qu, S. Y.; Qian, S. Q.; Tian, H. *J. Polym. Sci., Part A: Polym. Chem.* **2009**, *47*, 4400.
20. Guo, E. Q.; Ren, P. H.; Zhang, Y. L.; Zhang, H. C.; Yang, W. J. *Chem. Commun.* **2009**, 5859.
21. Harriman, A.; Mallon, L. J.; Goeb, S.; Ziessel, R. *Phys. Chem. Chem. Phys.* **2007**, *9*, 5199.
22. Harriman, A.; Mallon, L.; Ziessel, R. *Chem. Eur. J.* **2008**, *14*, 11461.
23. Harriman, A.; Mallon, L. J.; Goeb, S.; Ulrich, G.; Ziessel, R. *Chem. Eur. J.* **2009**, *15*, 4553.

24. Dewey, T. G. *Acc. Chem. Res.* **1992**, *25*, 195.
25. Harriman, A.; Sauvage, J. P. *Chem. Soc. Rev.* **1996**, *25*, 41.
26. Speiser, S. *Chem. Rev.* **1996**, *96*, 1953.
27. Barigelletti, F.; Flamigni, L. *Chem. Soc. Rev.* **2000**, *29*, 1.
28. Benniston, A. C.; Harriman, A. *Chem. Soc. Rev.* **2006**, *35*, 169.
29. Harriman, A.; Mallon, L. J.; Elliot, K. J.; Haefele, A.; Ulrich, G.; Ziessel, R. *J. Am. Chem. Soc.* **2009**, *131*, 13375.
30. Bohr, H.; Greisen, P.; Malic, B. *Condens. Matter Theor.* **2009**, *23*, 329.
31. Nakamura, Y.; Aratani, N.; Osuka, A. *Chem. Soc. Rev.* **2007**, *36*, 831.
32. Qin, W.; Leen, V.; Dehaen, W.; Cui, J.; Xu, C.; Tang, X.; Liu, W.; Rohand, T.; Beljonne, D.; Averbeke, B. V.; Clifford, J. N.; Driesen, K.; Binnemans, K.; Auweraer, M. V. d.; Boens, N. l. *J. Phys. Chem. C* **2009**, *113*, 11731.
33. Banuelos, J.; Lopez Arbeloa, F.; Arbeloa, T.; Salleres, S.; Vilas, J. L.; Amat-Guerri, F.; Liras, M.; Lopez Arbeloa, I. *J. Fluoresc.* **2008**, *18*, 899.
34. Bañuelos-Prieto, J.; Agarrabeitia, A. R.; Garcia-Moreno, I.; Lopez-Arbeloa, I.; Costela, A.; Infantes, L.; Perez-Ojeda, M. E.; Palacios-Cuesta, M.; Ortiz, M. J. *Chem. - Eur. J.* **2010**, *16*, 14094.
35. Duran-Sampedro, G.; Agarrabeitia, A. R.; Garcia-Moreno, I.; Costela, A.; Bañuelos, J.; Arbeloa, T.; López Arbeloa, I.; Chiara, J. L.; Ortiz, M. J. *Eur. J. Org. Chem.* **2012**, *2012*, 6335.
36. Ziessel, R.; Ulrich, G.; Olivier, J. H.; Bura, T.; Sutter, A. *Chem. Commun.* **2010**, *46*, 7978.
37. Ziessel, R.; Ulrich, G.; Harriman, A.; Alamiry, M. A. H.; Stewart, B.; Retailleau, P. *Chem. - Eur. J.* **2009**, *15*, 1359.
38. Hablot, D.; Retailleau, P.; Ziessel, R. *Chem. Eur. J.* **2010**, *16*, 13346.
39. Ziessel, R.; Alamiry, M. A. H.; Elliott, K. J.; Harriman, A. *Angew. Chem. Int. Ed.* **2009**, *48*, 2772.
40. Scholes, G. D. *Annu. Rev. Phys. Chem.* **2003**, *54*, 57.
41. Knox, R. S.; van Amerongen, H. *J. Phys. Chem. B* **2002**, *106*, 5289.
42. Rurack, K.; Kollmannsberger, M.; Daub, J. *Angew. Chem. Int. Ed.* **2001**, *40*, 385.
43. Coskun, A.; Deniz, E.; Akkaya, E. U. *Org. Lett.* **2005**, *7*, 5187.
44. Turfan, B.; Akkaya, E. U. *Org. Lett.* **2002**, *4*, 2857.
45. Gareis, T.; Huber, C.; S. Wolfbeis, O.; Daub, J. *Chem. Commun.* **1997**, 1717.
46. Rurack, K.; Kollmannsberger, M.; Resch-Genger, U.; Daub, J. *J. Am. Chem. Soc.* **2000**, *122*, 968.

47. Qin, W.; Rohand, T.; Baruah, M.; Stefan, A.; der Auweraer, M. V.; Dehaen, W.; Boens, N. *Chem. Phys. Lett.* **2006**, *420*, 562.
48. Harriman, A.; Ziessel, R. *Photochem. Photobiol. Sci.* **2010**, *9*, 960.
49. Catalán, J. *J. Phys. Chem. B* **2009**, *113*, 5951.
50. Qin, W.; Baruah, M.; Van der Auweraer, M.; De Schryver, F. C.; Boens, N. *J. Phys. Chem. A* **2005**, *109*, 7371.
51. Rohand, T.; Lycoops, J.; Smout, S.; Braeken, E.; Sliwa, M.; Van der Auweraer, M.; Dehaen, W.; De Borggraeve, W. M.; Boens, N. *Photochem. Photobiol. Sci.* **2007**, *6*, 1061.
52. Bovey, F. A.; Yanari, S. S. *Nature* **1960**, *186*, 1042.
53. Bosque, R.; Sales, J. *J. Chem. Inf. Comput. Sci.* **2002**, *42*, 1154.
54. Qin, W. W.; Baruah, M.; Van der Auweraer, M.; De Schryver, F. C.; Boens, N. *J. Phys. Chem. A* **2005**, *109*, 7371.
55. Englman, R.; Jortner, J. *Mol. Phys.* **1970**, *18*, 145.
56. Xu, Q.-H.; Fayer, M. D. *J. Chem. Phys.* **2002**, *117*, 2732.
57. McIntosh, A. R.; Siemiarczuk, A.; Bolton, J. R.; Stillman, M. J.; Ho, T. F.; Weedon, A. C. *J. Am. Chem. Soc.* **1983**, *105*, 7215.
58. Croce, R.; Zucchelli, G.; Garlaschi, F. M.; Jennings, R. C. *Biochem.* **1998**, *37*, 17355.
59. Zoon, P. D.; Brouwer, A. M. *Photochem. Photobiol. Sci.* **2009**, *8*, 345.
60. Metz, D. J.; Glines, A. *J. Phys. Chem.* **1967**, *71*, 1158.
61. Alamiry, M. A. H.; Bahaidarah, E.; Harriman, A.; Olivier, J. H.; Ziessel, R. *Pure Appl. Chem.* **2013**, *85*, 1349.
62. Alamiry, M. A. H.; Hagon, J. P.; Harriman, A.; Bura, T.; Ziessel, R. *Chem. Sci.* **2012**, *3*, 1041.
63. Alamiry, M. A. H.; Benniston, A. C.; Hagon, J.; Winstanley, T. P. L.; Lemmetyinen, H.; Tkachenko, N. V. *RSC Adv.* **2012**, *2*, 4944.
64. Harris, C. M.; Selinger, B. K. *J. Phys. Chem.* **1980**, *84*, 1366.
65. Ziessel, R.; Ulrich, G.; Harriman, A.; Alamiry, M. A. H.; Stewart, B.; Retailleau, P. *Chem. Eur. J.* **2009**, *15*, 1359.

Chapter 6. Experimental Methods

6.1 Materials

All solvents used in this work were of spectroscopic quality as obtained from Sigma-Aldrich and were used as received after checking for fluorescent impurities. An exception to this general rule concerns solvents used for electrochemistry, which were dried over appropriate reagents and freshly distilled before being stored in brown bottles and used quickly.[1,2] Tetra-*n*-butylammonium tetrafluoroborate (TBATFB) from Fluka was used as background electrolyte for all electrochemistry measurements. As is well known, solvent properties affect the physical behaviour of many molecules and this is evident from spectroscopic measurements, such as the peak energy and the intensity of absorption or emission transitions. These solvent properties were taken from the literature and, in order to avoid uncertainties caused by inconsistent reporting, a single source was used wherever possible.[3] On occasion, additional properties such as the Catalán factor was taken from primary literature sources as required.[4] The most common solvent used in our work is 2-methyltetrahydrofuran (MTHF) since this solvent can be employed over a wide temperature range and is not subject to unusual pressure sensitivity. The effects of temperature on the density and polarity of MTHF are available in the literature.[5] For the pressure effect on MTHF, we relied on results generated by Dr. M. A. H. Alamiry of the Molecular Photonics Laboratory.

The large range of compounds described in this study was obtained from Dr. Raymond Ziessel (Université Louis Pasteur de Strasbourg). These compounds were synthesized and purified in Strasbourg and were used as received. Any suspicion of an impurity was reported to Dr. Ziessel and further purification was undertaken. In all cases, the compounds were fully characterised by modern analytical procedures as reported in the primary publications resulting from this collaboration. We would like to acknowledge our deep gratitude for this collaboration.

The reference compounds used to calculate fluorescence quantum yields (Φ_{flu}) are Cresyl Violet,[6] sulfonated aluminium phthalocyanine (ALSPC),[7] Rhodamine 19,[8] and Merocyanine 540.[9] In certain cases, other Bodipy dyes with known Φ_{flu} were used as secondary control compounds for the Bodipy dyes under investigation. For example, compound 1 (**BODIPY**) in Figure 1, which was studied in Chapter 2, was used as a reference with which to determine Φ_{flu} for the Bodipy compounds examined in Chapter

3. Moreover, the blue Bodipy dye, **B**, (compound 2 in Figure 1) as studied in Chapter 5, was used also in Chapters 3 and 4 as a reference compound. It is worth noting that there are many requirements to take into account when selecting the reference compound for emission spectral measurements. For example, the lowest-energy absorption transitions of sample and reference should be comparable, the same excitation wavelength must be used, a common solvent has to be employed and the respective quantum yields should be in the same range.[10]

Poly(ethylene) film and poly(methyl methacrylate) (PMMA), respectively, were used to prepare solid films or to modify the viscosity of a solvent.[11,12]

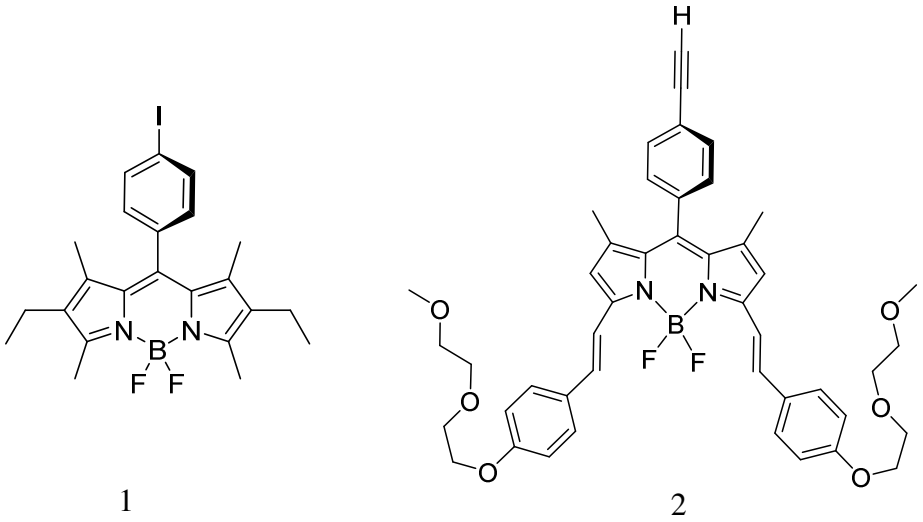

Figure 1. Chemical formulae of some BODIPY-based reference compounds.

6.2 UV-visible absorption spectroscopy

Routine absorption spectra were recorded using a Hitachi U3310 dual-beam spectrophotometer. An appropriate wavelength range, usually stretching from 250 to 800 nm, was chosen. The scan speed (usually set to120 nm/min) and slit width (usually 1 nm) were selected as appropriate. Automatic baseline correction was carried out for all samples with pure solvent in both optical cells, before replacing the solvent with the solution of interest. These sample cells were usually constructed from optical quality quartz with 1 cm path length and were cleaned with nitric acid, washed copiously with water, then with acetone and dried in an oven. In addition, the spectrophotometer was used to find the exact absorbance at a fixed wavelength. Other studies, notably the pressure-dependence work, used a Perkin-Elmer Lambda 35 spectrophotometer. Applying the Beer-Lambert law[13] (Equation 1) converts absorbance (A) to the molar

absorption coefficient (ε_{max}) in units of $M^{-1}cm^{-1}$ provided the actual molar concentration (c) and path length in cm (l) are known.

$$A = \varepsilon_{max}.c.l \qquad \text{Equation (1)}$$

6.3 Fluorescence spectroscopy

Routine emission spectra were collected using a Hitachi F-4500 fluorescence spectrophotometer. Fluorescence measurements were obtained using deoxygenated dilute solutions with absorbance between 0.05 - 0.1 at the excitation wavelength in a 1 cm path length quartz cell. The cuvette was cleaned and dried before use and the solvent was checked for fluorescent impurities. Appropriate scan rate (mostly often set to 240 or 60 nm/min), excitation and emission slit widths (in most cases 2.5 nm) and optical filters were chosen, depending on the experimental conditions. Moreover, in the case of a weak emission signal, larger slit widths (up to 10 nm) were used but this adds some uncertainty when determining the peak position. Wherever possible, this uncertainty was kept to a minimum by careful choice of the excitation wavelength. In addition, and in the case of any unexpected fluorescence peak, the solvent was further checked for fluorescent impurities. The main idea of using the optical filter is to remove any scattered light from the excitation source.

There is some debate about the exact form needed to correct for changes in the refractive index of the solvent. Chen[14] has stated that is no need for the refractive index correction as changing the refractive index does not affect the fluorescence signal, while Lampert et al.[15] and others[16] have confirmed the relationship between the refractive index and the emission radiative rate constant in many different systems. So, in order to avoid any error, the refractive index was taken into consideration as described later in this Chapter. Moreover, in order to avoid re-absorption or inner-filter effects, dilute solutions of the sample were used to record both fluorescence and excitation spectra. It might be pointed out that all emission spectra were fully supported on the basis of comparing the excitation spectrum with the corresponding absorption spectrum recorded in the same solvent. In the case of a solid sample, such as a KBr disk or microscope slide, it was not possible to obtain an accurate quantum yield.[10] Instead, relative emission intensities were used as appropriate.

6.4 Lifetime measurement

Fluorescence lifetimes were measured at room temperature using several complementary experimental protocols. Routine measurements were made with a PTI

EasyLife set-up using pulsed laser diodes (310, 440, 505, 525 or 635 nm output) as excitation source. Samples were optically dilute, with the absorbance at the excitation wavelength being approximately 0.10, and 150 runs were signalled averaged before data analysis. Fluorescence was isolated using a series of narrow band-pass filters. In each case, a minimum of three different time bases was used for data collection. This instrument gives highly reproducible lifetimes for the control compounds and also for the terminal acceptor in the arrays. In most cases, after iterative re-convolution of the instrument response function (IRF) and standard Marquardt analysis, single exponential fits were recovered as judged by the goodness-of-fit criteria established by Eaton[17] and by O'Connor and Phillips.[18] These analytical tests included minimization of chi-squared, visual inspection of weighted residuals, the Demas method of moments, and the phase plane method (for exponential decays only). The derived lifetimes, being in the range of several nanoseconds and well outside that of the IRF, were confirmed by frequency domain, phase modulation measurements made using the Fluorolog tau-3 spectrophotometer. In this latter mode, the emission wavelength was controlled by a monochromator / slit combination and data analysis was made by deconvolution against a reference compound having a mono-exponential decay. For this latter purpose, the reference compounds used after extensive purification were: 9-cyanoanthracene in cyclohexane (λ_{ex} = 310 nm, τ_s= 12.6 ns), Coumarin 153 in methanol (λ_{ex} = 355 nm, τ_s = 4.2 ns), Erythrosin B in methanol (λ_{ex} = 490 nm, τ_s = 0.50 ns), and Rhodamine B in methanol (λ_{ex} = 520 nm, τ_s = 2.6 ns).[9] In each case, 5 independent determinations of the lifetime were made and the error limits quoted in the text refer to standard deviations calculated as usual.[19] In our hands, the temporal resolution of the EasyLife TCSPC setup was restricted to around 200 ps after deconvolution. Frequency domain measurements made with the Fluorolog tau-3 showed a similar limitation, although in principle this instrument is capable of resolving faster decay processes.

Improvements in performance were obtained by using a pulsed LED as excitation source with high modulation depth. Thus, by replacing the xenon excitation source with a sub-ns (FWHM = 0.45 ns) UV LED emitting at 297 nm equipped with an appropriate driver and crystal clock as cross-correlation generator, together with an MCP PMT, it was possible to increase the modulation frequency to around 600 MHz.[20] With this set-up, and using Erythrosin B in water (τ_s= 85 ± 5 ps) as the reference for deconvolution analyses, it was possible to push the temporal resolution to ca. 20 ps as demonstrated by measurement of the[21] fluorescence lifetime of Xanthione in cyclohexane; the experimental value of τ_s was 21 ± 3 ps compared to the literature value[22] of 17 ps.

However, comparable lifetimes could not be obtained for mixtures of dyes or in cases of non-exponential kinetics. Suitable conditions were found using time-correlated, single photon counting with a picosecond laser diode (FWHM <70 ps) as excitation source and with a cooled MCP PMT as detector interfaced to a high radiance monochromator. With iterative re-convolution of the IRF, the temporal resolution of this set-up was better than 20 ps as estimated by measurement of[21] emission from Xanthione in methanol; the experimental value for τ_s was 15 ± 3 ps compared to the literature value[22] of 13 ps. With this particular set-up, global analysis protocols could be used whereby fluorescence decays were collected over a modest range of detection wavelengths, each measurement being made on several different time bases.[23] Low noise levels, taken in conjunction with fitting data to a predetermined model as outlined in the text, help circumnavigate[24] difficulties associated with the close overlap of fluorescence spectral profiles. Convergence of the global fitting algorithms was accelerated by providing appropriate initial guesses based on single wavelength measurements. The randomly distributed residuals were used to indicate good fits and thereby validate the proposed model.

Again, the sample absorbance was adjusted to be around 0.15 or less at the excitation wavelength. Solutions of Ludox in distilled water were used to measure the scattered laser light and obtained the IRF. Figure 2 presents an example of the emission decay curve.

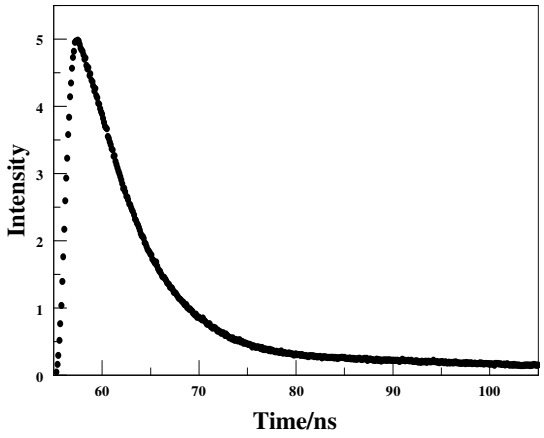

Figure 2. Example of an emission decay curve obtained in lifetime measurements.

6.5 Temperature-dependent spectroscopic studies

6.5.1 Low-temperature

Low-temperature dependent studies were performed using an Oxford Instruments Optistat DN cryostat connected to an ITC temperature controller (Figure 3). The cryostat can be installed into any of our existing spectrophotometers using adapters machined in the workshop. This allows absorption, excitation and emission spectra to be recorded within the range 77-340K. All solutions were purged with nitrogen gas for 15 minutes before lowering the temperature in order to eliminate problems caused by the presence of liquid oxygen. The sample solution were kept optically dilute, meaning that the absorbance at the excitation wavelength was less than 0.1, in order to prevent

any re-absorption processes or prevent aggregation in the low temperature regime. During the experiment, the sample was left to equilibrate for at least 10 minutes at each temperature before recording the spectrum and the temperature was increased systematically in 10-degree steps. Wherever possible, MTHF was used as the solvent as it forms a rigid, optical at temperatures below about 110K. As it cools, MTHF undergoes an increase in density that necessitates a correction of the emission intensity due to the corresponding increase in solute concentration. There is also a change in refractive index and dielectric constant that can affect the emission maximum.[25,26]

Figure 3. Photograph of the cryostat used for low-temperature studies.

6.5.2 High-temperature

High-temperature studies were carried out using solid samples (e.g., a KBr disc) with a temperature-controlled, demountable liquid cell from Harrick Scientific Corporation (Figure 4). The cell was fitted into the spectrophotometer in order to record emission spectra over the temperature range 290-540K. The sample was held for 10 minutes at each temperature before the measurement and the temperature was increased gradually. Some high-temperature studies in the range 10-60 °C were made for liquid samples using a Grant LT D6G circulating system connected directly to the instrument. Similar studies were made using a Peltier controller.

Figure 4. Picture of the high-temperature cell and the temperature controller used in this work.

6.6 High-pressure studies

The high-pressure rig from Stansted Fluid Power Ltd was used to apply pressure on the sample under study. The general layout comprises a hydraulic compressor constructed from stainless steel. Ethanol is used as the hydraulic medium. The two-stage pump is fitted with an intensifier and diaphragm compressor capable of reaching about 700 MPa (Figure 5). Figure 6 shows the sample chamber that has been machined from a block of stainless steel and is equipped with three optical windows and a Bourdon pressure gauge. The windows show good transmission at wavelengths longer than 370 nm. For

absorption measurements, the sample chamber was connected to a Perkin-Elmer Lambda-5 spectrophotometer using input and output optical fibre bundles. The absorbance signal was calibrated by reference to the sample solution being recorded in conventional cuvettes with background subtraction. Figure 7 shows an example of the absorption spectra after the correction regarding to the change of the solvent background under high pressure. Moreover, the changes in the absorption spectra under high pressure were used to correct the emission spectra because of changes in the intensity at the excitation wavelength induced by spectral shifting or increasing the solution density.

Figure 5. Photograph of the high-pressure rig used in this work.

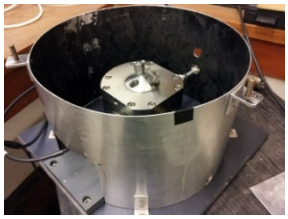

Figure 6. Cell chamber.

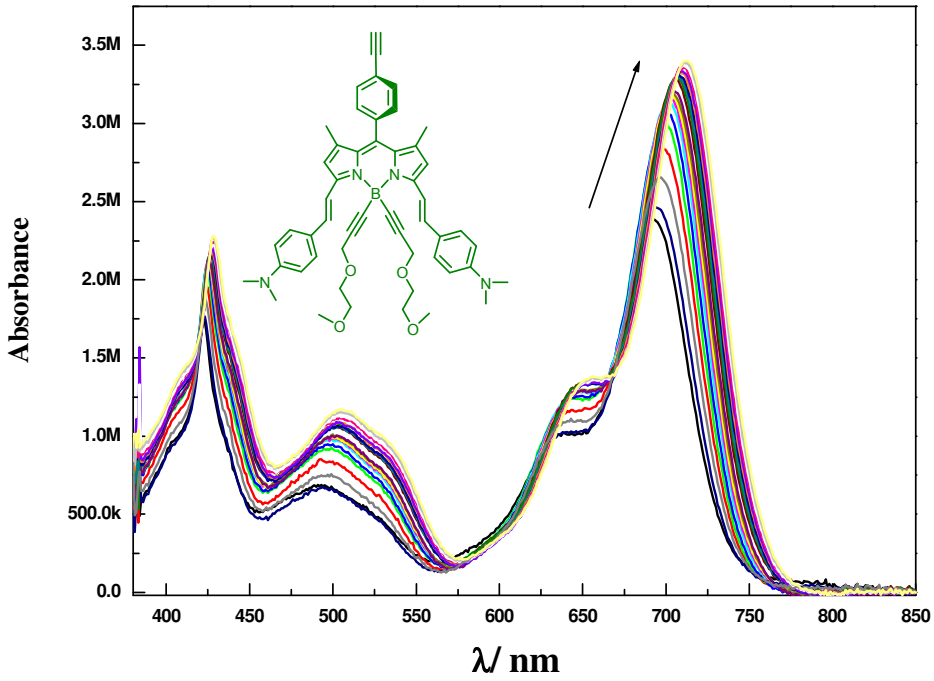

Figure 7. Example of corrected absorption spectra recorded under high pressure for the **G** dye in MTHF. The arrow indicates the direction of increasing pressure.

For emission studies, a high-power 406 nm laser diode was used as excitation source and output, collected at 90° to excitation, was directed to the spectrofluorimeter with an optical fibre bundle. Figure 8 shows an example of emission spectra recorded under high pressure.

Purpose-made cells are used to accommodate liquid samples of appropriate concentration (usually an absorbance of 0.1 at the excitation wavelength for the emission studies and 0.5 at the peak maximum for absorption studies). For fluorescence, the sample cell is a glass tube, diameter ca. 4 mm, having a narrow mouth that can be capped with a poly(ethylene) seal. The latter takes the form of a short tube that is heat-sealed at one end. For absorption measurements, a hollow glass disk fitted with a narrow inlet tube is used to hold the sample. This disk has a diameter of ca. 1 cm and a path length of 2 mm. Again, a poly(ethylene) tube is used as stopper for the cell and the actual path length can be calibrated by absorption spectroscopy. Sample cells and poly(ethylene) seals are used once and then discarded. Pressure was increased gradually up to 600 MPa in small increments.

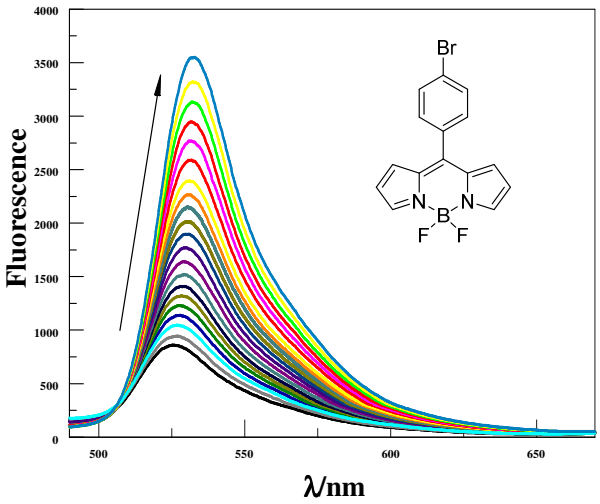

Figure 8. Recorded emission spectra under high pressure for **ROBOD** in MTHF.

6.7 Electrochemistry

Cyclic voltammetry experiments were done using an HCH Instruments Electrochemical Analyser connected to a 3-electrode system consisting of a Pt wire counter electrode, a Pt working electrode and an Ag wire or Ag/AgCl reference electrode. Tetra-*n*-butylammonium tetrafluoroborate was used as the background electrolyte and ferrocene was applied as an internal standard. These electrodes, and the solution of interest, were placed in a dry and clean glass cell to avoid any water or contamination. Dry solvent was used to prepare 0.1 M of the background electrolyte and an appropriate amount of sample (to get 1 x 10^{-3} M) was dissolved the same solution after running a

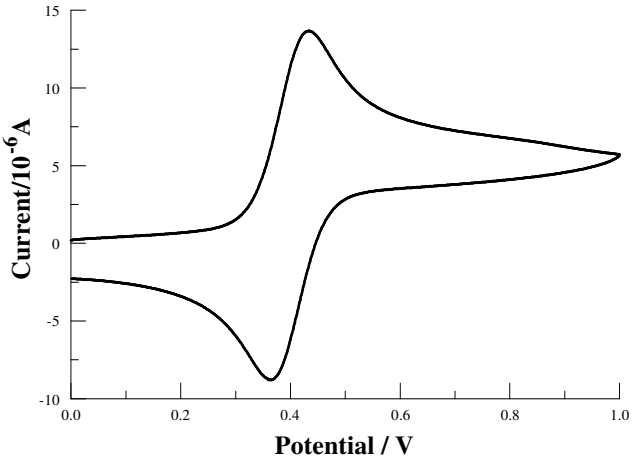

Figure 9. An example of a typical cyclic voltammogram recorded for ferrocene in dry acetonitrile containing background electrolyte.

background scan. It worth mentioning that the solution was purged with N_2 gas for around 10 minutes before and between scans so as to avoid any oxygen reduction peaks. After recording a suitable cyclic voltammogram, an appropriate amount of ferrocene (to get 1 x 10^{-3} M) was added and a new voltammogram collected under the same conditions. This strategy allows us to find the number of electrons involved in the oxidation-reduction process. Figure 9 presents an example of the reversible oxidation of ferrocene as an example of a cyclic voltammogram.

6.8 Sample preparation

Solutions were prepared by dissolving the compound in an appropriate volume of solvent. The resulting solution was diluted to produce samples suitable for spectroscopic measurements. Although the majority of our compounds were readily dissolved in organic solvents, all solutions were filtered through micro-porous disks before taking measurements in order to ensure complete dissolution. In the rare case of poor solubility of certain dyes in a particular organic solvent, putting the sample solution in an ultrasonic bath for 2-3 minutes before the filtration process usually helped overcome this problem. The KBr disks were prepared by grinding the proper weight of compound with oven-dried KBr to give 1% w/w concentration, the powdered mixture was placed in the sample holder between two metal discs and compressed under mild vacuum.

To prepare thin films, a concentrated dye solution was prepared using dichloromethane or chloroform as solvent before the required mass of PMMA was added (to get 10% w/v). The resultant solution was placed in an ultrasonic bath for 2 minutes and left to stand overnight. The spin coater from Laurell, which is shown in Figure 10, was used to obtain thin films supported on microscope slides. Minor modification of the step parameters affects the thickness and quality of the final film. In related studies, stretched films were prepared by soaking the polyethylene film in a concentrated solution of the dye in chloroform for two hours. The film was removed from the petri dish, dried with a hair dryer and cleaned by wiping with a tissue soaked in ethanol. This latter treatment is intended to remove any dye adsorbed onto the surface. The film was subsequently stretched a factor of 4-fold in length by pulling along the oriented axis.[27]

Figure 10. Photograph of the spin coater used to prepare polymer films.

6.9 Calculations

6.9.1 Fluorescence quantum yield

Fluorescence quantum yields were measured at room temperature relative to a particular reference compound by applying Equation (2).[9,28] The reference compound should possess a similar absorption spectral profile to that of the sample, in as much as this is possible, such that a suitable excitation wavelength can be identified. This needs to be on a vibrational shoulder, not on a sharp absorption band or close to an absorption minimum, in order to facilitate the excitation process at the same wavelength.

$$\Phi_{sam} = \Phi_{ref} \frac{F_{sam}(1-10^{-A_{ref}})n_{sam}^2}{F_{ref}(1-10^{-A_{sam}})n_{ref}^2} \qquad \text{Equation (2)}$$

Here, Φ is the fluorescence quantum yield for the sample (*sam*) or reference (*ref*), F is the fluorescence area, A is the absorption intensity at the excitation wavelength and n is the solvent refractive index. In order to prevent any problems relating to the concentration (i.e., self-absorption, aggregation, energy transfer) solutions of the sample and reference should have similar absorbance values at the excitation wavelength, A. Moreover, these values should be <0.1. In our experiments, data used for quantum yield determinations were collected in a single session and were taken as the average of several independent measurements. Often, several reference compounds were used in order to be sure of the final determination. Additional control studies were undertaken to ensure that the actual quantum yield was independent of solute concentration over a modest range. In all cases, the excitation spectrum was compared with the absorption spectrum recorded in the same solvent and, wherever possible, with the same slit widths. Under normal circumstances, quantum yields could be measured to within an accuracy of ±5%, although reproducibility is much higher than this limit. The correction facility installed on the instrument was checked regularly using a high concentration Rhodamine 6G in ethanol as standard; here, we used a triangular sample cell and collected emission from the front surface. The emission wavelength was standardised using a low-pressure lamp filled with a mixture of rare gases. It might be mentioned that both absorption and fluorescence spectrophotometers were serviced at 6-monthly intervals by the engineer.

Variable temperature and pressure emission studies were always referenced to the sample recorded under ambient conditions. Excitation and absorption spectra were recorded under the same conditions. In all cases, absorption spectra were recorded before and after the experiment in order to assess the importance of sample degradation. Temperature and pressure dependence studies were carried out with samples that had

been purged with dried N_2 but routine quantum yield measurements were made with air-equilibrated solutions. Spectroscopic data were exported from the operating computer and manipulated on dedicated PCs equipped with a battery of software for data analysis.

6.9.2 Radiative rate constant

The radiative rate constant serves an extremely important role in molecular photophysics, comparable to the excitation spectrum, and is seen as a critical control factor. As a matter of routine, the Strickler-Berg expression (Equation 3) was used to calculate the radiative rate constant (i.e., the inverse of the radiative lifetime of the emitter in the absence of quenching).[29]

$$1/\tau_s = k_{rad} = 2.88 \times 10^{-9} n^2 < \nu_{flu}^{-3} >_{av}^{-1} (\frac{g_l}{g_u}) \int \varepsilon d\, ln\nu \qquad \text{Equation (3)}$$

Here, τ_s is the radiative lifetime in s, k_{rad} is the radiative rate constant in s^{-1} for emission from an upper to a lower state, n is the solvent refractive index at the emission wavelength, ν_{flu} is the fluorescence maximum in cm^{-1}, g_l and g_u refer to the degeneracy of the respective lower and upper states, and the integration $\int \varepsilon d\, ln\nu$ represents the area under the curve of ε_{max} versus $ln\nu$ for the lowest-energy absorption transition as it appears in Figure 11. It should be mentioned that the Strickler-Berg expression has several important limitations. These include the notion that the Stokes' shift should be modest, thereby indicating the absence of major structural changes on excitation, and that the molar absorption coefficient should be reasonably large. The latter requirement is intended to eliminate n,π* and charge-transfer transitions from the analysis. Additional attention should be given to factors such as proton transfer, specific solvent effects, state degeneracy, distortions in refractive index caused by non-linear optical behaviour and corrections for solvent cavity effects.

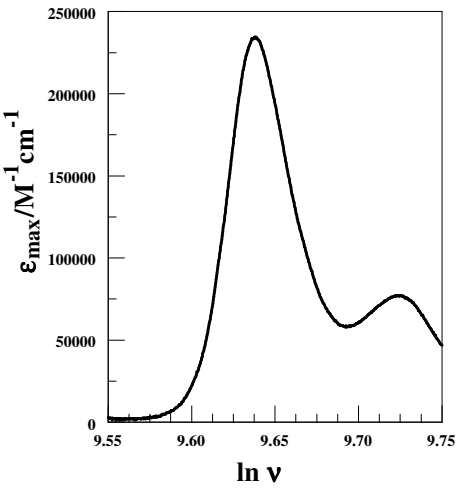

Figure 11. The integral of the main absorption transition in **B** Bodipy.

In most of our work, applying Equation (3) gave good agreement with the experimental values. Thus, the radiative and nonradiative rate constants; k_{rad} and k_{nrd}, can be found experimentally from Equations (4) and (5).

$$\Phi_{flu} = k_{rad}.\tau_s \qquad \text{Equation (4)}$$

$$k_{nrd} = (1 - \Phi_{flu})/\tau_s \qquad \text{Equation (5)}$$

6.9.3 Energy transfer rate constant

Throughout this work, we have made extensive use of the Förster theory for electronic energy transfer, although in certain cases the overall process probably contains a contribution from Dexter electron exchange. In treating the energy-transfer step in terms of the Förster mechanism we have applied Equation (6).[30]

$$k_{EET} = \frac{2\pi}{\hbar} |V_{DA} sK|^2 J_{DA} \qquad \text{Equation (6)}$$

$$J_{DA} = AB \int \frac{F_D(\nu)}{\nu^3} . \frac{\varepsilon_A(\nu)}{\nu} d\nu \qquad \text{Equation (7)}$$

$$\mathrm{V_{DA}} = \frac{\mu_D \mu_A}{\mathrm{R_{DA}^3}(4\pi\varepsilon_\circ)} \qquad \text{Equation (8)}$$

$$\mu^2 = 9.186 \times 10^{-3} n \int \frac{\varepsilon}{\nu} d\nu \qquad \text{Equation (9)}$$

$$s = \frac{3}{2n^2+1} \qquad \text{Equation (10)}$$

Here, k_{EET} is the intramolecular rate constant for electronic energy transfer as reported in s^{-1}, V is the electronic coupling matrix element between the donor and acceptor calculated from Equation (8) and converted into cm^{-1}, s is the Onsager cavity screening factor calculated from Equation (10), K is the orientation factor (which has a value of 0.67 for random orientations),[31] J_{DA} is the spectral overlap integral between the donor emission(F_D) and the acceptor absorption(ε_A) calculated using Equation (7). Other terms needed for the calculation include the transition dipole moment vector (μ) calculated from Equation (9),[32] the separation distance between donor centre and acceptor centre (R_{DA}) and the molar absorption coefficient (ε_{max}) for the molecule transition. In order to compute J_{DA}, the acceptor absorption and the donor fluorescence spectra are recorded in the same solvent, wavelength (λ) is converted to wavenumber (ν) and absorbance is presented in terms of ε_{max}. Both spectral profiles are reduced (absorption divided by wavenumber and emission divided by wavenumber cubed) and their total integrated area normalised to unity (Figure 12). Finally the overlap integral is calculated with respect to wavenumber and presented in units of cm.

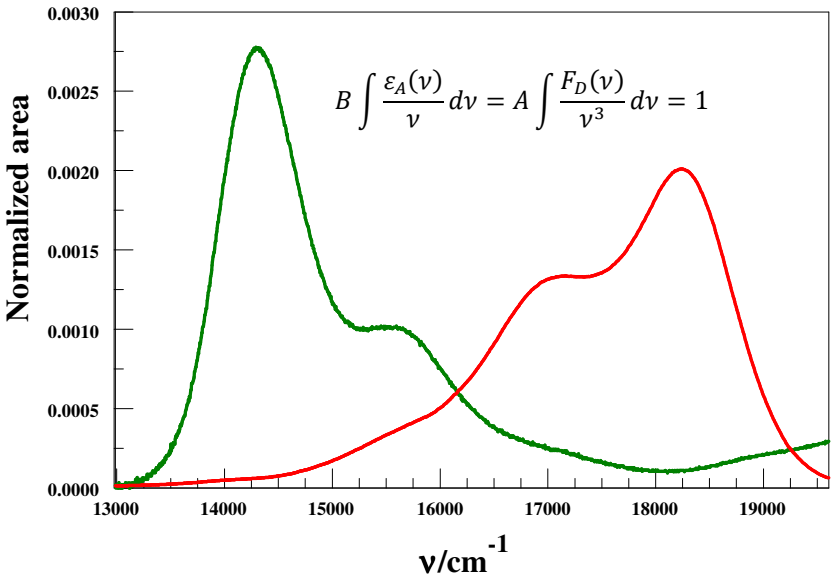

Figure 12. The reduced spectra of **G** Bodipy absorption and **DPP** emission as used to calculate the spectral overlap integral in MTHF.

It is necessary to calculate a value for μ using absorption spectral data according to Equation (9). Here, the absorption spectrum is presented as ν instead of λ while the reduced intensity is expressed in term of ε/ν as it appear in Figure (13). The integration $\int\frac{\varepsilon}{\nu}d\nu$ refers to the area under the curve in Figure 13 and by applying Equation (9) directly, the transition dipole moment is obtained in unit of Debye (D).

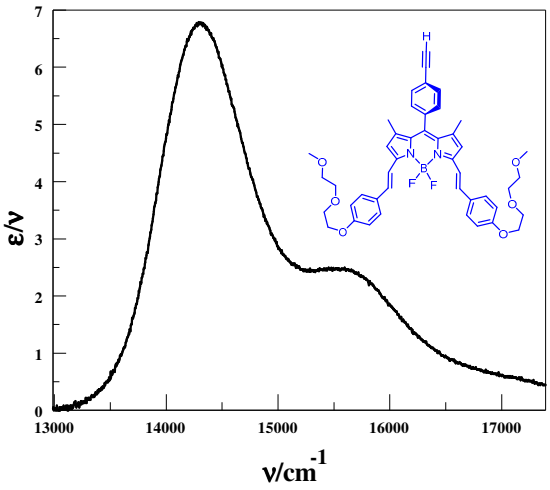

Figure 13. The integration curve of absorption spectrum of **B** Bodipy in MTHF.

It worth mentioning here that Equation (9) is a different representation of Equation (11), which is the original form derived by Förster, and the re-arranged Equation (12). [32]

$$\varepsilon_A(\nu) = \frac{8\pi^3}{3}\cdot\frac{N_A\nu}{1000hcnln10}\cdot\mu_A^2(\nu) \qquad \text{Equation (11)}$$

$$|\mu_A^2| = \frac{3000ln10hcn}{8N_A\pi^3}\int\frac{\varepsilon_A(\nu)}{\nu} \qquad \text{Equation (12)}$$

6.9.4 Energy transfer probability

The probability and the quantum yield for electronic energy transfer (EET) are different expressions of the efficiency of EET. There are many equations able to calculate the probability (P_{EET}) depending on the available information. In Equation (13), the probability can be calculated as a ratio between the energy transfer rate constants (k_{EET}) to the total rate of decay of the donor species in the absence of an acceptor (τ_S^{-1}). It can also be measured from the relative donor fluorescence or lifetime in the presence and absence of the acceptor as it appears in Equations (14) and (15), respectively. [33]

$$P_{EET} = \frac{k_{EET}}{(k_{EET}+\tau_S^{-1})} \qquad \text{Equation (13)}$$

$$P_{EET} = 1 - \frac{\Phi_{DA}}{\Phi_D} \qquad \text{Equation (14)}$$

$$P_{EET} = 1 - \frac{\tau_{DA}}{\tau_D} \qquad \text{Equation (15)}$$

The same probability is commonly expressed as Equation is (16), which depends on the critical distance for energy transfer between the particular set of reactants.[34]

$$P_{EET} = \frac{R_0^6}{R_0^6+R_{DA}^6} \qquad \text{Equation (16)}$$

Here, R_0 is the Förster critical distance at which the energy transfer probability is 50% and can be calculated from Equation (17) while R_{DA} is the effective distance between the donor and acceptor.[31]

$$R_0^6 = 5.86 \times 10^{-25} \frac{\Phi_D}{n^4} J_{DA} \qquad \text{Equation (17)}$$

6.10 Spartan

The Spartan'06 program was employed to compute energy-minimized geometries from which to obtain the separation distances used in the various calculations relating to electronic energy transfer. The same program was used to compute the properties of the respective HOMO and LUMO energies and iso-density representations as required. Figure 14 shows the HOMO and LUMO iso-density plots for the conventional Bodipy molecule as an example. A different example is presented in Figure 15 and this refers to the energy-minimized structure of **B -C_1- DPP,** which is described in Chapter 4. The labelled atoms are used to compute distances between the donor and the acceptor sites where the required distance is the average of the two values.

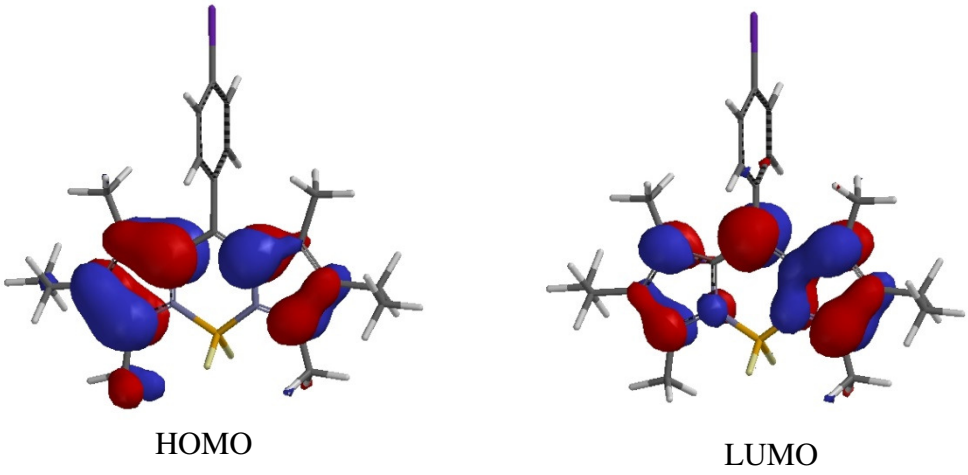

Figure 14. Pictorial representations of the computed iso-density plots for the HOMO and LUMO of the conventional Bodipy molecule as calculated by the semi-empirical AM1 method.

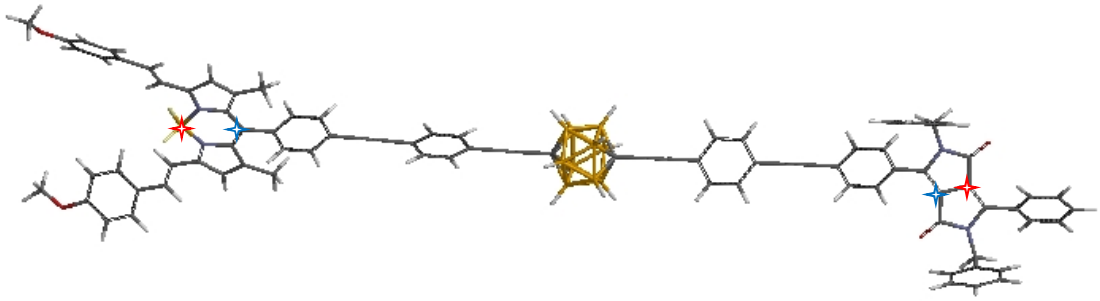

Figure 15. Energy-minimized structure of **B-C$_1$-DPP** and the measured distances as calculated using the Spartan program.

6.11 HyperChem

HyperChem is also a computational chemistry program that offers many different force fields and quantum mechanics capabilities. It was used to monitor the annealing process by calculating the molecular dynamics simulations and producing some possible structures likely to exist under different conditions. Figure 16 shows some of the computed geometries for **B-C$_1$-DPP** as an example of the annealing process.

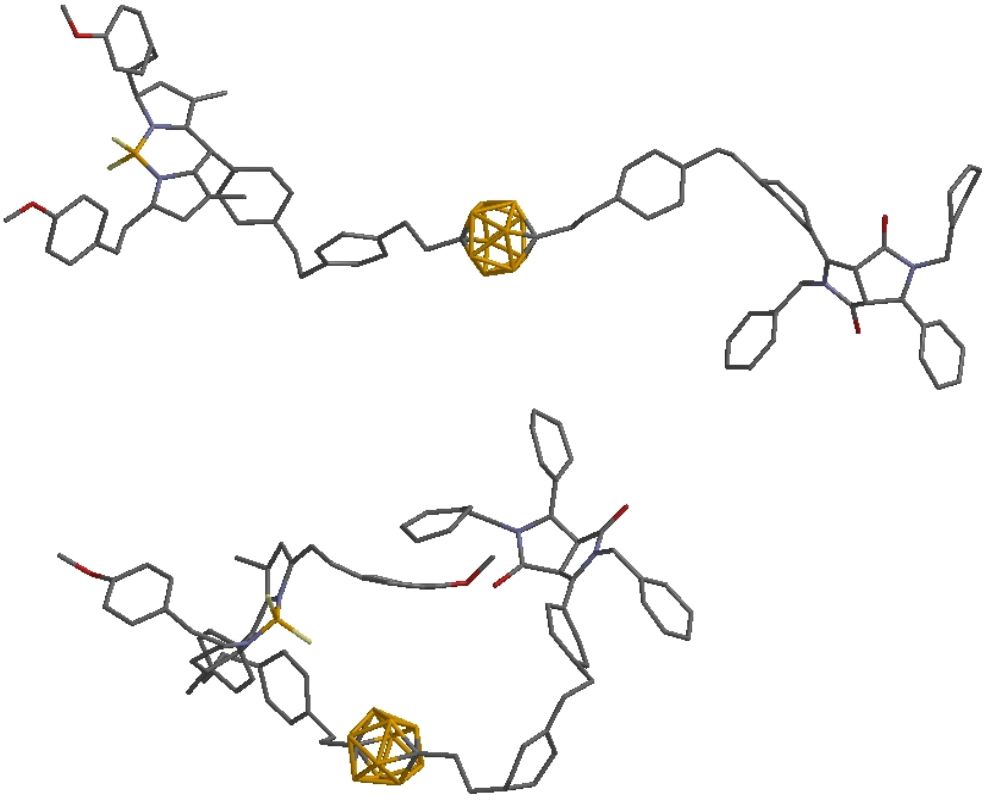

Figure 16. Examples of computed molecular geometries using the stepwise annealing process for **B-C$_1$-DPP**.

6.12 Scientist

The experimental data were fit to model equations using the statistical MicroMath Scientist program in order to derive the various parameters that accompany the process of interest. This software allows the operator to write a mathematical model, from the simplest linear functions to complex systems of differential equations or non-linear equations, and then compare the experimental data to the computed values. We have used the Scientist program for most of our routine computations. In particular, we have conducted analyses of temperature-dependent experiments in terms of multiple activated and activationless processes to find the barriers and limiting rate constants. As is shown in Figure 17, there is reasonable agreement between the fitted curve and the experimental points for a temperature-dependent emission process.

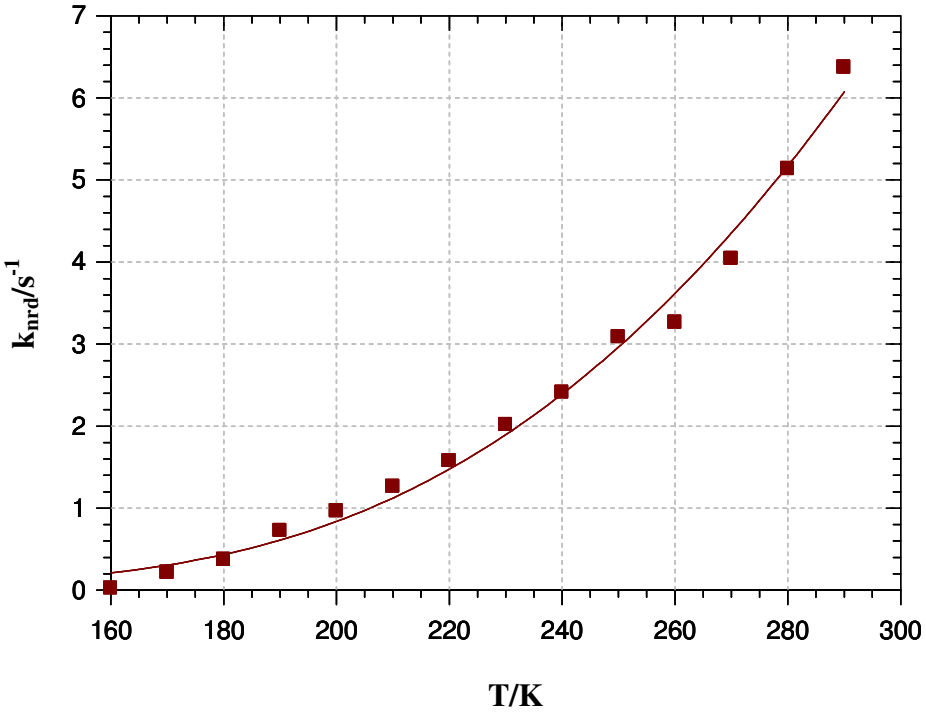

Figure 17. Example of fitted experimental data of temperature effect on k_{nrd} of **ROBOD** using the Scientist program.

6.13 PeakFit

The PeakFit V4 program is used to deconstruct a broad spectral profile into a series of components of predetermined band-shape and/or spectral bandwidth. The program was developed originally to analyse HPLC chromatograms but has become the standard with which to deconstruct emission and absorption spectral traces. In most cases, we have deconstructed the spectra into the minimum number of Gaussian-shaped bands.[35] Output from the program includes such parameters as the peak position, intensity, area, and the full-width at half-maximum (FWHM). Prior to fitting the spectrum, it is necessary to convert wavelength into wavenumber, correct for any obvious distortions in the baseline, isolate the spectral region of interest (i.e., the lowest-energy absorption transition for calculation of the oscillator strength) and convert the spectral profile into reduced spectra. The program estimates the number of Gaussian components needed to obtain a good fit but the operator needs to decide if these components need to be of the same half-width. Fitting then proceeds until the residuals are minimised. Additional components can be added or removed in order to improve the significance of the fit.[36] Figure 18 shows an example of a typical PeakFit analysis. Application of this fitting routine tends to work well when the same compound is analysed under different temperature or pressure changes or as a function of solvent polarity.

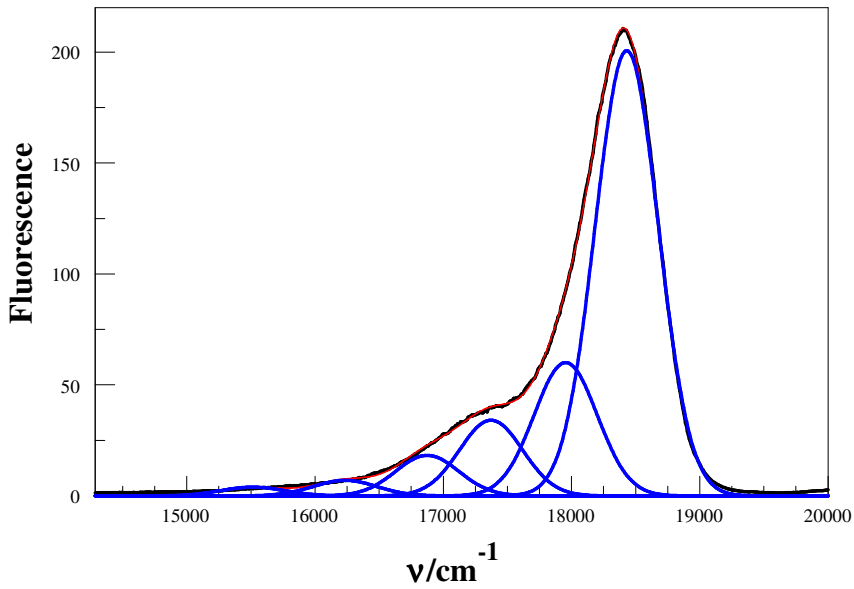

Figure 18. Example of Peak fit result. The black and red lines are the original and fitted spectra while the blue lines are individual Gaussian bands.

6.14 References

1. Williams, D. B. G.; Lawton, M. *J. Org. Chem.* **2010**, *75*, 8351.
2. Riddick, J. A. B., W. B.; Sakano, T. K. *Organic solvents*; 4th ed.; Wiley-Interscience: New York, 1986.
3. Abboud, J. L. M.; Notario, R. *Pure Appl. Chem.* **1999**, *71*, 645.
4. Catalán, J. *J. Phys. Chem. B* **2009**, *113*, 5951.
5. Zoon, P. D.; Brouwer, A. M. *Photochem. Photobiol. Sci.* **2009**, *8*, 345.
6. Magde, D.; Brannon, J. H.; Cremers, T. L.; Olmsted, J. *J. Phys. Chem.* **1979**, *83*, 696.
7. Ambroz, M.; Beeby, A.; MacRobert, A. J.; Simpson, M. S. C.; Svensen, R. K.; Phillips, D. *J. Photochem. Photobiol., B* **1991**, *9*, 87.
8. Magde, D.; Wong, R.; Seybold, P. G. *Photochem. Photobiol.* **2002**, *75*, 327.
9. Rurack, K.; Spieles, M. *Anal. Chem.* **2011**, *83*, 1232.
10. Lakowicz, J. R. *Principles of Fluorescence Spectroscopy*; 3rd ed.; Springer Science: New York, USA, 2006.
11. Thulstrup, E. W.; Michl, J. *J. Am. Chem. Soc.* **1982**, *104*, 5594.
12. Annable, T.; Buscall, R.; Ettelaie, R.; Whittlestone, D. *J. Rheol.* **1993**, *37*, 695.
13. Atkins, P. W. *Physical chemistry*; 6th ed.; Oxford university press: Oxford, 1998.
14. Chen, R. F. *Anal. Lett.* **1981**, *14*, 1591.
15. Lampert, R. A.; Meech, S. R.; Metcalfe, J.; Phillips, D.; Schaap, A. P. *Chem. Phys. Lett.* **1983**, *94*, 137.
16. Toptygin, D. *J. Fluoresc.* **2003**, *13*, 201.
17. Eaton, D. F. *Pure Appl. Chem.* **1990**, *62*, 1631.
18. O'Connor, D. V.; Phillips, D. *Time-Correlated Single Photon Counting*; Academic Press: London, 1984.
19. *Guide to the Expression of Uncertainty in Measurement*; 1st edition ed.; International Organization for Standardization: Geneva, 1993.
20. Herman, P.; Vecer, J. *Ann. N.Y. Acad. Sci.* **2008**, *1130*, 56.
21. Fischer, M.; Georges, J. *Chem. Phys. Lett.* **1996**, *260*, 115.
22. Ho, C.-J.; Motyka, A. L.; Topp, M. R. *Chem. Phys. Lett.* **1989**, *158*, 51.
23. Resch-Genger, U.; Hoffmann, K.; Hoffmann, A. *Ann. N.Y. Acad. Sci.* **2008**, *1130*, 35.
24. Van Stokkum, I. H. M. In *Instrumentation and Measurement Technology Conference, 1996. IMTC-96. Conference Proceedings. Quality Measurements: The Indispensable Bridge between Theory and Reality., IEEE* 1996; Vol. 1, p 168.

25. Xu, Q.-H.; Fayer, M. D. *J. Chem. Phys.* **2002**, *117*, 2732.
26. Renge, I. *J. Phys. Chem. A* **2000**, *104*, 7452.
27. Hasegawa, M.; Enomoto, S.; Hoshi, T.; Igarashi, K.; Yamazaki, T.; Nishimura, Y.; Speiser, S.; Yamazaki, I. *J. Phys. Chem. B* **2002**, *106*, 4925.
28. Williams, A. T. R.; Winfield, S. A.; Miller, J. N. *Analyst* **1983**, *108*, 1067.
29. Strickler, S. J.; Berg, R. A. *J. Chem. Phys.* **1962**, *37*, 814.
30. Scholes, G. D. *Annu. Rev. Phys. Chem.* **2003**, *54*, 57.
31. Forster, T. *Disc. Faraday Soc.* **1959**, *27*, 7.
32. Knox, R. S.; van Amerongen, H. *J. Phys. Chem. B* **2002**, *106*, 5289.
33. Berney, C.; Danuser, G. *Biophys. J.* **2003**, *84*, 3992.
34. Stryer, L. *Annu. Rev. Biochem* **1978**, *47*, 819.
35. Harriman, A.; Hissler, M.; Ziessel, R. *Phys. Chem. Chem. Phys.* **1999**, *1*, 4203.
36. Benniston, A. C.; Harriman, A.; Li, P. Y.; Sams, C. A. *J. Phys. Chem. A* **2005**, *109*, 2302.